Dense Stellar Systems and Massive Black Holes: Sources of Gravitational Radiation and Tidal Disruptions

Dissertation zur Erlangung des akademischen Grades
doctor rerum naturalium habilitatus (Dr. rer. nat. habil)
in der Wissenschaftsdisziplin "Astronomie"

eingereicht als *kumulative Dissertation*
an der Mathematisch-Naturwissenschaftlichen Fakultät
der Universität Potsdam

von

Dr. Pau Amaro Seoane

Potsdam, September 4, 2015

Max-Planck-Institut für Gravitationsphysik (Albert-Einstein-Institut)

Published online at the
Institutional Repository of the University of Potsdam:
URN urn:nbn:de:kobv:517-opus4-95439
http://nbn-resolving.de/urn:nbn:de:kobv:517-opus4-95439

CONTENTS

GLOSSARY

Acronym	Meaning
$1\,M_\odot$	1 Solar Mass = 1.99×10^{30} kg
1 pc	1 parsec $\approx 3.09 \times 10^{16}$ m
1 Myr/Gyr	One million/billion years
AGN	Active Galactic Nucleus
BH	Black Hole
CO	Compact Object (a white dwarf or a neutron star), or a stellar-mass black hole. In general, a collapsed star with a mass $\in [1.4, 10]\,M_\odot$ in this work
EMRI	Extreme Mass Ratio Inspiral
GC	Galactic Centre
GPU	Graphics Processing Unit
GW/GWs	Gravitational Wave/s
HB	Giant stars in the horizontal branch
IMBH	Intermediate-Mass Black Hole ($M \in [10^2, 10^5]\,M_\odot$)
IMRI	Intermediate Mass Ratio Inspiral
MBH	Massive Black Hole ($M \approx 10^6 M_\odot$)
MW	Milky Way
NB6	Direct-summation $N-$body6
NS	Neutron Star
PN	post-Newtonian
RG	Red giant
SMBH	Super Massive Black Hole ($M > 10^6 M_\odot$)
SNR	Signal-To-Noise Ratio
SPH	Smoothed Particle Hydronamics
TDE	Tidal Disruption Event
UCD	Ultra-Compact Dwarf Galaxy

Abstract:

Massive, dark objects, very likely supermassive black holes (SMBH), are found in the majority of galaxies. The observed tight correlations between their masses and the surrounding stellar system indicate an enigmatic coevolution. Why does the mass of an object, whose typical size is $\sim 10^{-7}$ parsec (pc, for a mass of $10^6\,M_\odot$) correlates with the stellar properties of the entire galaxy, which can be some 10^3 pc in size? Are these objects black holes, as predicted by Einstein's theory of general relativity or do we need alternatives? The answer lies in the event horizon, the single and unique characteristic that defines SMBHs. To probe it, we have at our disposal stars. Nuclear star clusters harboring a massive, dark object with a mass of up to $\sim 10^7\,M_\odot$ are good testbeds to probe the event horizon of the potential SMBH with stars. The advantage is clear: Stellar dynamics around a massive object is a relatively simple multi-particle problem, and we have data: In our own galaxy we have observations of stars and clouds that are on very close orbits to our SMBH. In other galaxies we have detected about 50 stellar tidal disruption candidates, and this number should rapidly increase with the upcoming transient surveys. One of the most important sources of gravitational waves (GWs) for a space-based detector are extreme-mass-ratio binaries (EMRIs) in the stage where the dynamics are driven by GW emission. These systems are composed of a stellar-mass compact object (a white dwarf, a neutron star, or a stellar-mass black hole) that inspirals into a massive black hole located at a galactic centre. The masses of interest for the small compact object are in the range $m = 1 - 10^2\ M_\odot$, and for the massive black hole in the range $M = 10^5 - 10^7\ M_\odot$. Then, the mass-ratio for these systems is in the interval $\mu = m/M \sim 10^{-7} - 10^{-3}$. The GW signals emitted by EMRIs are long lasting (months to years) and contain many GW cycles, of the order of 10^5 during the last year before the small compact object plunges into the massive black hole. Many of these cycles are spent in the neighbourhood of the massive black hole horizon, meaning GWs encode a map of the strong-field region of the massive black hole, the fabric of space and time. These extraordinary features of EMRIs allow for a revolutionary research program, which could lead to understanding different aspects of stellar dynamics in galactic centres, tests of the geometry of BHs, and tests of General Relativity and alternative theories of gravity. In this habilitation I present my main results in this line of research.

Part I

INTRODUCTION

1

MOTIVATION

The centre-most part of a galaxy, its *nucleus* consists of a cluster of a few 10^7 to a few 10^8 stars surrounding the DCO, assumed from now onward to be a MBH, with a size of a few pc. The nucleus is naturally expected to play a major role in the interaction between the DCO and the host galaxy, as we mentioned before. In the nucleus, stellar densities in excess of $10^6\,\mathrm{pc}^{-3}$ and relative velocities of order a few 100 to a few $1000\,\mathrm{km\,s}^{-1}$ are reached. In these exceptional conditions, unlike anywhere else in the bulk of the galaxy, collisional effects come into play. These include 2-body relaxation, i.e., mutual gravitational deflections, and genuine contact collisions between stars.

This means that, if a star happens to pass very close to the MBH, some part of it or all of it may be torn apart because of the so-called tidal gravity of the central object. The difference in gravitational forces on points diametrically separated on the star alter its shape, from its initial approximately spherical architecture to an ellipsoidal one and, in the end, the star is disrupted.

These processes may contribute significantly to the mass of the MBH. Tidal disruptions trigger phases of bright accretion that may reveal the presence of a MBH in an otherwise quiescent, possibly very distant, galaxy.

In Figure 1 we give an intuitive image of a tidal disruption of an extended star, where distortions due to gravitational-lens have not been taken into consideration. In Figure 2, on the left we show a Chandra X-ray image of J1242-11 with a scale of 40 arcsec on a side. This figure pinpoints one of the most extreme variability events ever detected in a galaxy. One plausible explanation for the extreme brightness of the ROSAT source could be accretion of stars on to a super-massive black hole. On the right we have its optical companion piece, obtained with the 1.5 m Danish telescope at ESO/La Silla. The right circle indicates the position of the Chandra source in the centre of the brighter galaxy.

These processes may contribute significantly to the mass of the MBH [30, 53]. Tidal disruptions trigger phases of bright accretion that may reveal the presence of a MBH in an otherwise quiescent, possibly very distant, galaxy [29, 34].

On the other hand, stars can be swallowed whole if they are kicked directly through the horizon of the MBH (so-called *direct plunges*) or gradually inspiral due to the emission of GWs The latter process, known as an " *Extreme Mass Ratio Inspiral*" (EMRI) is one of the main objects of interest for eLISA [Evolved Laser Interferometer Space Antenna 3]. A compact object, such as a star so dense that it will not be disrupted

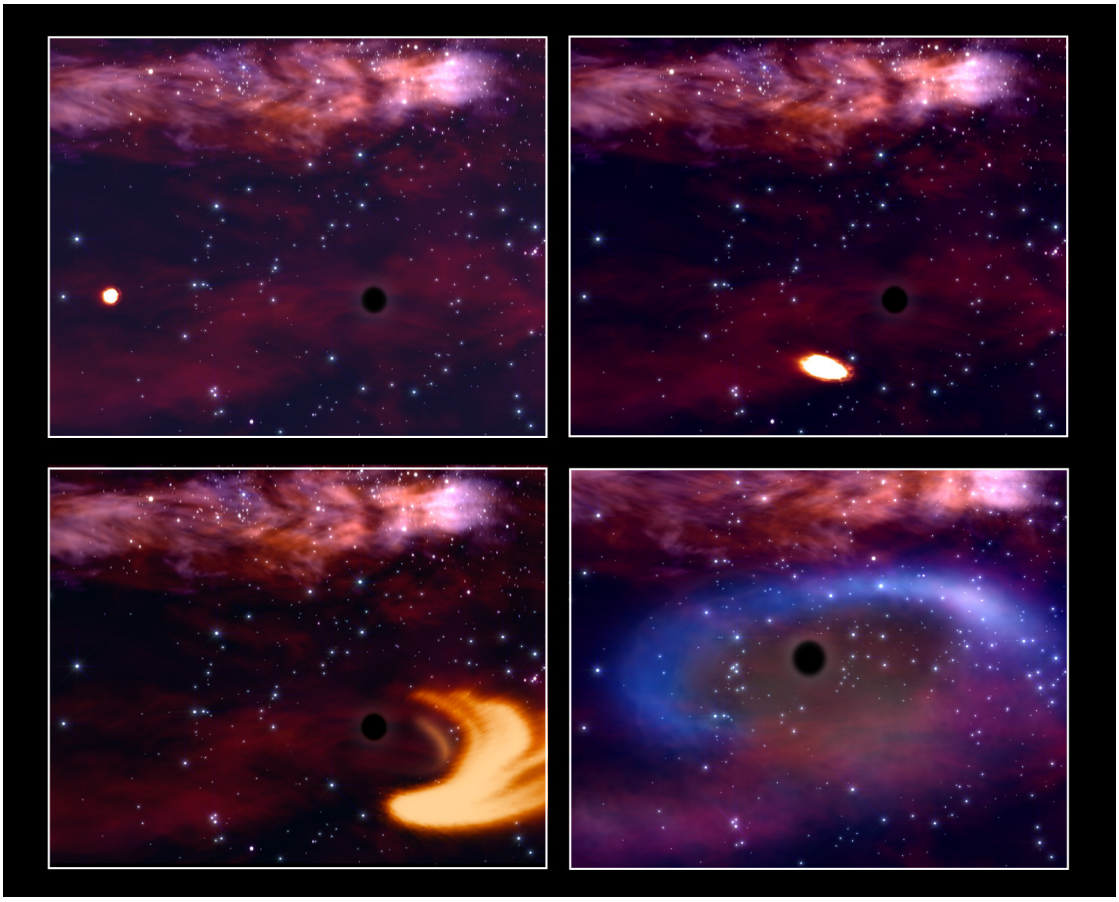

Figure 1: Schematic representation of the tidal disruption process. In the first panel on the left, an extended star approaches the central MBH. As soon as the star feels the overwhelming tidal forces acting on it, the initial spherical architecture becomes spheroidal and the star stars to be torn apart. On the third panel the star is totally ripped and about 50% of it accreted on to the MBH. Credits: ESA and Stefanie Komossa. Illustration credit M. Weiss.

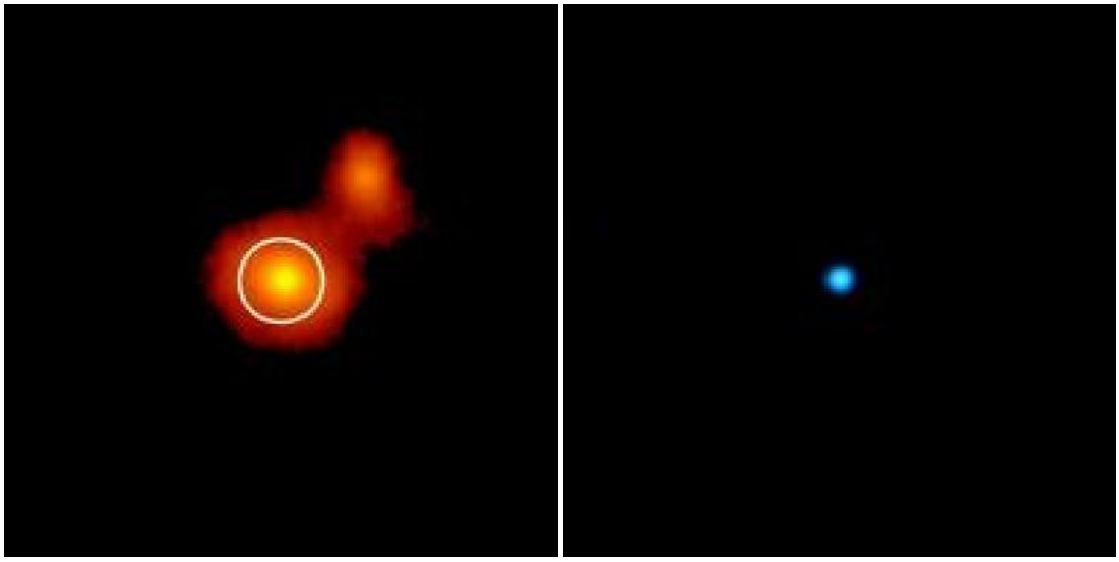

Figure 2: Optical and X-ray images of RX J1242-11. Credits: (left) ESO/MPE/S.Komossa and (right) NASA/CXC/MPE, [37].

by the tidal forces of the MBH, (say, a neutron star, a white dwarf or a small stellar black hole), is able to approach very close to the central MBH. When the compact object comes very close to the MBH, a large amount of orbital energy is radiated away, causing the semi-major axis shrink. This phenomenon will be repeated thousand of times as the object inspirals until is swallowed by the central MBH.

The "doomed" object spends many orbits around the MBH before it is swallowed. When doing so, it radiates energy which can be conceptualised as a snapshot containing detailed information about space-time and *all the physical parameters* which characterise the binary, the MBH and the small stellar black hole: their masses, spins, inclination and their sky position. The emitted GWs encode a map of the space-time. If we can record and decode it, then we will be able to test the theory that massive dark objects are indeed Kerr black holes as the theory of general relativity predicts, and not exotic objects such as boson stars. This would be the ultimate test of general relativity.

The detection of such an EMRI will allow us to do very exciting science: EMRIs will give us measurements of the masses and spins of BHs to an accuracy which is beyond that of any other astrophysical technique. Such information will tell us about cosmic evolution, about the history and growth of MBHs in the nearby universe, with an accuracy which has no precedent.

2

RELAXATION IN GALACTIC NUCLEI

For convenience, we will consider that our system is spherically symmetric. Since we are interested in the close interaction between stars (both compact objects and extended stars, such as our sun), we need a source of exchange of E and J. We use and abuse the term collisional by any effect not present in a smooth, static potential including what is known in planetary dynamics as secular effects. Among these, standard two-body relaxation excells not due to its relevance of contributing to EMRI or TDE sources, but due to the fact that this is the best-studied effect; namely the exchange of E and J between stars due to gravitational interactions.

Another possibility is physical collisions[1]. The stars come so close to each other that they collide, they have a hydrodynamic interaction; the outcome depends on a number of factors, but the stars involved in the collision could either merge with each other or destroy each other completely or partially. Surprisingly, the impact of these processes for the global evolution of the dynamics of galactic nuclei is negligible [30]. In most of the cases when these extended stars, such as main-sequence stars (MS) collide, they do not merge due to the very high velocity dispersion, and they will also not be totally destroyed, because for that they would need a nearly head-on collision, so that they have a partial mass-loss and are for our purposes uninteresting. For the kind of objects of interest to us in this review, stellar black holes, the probability that they physically collide or have a non-Newtonian interaction is negligible.

A third way of altering the J of stars are secular effects. They do nevertheless *not* modify the E. If we assume that the orbits around the MBH are nearly Keplerian, the shape, an ellipse, does not change and the orientation will not change much. If we have another orbit with a different orientation, both orbits will exert a torque $\mathcal{T}$ on each other. This will change J but not E. A Keplerian orbit can be described with its semi-major axis a and eccentricity e. The a is only connected to E and, for a given a the e is connected to the J. If one changes the J but not the E, the e will vary but not the a. By decreasing the J, one increases the e.

In this section, however, we introduce the fundamentals of relaxation theory, focusing on the aspects that will be more relevant for the main interest of this review. Further ahead we will address resonant relaxation and other "exotic" (in the sense

1 The terminology is somehow and as forewarned misleading; whilst in general we refer to "collisional" to any effect leading to exchange of E and J among stars, here we mean real collisions between two stars. For a thorough discussion of the mechanism and an extremely detailed numerical study, we refer the reader to [30].

that they are not part of the traditional two-body relaxation theory) processes. For a comprehensive discussion on two-body relaxation, we recommend the text books [59] and [11] or, for a shorter but very nice introduction, the article [24].

We will first introduce handy timescales in Section 2.1 that will allow us to pinpoint the relevant physical phenomena that reign the process of bringing stars (extended or compact) close to the central MBH. We will then address a particular case of relaxation, in Section 2.2, dynamical friction. Later, in Section 2.3, we will define more concisely the region of space-phase in which we expect stars to interact with the central MBH. Once we have all of these concepts, we can cope with the problem of how mass segregates in galactic nuclei. We will first see in detail the "classical" solution to introduce in the papers a more recent and very important result, the so-called strong mass segregation.

2.1 TWO-BODY RELAXATION

We introduce in this subsection some useful time-scales to which we will refer often throughout this review; namely the relaxation time, the crossing time and the dynamical time. These three time-scales allow us to delimit our physical system.

THE RELAXATION TIME [19] defined as a time-scale which stems from the 2-body small-angle encounters and gives us a typical time for the evolution of a stellar system.

This relaxation time could be regarded as an analogy of the shock time of the gas dynamics theory, by telling us when a particle (a star) has forgotten its initial conditions or, expressed in another way, when the local thermodynamical equilibrium has been reached. Then we can roughly say that the most general idea is that this is the time over which the star "forgets" its initial orbit due to the series of gravitational tugs caused by the passing-by stars. After a relaxation time the system has lost all information about the initial orbits of all the stars. This means that the encounters alter the star orbit from the one it would have followed if the distribution of matter were smooth. Therewith can we regard *the relaxation time* as the time interval required for the velocity distribution to reach the Maxwell-Boltzmann form.

Consider two stars of masses m_1 and m_2 deflecting eachother such as in Figure 3. The deflection angle θ is given by the relation

$$\tan\frac{\theta}{2} = \frac{b_0}{b}, \text{ with } b_0 = \frac{G(m_1+m_2)}{v_{\text{rel}}^2} \tag{1}$$

If the relative velocity v_{rel} is high, θ is small and the larger the mass, the stronger the deflection. This simple relation expresses the kernel of relaxation. One has to integrate it over all possible parameters to get the relaxation rate. When we do the integration over the impact parameter b whilst keeping v_{rel} and the masses fixed, we have the following picture of Figure 4. The test star encounters a lot of field stars, all of them

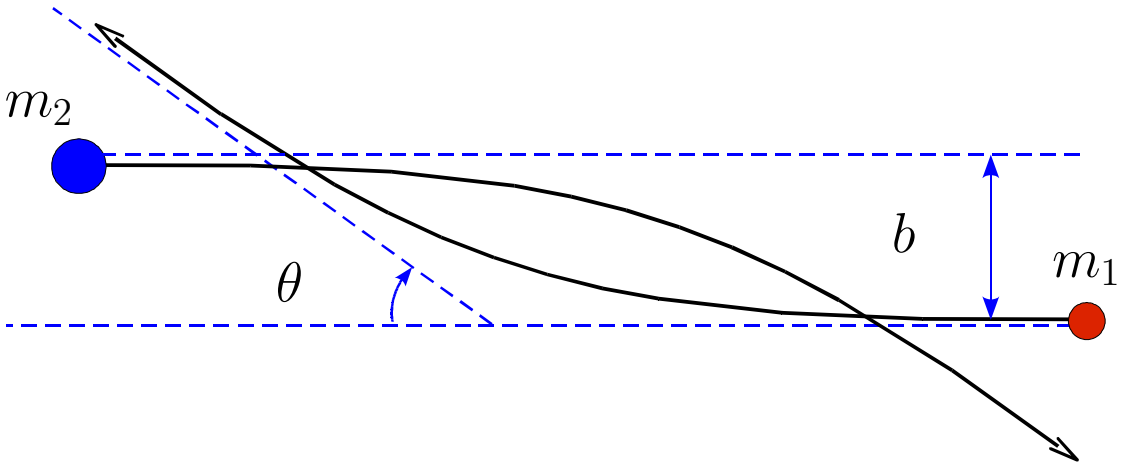

Figure 3: Deflection angle θ of a "test" star of mass m_1 with a field star of mass m_2.

with the same mass m_2 and relative velocity $\mathbf{v}_{\rm rel}$. After a time δt, the velocity vector of the test star has slightly changed direction by an angle $\theta_{\delta t}$. On average, $\langle \theta_{\delta t} \rangle = 0$ but

$$\langle \theta^2_{\delta t} \rangle = \left(\frac{\pi}{2}\right)^2 \frac{\delta t}{\hat{t}_{\rm rlx}} \tag{2}$$

Therefore it is a *diffusion* process; $\langle \theta^2_{\delta t} \rangle \propto \delta t$ [see, e.g., 33, 60]. We have introduced the special relaxation time for this situation as

$$\hat{t}_{\rm rlx} = \frac{\pi}{32} \frac{v^3_{\rm rel}}{\ln\Lambda\, G^2\, n_\star (m_1 + m_2)^2} \tag{3}$$

In this last equation, $\ln\Lambda$, the Coulomb logarithm, has appeared as a result of integrating for all impact parameters. The information encoded in it is how many orders of magnitude of b contribute to the relaxation,

$$\ln\Lambda = \ln \frac{b_{\rm max}}{b_0} \simeq \ln \frac{P_{\rm orb}}{b_0 / v_{\rm rel}} \tag{4}$$

In this last equation b_0, which we introduced before, is the effective minimum impact parameter for relaxation. Our main focus is not a detailed review of stellar dynamics. For a detailed description of the Coulomb logarithm, we refer the reader to [11, 40]. Therefore, we will simply comment that, for our purposes, $\ln\Lambda \approx 10 - 15$ always. This is very useful because the exact calculation can be rather arduous and almost an incubus which to our knowledge nobody has attempted to implement in any calculation. Therefore we mention only two special cases for the argument of the logarithm,

$$\Lambda \approx \begin{cases} 0.01\, N_\star & \text{(a) for self-gravitating} \\ & \text{stellar cluster} \\ \mathcal{M}_\bullet / m & \text{(b) close to the MBH} \end{cases} \tag{5}$$

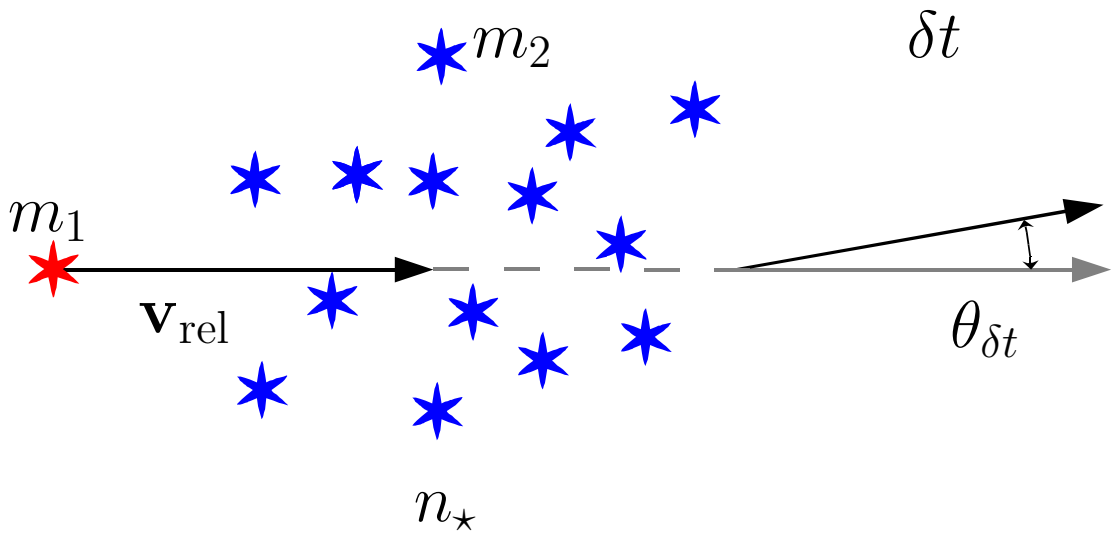

Figure 4: The test stars suffers a change in direction by $\theta_{\delta t}$ due to the accumulation of encounters with field stars.

In case (a) we have a self-gravitating cluster of stars in equilibrium with itself but lacking a central MBH. The argument is proportional to the number of stars in the system. In the situation in which a star is orbiting the MBH, the previous value is formally no longer valid and one should use the value (b). Nevertheless, in effect this is neglected because the value turns out to be ~ 10. To define a local average value of the relaxation time by integrating over the distribution of relative velocities.

It must nevertheless be noted that the way in which we have introduced the concept of the relaxation time is a particular one. In equation 3 we have introduced the "encounter relaxation time" to stress that it depends on the characteristics of a peculiar class of encounter: a star of mass m_1 with "field stars" of mass m_2 with a local density $n_\star$ and a relative velocity $v_{\rm rel}$. It can be envisaged as the required time to deflect gradually the motion of star m_1 due to encounters with field stars by a RMS angle $\pi/2$. This definition is useful to understand the fundamentals of relaxation, but it must be noted that it is subject to this very peculiar type of encounter. However, in a general case, we define the relaxation time inside the radius of influence for a system in which the distribution of stars is spherically symmetric, the stellar-mass compact objects are treated as single objects, with a two-body relaxation as the only mechanism that can change the angular momentum and no mass segregation within the influence radius

$$r_{\rm infl} = \frac{GM_{\rm BH}}{\sigma_0^2} \approx 1 \text{ pc} \left(\frac{M_{\rm BH}}{10^6\, M_\odot}\right) \left(\frac{60 \text{ km/s}}{\sigma_0}\right)^2, \tag{6}$$

Figure 5: Definition of the collision time.

within which the central MBH dominates the gravitational field, as

$$t_{\rm rlx}(r) = \frac{0.339}{\ln\Lambda}\frac{\sigma^3(r)}{G^2\langle m\rangle m_{\rm CO} n(r)} \simeq 1.8\times10^8\,{\rm yr}\left(\frac{\sigma}{100\,{\rm km\,s^{-1}}}\right)^3\left(\frac{10\,M_\odot}{m_{\rm CO}}\right)\left(\frac{10^6\,M_\odot{\rm pc}^{-3}}{\langle m\rangle n}\right). \tag{7}$$

Here $\sigma(r)$ is the local velocity dispersion. It is approximately equal to the Keplerian orbital speed $\sqrt{GM_{\rm BH}r^{-1}}$ for $r < r_{\rm infl}$ and has a value $\approx \sigma_0$ outside of it. $n(r)$ is the local number density of stars, $\langle m\rangle$ is the average stellar mass, $m_{\rm CO}$ is the mass of the compact object (we take a standard $m_{\rm CO} = 10\,M_\odot$ for stellar-mass black holes).

For typical density profiles, $t_{\rm rlx}$ decreases slowly with decreasing r inside $r_{\rm infl}$. It should be noted that the exchange of energy between stars of different masses — sometimes referred to as dynamical friction, as we will see ahead, in section 2.2 in the case of one or a few massive bodies in a field of much lighter objects— occurs on a timescale shorter than $t_{\rm rlx}$ by a factor of roughly $M/\langle m\rangle$, where M is the mass of a heavy body.

As we will see later, relaxation redistributes orbital energy amongst stellar-mass objects until the most massive of them (presumably stellar-mass black holes) form a power-law density cusp, $n(r) \propto r^{-\gamma}$ with γ ranging between $\simeq 1.75-2.1$ around the MBH –depending on the solution to mass segregation considered– while less massive species arrange themselves into a shallower profile, with $\alpha \simeq 1.4-1.5$ [2, 4, 8, 12, 13, 22, 28, 44, 48]. Nuclei likely to host MBHs in the LISA mass range ($M_{\rm BH} \lesssim$ few $\times\,10^6\,M_\odot$) probably have relaxation times comparable to or less than a Hubble time, so that it is expected that their heavier stars form a steep cusp.

COLLISION TIME $t_{\rm coll}$ is defined as the mean time which has passed when the number of stars within a volume $V = \Sigma v_{\rm rel}\triangle t$ is one (see Figure 5), where $v_{\rm rel}$ is the relative velocity at infinity of two colliding stars.

Computed for an average distance of closest approach $\bar{r}_{\rm min} = \frac{2}{3} r_\star$, this time is

$$n_\star V(t_{\rm coll}) = 1 = n_\star \, \Sigma \, v_{\rm rel} \, t_{\rm coll}. \tag{8}$$

And so,

$$t_{\rm coll} = \frac{m_\star}{\rho_\star \Sigma \sigma_{\rm rel}}, \tag{9}$$

with

$$\Sigma = \pi \bar{r}_{\rm min}^2 \left(1 + \frac{2 G m_\star}{\bar{r}_{\rm min} \sigma_{\rm rel}^2} \right); \tag{10}$$

$\sigma_{\rm rel}^2 = 2\sigma_\star^2$ is the stellar velocity dispersion and Σ a collisional cross section with gravitational focusing

THE CROSSING TIME As the name suggests, this is the required time for a star to pass through the system, to *cross* it. Obviously, its value is given by the ratio between space and velocity,

$$t_{\rm cross} = \frac{R}{v}, \tag{11}$$

where R is the radius of the physical system and v the velocity of the star crossing it.

For instance, in a star cluster it would be:

$$t_{\rm cross} = \frac{r_{\rm h}}{\sigma_{\rm h}}; \tag{12}$$

where $r_{\rm h}$ is the radius containing 50 % of the total mass and $\sigma_{\rm h}$ is a typical velocity taken at $r_{\rm h}$. One denominates it *velocity dispersion* and is introduced by the statistical concept of root mean square (RMS) dispersion; the *variance* σ^2 gives us a measure for the dispersion, or scatter, of the measurements within the statistical population, which in our case is the star sample,

$$\sigma^2 = \frac{1}{N} \sum_{i=1}^{N} (x_i - \mu_a)^2.$$

Where x_i are the individual stellar velocities and μ_a is the arithmetic mean,

$$\mu_a \equiv \frac{1}{N} \sum_{i=1}^{N} x_i.$$

If Virial equilibrium prevails, we have $\sigma_{\rm h} \approx \sqrt{G M_{\rm h} / r_{\rm h}}$, then we get the dynamical time-scale

$$t_{\rm dyn} \approx \sqrt{\frac{r_{\rm h}^3}{G M_{\rm h}}} \approx \frac{1}{\sqrt{G \rho_\star}}, \tag{13}$$

where $\rho_\star$ is the mean stellar density.

On the contrary to the gas dynamics, the thermodynamical equilibrium time-scale $t_{\rm rlx}$ in a stellar system is large compared with the crossing time $t_{\rm cross}$. In a homogeneous, infinite stellar system, we expect in the limit $t \to \infty$ some kind of stationary state to be established. The decisive feature for such a Virial equilibrium is how quick a perturbation of the system will be smoothed down.

The dynamical time in Virial equilibrium is [cf., e.g., 40]:

$$t_{\rm dyn} \propto \frac{\log(\gamma N)}{N} t_{\rm rlx} \ll t_{\rm rlx}. \tag{14}$$

If we have perturbations in the system because of the heat conduction, star accretion on the BH, etc. a new Virial equilibrium will be established within a $t_{\rm dyn}$, which is short. This means that we get again a Virial-type equilibrium in a short time. This situation can be considered not far from a Virial-type equilibrium. We say that the system *changes in a quasi-stationary way*.

2.2 DYNAMICAL FRICTION

Consider now a star more massive than the average. In this case, relaxation boils down to dynamical friction. The massive intruder will suffer from dynamical friction, which is an effect of all encounters with lighter stars. For this special kind of star, the timescale over which its orbital parameters change is not the usual relaxation time. This star will lose kinetic energy in the following timescale:

$$t_{\rm DF} \sim \frac{\langle m \rangle}{m} t_{\rm rlx} \tag{15}$$

As we can see, if the object is $10-20$ times more massive than the average, as in the case of a stellar black hole, this timescale is 20 times shorter than the $t_{\rm rlx}$.

In Figure 6 we have an illustration for what DF is. A massive intruder, a stellar black hole, is travelling in a homogeneous sea of stars of density ρ and velocity dispersion σ. The velocity vectors of the stars are rotated after the deflection and the projected component in the direction of the deflection is shorter. Therefore, the massive object is accumulating just after it a high-density stellar region. The perturber will feel a drag from that region from the conservation of J in the direction of its velocity vector, just as depicted in Figure 7. The direction does not change to first-order, but the amplitude decreases. The intruder will feel a force given by the Chandrasekhar formula,

$$\begin{aligned} \vec{a}_{\rm DF} = & -\frac{\vec{v}}{t_{\rm DF}} \\ & - \frac{4\pi \ln\Lambda\, G^2 \rho\, M}{v^3}\, \xi(X)\vec{v} \end{aligned} \tag{16}$$

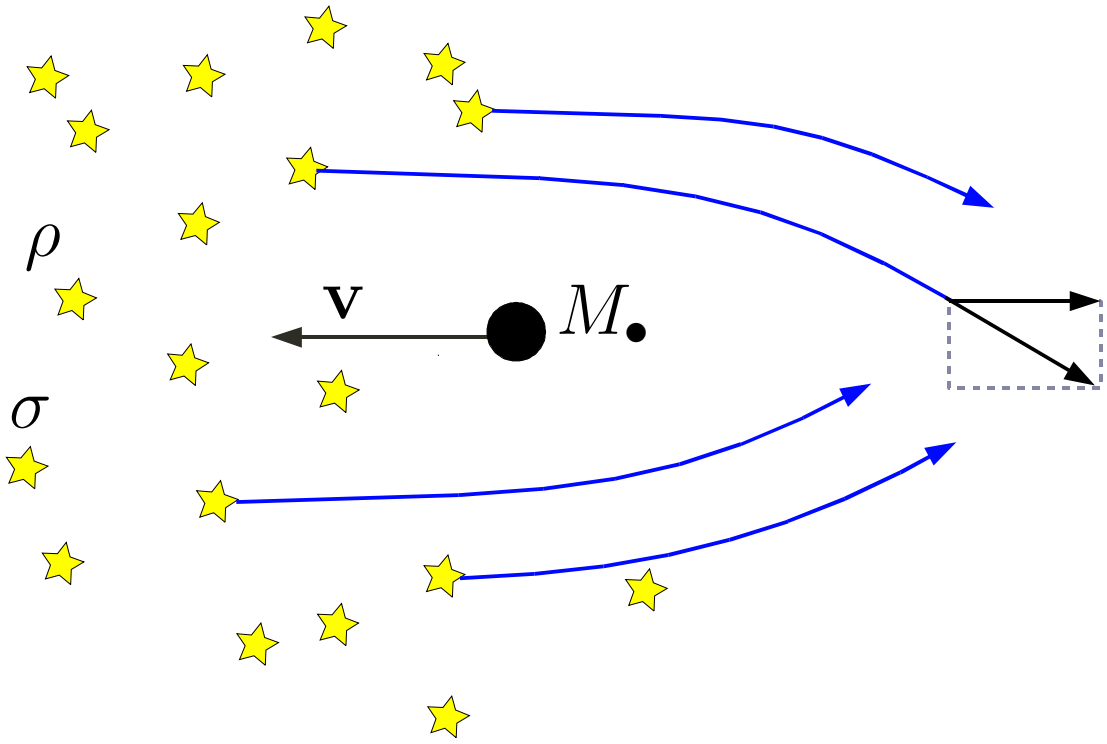

Figure 6: In the reference frame of the encounter we depict a massive interloper, a stellar black hole, traversing a sea of lighter stars which are deflected by it. The velocity vector of the stellar black hole is bearely modified (at least in direction) by the deflections, because they cancel out on average.

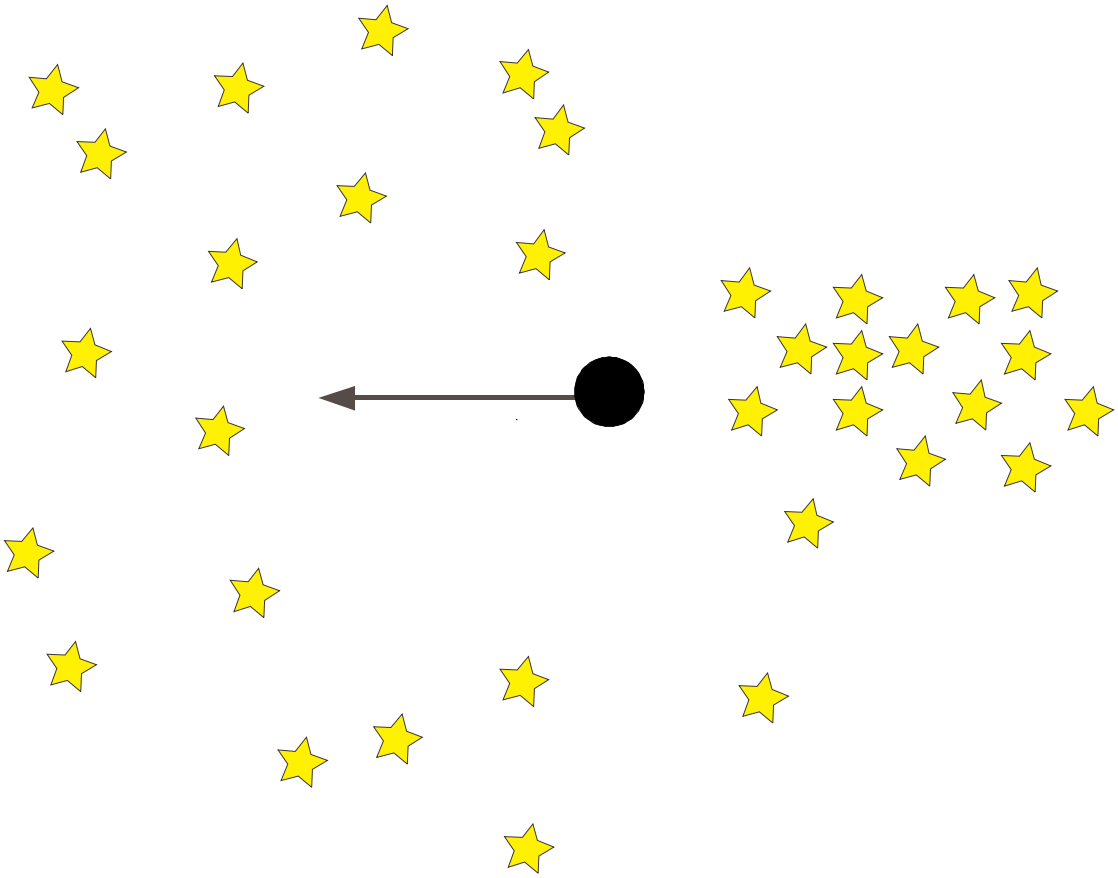

Figure 7: The agglomeration of stars right behind the massive perturber creates a region of stellar overdensity that acts on the perturber, slowing it down, braking it.

In this last equation,

$$\xi(X) = \mathrm{erf}(X) - 2\pi^{-1/2} X e^{-X^2} \tag{17}$$
$$X = \frac{v}{\sqrt{2}\sigma}$$

The most interesting point is that if we plug into Eq. 17 the velocity of the perturber which is $v \approx \sigma$, we have that

$$t_{\mathrm{DF}} \sim \frac{m}{M} t_{\mathrm{rlx}} \ll t_{\mathrm{rlx}} \tag{18}$$

As we have already mentioned before, galactic nuclei in the range of what a mission like LISA could observe have relaxation times that are shorter than a Hubble time. In Figure 8, which is an adapted version of the figure to be found in the article of [26], we have a schematic representation of what relaxation times in other observed

galaxies could be. Each dot shows the mass of the central MBH or the upper limit to it (the arrows). From this mass we can derive what the velocity dispersion would be at 0.1 pc and from observations of the brightness surface profiles we can estimate what the stellar density at that distance would be. In many cases this distance is usually not resolvable, so that one has to extrapolate in order to obtain the density at 0.1 pc, which is what has been done in the figure. The blue, dashed lines correspond to $t_{\rm rlx}(r = 0.1\,{\rm pc})$, the relaxation time at that distance. Any system below 10^{10} yrs should be relaxed and is, hence, interesting. For the range of frequencies we are interested in, MBHs with masses typically less than a few $10^7\,M_\odot$ (the region below the red line) we can see only three systems (since M110 is only an upper limit) and M33 possibly lacks an MBH. This low number does not mean that nuclei in the range of frequencies of interest are rare, it simply means that it is hard to observe MBHs in that range of masses. In this regard, a GW mission that could observe MBHs in that region would provide us with very valuable information, since in the electromagnetic domain we are still far from resolving those nuclei.

2.3 THE DIFUSSION AND LOSS-CONE ANGLES

As we have seen, the relaxation time is the required time for $\triangle v_\perp^2 / v_\perp^2 \simeq 1$ (i.e., the change in the perpendicular velocity component is of the same order as the perpendicular velocity component itself);

$$\begin{aligned} \triangle v_\perp^2 &= n_{\rm rlx} \cdot \delta v_\perp^2, \\ \triangle v_\perp^2 / v_\perp^2 &= 1 = \frac{n_{\rm rlx} \cdot \delta v_\perp^2}{v_\perp^2} \end{aligned} \tag{19}$$

$$t_{\rm rlx} = n_{\rm rlx} \cdot t_{\rm dyn} = \left(\frac{v_\perp^2}{\delta v_\perp^2} \right) \cdot t_{\rm dyn}, \tag{20}$$

where $n_{\rm rlx}$ is the numbers of crossings for $\triangle v_\perp^2 / v_\perp^2 \simeq 1$. This conforms to the definition of the relaxation time,$\triangle v_\perp^2 / v_\perp^2 = t / t_{\rm rlx}$ [17].

If we consider that $\theta_{\rm D}$ is very small,

$$\begin{aligned} \sin\theta_{\rm D} &\simeq \frac{\delta v_\perp}{v} \simeq \theta_{\rm D} \\ t_{\rm rlx} &\simeq \frac{t_{\rm dyn}}{\theta_{\rm D}^2} \end{aligned} \tag{21}$$

$$\theta_{\rm D} \simeq \sqrt{\frac{t_{\rm dyn}}{t_{\rm rlx}}}. \tag{22}$$

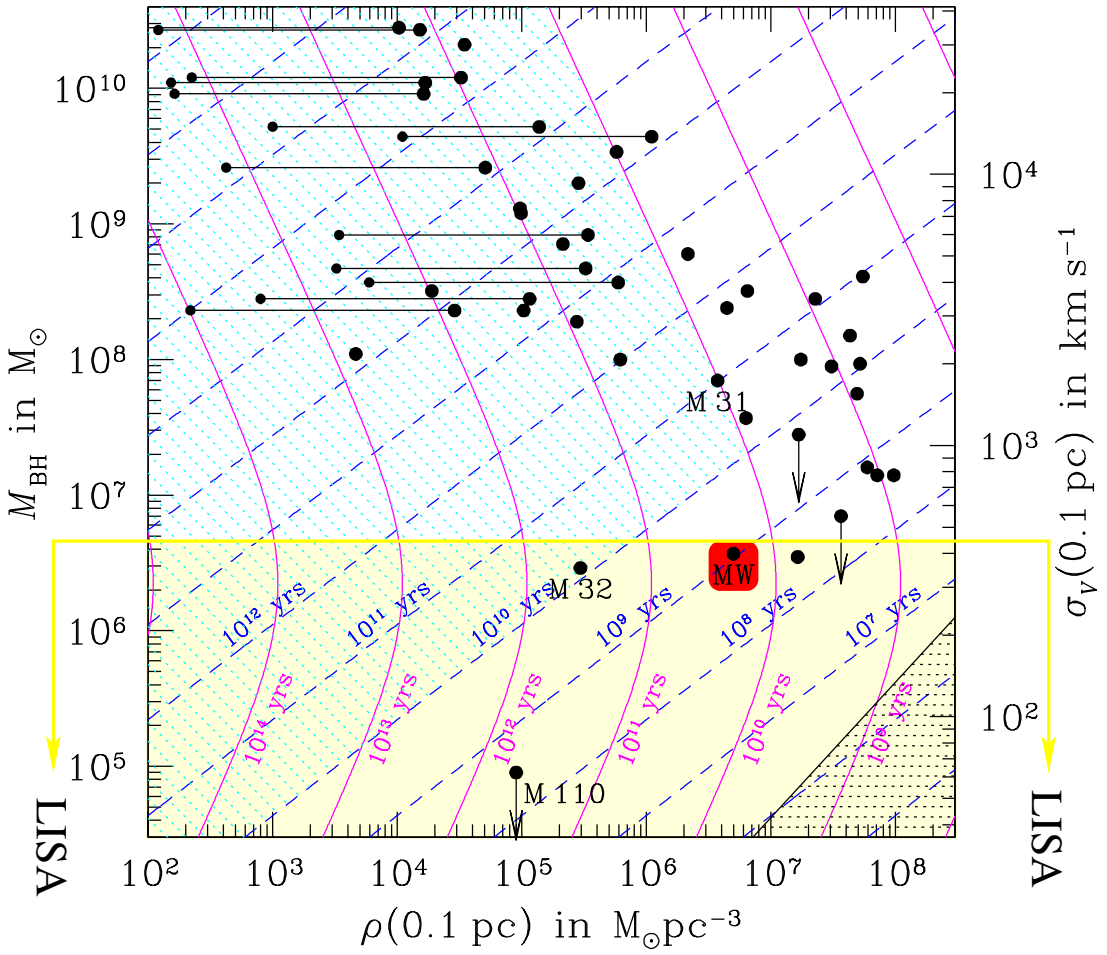

Figure 8: Plane of the stellar density at 0.1 pc and the mass of the central MBH [taken from 26] Relaxation (and collision times) at 0.1 pc from an MBH in the centre of a galactic nucleus.

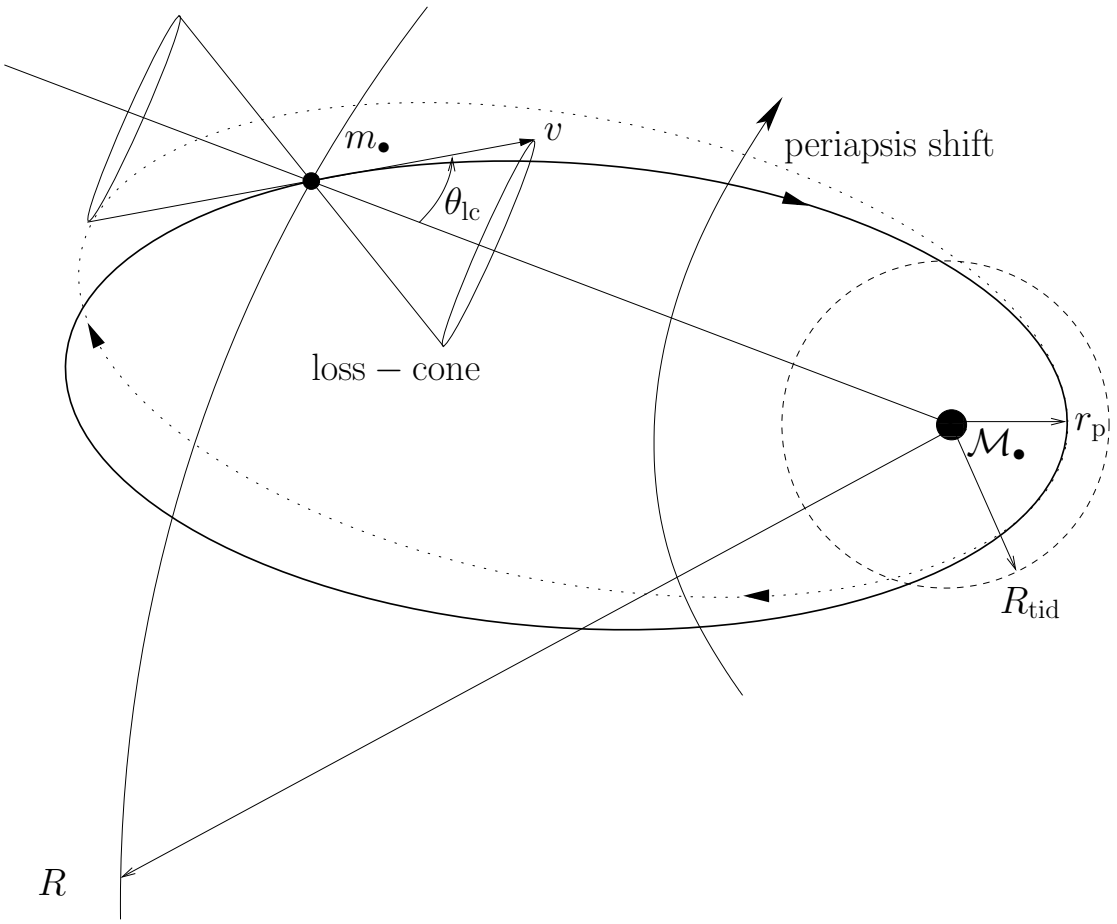

Figure 9: Definition of the angle $\theta_{\rm lc}$.

We now introduce the loss-cone angle $\theta_{\rm lc}$ as an illustrative example. Suppose that the central object with mass $\mathcal{M}_\bullet$ has an influence radius $r_{\rm h}$. To define this radius we say that a star will interact with the central object only when $r \leq r_{\rm h}$. Then we look for a condition at a place $r > r_{\rm h}$ for a star to touch or to cross the influence radius of the central object within a crossing time $t_{\rm cross} = r/\sigma_{\rm r}$.

As we saw in the text, the condition that defines this angle is the following:

$$\begin{aligned} r_{\rm p}(E, L) &\leq r_{\rm t}, \\ \theta &\leq \theta_{\rm lc}. \end{aligned} \tag{23}$$

$$\sin\theta = \frac{v_t}{v}, \text{ with } \theta \ll 1$$
$$\theta \simeq \frac{v_t}{v} = \frac{L/r}{v}. \tag{24}$$

Where $L := r\, v_t$ is the specific angular momentum.

Now we derive an expression for this angle in terms of the influence radius. Within the region $r \leq r_h$ the star moves under the MBH potential influence, then

$$\sigma(r) \approx \sqrt{\frac{G\mathcal{M}_\bullet}{r}} = \sqrt{\frac{G\mathcal{M}_\bullet}{R_h}}\sqrt{\frac{R_h}{r}}$$
$$= \sigma(R_h)\sqrt{R_h/r} = \sigma_c\sqrt{R_h/r}, \tag{25}$$

since $\sigma_c^2 \equiv G\mathcal{M}_\bullet/R_h$. The typical velocity of the orbit is $\langle v^2\rangle \simeq 3\sigma^3$, where the factor three stands for the three directions in the space. Since σ means the one- dimensional dispersion, we have to take into account the dispersion of the velocity in each direction. Then,

$$\langle v\rangle \simeq \sqrt{3}\sigma_c\sqrt{r_h/r}. \tag{26}$$

Finally, we obtain the loss-cone angle,

$$\theta_{lc} = \sqrt{\frac{2}{3}\frac{r_t}{r}}. \tag{27}$$

In the region in which $r \geq r_h$ we can consider that the velocity dispersion is more or less constant from this r_h onwards, $v \approx \sqrt{3}\sigma_c$,

$$\theta_{lc} = \frac{\sqrt{2G\mathcal{M}_\bullet r_t}}{\sqrt{3}r\sigma_c};$$
$$\sigma_c = \sqrt{G\mathcal{M}_\bullet/r_h}. \tag{28}$$

The angle is

$$\theta_{lc} \approx \frac{1}{r}\sqrt{\frac{2\, r_t\, r_h}{3}} \tag{29}$$

We derive the loss-cone velocity $v_{lc}(r)$ using angular momentum and energy conservation arguments. We just have to evaluate it at a general radius r and at the tidal radius r_t, where the tangential velocity is maximal and the radial velocity cancels (see Figure 10).

For a general radius we have that

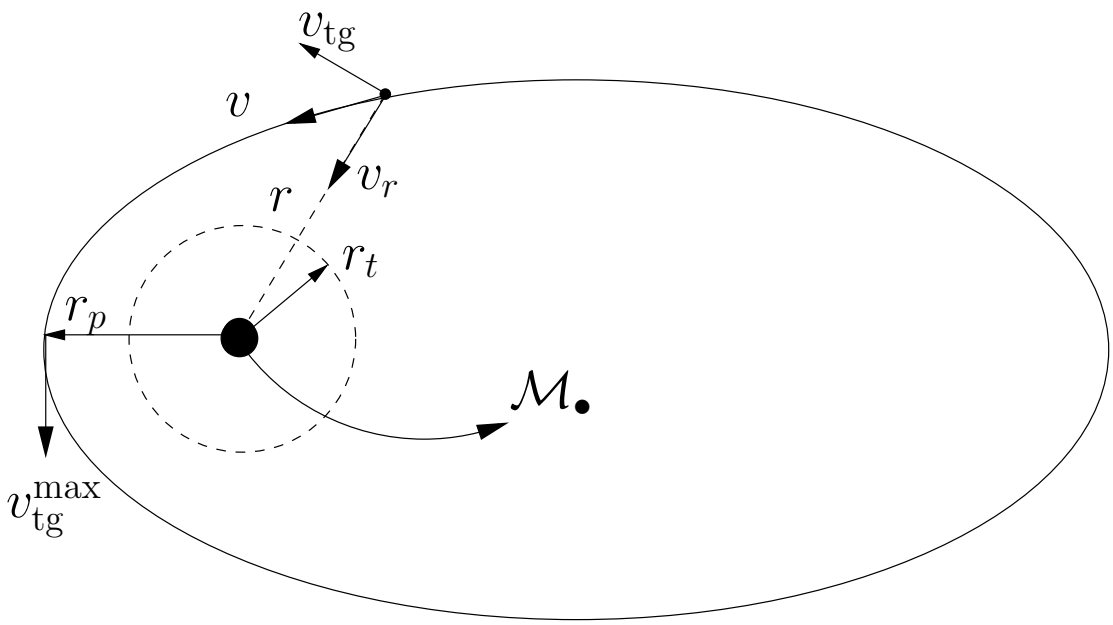

Figure 10: Definition of the distance of closest approximation of the star in its orbit to the MBH. In this point the radial component of the velocity of the star cancels and the tangential component is maximum. In the figure "$r_{\rm p}$" stands for the periapsis radius and "$r_{\rm t}$" for the tidal radius.

$$\begin{aligned} E(r) =& \phi(r) - \frac{v_{\rm tg}(r)^2}{2} - \frac{v_{\rm r}(r)^2}{2} \\ L(r) =& r v_{tg}(r) \end{aligned} \tag{30}$$

For the tidal radius:

$$\begin{aligned} E(r_{\rm t}) =& \phi(r_{\rm t}) - \frac{v_{tg}(r_{\rm t})^2}{2} \\ L(r_{\rm t}) =& r_{\rm t} v_{tg}(r_{\rm t}), \end{aligned} \tag{31}$$

from the momentum conservation and the fact that $v_{\rm r}(r_{\rm t}) = 0$ we get that:

$$v_{\rm tg}(r_{\rm t}) = \frac{r}{r_{\rm t}} v_{\rm tg}(r). \tag{32}$$

With energy conservation, and using the last result,

$$\begin{aligned} \phi(r) - \frac{v_{tg}(r)^2}{2} - \frac{v_{\rm r}(r)^2}{2} = \\ \phi(r_{\rm t}) - \frac{r^2}{2 r_{\rm t}^2} v_{tg}(r)^2. \end{aligned} \tag{33}$$

Then we get the tangential velocity of the stars in terms of r; namely, the loss-cone velocity:

$$\begin{aligned} v_{\rm lc}(r) = \frac{r_{\rm t}}{\sqrt{r^2 - r_{\rm t}^2}} \times \\ \sqrt{2[\phi(r_{\rm t}) - \phi(r)] + v_{\rm r}(r)^2}. \end{aligned} \tag{34}$$

Therewith, the angular momentum is

$$\begin{aligned} L(r_{\rm t}) =& r_{\rm t} v_{\rm tg}(r)|_{\rm max} = r_{\rm t} \frac{r}{r_{\rm t}} v_{\rm tg}(r) = \\ r v_{\rm tg}(r) =& r \frac{r_{\rm t}}{\sqrt{r^2 - r_{\rm t}^2}} \sqrt{2 \triangle \phi + v_{\rm r}(r)^2}, \end{aligned} \tag{35}$$

where

$$\triangle\phi \equiv \phi(r_t) - \phi(r) = \frac{G\mathcal{M}_\bullet}{r_t} + \phi_\star(r_t) - \frac{G\mathcal{M}_\bullet}{r} - \phi_\star(r) \tag{36}$$

If we use the fact that $r \gg r_t$, then

$$\frac{G\mathcal{M}_\bullet}{r_t} \gg \left(\frac{G\mathcal{M}_\bullet}{r} + \phi_\star(r)\right) = \phi(r) \tag{37}$$

Also, since $\mathcal{M}_\bullet \gg \mathcal{M}_\star(r_t)$,

$$\frac{G\mathcal{M}_\bullet}{r_t} \gg \phi_\star(r_t). \tag{38}$$

Thus,

$$v_{lc}(r) \approx \frac{r_t}{r}\sqrt{\frac{2G\mathcal{M}_\bullet}{r_t}}. \tag{39}$$

If we use now the fact that

$$\sigma_r(r) = \sigma_r(r_t)\left(\frac{r}{r_t}\right)^{-1/2} = \sqrt{\frac{G\mathcal{M}_\bullet}{r_t}}\left(\frac{r}{r_t}\right)^{-1/2}, \tag{40}$$

we have that

$$\sqrt{\frac{G\mathcal{M}_\bullet}{r_t}} = \sigma_r(r)\left(\frac{r}{r_t}\right)^{-1/2} \tag{41}$$

And so, it is in fair approximation

$$v_{lc}(r) \approx \frac{r_t}{r}\sqrt{\frac{2G\mathcal{M}_\bullet}{r_t}} \approx \sigma_r(r)\left(\frac{r_t}{r}\right)^{1/2}. \tag{42}$$

3

STELLAR DYNAMICS AND THE COSMIC GROWTH OF SMBHS

3.1 TIDAL DISRUPTIONS, GWS AND STELLAR DYNAMICS

The challenge of detection and characterization of gravitational waves and TDEs is strongly coupled with the dynamics of dense stellar systems. This is especially true in the case of the capture of a compact object by a MBH. In order to estimate how many events one can expect and what we can assess about the distribution of parameters of the system, we need to have a very detailed comprehension of the physics. In this regard, the potential detection of GWs and TDEs is an incentive to dive into a singular realm otherwise irrelevant for the global dynamics of the system.

A harbinger in this respect has been the tidal disruption of stars as a way to feed the central MBH. About 50% of the torn star remains are bound to the MBH and accreted on to it, producing an electromagnetic flare which tops out in the UV/X-rays, emitting a luminosity close to Eddington. This has been scrutinized attentively as a possible way of identifying and characterizing an otherwise quiescent, possibly very distant, galaxy [some possible TDEs have been recently reported in e.g. 9, 17, 18, 35, 42, 61]. Nonetheless, the complications of accretion are particularly intricate, tight on many different timescales to the microphysics of gasous processes. Even on local, galactic accreting objects the complications of accretion are convoluted. It is thus extremely difficult to understand how to extract very detailed information about extragalactic MBHs from the flare. The question of feeding a MBH is a statistical one. We do not care about individual events to understand the growth in mass of the hole, but about the statistics of the rates on cosmological timescales. Obviously, if we tried to understand the individual processes, we would fail.

The question of what happens to a compact object as it approaches the central MBH was never raised before we had the incentive of direct detection of gravitational radiation. When we started to address this problem, we realised that there were many questions of stellar dynamics that either did not have an answer or that had not even been addressed at all. We now have more questions than answers.

We will discuss the relaxation processes that we know to play a major role in the dynamics of this particular regime. This involves two-body as well as many bodies coherent or non-coherent relaxation. The list of processes is most likely incomplete, for there can still be additional, even more complicated processes unknown to us.

Astrophysical objects such as a binary of black holes, generate perturbations in space and time that spread like ripples on a pond. Such ripples, known as "gravitational waves" or "gravitational radiation", travel at the speed of light, outward from their source. These gravitational waves are predicted by general relativity, first proposed by Einstein. Whilst the strength of gravitational waves diminishes with distance, they neither stop nor slow.

Measurement of these gravitational waves will give astrophysicists a totally new and different way of studying the Universe: instead of analysing the propagation and transformation of particles such as photons, we will have direct information from the fabric of spacetime itself. The information carried by the gravitational radiation will tell us in exquisite detail about the history, behaviour and structure of the universe: from the Big Bang to black holes. Nonetheless, gravitational radiation has yet to be detected.

3.2 THE MYSTERY OF THE GROWTH OF MBHS

The understanding of galactic nucleus (GN, the central-most core of a galaxy) has advanced rapidly during the past decade, not least due to major advances in high angular resolution instrumentation at a variety of wavelength domains. Observations carried out with space-borne telescopes, such as the Hubble Space Telescope, or from the ground, using adaptive optics, have allowed us to study the kinematics of stars and gas in regions reaching down to sub-parsec scales for external galaxies and to the milliparsec range for the Milky Way. An outstanding conclusion is that dark compact objects, very probably supermassive black holes (SMBH), with masses of $M_\bullet \simeq 10^6 - 10^9\, M_\odot$, occupy the centres of most galaxies for which such observations can be made (see Kormendy & Ho 38 and Gültekin et al. 41). We have discovered that an intimate deep link exists between the central SMBH and its host galaxy [38], illuminated by the discovery of correlations between the mass of the SMBH, $M_\bullet$, and global properties of the surrounding stellar system, e.g. the velocity dispersion σ of the spheroid of the galaxy, known as the $M - \sigma$ relation. In spite of some progress in recent decades, many fundamental questions remain open. There is still no clear evidence of SMBH feedback in galaxies, and the low mass end of the $M - \sigma$ relation is very uncertain. Claims of detection of "intermediate-mass" black holes (IMBHs) [1] at the center of globular clusters raise the possibility that these correlations could extend to much smaller systems [see e.g. 27, 28]. but the strongest –if not totally conclusive– observational evidences for the existence of IMBHs are ultra-luminous X-ray sources. The origin of these (I)MBH is still shrouded in mystery, and many aspects of their interplay with the surrounding stellar cluster remain to be elucidated. The centre-most part of a galaxy, its *nucleus*, consists of a nuclear star cluster of a few millions of stars surrounding the SMBH within a distance of a few parsecs [see e.g. 55]. The nucleus is naturally expected to play a major role in the interaction between the SMBH and

1 Black holes smaller than supermassive, found in the centre of galaxies, but heavier than stellar black holes. Typically their masses range between 100 and 10,000 solar masses

the host galaxy. In the nucleus, stellar densities in excess of a million stars per cubic parsec and relative velocities of the order $\sim 100 - 1000\,\mathrm{km\,s^{-1}}$ can be reached. In these exceptional conditions, and unlike anywhere else in the bulk of the galaxy, collisional effects come into play (except in globular clusters, but one important difference is that the SMBH gives the central part of the cluster almost a Keplerian potential, and thus very tricky resonance characteristics. This is one reason it has been difficult to analyze). These include the so-called "2-body relaxation" (i.e. mutual gravitational deflections) and impact between stars.

Although there is an emerging consensus about the growth of large-mass MBHs thanks to Sołtan's argument [60], MBHs with masses up to $10^7\,M_\odot$, such as our own MBH in the Galactic Centre (with a mass of $\sim 4 \times 10^6\,M_\odot$), are enigmatic. In particular because the SMBH mass in the universe is roughly in SMBHs of masses $\sim 10^8\,M_\odot$. There are many different arguments to explain their masses: accretion of multiple stars from arbitrary directions [34], mergers of compact objects such as stellar-mass black holes and neutron stars [51] or IMBHs falling on to the MBH [38], or by more peculiar means such as accretion of dark matter [48] or collapse of supermassive stars [4, 11, 32, 56, 80]. Low-mass MBHs and, thus, the early growth of *all* MBHs, are still a conundrum.

3.3 THE INTERPLAY BETWEEN STARS AND SMBHS

The way stars revolve around a SMBH and interact with it provides us with precious information: the mass of the SMBH and its spin. Two fundamental observational probes are (i) *Tidal disruptions:* If a star happens to pass very close to the SMBH, some part of it or all of it may be torn apart because of the tidal effects. Many candidate tidal disruption events (TDEs) have already been detected with ROSAT, Chandra and Swift (see `http://astrocrash.net/resources/tde-catalogue`). They also have significant optical/UV signatures in addition to X-rays and are therefore being found with ground-based transient surveys. This number will explode with upcoming transient surveys like the Zwicky Transient Facility (ZTF) and the Large Synoptic Survey Telescope (LSST), but also with SRG/eROSITA [36]. TDEs can be used as a probe of accretion physics close to the event horizon of the SMBH, and hence of gravitation in the strong regime [16, 53]: It is important to understand how stars can affect the accretion flow and its variability [15] [2] , but also with SRG/eROSITA[3] (ii) The spin and quadrupole moment of the supermassive black hole at the Galactic center can

2 A planned X-ray telescope, `http://www.the-athena-x-ray-observatory.eu/` – The second (L2) large class mission within ESA Cosmic Vision Program, scheduled to start being constructed in 2019. Athena+ will be *a hundred times more sensitive* than the best of existing X-ray telescopes - Chandra X-ray Observatory, and XMM-Newton[47]

3 The Extended Roentgen Survey with an Imaging Telescope Array, `http://www.mpe.mpg.de/eROSITA` – eRosita is the primary instrument on-board the Russian "Spectrum-Roentgen-Gamma" (SRG) satellite which will be launched in 2016 and placed in an L2 orbit. It will perform the first imaging all-sky survey in the medium energy X-ray range up to 10 keV, and will be sensitive to TDEs occurring near SMBHs of mass between $10^{6-7}\,M\odot$ in the local Universe ($z \lesssim 0.15$)[36]

in principle be measured via astrometric monitoring of stars orbiting at milliparsec (mpc) distances, allowing to test the "no-hair" theorem [50]. (iii) *Gravitational capture of compact remnants:* The gradual inspiral onto an SMBH of a stellar remnant due to the emission of GWs, known as an "*Extreme Mass Ratio Inspiral*" because typically the remnant has a mass of $\sim 10\,M_\odot$ and the SMBH of $10^6\,M_\odot$ [3, 5] is one of the main objects of interest for the ESA eLISA L3 mission, presented in my papers [3, 7] It is important to note that the precursor mission, LISA Pathfinder, which will test eLISA technology, is scheduled to fly this year). A compact object, such as a star so dense that it will not be disrupted by the tidal forces of the SMBH, (say, a neutron star, a white dwarf or a small stellar black hole, althought a white dwarf can be tidally disrupted by an IMBH, and we have a candidate for this, see Krolik & Piran 39), is able to approach the central SMBH to very short distances and, hence, a large amount of orbital energy is radiated away, causing the semi-major axis shrink.

This phenomenon will be repeated thousand of times as the object inspirals until is swallowed by the central SMBH. The emitted GWs encode a map of the space-time. If we can record and decode it, then we will be able to test the theory that massive dark objects are indeed Kerr black holes as the theory of general relativity predicts, and not exotic objects such as boson stars. This would be the ultimate test of general relativity. The detection of such an EMRI will allow us to do very exciting science: EMRIs will give us measurements of the masses and spins of SMBHs to an accuracy which is beyond that of any other astrophysical technique. Such information will tell us about cosmic evolution, about the history and growth of SMBHs in the nearby universe, with an accuracy which has no precedent. For the success and future descopes of the eLISA mission, it is important that we understand the systems that it will observe. A deep theoretical comprehension of the sources which will populate eLISA's field of view is crucial to achieve its main goals.

3.4 A MAGNIFYING GLASS

The evolved Laser Interferometer Space Antenna / New Gravitational Wave Observatory [eLISA, see 3, 7, and also the official AEI URL[4]], based on the the former NASA-ESA configuration [LISA, see e.g., 21], is a conceived space-borne observatory for detecting low frequency gravitational waves (GW). The "full version of " LISA, which will be our reference point throughout the review, consists of three spacecraft arranged in an equilateral triangle with sides of length 5 million kilometres, all in a heliocentric orbit. LISA is designed to cover the low-frequency broadband of gravitational radiation, from about 0.1 to 100 millihertz. In this band of frequencies, the Universe is populated by strong sources of GWs such as binaries of supermassive black holes merging in galaxies, massive black holes "swallowing" entirely small compact objects like stellar black holes, neutron stars and white dwarfs. The information is encoded in the gravitational waves: the history of galaxies and black holes, the physics of dense matter and stellar remnants like stellar black holes, as well as general relativity

4 http://elisa-ngo.org/

and the behaviour of space and time itself. Chinese mission study options ["ALIA" from now onwards, see 15, 20, 39] will also be able to catch these systems with good signal-to-noise ratios, although the mass-ratio for the capture of COs by MBHs will not be as extreme. ALIA focuses rather on intermediate-mass ratio inspirals.

In any case, a key property of GW astrophysics is the fact that GWs interact only very weakly with matter. The observations we will make with LISA will not suffer any of the usual problems in astrophysics - absorption, scattering, or obscuration. This is what makes LISA-like missions such as eLISA/NGO or ALIA unique. It is not "merely" a test of general relativity; these missions would be able to corroborate the underlying theory of the nature of the central dark objects which we now observe in most galaxies. We will get direct information from the heart of the densest stellar systems in the Universe: galactic nuclei, nuclear stellar clusters and globular clusters. The LISA mission technology will be tested with the LISA Pathfinder[5] mission, a 100% European effort (from the European Space Agency), scheduled for launch in 2014 from Kourou, French Guiana. LISA Pathfinder will contain one shortened arm of the full-LISA interferometer. The main goal of LISA Pathfinder mission is to check that the technology required by a LISA-like mission is feasible. Moreover, LISA Pathfinder will be the first in-flight test of gravitational wave detection metrology.

For the full success of a mission such as LISA, it is important that we *understand* the systems that we expect to observe. A deep theoretical comprehension of the sources which will populate LISA's field of view is important to achieve its main goals.

Whilst main-sequence stars are tidally disrupted when approaching the central MBH, compact objects (stellar black holes, neutron stars, and white dwarfs) slowly spiral into the MBH and are swallowed whole after some $\sim 10^5$ orbits in the LISA band. At the closest approach to the MBH, the system emits a burst of GWs which contains information about spacetime and the masses and spins of the system. We can envisage each such burst as a snapshot of the system. This is what makes EMRIs so appealing: a set of $\sim 10^5$ bursts of GWs radiated by *one* system will tell us with the utmost accuracy about the system itself, it will test general relativity, it will tell us about the distribution of dark objects in galactic nuclei and globular clusters and, thus, we will have a new understanding of the physics of the process. New phenomena, unknown and unanticipated, are likely to be discovered.

If the central MBH has a mass larger than $10^7\,M_\odot$, then the signal of an inspiraling stellar black hole, even in its last stable orbit (LSO) will have a frequency too low for detection. On the other hand, if it is less massive than $10^4\,M_\odot$, the signal will also be quite weak unless the source is very close. This is why one usually assumes that the mass range of MBHs of interest in the search of EMRIs for LISA is between $[10^7, 10^4]\,M_\odot$. Nonetheless, if the MBH is rotating rapidly, then even if it has a mass larger than $10^7\,M_\odot$, the LSO will be closer to the MBH and thus, even at a higher frequency, the system should be detectable. This would push the total mass to a few $\sim 10^7\,M_\odot$.

5 http://sci.esa.int/lisapf

For a binary of a MBH and a stellar black hole to be in the LISA band, it has to have a frequency of between roughly 1 and 10^{-5} Hz. The emission of GWs is more efficient as they approach the LSO, so that LISA will detect the sources when they are close to the LSO line. The total mass required to observe systems with frequencies between 0.1 Hz and 10^{-4} is of $10^4 - 10^7\, M_\odot$. For masses larger than $10^7\, M_\odot$ the frequencies close to the LSO will be too low, so that their detection will be very difficult. On the other hand, for a total mass of less than $10^3\, M_\odot$ we could in principal detect them at an early stage, but then the amplitude of the GW would be rather low.

On the top of this, the measurement of the emitted GWs will give us very detailed information about the spin of the central MBH. With current techniques, we can only hope to measure MBH spin through X-ray observations of Fe Kα profiles, but the numerous uncertainties of this technique may disguise the real value. Moreover, such observations can only rarely be made.

This means that LISA will scrutinize exactly the range of masses fundamental to the understanding of the origin and growth of supermassive black holes. By extracting the information encoded in the GWs of this scenario, we can determine the mass of the central MBH with an astonishing relative precision of $\sim 10^{-4}$. Additionally, the mass of the compact object which falls into the MBH and the eccentricity of the orbit will be recovered from the gravitational radiation with a fractional accuracy also of $\sim 10^{-4}$. All this means that LISA will not be "just" the ultimate test of general relativity, but an exquisite probe of the spins and range of masses of interest for theoretical and observational astrophysics and cosmology.

3.5 A PROBLEM OF $\sim$ 10 ORDERS OF MAGNITUDE

For the particular problem of how does a compact object end up being an extreme-massratio inspiral, we have to study very different astrophysical regimes, spanning over many orders of magnitude.

GALACTIC OR COSMOLOGICAL DYNAMICS In Figure 11 we depict the three different realms of stellar dynamics of relevance for the problem of EMRIs. At the largest scale exists the galaxy, with a size of a few kiloparsecs. Just as a point of reference, the gravitational radius of a MBH of $10^6\, M_\odot \sim 5 \cdot 10^{-8}$ pc. The relaxation time, $t_{\rm rlx}$ which we will introduce with more detail ahead, is a timescale which can be envisaged as the required time for the stars to exchange energy E and angular momentum J between them, it is the time that the stars need to "see" eachother individually and not only the average, background stellar potential of the whole stellar system, for the galaxy $t_{\rm rlx}$ is larger than the Hubble time, which means that, on average, it has no influence on the galaxy at all. A test star will only feel the mean potential of the rest of the stars and it will never exchange either E or J with any other star. The system is "collisionless", in the meaning that two-body interactions can be neglected. This defines the realm of stellar galactic dynamics, the one investigated in Cosmological simulations using, e.g.,

N-body integrators. Since we do not have to take into account the strong interactions between stars, one can easily simulate ten billion particles with these integrators.

CLUSTER DYNAMICS If we zoom in by typically a factor of 10^3, we enter the (mostly Newtonian) stellar dynamics of galactic nuclei. There, $t_{\rm rlx} \sim 10^8 - 10^{10}$ yrs. In this realm stars do feel the graininess of the stellar potential. The closer we get to the central MBH, the higher σ will be, if the system is in centrifugal equilibrium; the stars have to orbit around the MBH faster. In particular, S2 (or S02), one of the S-stars (So-stars) for which we have enough data to reconstruct the orbit to a very high level of confidence – as we saw in the previous section – has been observed to move with a velocity of $15 \cdot 10^3\,{\rm km\,s^{-1}}$. Typically, $t_{\rm rlx}$ is (on occasion *much*) shorter than the age of the system, of a few $\sim 10^8 - 10^{10}$ yrs. For these kind of systems one has to take into account relaxation, exchange of E and J between stars. The system is "collisional". When we have to take into account this in the numerical simulations, the result is that we cannot simulate with N-body integrators more than some thousands of stars on a computer. To get to more realistic particle numbers one has to resort to beowulf supercomputers, special-purpose hardware or the graphic processor units.

RELATIVISTIC STELLAR DYNAMICS Last, in the right panel, we have the relativistic regime of stellar dynamics when we enlarge the previous by a factor of ten million. There the role of relativistic effects is of paramount importance for the evolution of the system. In this zone, generally, *there are no stars*. Even at the densities which characterise a galactic nucleus, the probability of having a star in such a tiny volume is extremely small. What's more, even if we had a significantly larger volume, or a much higher density for the galactic nucleus, so that we had a few stars close to the MBH, these would quickly merge with the MBH due to the emission of GWs, which is what defines an EMRI. But they do it *too* fast. These systems can be collisional or collisionless, depending on how many stars we have at a given time. If they are there, they will exchange E and J between them. Nevertheless, relaxation is not well-defined in this regime.

he key point here is how to replenish that area, so that there are other stars replacing those which merge quickly with the central MBH. On average, there are *zero* stars. As a matter of fact, and in general, for the general study of the stellar dynamics of galactic nuclei, the role of this last realm is negligible. One does not have to bother with the effects of GR; most, if not all, stars are on a Newtonian regime. The impact on the dynamics of galactic nuclei is zero. It is somewhat impressive that this last region dominated by the effects of GR has an effect worth studying at all. But, as we will see ahead, the encoded information that one can recover from the detection of an EMRI about its surrounding dynamical system is dramatic. If we want to address this problem, we are, therefore, "forced" to cope with a problem of some seven orders of magnitude in particular, when understanding the role of the dynamics of galactic nuclei in relativistic dynamics, and of ten orders of magnitude in the big picture.

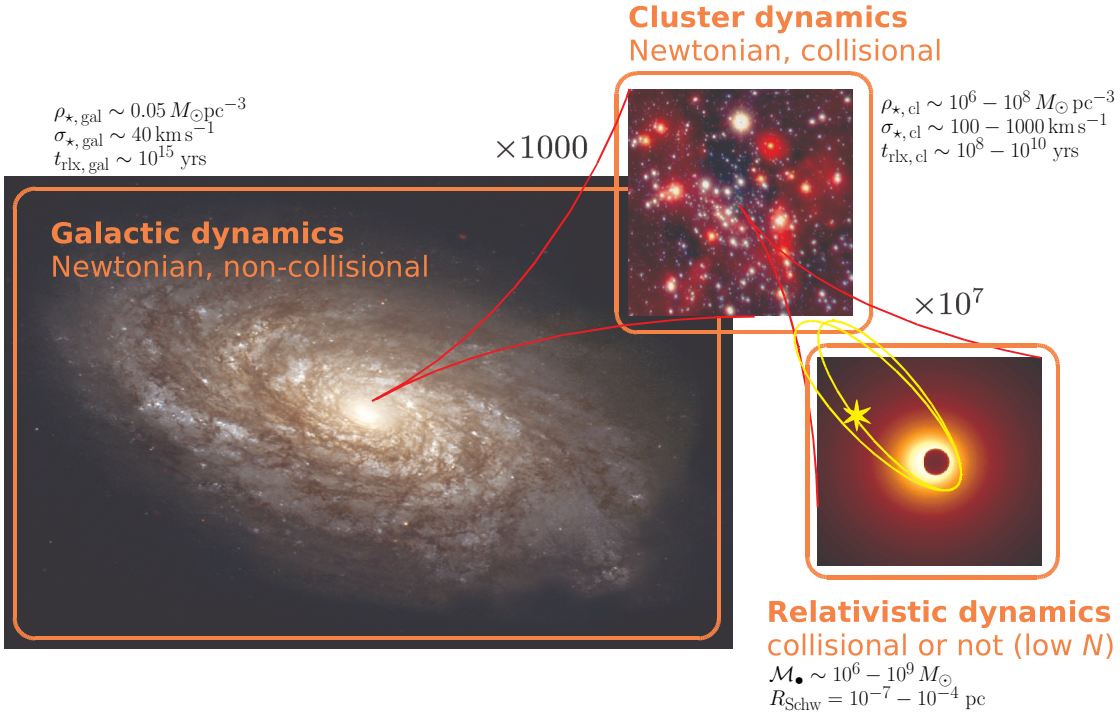

Figure 11: On the left and with the largest scale the galaxy has an average density of stars of about $0.05\, M_\odot \mathrm{pc}^{-3}$. The velocity dispersion is $\sim 40\,\mathrm{km\,s}^{-1}$. From these quantities one can infer that the relaxation time in the vicinity of our Sun is $t_{\mathrm{rlx}} \sim 10^{15}$ yrs. The upper panel shows the galactic nucleus that such a galaxy has. A typical size for it is ~ 1 pc, the stellar density ranges between $10^6 - 10^8\, M_\odot\,\mathrm{pc}^{-3}$ and the velocity dispersion is of $\sigma \sim 100 - 1000\,\mathrm{km\,s}^{-1}$. In this region, $t_{\mathrm{rlx}} \sim 10^8 - 10^{10}$ yrs. In the last panel, we have that the dynamics of the system is dominated by General Relativity. The mass of the central object, an MBH, ranges between 10^8 and $10^9\, M_\odot$ and its size is given by the Schwarschild radius, $R_{\mathrm{Schw}} = 10^{-7} - 10^{-4}$ pc.

3.5.1 *Actual data*

In Figure 12 we show data constrainted by actual measurements. One of the very first questions one has to address when trying to understand the stellar dynamics around a MBH is *how many stars are there and how do they distribute around it*? Unfortunately there are very few observations for this because we are interested in nuclei that harbour lower-mass MBHs, so they therefore have a small radius of influence $r_{\rm inf}$ and, thus, they are observationally very difficult to resolve. Currently there are only a very few galaxies that are both in the range of GW frequencies interesting to us and that have a resolved $r_{\rm inf}$. For these we have information on how bound stars that can become EMRIs are distributed around the central MBH. Obviously, the Milky Way (MW) is one of these galaxies. In thefigure the stellar density profile of the MW is displayed. We see that it goes up to at least $10^8\,M_\odot/\mathrm{pc}^3$ in the inner regions. This number has been calculated by assuming a population of stars; one has to deproject the observation, because we are only seeing a few of the total amount of stars, the brightest ones. One assumes that the observed stars are tracing an underlying population invisible to us. This requires a considerable amount of modelling to obtain the final results. These are uncertain by, at most, a factor of ten. In the same figure we have another nucleus, M32, which should be harbouring an MBH with a mass similar to the one located in the GC. The density profile happens to be similar to the one corresponding to the GC. Whether this is a coincidence or something deeper is not clear. In any case, and to *first order of approximation*, we can state that once we know the mass of the MBH, we know the way stars distribute around it. Later the relevance of this point will be obvious to the lector.

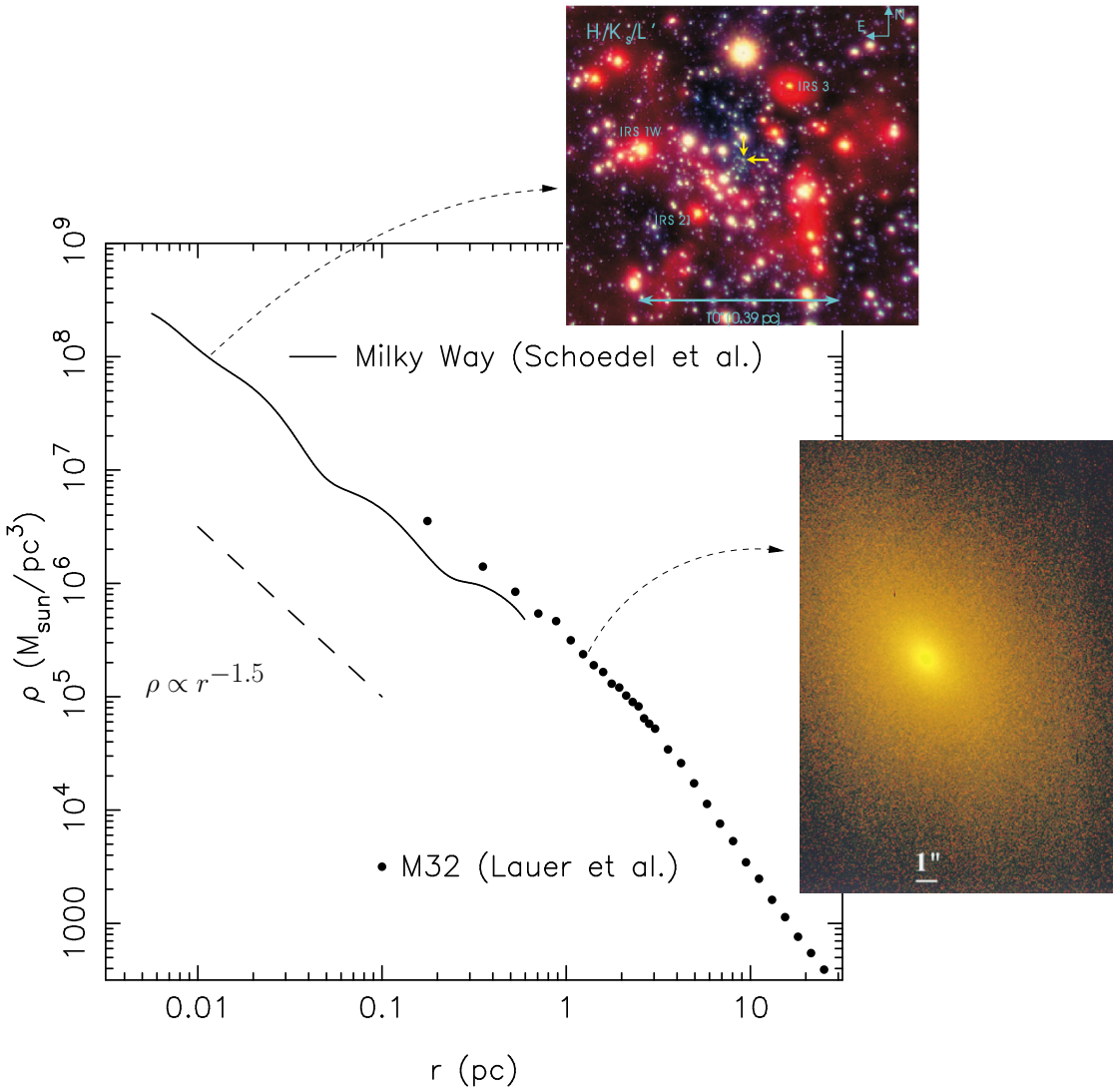

Figure 12: Density profile for the GC of the MW and for M32, both with MBHs of masses $3 \times 10^6\, M_\odot$ and influence radii ~ 3 pc. The dashed curve on the very left corresponds to a slope of $\rho \propto r^{-3/2}$ [adapted from 40, 43, 54].

BIBLIOGRAPHY

[2] Alexander, T., & Hopman, C. 2009, ApJ, 697

[4] Amaro-Seoane, P. 2004, PhD thesis, PhD Thesis, Combined Faculties for the Natural Sciences and for Mathematics of the University of Heidelberg, Germany. VII + 174 pp. (2004), http://www.ub.uni-heidelberg.de/archiv/4826

[3] ——. 2012, ArXiv e-prints

[3] Amaro-Seoane, P. et al. 2012, GW Notes, Vol. 6, p. 4-110

[7] ——. 2012, Classical and Quantum Gravity, 29, 124016

[4] Amaro-Seoane, P., Freitag, M., & Spurzem, R. 2004, MNRAS

[5] Amaro-Seoane, P., Gair, J. R., Freitag, M., Miller, M. C., Mandel, I., Cutler, C. J., & Babak, S. 2007, Classical and Quantum Gravity, 24, 113

[8] Amaro-Seoane, P., & Preto, M. 2011, Classical and Quantum Gravity, 28, 094017

[9] Arcavi, I. et al. 2014, ApJ, 793, 38

[12] Bahcall, J. N., & Wolf, R. A. 1976, ApJ, 209

[11] Begelman, M. C. 2010, MNRAS, 402, 673

[15] Bender, P. L., Armitage, P. J., Begelman, M. C., & Pema, R. 2005, White Paper submitted to the NASA SEU Roadmap Committee

[17] Binney, J., & Tremaine, S. 1987, Galactic Dynamics (Princeton University Press)

[11] ——. 2008, Galactic Dynamics: Second Edition, ed. J. Binney & S. Tremaine (Princeton University Press)

[15] Bregman, M., & Alexander, T. 2012, ApJ, 748, 63

[16] Brenneman, L. 2013, Measuring the Angular Momentum of Supermassive Black Holes

[17] Brown, G. C., Levan, A. J., Stanway, E. R., Tanvir, N. R., Cenko, S. B., Berger, E., Chornock, R., & Cucchiaria, A. 2015, MNRAS, 452, 4297

[18] Cenko, S. B. et al. 2012, ApJ, 753, 77

[19] Chandrasekhar, S. 1942, Physical Sciences Data

[20] Crowder, J., & Cornish, N. J. 2005, Physical Review D, 72, 083005

[21] Danzmann, K. 2000, Advances in Space Research, 25

[22] Freitag, M., Amaro-Seoane, P., & Kalogera, V. 2006, Journal of Physics Conference Series, 54, 252

[13] ——. 2006, ApJ, 649, 91

[24] Freitag, M., & Benz, W. 2001, A&A, 375

[30] ——. 2002, A&A, 394

[26] ——. 2005, MNRAS, 358

[27] Gebhardt, K., Rich, R. M., & Ho, L. C. 2002, ApJ Lett., 578

[28] Gerssen, J., van der Marel, R. P., Gebhardt, K., Guhathakurta, P., Peterson, R. C., & Pryor, C. 2002, AJ, 124

[29] Gezari, S., Halpern, J. P., Komossa, S., Grupe, D., & Leighly, K. M. 2003, ApJ, 592

[39] Gong, X. et al. 2011, Classical and Quantum Gravity, 28

[41] Gültekin, K. et al. 2009, ApJ, 698, 198

[32] Hara, T. 1978, Progress of Th. Phys., 60

[33] Hénon, M. 1975, in IAU Symp. 69: Dynamics of Stellar Systems, ed. A. Hayli, 133

[34] Hills, J. G. 1975, Nat, 254

[35] Hryniewicz, K., & Walter, R. 2015, ArXiv e-prints

[36] Khabibullin, I., Sazonov, S., & Sunyaev, R. 2014, MNRAS, 437, 327

[37] Komossa, S., Halpern, J., Schartel, N., Hasinger, G., Santos-Lleo, M., & Predehl, P. 2004, ApJ Lett., 603, L17

[38] Kormendy, J., & Ho, L. C. 2013, ARA&A, 51, 511

[39] Krolik, J. H., & Piran, T. 2011, ApJ, 743, 134

[40] Lauer, T. R., Faber, S. M., Ajhar, E. A., Grillmair, C. J., & Scowen, P. A. 1998, AJ, 116

[48] Lightman, A. P., & Shapiro, S. L. 1977, ApJ, 211

[42] Maksym, W. P., Ulmer, M. P., Eracleous, M. C., Guennou, L., & Ho, L. C. 2013, MNRAS, 435, 1904

[43] Merritt, D. 2006, Reports on Progress in Physics, 69, 2513

[44] ——. 2010, ApJ, 718, 739

[50] Merritt, D., Alexander, T., Mikkola, S., & Will, C. M. 2011, Phys. Rev. D, 84, 044024

[53] Murphy, B. W., Cohn, H. N., & Durisen, R. H. 1991, ApJ, 370

[47] Nandra, K. et al. 2013, ArXiv e-prints

[48] Ostriker, J. P. 2000, Physical Review Letters, 84, 5258

[38] Portegies Zwart, S. F., Baumgardt, H., McMillan, S. L. W., Makino, J., Hut, P., & Ebisuzaki, T. 2006, ApJ, 641, 319

[28] Preto, M., & Amaro-Seoane, P. 2010, ApJ Lett., 708, L42

[51] Quinlan, G. D., & Shapiro, S. L. 1990, ApJ, 356

[80] Rees, M. J. 1984, ARA&A, 22

[53] Reynolds, C. S. 2014, Space Science Reviews, 183, 277

[54] Schödel, R. et al. 2002, Nat, 419

[55] Schödel, R., Feldmeier, A., Neumayer, N., Meyer, L., & Yelda, S. 2014, Classical and Quantum Gravity, 31, 244007

[56] Shapiro, S. L., & Teukolsky, S. A. 1979, ApJ Lett., 234

[60] Sołtan, A. 1982, MNRAS, 200

[40] Spitzer, L. 1987, Dynamical evolution of globular clusters (Princeton, NJ, Princeton University Press, 1987, 191 p.)

[59] Spitzer, L. J. 1969, ApJ Lett., 158

[60] Spitzer, L. J., & Hart, M. H. 1971, ApJ, 164

[61] Wang, T.-G., Zhou, H.-Y., Komossa, S., Wang, H.-Y., Yuan, W., & Yang, C. 2012, ApJ, 749, 115

4

FEATURED ARTICLES

For this dissertation I have decided to put together a series of papers that I have published in the last years in The Astrophysical Journal (and Letters), Monthly Notices of the Royal Astronomical Society, Astronomy & Astrophysics and Classical and Quantum Gravity (this one is more focused on topics related to General Relativity and Gravitation, and is leading in the field).

The nine articles that I have selected have as a common denominator the study of the creation and evolution of sources of tidal disruption events and gravitational waves. The order I have chosen is not chronological, but logical and allows the reader to follow a natural flow of ideas to better picture the main goals of this dissertation (for the full titles of the papers, acronyms, as well as an explanation of my contribution and journal references, please see table 4). Here I give a succinct description of the most important goals of every individual article. The papers are presented fully in the next chapters and in the final one, in chapter iii, I present the general discussion of the dissertation.

[Frag1] introduces the idea that the responsible for the observed kinematical properties of the Galactic Center was an accretion disc around our supermassive black hole that went under fragmentation in the past. This paper is an analytical calculation that solves a fundamental problem that has been open for a long time; namely the observational absence of red giants, and has direct implications on the distribution of compact remnants, in particular of compact cores, similar to white-dwarfs, that eventually could end up being sources of GWs for a space-borne observatory.

[Frag2] is a work that addresses a related problem: The fragmentation and formation of stars in a gaseous disc, which in this case is surrounding not a single supermassive black hole, but a binary of them. The disc is called therefore circumbinary. This article was a major numerical effort that combined for the first time two different approaches: Smoothed-particle hydrodynamics (SPH) and direct-summation N-body. I investigated the impact of the binary on the event rate of tidal disruptions.

[RER] is the natural follow-up of **[Frag1]**. My collaborator and I realised that the stellar disc that forms once the gas has been depleted and stellar formation has

finished, induces a resonance in the innermost stellar population. This resonance, a Kozai-Lidov-like one, gives a simple and elegant answer to the observed super-thermal eccentricity distribution of the so-called S-stars in our Galactic Centre and explains also the fact that these lighter stars (the S-stars) are closer to Sgr A* and more massive ones, Wolf-Rayet (WR) and O-stars, are farther out. This was a conondrum known as the "inverse mass-segregation" until now.

[Sep] addresses a scenario that has been thought to deliver the so-called S-stars close to the SMBH. The tidal separation of a binary by the gravitational pull of an SMBH is similar to the disruption of a star. The binary is separated and one of the stars re-ejected into the stellar system at a much higher velocity, which might produce a hyper-velocity star, and the remaining one is bound to the SMBH. The tidal disruption, however, will have a particular signature that might be used to charecterise the event.

[MS] was published before the previous articles, and it can be envisaged as the logical next step that investigates the question of how stars distribute around the supermassive black hole once all gas has been depleted. This work has a direct impact on the event rate of tidal disruptions of extended stars and the formation of extreme-mass ratio inspirals, because it provides us with a realistic –and more efficient– answer to the question of how stars segregate towards the centre according to their masses.

[BF] describes an interesting effect I discovered when looking more closely to the problem of extreme-mass ratio inspirals in the context of relativistic stellar dynamics. What would happen if a stellar black hole, on its way to become a probe to space and time around a supermassive black hole, had relatively close a perturbing star? I show that in such a case, the evolution of the EMRI is non-deterministic because of a new dynamical effect that I have discovered, which is a result of relativistic periastron shift and secular effects. If the observation of an EMRI with a space-borne observatory turns out to be very difficult because of the lack of determinism, this does not necessarily mean that General Relavitity is a wrong theory – A mere, simple nearby star could be the reason.

[Spin] is probably one of the most important breakthroughs in this field of research in the last years. I show that, contrary to what had been previously thought, stellar black holes on extremely radial orbits do not "plunge" into the supermassive black hole after a very small series of bursts of gravitational radiation. If the supermassive black hole is spinning, which is very likely in nature, the smaller black hole does not plunge through the horizon, but becomes a coherent, very loud source of gravitational waves, which means that the event rate of EMRIs is larger than thought and also that they are more powerful. This allows us to reach farther horizon distances, and hence expands the observable universe with these unique probes of space and time.

[IMRI] is to date the only existing numerical investigation of a globular cluster with an intermediate-mass black hole (IMBH) using a direct-summation code that displays the creation of an intermediate-mass ratio inspiral and follows it down to a few Schwarzschild radii. Moreover, the numerical code that we use has the implementation of the velocity recoil that the merged massive black hole system receives after coalescence. Due to the relatively low velocity dispersion of the cluster, as compared to e.g. a galactic nucleus, the IMBH escapes the whole system, which has an impact on the global evolution.

[UCDs] uses the previous paper as a motivation to study the effect of recoiling IMBHs in the observed cluster complexes of interacting galaxies, such as the Antennæ. Such complexes harbour hundreds to thounsands of young clusters. If even a very small fraction of them contain an IMBH, the black hole can escape after coalescence with another black hole the host cluster and become a massive black hole at large, i.e. free-floating between the many clusters. In this article I produced two big sets of numerical simulations: The first analyses the different possible interactions between an IMBH and a cluster, depending on mass ratio, relative velocity and impact parameter, and the second one studies the global evolution of a cluster complex with many clusters while tracking the orbit of one or many free-floating IMBHs, and their mutual interactions. I show that the cluster complex can eventually form an Ultra-Compact Dwarf Galaxy, such as e.g. Omega Centauri in the Milky Way, and that the IMBHs typically are accumulated in the centre of it. This has important consequences in our understanding of dwarf galaxy formation and evolution as well in sources of gravitational radiation and tidal disruption of stars.

[Frag1] "The Fragmenting Past of the Disk at the Galactic Center:
The Culprit for the Missing Red Giants"
The Astrophysical Journal Letters, Volume 781, Issue 1, article id. L18, 5 pp. (2014).
Amaro-Seoane, Pau; Chen, Xian
My contribution: I proposed the problem and contributed 50% to the calculations and write-up.
Percentage of my contribution: 50%.

[Frag2] "Tidal Disruptions in Circumbinary Disks.
Star Formation, Dynamics, and Binary Evolution"
The Astrophysical Journal, Volume 764, Issue 1, article id. 14, 9 pp. (2013).
Amaro-Seoane, Pau; Brem, Patrick; Cuadra, Jorge
My contribution: I proposed the problem, ran the SPH simulations, helped with the N-body simulations, and contributed to the plots and write-up.
Percentage of my contribution: 50%.

[RER] "A Rapidly Evolving Region in the Galactic Center:
Why S-stars Thermalize and More Massive Stars are Missing"
The Astrophysical Journal Letters, Volume 786, Issue 2, article id. L14, 5 pp. (2014).
Chen, Xian; **Amaro-Seoane, Pau**
My contribution: I proposed the problem and contributed 50% to the calculations and write-up.
Percentage of my contribution: 50%.

[Sep] "Tidal disruptions of separated binaries in galactic nuclei"
Monthly Notices of the Royal Astronomical Society, Volume 425, Issue 4, pp. 2401-2406 (2012).
Amaro-Seoane, Pau; Miller, M. Coleman; Kennedy, Gareth F.
My contribution: For this paper I proposed the problem, participated in the numerical simulations as well as in the analytical model. I did the write-up of most of the article.
Percentage of my contribution: 60%.

[MS] "The impact of realistic models of mass segregation
on the event rate of extreme-mass ratio inspirals and cusp re-growth"
Classical and Quantum Gravity, Volume 28, Issue 9, id. 094017 (2011).
Amaro-Seoane, Pau; Preto, Miguel
My contribution: In this work, which is a continuation of the former one, I have analyzed, interpreted and visualized the results for the main results. I did the write-up.
Percentage of my contribution: 50%.

[BF] "The butterfly effect
in the extreme-mass ratio inspiral problem"
The Astrophysical Journal Letters, Volume 744, Issue 2, article id. L20, 6 pp. (2012).
Amaro-Seoane, Pau; Brem, Patrick; Cuadra, Jorge; Armitage, Philip J.
My contribution: I proposed the problem, developed the relativistic correction terms for the code and carried out the analysis and interpretation of the results.
I did the write-up.
Percentage of my contribution: 80%.

[Spin] "The role of the supermassive black hole spin
in the estimation of the EMRI event rate"
Monthly Notices of the Royal Astronomical Society, Volume 429, Issue 4, p.3155-3165 (2013).
Amaro-Seoane, Pau; Sopuerta, Carlos F.; Freitag, Marc D.
My contribution: I proposed the problem, contributed to the derivation of the separatrices, and estimated the event rates. I did the write-up.
Percentage of my contribution: 70%.

[IMRI] "Investigating the retention of intermediate-mass
black holes in star clusters using N-body simulations"
Astronomy & Astrophysics, Volume 557, id. A135, 8 pp. (2013).
Konstantinidis, Symeon; **Amaro-Seoane, Pau**; Kokkotas, Kostas D.
My contribution: I proposed the problem, analyzed the simulations, did the plots and did the write-up.
Percentage of my contribution: 50%.

[UCDs] "Sowing the seeds of massive black holes in small galaxies:
Young clusters as the building blocks of Ultra-Compact-Dwarf Galaxies"
The Astrophysical Journal, Volume 782, Issue 2, article id. 97, 14 pp. (2014).
Amaro-Seoane, Pau; Konstantinidis, Symeon; Dewi Freitag, Marc; Miller, M. Coleman; Rasio, Frederic A.
My contribution: I proposed the problem, ran half of all simulations, did the plots and did most of the write-up.
Percentage of my contribution: 70%.

Part II

ARTICLES

5

THE FRAGMENTING PAST OF THE DISK AT THE GALACTIC CENTER : THE CULPRIT FOR THE MISSING RED GIANTS

Pau Amaro-Seoane[1] *and Xian Chen*[1]

Published in *The Astrophysical Journal Letters, Volume 781, Issue 1, article id. L18, 5 pp. (2014).*

Abstract: Since 1996 we have known that the Galactic Center (GC) displays a core-like distribution of red giant branch (RGB) stars starting at $\sim 10''$, which poses a theoretical problem, because the GC should have formed a segregated cusp of old stars. This issue has been addressed invoking stellar collisions, massive black hole binaries, and infalling star clusters, which can explain it to some extent. Another observational fact, key to the work presented here, is the presence of a stellar disk at the GC. We postulate that the reason for the missing stars in the RGB is closely intertwined with the disk formation, which initially was gaseous and went through a fragmentation phase to form the stars. Using simple analytical estimates, we prove that during fragmentation the disk developed regions with densities much higher than a homogeneous gaseous disk, i.e. "clumps", which were optically thick, and hence contracted slowly. Stars in the GC interacted with them and in the case of RGB stars, the clumps were dense enough to totally remove their outer envelopes after a relatively low number of impacts. Giant stars in the horizontal branch (HB), however, have much denser envelopes. Hence, the fragmentation phase of the disk must have had a lower impact in their distribution, because it was more difficult to remove their envelopes. We predict that future deeper observations of the GC should reveal less depletion of HB stars and that the released dense cores of RGB stars will still be populating the GC.

5.1 INTRODUCTION

The observations of the inner 0.5 pc ($12''$) of the GC has led in recent years to interesting and challenging discoveries that cannot be fully addressed in the context of standard two-body relaxation theory (for a general summary about the GC, see e.g. Genzel et al. 2010). On the one hand, Buchholz et al. (2009); Do et al. (2009) discovered a spherical core of RGs with a flat surface density profile. If these RGs trace an underlying old stellar population (of $\sim 10^9$ years), the total mass of the old stars might be $\sim 10^5\ M_\odot$ (Merritt 2010). Moreover, Bartko et al. (2010); Levin & Beloborodov (2003); Lu et al.

1 Max Planck Institut für Gravitationsphysik (Albert-Einstein-Institut), D-14476 Potsdam, Germany

(2006); Paumard et al. (2006); Tanner et al. (2006) unveiled the presence of a mildly thick ($H/R \simeq 0.1$, with H the height and R the radius) and young (2–7 Myr) stellar disk, of about 100 Wolf-Rayet (WR) and O-type stars in near-circular orbits ($e < 0.4$). The disk has a total mass of $\sim 10^4\ M_\odot$ and a surface density profile of $\Sigma_d(R) \propto R^{-2}$. The inner and outer edges of the disk are approximately at $R_{\rm in} \simeq 0.04$ pc and $R_{\rm out} \simeq 0.5$ pc. There is also an indication for a second disk, with more eccentric stellar orbits ($e > 0.6$) and smaller disk mass ($< 5 \times 10^3\ M_\odot$), inclined by about 115° relative to the first one, and with a contrary rotation. However, the existence of this second disk is still in debate (Bartko et al. 2009; Lu et al. 2006; Paumard et al. 2006).

The problem of the missing RGs has been addressed by a number of different authors whose approaches can be divided into three general scenarios: (i) along with the discovery of the missing stars in the RGB, Genzel et al. (1996) suggested the interpretation that this could be attributed to stellar collisions due to the extreme stellar densities reached in the GC. This idea has been explored extensively in the works of Alexander (1999); Bailey & Davies (1999); Dale et al. (2009); Davies et al. (1998), but it cannot fully explain the observations; (ii) it has also been hypothesized that a massive black hole binary could scour out a core in the GC via three-body slingshots (Baumgardt et al. 2006; Gualandris & Merritt 2012; Löckmann & Baumgardt 2008; Matsubayashi et al. 2007; Portegies Zwart et al. 2006), but in order to reproduce a core as large as what is observed, the mass of the secondary MBH at the GC should be at least $\sim 10^5\ M_\odot$. This would imply that the Milky Way recently had a major merger, ruled out by current observations (e.g. Chen & Liu 2013; Hansen & Milosavljević 2003; Yu & Tremaine 2003); (iii) infalling clusters towards the GC could also steepen the density profile outside $10''$, making the inner $10''$ like a core (Antonini et al. 2012; Ernst et al. 2009; Kim & Morris 2003), but strong mass segregation can rebuild the cusp in the MW in about $1/4$ of the relaxation time (Alexander & Hopman 2009; Amaro-Seoane & Preto 2011; Preto & Amaro-Seoane 2010). Hence, this argument would require a steady inflow of a cluster roughly every 10^7 years to avoid cusp regrowth.

In this article we propose a simple, new scenario in which the depletion of RGs is merely a consequence of the natural fragmentation phase that the gaseous disk experienced. We prove that the regions of overdensity in the star-forming disk could have removed the envelope of stars in the RGB after a rather low number of crossings through the disk. The exact number depends on effects of non-linearity that cannot be addressed in our simple analytical model. In section 5.2 we introduce the formation of overdensity regions in the star-forming disk and the conditions for them to annul the envelope of RGB stars. In 5.3 we derive the mean number of crossing times that a star will hit one of the clumps in the disk depending on its orbital parameters and in 5.4 the net effect on the clumps. We summarize our findings in section 5.5 as well as the main implications.

5.2 FORMATION OF CLUMPS IN THE GASEOUS DISK AND ENVELOPE REMOVAL CRITERION

The *in situ* star formation model suggests that the disk of WR/OB giant stars formed 2–7 Myrs ago in an accretion disk around the central MBH (Genzel et al. 2003; Levin & Beloborodov 2003). To become self-gravitating and trigger star formation, the disk initially should have had at least $10^4\ M_\odot$ of gas, and could have been as massive as $10^5 M_\odot$ (Nayakshin & Cuadra 2005). When a RG crosses the gaseous disk with a relative velocity v_*, only that part of the envelope with a surface density lower than

$$\Sigma_* \simeq \frac{v_*}{\sqrt{Gm_*/r_*}}\Sigma_d \tag{43}$$

will be stripped off the RG by the disk because of the momentum imparted to that section of the RG (Armitage et al. 1996). In the above equation, Σ_d denotes the surface density of the disk where the impact happens, and m_* and r_* are the mass and radius of the RG, so that $\sqrt{Gm_*/r_*}$ represents the escape velocity from the RG calculated at its surface. The reason why we use the value of the escape velocity here and not at deeper radii in the RG is that the density of a *homogeneous* disk,

$$\Sigma_d \sim \frac{10^4 M_\odot}{(0.1\ \mathrm{pc})^2} \sim 10^6\ M_\odot\ \mathrm{pc}^{-2} \sim 200\ \mathrm{g\ cm}^{-2}, \tag{44}$$

is so low that when the RG crosses the disk, it will be barely scratched, i.e. only material at the surface will be removed from it. For example, an impact at a distance 0.1 pc from the central MBH of mass $M_\bullet \simeq 4 \times 10^6\ M_\odot$ has a relative velocity of $v_* \sim 400\ \mathrm{km\,s}^{-1}$. By comparing Σ_* from Equation (43) and the RG model from Armitage et al. (1996) for $m_* \sim 1\ M_\odot$ and $r_* \sim 100\ R_\odot$, less than $\sim 10^{-7}\ M_\odot$ of the RG envelope will be lost due to the impact. Such a gaseous disk will not induce any noticeable change in the structure of the RG. Only more massive disks, $\gtrsim 10^5\ M_\odot$, and long-lived in the gaseous phase, $\gtrsim 10^7$ yrs, can lead to a more efficient depletion of the envelope[1], but these numbers strongly contradict current observations (Nayakshin & Cuadra 2005; Paumard et al. 2006).

Because the disk itself is too tenuous to strip the entire envelope of any RG flying through it, we postulate that the regions of overdensity that progressively form in the disk, referred to as "clumps", are dense enough to efficiently remove it completely and release the inner compact core of the RGs. This depletion of RGs leads to their flat spatial distribution *and* implicates the existence of a similar number of dense cores within the same volume.

During fragmentation, a clump must satisfy the Jeans criterion to become self-gravitating, that is, if its radius is R_c, the initial diameter must be comparable to the Jeans length, i.e. $2R_c \sim \lambda_J \simeq c_s/(G\rho)^{1/2}$, where ρ is the local gas density, and c_s the effective sound speed. Using $M_c \simeq \rho R_c^3$ and $c_s \simeq H\sqrt{GM_\bullet/R^3}$ in hydrostatic

1 As in the work of Davies & Church (in preparation), private communication

equilibrium, we can now link the properties of the clump, its mass M_c and radius R_c, with the scale height H of the disk and the distance R to SgrA*,

$$\frac{R_c}{R} \simeq \frac{4M_c}{M_\bullet}\left(\frac{R}{H}\right)^2 \simeq 10^{-2}\left(\frac{M_c}{10^2\ M_\odot}\right)\left(\frac{H/R}{0.1}\right)^{-2}, \tag{45}$$

From the last equation we can derive the volume density ρ_c and surface density Σ_c for the clumps,

$$\begin{aligned}\rho_c \simeq \rho \simeq \frac{M_c}{R_c^3} &\simeq \frac{M_\bullet}{64R^3}\left(\frac{M_\bullet}{M_c}\right)^2\left(\frac{H}{R}\right)^6 \\ &\simeq 10^{-11}\mathrm{g\ cm^{-3}}\left(\frac{M_c}{10^2 M_\odot}\right)^{-2}\left(\frac{H}{0.1R}\right)^6\left(\frac{R}{0.1\mathrm{pc}}\right)^{-3}, \qquad (46)\\ \Sigma_c \simeq \rho_c R_c &\simeq \frac{M_\bullet}{16R^2}\left(\frac{M_\bullet}{M_c}\right)\left(\frac{H}{R}\right)^4 \\ &\simeq 2\cdot 10^4\mathrm{g\ cm^{-2}}\left(\frac{M_c}{10^2 M_\odot}\right)^{-1}\left(\frac{H}{0.1R}\right)^4\left(\frac{R}{0.1\mathrm{pc}}\right)^{-2}. \qquad (47)\end{aligned}$$

The stars in the disk are mainly O/WR, which have been observationally constrained to have masses ranging between $64-128\,M_\odot$ (Zinnecker & Yorke 2007), so in the following we adopt $M_c = 10^2\ M_\odot$ as the fiducial value. We take $H/R = 0.1$ as the thickness in view of the current observations of the disk at the GC. Then from Equations (44) and (47), we can see that a clump is typically $\sim 10^2$ more efficient in destroying RGs than its analogue in an homogeneous gaseous disk.

We note that the argument that led to Equation (45) at the same time ensures that the clumps will withstand the tidal forces arising from the MBH, because the Roche radius, $R(M_c/M_\bullet)^{1/3} \simeq (R/34)[M_c/(10^2 M_\odot)]^{1/3}$, is about three times larger than R_c for an $100\,M_\odot$ clump.

When a clump collides with a RG of mass $m_* \simeq 1\ M_\odot$ and radius $r_* \simeq 150\ R_\odot$, at a relative velocity comparable to the orbital velocity of the clump $v_c \simeq 400[R/(0.1\ \mathrm{pc})]^{-1/2}$ $\mathrm{km\,s^{-1}}$, the amount of mass stripped off from the star is

$$\begin{aligned}M_{\mathrm{loss}} \sim &10^{-5}\ M_\odot \frac{v_c}{\sqrt{Gm_*/r_*}}\left(\frac{\Sigma_c}{10^4\ \mathrm{g\ cm^{-2}}}\right) \\ \sim &10^{-4.6}\ M_\odot\ \left(\frac{M_c}{10^2 M_\odot}\right)^{-1}\left(\frac{R}{0.1\ \mathrm{pc}}\right)^{-5/2}. \qquad (48)\end{aligned}$$

The first line was derived by Armitage et al. (1996) numerically, and in the second line we have used Σ_c from Equation (47) for scaling.

Successive impacts will remove *even more efficiently* the outer layer of the RG. This is so, because the density gradient of the RG decreases (see equation 9 of Armitage

et al. 1996 or Kippenhahn & Weigert 1990): The enclosed mass is reduced, and the polytropic constant increases. The envelope therefore expands to even larger radii (see upper panel of Figure 7 in Armitage et al. 1996). The timescale for the expansion is the convective time, much shorter than the orbital period of the star – The RG has achieved hydrostatic equilibrium much before the next impact. To account for this effect, we assume that the nth impact strips a mass of $f_{\rm loss}^{n-1} M_{\rm loss}$ from the RG, where $f_{\rm loss} > 1$. After n impacts, the RG has lost a total mass of $M_{\rm loss}(f_{\rm loss}^{n} - 1)/(f_{\rm loss} - 1)$. In order to *totally* lose the envelope, we have to equate

$$M_{\rm loss} \frac{f_{\rm loss}^{n} - 1}{f_{\rm loss} - 1} = M_{\rm env} \sim 0.5\, M_{\odot}, \tag{49}$$

where $M_{\rm env}$ is the mass in the envelope, and so

$$n_{\rm loss} \simeq \frac{1}{\ln f_{\rm loss}} \left[10 + \ln(f_{\rm loss} - 1) + \ln\left(\frac{M_c}{10^2 M_{\odot}}\right) + 2.5 \ln\left(\frac{R}{0.1\ {\rm pc}}\right) \right]. \tag{50}$$

For a RG of size $r_* \simeq 150\ R_{\odot}$, the typical value of $f_{\rm loss}$ is 2 (Armitage et al. 1996). Hence, it takes about 14 impacts with clumps of $M_c \sim 10^2\ M_{\odot}$ located at $R \sim 0.1$ pc to completely remove the RG envelope. The corresponding $n_{\rm loss}$ will increase to 80 (530) if we assume $f_{\rm loss} = 1.1$ (1.01). We note that for smaller but more common RGs, such as those at the base of the RG branch, $f_{\rm loss} < 2$ is more likely.

5.3 NUMBER OF INTERACTIONS WITH CLUMPS

We now estimate the number of impacts that a RG experiences during successive passages through the fragmenting accretion disk. At a given moment, suppose the disk has a total of N clumps. The eccentricities of these clumps, as we saw in Section 5.1, are not zero, but range between $0.1 - 0.4$, ensuring a covering of the disk surface by a fraction of $N(R_c/R)^2$ for an infalling RG whose *velocity vector* is perpendicular to the disk plane. Such a RG with semimajor axis $a \lesssim 10''$ and period $P(a) \simeq 10^{3.2}\ (a/0.1\ {\rm pc})^{3/2}$ yrs, will collide with clumps at a rate $\Gamma \sim 2N(R_c/R)^2/P(a)$. Any RG on such an orbit will interact with clumps for a time scale comparable with the fragmentation phase of the disk, $t_{\rm frag}$. The exact value of this time depends strongly on the initial conditions, but also on the cooling function and other variables (Amaro-Seoane et al. 2013; Bonnell & Rice 2008; Mapelli et al. 2012; Nayakshin et al. 2007; Wardle & Yusef-Zadeh 2008). Notwithstanding, we note that our model does not rely on $t_{\rm frag}$: Whatever its value is, a *total* number of at least $N_c \sim 10^2$ clumps with $M_c \sim 10^2\ M_{\odot}$ will have formed if we want to match the observed number of WR/O stars in the GC stellar disk. Consequently, at any given moment, the disk will harbor $N \sim N_c(t_c/t_{\rm frag})$ clumps, where we have introduced t_c, the lifetime of a clump, whose

value is derived later in this section. The total number of perpendicular collisions during $t_{\rm frag}$, $n_\perp$, can be estimated to be

$$n_\perp \sim \Gamma t_{\rm frag} \sim N_c \left[\frac{2t_c}{P(a)}\right] \left(\frac{R_c}{R}\right)^2. \tag{51}$$

As mentioned before, there is no dependence on $t_{\rm frag}$ itself. On the other hand, if the orbital plane of RG is coplanar with the disk, the path of the RG covered inside the disk will be longer than in the perpendicular configuration by a factor of $\pi R/H$, then the number of collisions in the coplanar case is

$$n_\parallel \simeq 31\, n_\perp. \tag{52}$$

For a RG with random orbital inclination, the number of collisions with clumps in the disk will range between $n_\perp$ and $n_\parallel$. So as to derive their values, we still need to estimate t_c.

In the standard picture of massive star formation, different parts of a star-forming clump evolve on different timescales (Zinnecker & Yorke 2007): the central part collapses first due to its higher density and hence shorter free-fall timescale. This leads to the formation of a protostar in the core of the clump. The outer layer contracts on a longer timescale because of its lower density, but also due to the new source of heat at the core of the clump, the forming protostar.

Unlike the standard star formation picture, in our case the clump is optically thick. So the heat released by the protostar is kept in the clump, and must be dissipated before the outer layer can contract further, in a self-regulating process of the growth of the protostar and the contraction of the outer layer. This allows us to define t_c. It has been shown that the temperature of the clumps can achieve a value of the order of $T \sim 10^3$ K (Bonnell & Rice 2008; Mapelli et al. 2012). The opacity in the context of molecular clouds has been estimated to be $\kappa \simeq 0.1(T/1\,{\rm K})^{1/2}\ {\rm cm}^2\ {\rm g}^{-1}$ (Bell & Lin 1994). We can then calculate the optical thickness from Equation (47), $\kappa\Sigma_c \sim 10^5 (T/10^3\ {\rm K})^{1/2}$. The assumption of black-body in this context holds, so that the radiative cooling rate at the surface of the outer layer is $4\pi\sigma R_c^2 T^4$, where σ is the Stefan-Boltzmann constant.

For a *given size* of a clump, i.e. before it can contract to a smaller size, the outer layer will emit a *total* energy of $\left(4\pi\sigma T^4 R_c^2\right) t_c$. If we equate this energy with the total amount of heat contained in the clump (i.e. in the gas and the protostar), $GM_c^2/R_c + GM_*^2/R_*$, we have that

$$\begin{aligned} t_c &\sim \frac{GM_*^2/R_*}{4\pi\sigma T^4 R_c^2} \\ &\sim 10^5 {\rm yr} \left(\frac{R}{0.1\ {\rm pc}}\right)^{-2} \left(\frac{M_*}{10^2 M_\odot}\right)^{-2} \left(\frac{T}{10^3\ {\rm K}}\right)^{-4}. \end{aligned} \tag{53}$$

To relate the radius R_* of the protostar to its mass M_*, we adopt the empirical relation for H-burning stars that $R_* \sim 1.29 R_\odot (M_*/M_\odot)^{0.60}$ for $M_* > 1\,M_\odot$ and $R_* \sim R_\odot (M_*/M_\odot)^{0.97}$ for $M_* < 1\,M_\odot$ (see e.g. Nayakshin et al. 2007). This is the reason why in Equation 53 we have neglected the contribution from from the gas, GM_c^2/R_c, since for protostars as light as $0.2\,M_\odot$, the heat released is already comparable to the gravitational energy of the gas in the clump.

Knowing that $N_c \sim 10^2$ clumps with $M_c = 10^2\ M_\odot$ have formed in the disk at $a \sim 0.1$ pc, we find $n_\perp \sim 2$ and $n_\parallel \sim 60$, therefore RGs with $f_{\rm loss} = 2$ generally satisfy the condition $n_\perp < n_{\rm loss} < n_\parallel$. This means a complete loss of the envelope if the RG is in a low-inclination orbit with respect to the disk, and a partial depletion of the envelope if the RG is in a high-inclination orbit.

There is no good reason to believe that the clumps form in a single-mass distribution. A more realistic one would naturally produce also lighter clumps. This is important, because they are more efficient at removing RG envelopes: They have higher surface densities ($\Sigma_c \propto M_c^{-1}$), and each one contributes as many collisions with RGs as a more massive clump can do; while the collisional cross section, $R_c^2 \propto M_c^2$ is smaller, the lifetime, $t_c \propto R_c^{-2} \propto M_c^{-2}$, is elongated. Therefore, a disk harboring smaller clumps, of masses $M_c \sim 1 - 10\ M_\odot$, could in principle contribute significantly more to the depletion of RGs, but this depends on their abundance, which unfortunately is not available from observations yet.

Hence, during the self-gravitating past of the disk at the GC, a stellar core of RGs with flat surface density distribution will be created. This core, once formed, will last for a relaxation time. We note that these results are in agreement with the best fit to the observed surface density of the RGs in our GC with an anisotropic angular-momentum distribution and a core size of 0.1 pc (Merritt 2010).

5.4 IMPACT ON THE CLUMPS

At this point one could wonder whether the accumulated impacting of RGs on to the clumps could eventually disrupt or heat them before a successful RG depletion. To address this question, we estimate the amount of gas removed from a clump after one crossing, i.e. the amount of gas "scooped" away in a cylinder of height comparable to the size of the clump, R_c. As for the radius of the cylinder, we note that the ratio between the radius of a RG (as the ones considered so far) and its Bondi radius $r_{\rm B}$ is

$$\frac{r_*}{r_{\rm B}} \simeq 80 \left(\frac{R}{0.1\ \text{pc}}\right), \tag{54}$$

with $r_{\rm B} := \left(Gm_*/v_{\rm c}^2\right)$. Therefore the radius is determined by r_* and not $r_{\rm B}$. The RG *does* scoop away matter from the clump because its surface density is $3-4$ orders of magnitude larger than that of the clump. The mass loss, $\Delta m \sim r_*^2 \Sigma_c$, for a typical value of $\Sigma_c \sim 10^{7-8}\ M_\odot\ \text{pc}^{-2}$ and $r_* = 100\,R_\odot$, is negligible.

One could also be worried that the energy deposition could heat up the clump and make it less dense, but this is not the case: The maximum energy that can be deposited

into a clump during each transit, $\Delta m v_c^2$, is trifling compared to the binding energy of the clump, GM_c^2/R_c, since

$$\frac{\Delta m v_c^2}{GM_c^2/R_c} \sim \left(\frac{r_*^2}{R_c R}\right)\left(\frac{M_\bullet}{M_c}\right) \sim 10^{-3} \tag{55}$$

for our fiducial massive clumps. The envelope of a RG is lost after $n_{\rm loss}$, i.e. some 15 passages. Such number of hits do not suffice to heat up a clump in disk to stop star formation in it.

5.5 DISCUSSION

The problem of the missing bright red giants has been the focus of an ongoing debate since its discovery, more than 15 years ago, by Genzel et al. (1996). A number of different scenarios have been invoked to explain this deficit of old stars, but none has until now provided a simple and efficient mechanism to solve the problem. In this paper, *considering a single episode of disk formation* at the GC, we explain the missing stars in the RGB in the natural context of the star-forming disk that after fragmentation led to the currently observed stellar disk in our GC. We prove with simple analytical estimates that the distribution of clumps in the disk is sufficient to ensure the removal of the envelopes of the brightest RGs. Successive episodes of disk formation, separated by $\sim 10^8$ yrs, based on AGN duty cycle, would have formed of the order of ten generations of clumps at the GC.

Toward lower luminosities, the HB stars however have an envelope about 100 times denser (in surface density) than those of RGB stars, as it can be easily derived from the calculated structures of solar-metalicity of HB giants of Girardi et al. (2000). Therefore, due to momentum conservation (Equation 43), an HB star requires on the order of 100 more impacts with clumps to remove its envelope, although the non-linearity factor $f_{\rm loss}$ is less clear in this case due to the lack of numerical investigations. We hence predict that only a low percentage of them, those with a low inclination with respect to the disk, will have received significant envelope damage. Number counting of stars in the bin between 16.75 and 17.75 magnitudes in the K-band may indicate a steepening of surface-density distribution for stars fainter than the HB (Schödel et al. 2007,their figure 17), pointing to the picture of partial depletion.

We also predict that the released cores of the RGB stars populate the region of the GC where they lost their envelopes. However, detecting these cores in infrared (IR) surveys may be difficult: (i) the core would exhaust the remaining hydrogen envelope in a couple of Myrs, and would hence appear as very faint now while (ii) shifting its peak emission to shorter wavelengths, becoming invisible in the IR filters (Davies & King 2005).

To prove the densities of HB stars, we need deeper spectroscopic observations and more complete photometric surveys down to the 18th K-magnitude. On the other hand, numerical simulations are required to study the effects of non-linearity, our $n_{\rm loss}$

and f_{loss}, in the interaction between the clumps and the envelops of stars in the RGB but, more importantly, of those in the HB.

BIBLIOGRAPHY

Alexander, T. 1999, ApJ, 527, 835

Alexander, T., & Hopman, C. 2009, ApJ, 697, 1861

Amaro-Seoane, P., & Preto, M. 2011, Classical and Quantum Gravity, 28, 094017

Amaro-Seoane, P., Brem, P., & Cuadra, J. 2013, ApJ, 764, 14

Antonini, F., Capuzzo-Dolcetta, R., Mastrobuono-Battisti, A., & Merritt, D. 2012, ApJ, 750, 111

Armitage, P. J., Zurek, W. H., & Davies, M. B. 1996, ApJ, 470, 237

Bailey, V. C., & Davies, M. B. 1999, MNRAS, 308, 257

Bartko, H., Martins, F., Fritz, T. K., et al. 2009, ApJ, 697, 1741

Bartko, H. 2010, ApJ, 708, 834

Baumgardt, H., Gualandris, A., & Portegies Zwart, S. 2006, MNRAS, 372, 174

Bell, K. R., & Lin, D. N. C. 1994, ApJ, 427, 987

Bonnell, I. A., & Rice, W. K. M. 2008, Science, 321, 1060

Buchholz, R. M., Schödel, R., & Eckart, A. 2009, A&A, 499, 483

Chen, X., & Liu, F. K. 2013, ApJ, 762, 95

Dale, J. E., Davies, M. B., Church, R. P., & Freitag, M., 2009, MNRAS, 393, 1016

Do, T., Ghez, A. M., Morris, M. R., et al. 2009, ApJ, 703, 1323

Davies, M. B., Blackwell, R., Bailey, V. C., & Sigurdsson, S. 1998, MNRAS, 301, 745

Davies, M. B., & Church, R. P., in preparation

Davies, M. B., & King, A. 2005, ApJ Letts., 624, L25

Ernst, A., Just, A., & Spurzem, R. 2009, MNRAS, 399, 141

Genzel, R., Thatte, N., Krabbe, A., Kroker, H., & Tacconi-Garman, L. E. 1996, ApJ, 472, 153

Genzel, R., Schödel, R., Ott, T., et al. 2003, ApJ, 594, 812

Genzel, R., Eisenhauer, F., & Gillessen, S. 2010, RvMP, 82, 3121

Girardi, L., Bressan, A., Bertelli, G., & Chiosi, C. 2000, A&A Supp., 141, 371

Gualandris, A., & Merritt, D. 2012, ApJ, 744, 74

Hansen, B. M. S., & Milosavljević, M. 2003, ApJ Letts., 593, L77

Kim, S., & Morris, M., 2003, ApJ, 597, 312

Kippenhahn, R., & Weigert, A. 1990, Stellar Structure and Evolution, XVI, 468 pp. 192 figs.. Springer-Verlag Berlin Heidelberg New York. Also Astronomy and Astrophysics Library,

Levin, Y., & Beloborodov, A. M. 2003, ApJ Letts., 590, L33

Löckmann, U., & Baumgardt, H. 2008, MNRAS, 384, 323

Lu, J. R., et al. 2009, ApJ, 690, 1463

Mapelli, M., Hayfield, T., Mayer, L., & Wadsley, J. 2012, ApJ, 749, 168

Matsubayashi, T., Makino, J., & Ebisuzaki, T. 2007, ApJ, 656, 879

Merritt, D., 2010, ApJ, 718, 739

Nayakshin, S., & Cuadra, J. 2005, A&A, 437, 437

Nayakshin, S., Cuadra, J., & Springel, V. 2007, MNRAS, 379, 21

Paumard, T., et al. 2006, ApJ, 643, 1011

Portegies Zwart, S. F., Baumgardt, H., McMillan, S. L. W., et al. 2006, ApJ, 641, 319

Preto, M., & Amaro-Seoane, P. 2010, ApJ Letts., 708, L42

Schödel, R., Eckart, A., Alexander, T., et al. 2007, A&A, 469, 125

Tanner, A., et al. 2006, ApJ, 641, 891

Wardle, M., & Yusef-Zadeh, F. 2008, ApJ Letts., 683, L37

Yu, Q., & Tremaine, S. 2003, ApJ, 599, 1129

Zinnecker, H., & Yorke, H. W. 2007, Annual Review of Astronomy & Astrophysics, 45, 481

6

TIDAL DISRUPTIONS IN CIRCUMBINARY DISCS: STAR FORMATION, DYNAMICS, AND BINARY EVOLUTION

Pau Amaro-Seoane[1], *Patrick Brem*[1] *& Jorge Cuadra*[2]

Published in *The Astrophysical Journal*, Volume 764, Issue 1, article id. 14, 9 pp. (2013).

Abstract: In our current interpretation of the hierarchical structure of the universe it is well established that galaxies collide and merge with each other during their lifetime. If massive black holes (MBHs) reside in galactic centres, we expect them to form binaries in galactic nuclei surrounded by a circumbinary disc. If cooling is efficient enough, the gas in the disc will clump and trigger stellar formation in situ. In this first paper we address the evolution of the binary under the influence of the newly formed stars, which form individually and also clustered. We use SPH techniques to evolve the gas in the circumbinary disc and to study the phase of star formation. When the amount of gas in the disc is negligible, we further evolve the system with a high-accurate direct-summation $N-$body code to follow the evolution of the stars, the innermost binary and tidal disruption events (TDEs). For this, we modify the direct $N-$body code to (i) include treatment of TDEs and to (ii) include "gas cloud particles" that mimic the gas, so that the stellar clusters do not disolve when we follow their infall on to the MBHs. We find that the amount of stars disrupted by either infalling stellar clusters or individual stars is as large as 10^{-4}/yr per binary, higher than expected for typical galaxies.

6.1 INTRODUCTION

Super-massive black hole (MBHs) binaries are expected to form after major galaxy mergers. The main driving mechanism for the MBHs to sink to the centre is dynamical friction, where they will form a binary and start to shrink the semi-major axis on their way to the final merger. Slingshot of stars from the surrounding stellar environment help the binary to further decay by exchanging energy and angular momentum, down to distances of about 1 pc (Begelman et al. 1980). However, if the amount of stars to interact with is depleted, there is a risk of stalling, so that the MBHs would not coalesce within a Hubble time. This is the so-called "last-parsec problem" (see Merritt & Milosavljević 2005,for a review on the whole process and references therein).

1 Max Planck Institut für Gravitationsphysik (Albert-Einstein-Institut), D-14476 Potsdam, Germany
2 Departamento de Astronomía y Astrofísica, Facultad de Física, Pontificia Universidad Católica de Chile, 782-0436 Santiago, Chile

Key factors to surmount this last "snag" in the evolution are, among others, the fact that (i) in the case of binaries with a total mass of $\leq 10^7\,M_\odot$, slingshot ejections suffice to guarantee coalescence within a Hubble time (Milosavljević & Merritt 2003); (ii) the role of gas may be crucial in the evolution of the binary, starting at larger scales. It might well be that in a merger of gas-rich galaxies, if MBHs are present, they will coalesce soon after the galaxies merge, in some 10^7 Myr, if the gas is distributed spherically. If, on the other hand, the gas is forming a nuclear disc, the galaxies need only to have 1% of their total mass in gas for this to happen. (Escala et al. 2004, 2005). Cuadra et al. (2009) found that such gas discs could indeed commonly help in the merger of SMBHs with masses in the range of our study, whilst this mechanism fails for masses larger than $\sim 10^7\,M_\odot$; (iii) following with stellar dynamics, resonant relaxation creates a steady state current of stars which can be as large as ten times the non-coherent two-body relaxation (Hopman & Alexander 2006). This is a potential source of new stars populating the depleted loss-cone; (iv) the work of Berczik et al. (2006) shows that considering a non-spherically symmetric system the final parsec problem is largely solved (v) massive perturbers, such as giant molecular clouds or intermediate-mass black holes, can accelerate relaxation by orders of magnitude compared to two-body stellar relaxation, so that many new stars are supplied to interact with (Perets & Alexander 2008); (vi) it has been observed that young, compact star clusters such as the Arches and Quintuplet systems reside near the Galactic centre. If these star clusters have masses larger than $10^5\,M_\odot$, they can make their way down to the Galactic centre even if they start from a distance as large as 60 pc within a few million years (McMillan & Portegies Zwart 2003). The tidal stripping of these young stars could eventually provide the binary system with a new set of some $\approx 10^5$ stars; (vii) if intermediate-mass black holes (IMBHs), with masses ranging between $10^{2-4}\,M.$ exist in the centre of clusters, it has been predicted that within the innermost central 10 pc, we can expect to have some 50 IMBHs of masses $10^3\,M_\odot$, and still some of them at scales of a few milliparsecs (Portegies Zwart et al. 2006). The interaction of one of these IMBHs with the binary of SMBHs would obviously accelerate the process of shrinkage.

The studies just cited provide a number of mechanisms to make the binary shrink. We expect then that a typical binary will be able to reach sub-pc separations, especially in the case of relatively low-mass MBHs in gas-rich environments. In this study, we concentrate on such a case (see section 6.2.1 for details), which is expected when the parent galaxies are gas-rich and large amounts of gas fall to the centre of the new system, together with the MBHs. At that location, the black holes get bound to each other, thus forming a binary, and are surrounded by a massive, parsec-scale gaseous disc (e.g., Dotti et al. 2007; Escala et al. 2005; Mayer et al. 2007).

Such gaseous discs are similar to proto-stellar discs: due to their high density compared to the central object tidal force, the discs will be locally unstable to self-gravity, meaning that perturbations in their density field will grow. However, if the gas is unable to cool efficiently, then the gas will not be able to contract and form clumps, and the density perturbations will be sheared apart, creating a quasi-steady spiral

pattern. Remarkably, the spiral pattern transports the angular momentum outward, making the disc behave as an accretion disc. On the contrary, if the gas is able to cool quickly enough, then the density perturbations grow and form clumps, which shrink and further accrete gas, breaking up the gaseous disc completely and turning it into stars – the so-called *fragmentation* (e.g., Alexander et al. 2008; Gammie 2001; Lodato 2007; Nayakshin et al. 2007; Paardekooper 2012; Rice et al. 2005).

In either cooling regime, the situation where at the centre of the disc the central object is a binary will lead to a non-trivial interaction between them. On previous studies we have focused on the inefficient-cooling regime, showing that torques between the gas and the binary will shrink the orbit of the latter, while the angular momentum is driven out through the disc (Cuadra et al. 2009; Roedig et al. 2011, 2012). In this paper we present the first numerical study of the fast cooling regime in which the disc fragments into stars, and follow the dynamical evolution of the binary–stars system. We carry out our study in two stages (see also Khan et al. 2012): first we model the fragmentation of the disc using smoothed particle hydrodynamics, and then we switch to our direct-summation $N-$body models to both follow the long-term evolution of the system and to study the occurence of TDEs.

The reason for this two-step approach is that we first need to model the gas hydrodynamics in order to follow the fragmentation process of the gas, including the formation of stars and their growth via mergers and accretion of gas. In principle, one could wait for the gas to disperse or be accreted, and simply continue the same integration to follow the dynamical evolution of the stars for long time-scales. However, the SPH code we are using is not designed to follow the collisional N-body dynamics of the system, therefore, it is necessary to use a different code that allow us to model the system of MBHs and stars in a meaningful way.

6.2 FIRST STAGE IN THE EVOLUTION: GASEOUS DISC AND STAR FORMATION IN SITU

6.2.1 *Two MBHs and a circumbinary disc*

Following Cuadra et al. (2009), we concentrate on a binary with the following initial parameters: total mass $M_{\rm bbh} = M_1 + M_2$, where M_1 and M_2 are the masses of the individual MBHs, and mass ratio $M_1/M_2 = 3$, in a circular (Newtonian) orbit of separation a. The binary is surrounded by a corotating gaseous disc with an initial mass $M_{\rm d} = 0.2M_{\rm bbh}$ and radial range $2a$–$5a$. The gas is modelled as an ideal gas with $\gamma = 5/3$, and radiative cooling is mimicked with a cooling time defined as $t_{\rm cool}(r) = \beta/\Omega(r)$, where β is a free parameter that fixes the cooling rate, $\Omega(r) = \sqrt{GM_{\rm bbh}/r^3}$ is the orbital frequency around the binary, and r is the distance from the binary centre of mass. Since we are interested in the fragmentation regime, in this paper we consider fast cooling rates, $\beta \leq 5$. The choice of a disc that fragments is realistic for self-gravitating discs that cool thermally, above a certain surface density

threshold. Levin (2007) showed that, for the masses and distances we are interested in here, that threshold lies in the 10–100 g/cm^2 range.

This model for the system dynamics is scale-free, meaning that it can be scaled up or down to different masses and lenghts. However, in order to introduce star formation and also to estimate the rate of tidal disruption events (TDEs), we need to choose physical units. With that aim we set the total mass of the binary as $M_{\rm bbh} = 3.5 \cdot 10^6 M_\odot$ and we choose $a = 0.04\,$pc. This would be a typical mass for binary black holes in the range that could be detected by a LISA-like experiment (Amaro-Seoane et al. 2012; Amaro-Seoane et al. 2012b). The chosen separation corresponds roughly to the value where we would expect binaries to spend the longest of their evolution in a simple model that considers binary shrinking due to stellar scattering from a spherical cusp (Milosavljević & Merritt 2003) and torques from a non-fragmenting disc (see Cuadra et al. 2009, their eq. 12). [1]

While several studies (Amaro-Seoane et al. 2010, 2009; Amaro-Seoane & Freitag 2006; Khan et al. 2012, 2011; Preto et al. 2011) have shown that stellar dynamical processes pump up the eccentricity of a binary MBH, in this case we are assuming the binary has reached the inner parsec in a gas-rich environment. In such a case, the dynamical friction of the gas on the MBHs drives them to form a circular binary (e.g., Dotti et al. (2007)). Thus we choose a circular orbit for the initial configuration.

6.2.2 *Implementation and treatment of the disc fragmentation*

To follow the process of circumbinary disc fragmentation, we use a modified version of the smoothed particle hydrodynamics (SPH) code (GADGET, Springel 2005; Springel et al. 2001), combining the numerical methods of Nayakshin et al. (2007) and Cuadra et al. (2009). Here we only briefly describe the methods, and refer the interested reader to those papers for more details. We model the gaseous disc as an ensemble of initially $\approx 2 \times 10^6$ particles of $\approx 0.35 M_\odot$ each. The code calculates the gravitational and hydrodynamical interaction between gas particles, plus the gravitational interaction between all particles, including the MBHs as well as the "proto-stars" and "stars" that form during the simulation (see below). We use a softening of $0.001a$ for the gas particles and of $0.01a$ for the proto-stars. The MBHs do not use softening, but a sink radius within which gas particles are accreted. This radius had a value of $0.3a$.

As initial conditions, we take the initially-circular system modelled by Cuadra et al. (2009), at a time $T \approx 500\,\Omega_0^{-1}$. In this way we skip the transient initial evolution caused by the homogeneous initial conditions described in their work, and start from a steady-state configuration in which the circumbinary disc has developed spiral arms. Notice, however, that their simulations used $\beta = 10$, avoiding fragmentation. In our new simulations we set the value of β to either 1, 2, 3, or 5. As a result, the disc now forms clumps, which grow in a runaway fashion. Treating this this with a pure

1 Notice that the choice of $a = 0.04\,$pc is below the classical $\sim 1\,$pc separation of the "final parsec problem", but for the range of masses considered in this work we deem it not a problem, as we summarized in the introduction.

SPH model is not feasible, as the growing densities require ever shorter time-steps. To circumvent this problem, we introduce sink particles to model the proto-stars that we expect would form in these large density regions.

Proto-star particles are created when the gas density reaches 30 times the Roche tidal limit, $M_{\rm bbh}/(2\pi r^3)$. How many stars will form out of a gas density peak is a very complex question, whose solution is well outside the possibilities of our study. In our model we deal with this issue in an individual particle basis, i.e., each gas particle is turned into one proto-star particle of the same mass. However, the newly formed proto-star particles can merge with each other, thus forming higher mass stars. The merger criterion is simply that their distance is smaller than $2f_{\rm m}R_{\rm p}$, where $R_{\rm p}$ is the size of the proto-stars, which we typically take as 10^{15} cm, and $f_{\rm m}$ is a free parameter with fiducial value of unity that mimics the effect of gravitational focusing. The size parameter corresponds to $\sim H/10$ (where H is the disc scale-height), which is roughly the thickness of the gas arms we observe in the simulations. Thus, in a two-step process we are in principle allowing all the dense gas within the same overdensity to form one proto-star. However, we only allow the proto-stars to merge with each other as long as their masses do not exceed $30M_{\odot}$. Once they reach this mass we turn the proto-star particle into an actual *star particle*. The motivation for this threshold is twofold: numerically, we form an actual star out of $\gtrsim 100$ gas particles; physically, we avoid the rapid formation of extremely massive stars. Stars can merge with proto-stars, but not among each other.

Stars and proto-stars also grow by accreting their surrounding gas. We use an Eddington-limited Bondi–Hoyle prescription to calculate their accretion rate, and then pick up at random enough particles from the (proto-)star neighbours that are merged with the sink particle (Springel et al. 2005). To calculate the Bondi–Hoyle and Eddington accretion rates, we use the mass of the (proto) star, and a radius that is either the main sequence value corresponding to that mass (eq. 11 in Nayakshin et al. 2007) for the star particles, or the fixed value $R_{\rm p}$ for the proto-stars. This difference results in a much faster growth for proto-stars than for stars.

The black holes also accrete the few gas particles that get too close to them. This procedure is done mostly to avoid the short time-steps that would be required to follow those gas particle orbits. Accretion on to the black holes is modelled simply with a sink radius – all gas particles entering the region around $0.3a$ of either black hole are taken away from the simulation, with their mass and momentum being added to the corresponding MBH (Cuadra et al. 2006).

We have ran 6 different SPH simulations. Four of them use the fiducial values mentioned above, but differ on the strength of the cooling. We refer to these runs as `beta1`, `beta2`, `beta3a` and `beta5`. Additionally, since we tend to form many very massive stars, we explore the effect of decreasing the numerical size of the proto-stars, hindering their growth. For $\beta = 3$ then we run two additional simulations, `beta3b` and `beta3c`, in both of which we use a smaller size for the protostars of $1436.8\,R_{\odot}$ instead of the fiducial value of $14,368\,R_{\odot}$. Run `beta3c` has however a larger gravitational focusing factor of $f_{\rm m} = 10$ instead of the fiducial $f_{\rm m} = 1$. For both extra simulations then

there is a more severe (Eddington) limit on the accretion rate for the proto-stars than in the fiducial `beta3a`, while simulation `beta3b` has additionally a smaller likelihood of proto-stellar mergers.

These choices in the conditions for gas cooling and for transforming gas particles into "stars" arguably capture a sufficiently broad number of potential fragmentation scenarios so as to envisage our analysis representative of a self-gravitating disc, within the limitations of the rather expensive numerical experiments.

6.3 FRAGMENTING DISCS

We run the SPH simulations of circumbinary discs for several hundred binary dynamical times. Due to the gas self-gravity, clumps grow in the disc. Given the short cooling times, these clumps contract, achieving the disc fragmentation. In most simulations, after only $\approx 200\,\Omega_0^{-1}$, the vast majority ($\gtrsim 90\%$) of the gas is turned into stars, as expected. The system then reaches a quasi-steady state in which stars very slowly accrete the tenous left-over gas (see Nayakshin et al. 2007). The gas morphology at that stage for the different simulations is shown in Fig. 13.

The fragmentation rate is set by the cooling time of the disc, thus discs with lower values of β will evolve faster. We can see this in figure 14, which shows the mass in stars as a function of time for all the simulations. The fourth column in Table 1 shows the number of stars formed in each simulation. Considering only the variation of β, it is clear that shorter cooling times result in larger amounts of stars, as expected (Nayakshin et al. 2007). As the total stellar mass is approximately constant, the typical stellar masses will be lower for shorter cooling times.

It is interesting to note that the star formation process is not uniform. Instead, it happens preferentially in a few localised, relatively large regions, whose sizes are set by the spiral-arm overdensities. Even though we allow proto-stars to merge when they form close together, our numerical recipe avoids the formation of very large stars, which forces the formation of "stellar clusters" (see the left panel of Fig. 17) [2]. Some of these clusters feel a strong torque from the spiral arm and are driven towards the centre of the system, where the tidal force of the binary disperses them. This stellar distribution affects the long-term dynamics of the system and has interesting consequences for the production of tidal disruption events (§6.4.1).

In our tests with $\beta = 3$ and different stellar growth recipes we first notice that runs `beta3a` and `beta3c` are practically identical, and that run `beta3b` has the same curve of stellar mass growth. From this we conclude that in our simulations accretion is

2 For a movie of this simulation, visit the URL
`http://members.aei.mpg.de/amaro-seoane/fragmenting-discs`.
The encoding of the movie is the free OGG Theora format and should stream automatically with a gecko-based browser (such as mozilla or firefox) or with chromium or opera. Otherwise please see e.g. `http://en.wikipedia.org/wiki/Wikipedia:Media_help_(Ogg)` for an explanation on how to play it.

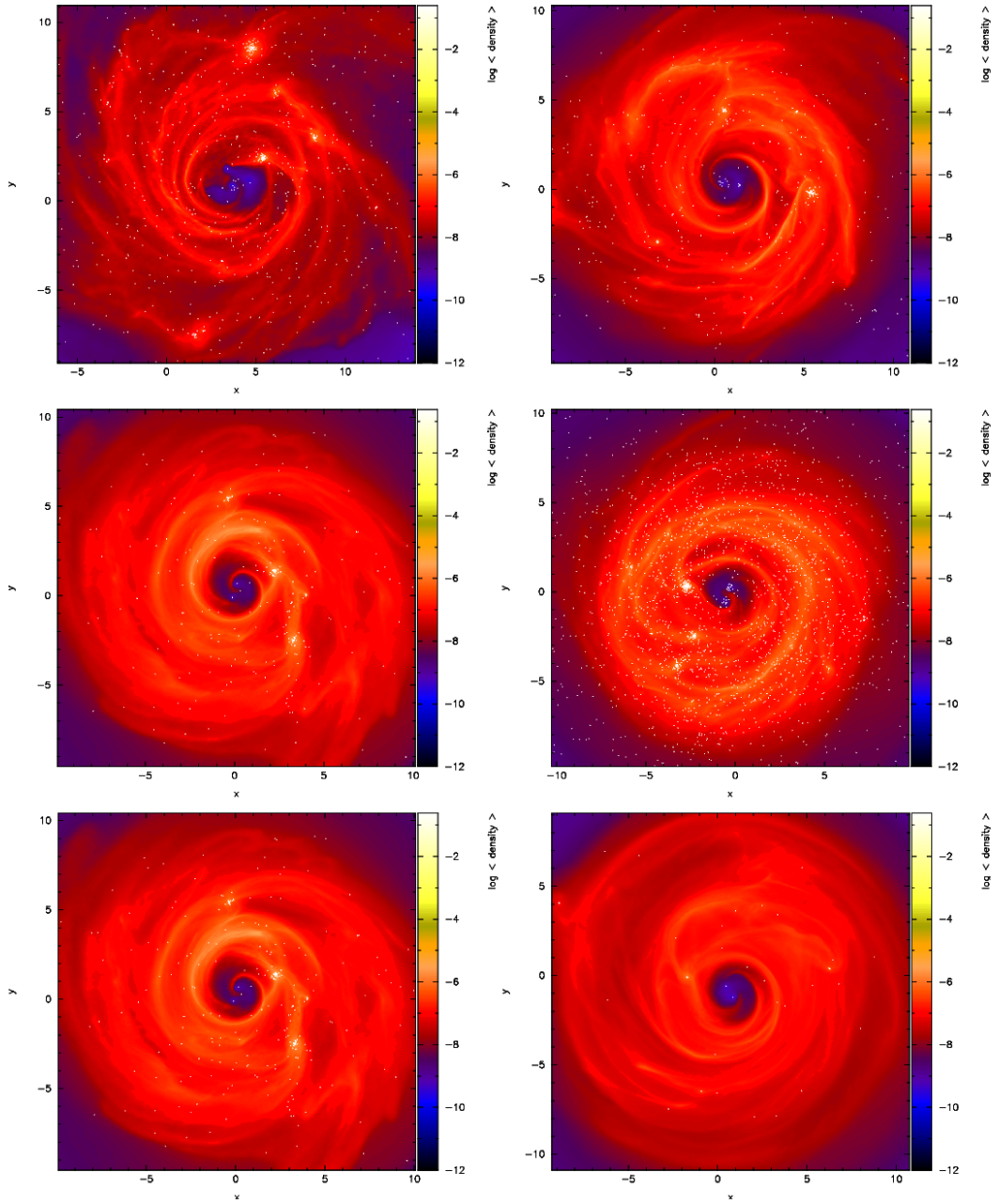

Figure 13: Gas density projected in the X–Y plane perpendicular to the angular momentum vector of the system for `beta1`, `beta2`, `beta3a`, `beta3b`, `beta3c` and `beta5`, from the left to the right and from the top to the bottom. White dots represent the "sink" particles, i.e. the MBHs and the stars formed during the simulations. All snapshots are at $T = 300\,\Omega_0^{-1}$ but for the last one, which was integrated up to $T = 1000\,\Omega_0^{-1}$, because in that run cooling is quite slow and the number of stars is still very low at earlier times (see Fig. 14). Note that there is virtually no difference betwen `beta3a` and `beta3c`. The figures were made with SPLASH (Price 2007).

not important and that stellar growth is driven by mergers of sink particles. [3] We also notice that the number of stars formed is about an order of magnitude higher in `beta3b`, which has 10 times smaller proto-stars than the fiducial run, and that the effect of having smaller proto-stars in the simulation is similar to having a shorter cooling time.

To continue our study of the evolution of the MBHs and circumbinary disc system, we will take the masses, positions, and velocities of all sink particles and use them as input in direct-summation $N-$body simulations. For simplicity, we take the snapshot at time $T = 300\,\Omega_0^{-1}$ for all configurations, except for `beta5`. Since in that run the evolution is slower, we use the snapshot at $T = 1000\,\Omega_0^{-1}$, by which time 90% of the gas has turned into stars.

6.4 THE ROLE OF STARS IN THE SHRINKING OF THE BINARY

To analyse the dynamical evolution of the MBH binary embedded in the stellar system product of the stellar formation we use a direct-summation code, NBODY6. This is a very expensive method because we integrate all gravitational forces for all formed stars at every time step, without making any a priori assumptions about the system. This code belongs to the family of dynamical codes for particle systems with relaxation processes of Sverre Aarseth. The code uses the improved Hermite integration scheme as described in (Aarseth 1999, 2003). Since these approaches integrate Newton's equations directly, all Newtonian gravitational effects are included naturally. More crucial for this subject is that it also incorporates both the *KS regularisation* and the *chain regularisation*, so that when stars are tightly bound or their separation becomes too small during a hyperbolic encounter, the system is regularised (Kustaanheimo & Stiefel 1965). The advantages of this code as compared to the leap frog integrator of GADGET for our particular problem are obvious, namely the high accuracy in the energy conservation, since we are interested in the correct evolution of the inner binary of MBHs as well as in potential TDEs. For this aim, as we describe later, we modified the standard version of NBODY6.

For each simulation, the initial masses, coordinates and velocities for the stars and MBHs are taken from the GADGET data at the times shown in table 1. At that moment, the gas mass – stellar mass ratio is very low (see table 1, column $M_{\rm gas}/M_\star$). The gravitational effect of gas is almost negligible and we do not include it in the simulations. Despite our limit to the growth of "proto-star particles" in the SPH simulations (see section 6.3), some "star particles" did manage to achieve very large masses. We deem those unphysical, so in the initial conditions for our $N-$body runs we replace

3 This is actually not surprising, as stars grow by mergers in roughly the dynamical time inside an overdensity, $t_{\rm dyn} \sim (G\rho)^{-1/2}$, which corresponds to about hundred years for the density values required for the introduction of sink particles. On the other hand, the Bondi accretion rate for a solar mass sink, even for those very high densities, is only $\dot{M}_{\rm Bondi} \sim 10^{-5} M_\odot {\rm yr}^{-1}$ in our models, so the time required to accrete *a single* SPH particle turns out to be $t_{\rm acc} \sim 3 \times 10^4$ yr.

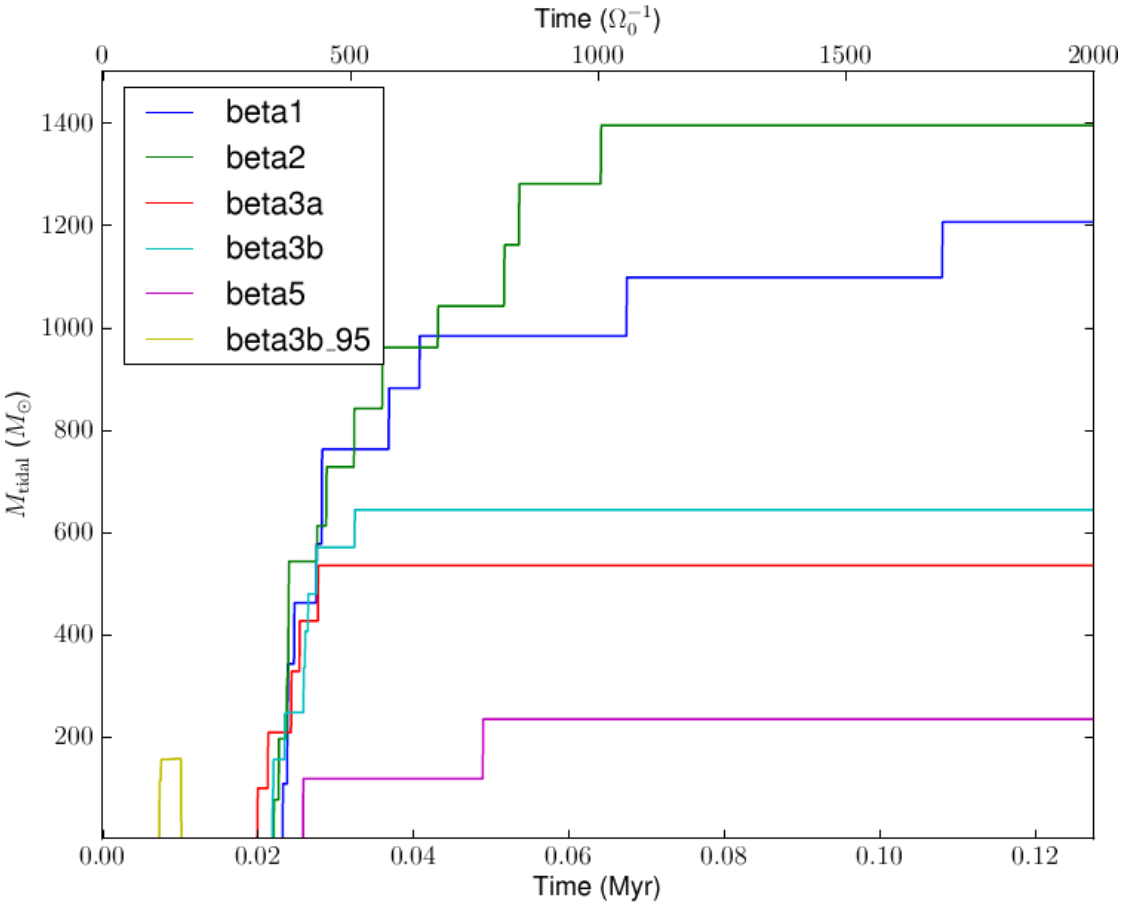

Figure 14: Accumulated stellar mass formed in the disc in $M_\odot$ for our fiducial case of a binary of $3.5 \cdot 10^6\, M_\odot$. All simulations but for $\beta = 5$, which needs a bit longer, reach relatively fast the maximum of stellar mass and saturate with values below $10^6\, M_\odot$.

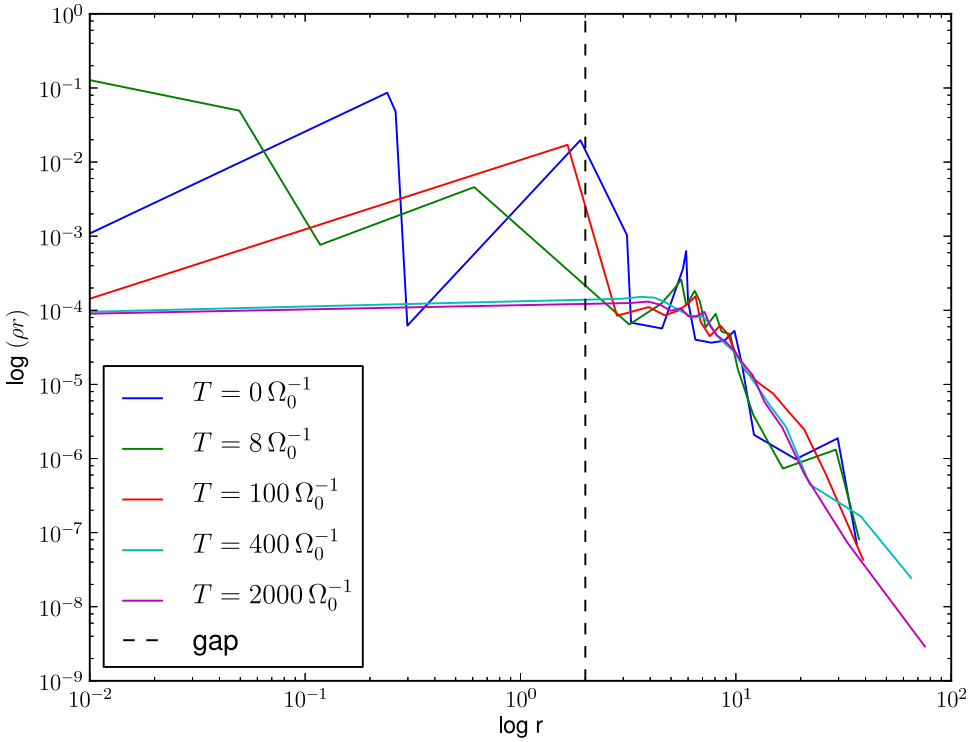

Figure 15: Evolution of the density profile in one $N-$body simulation `beta1` at different times in the evolution. The dashed line corresponds approximately to the position of the inner gap in the SPH simulation.

stars with masses m above $120\,M_\odot$ with a cluster following a Plummer distribution (Plummer 1911) consisting of equal mass stars with total mass m and radius

$$R = \left(\frac{m}{3M_{\rm bbh}}\right)^{1/3} r, \tag{56}$$

with r the distance to the centre-of-mass of the binary. The last equation corresponds to the Roche lobe of the massive star with respect to the MBH binary with mass $M_{\rm bbh}$.

In our $N-$body simulations, table 1, we exclude stars which are at a distance $r > 100a$, where a is the semi-major axis of the MBH binary. We assume those stars would have only a negligible effect on the binary evolution. They correspond to about a quarter of all stars in each simulation. As shown in figure 15, this cut in the cluster did not affect its global structure, its density profile remains roughly constant at large radii. The figure also shows that the region inside a few times the binary semi-major axis gets depleted quickly by sling-shot interactions, as expected.

Model	SPH time	$M_{\rm gas}/M_\star$	$N_{\rm SPH}$	$N_{\rm NB}$	$N_{\rm split}$
`beta1`	300	3%	2536	1895	4469
`beta2`	300	7%	1429	1141	2768
`beta3a`	300	9%	699	585	1924
`beta3b`	300	9%	5487	4486	5193
`beta5`	1000	10%	167	144	1146
`beta3b95`	95	–	5540	5540	5540

Table 1: Initial data for the NBODY6 runs. Notice that we do not integrate run `beta3c` using the $N-$body technique, because it turned out to be identical to `beta3a`. SPH time is the moment at which we stop the GADGET simulation, in units of Ω_0^{-1}, $M_{\rm gas}/M_\star$ is the ratio between gas and stellar mass at that moment, $N_{\rm SPH}$ is the number of stars that have been formed at that moment in the GADGET simulation, $N_{\rm NB}$ is the number of stars within a distance $r < 100a$ from the centre of mass of the binary and $N_{\rm split}$ is the number that we get after splitting all very massive stars into sub-clusters, as explained in section 6.4. The reason why the last model has more stars than `beta3b` at $T = 300$ is because it corresponds to a previous moment in the evolution and, as we explained above, protostars are allowed to merge with each other. This last case is a special one, and we ran a dedicated simulation for it. See section 6.4.1. Also, we note that while the gas was originally distributed in a rather narrow radial range ($2a - 5a$), we end up with stars even at distances $> 100\,a$. This is due to $N-$body scattering, as many star particles are formed in relatively crowded regions of the disc.

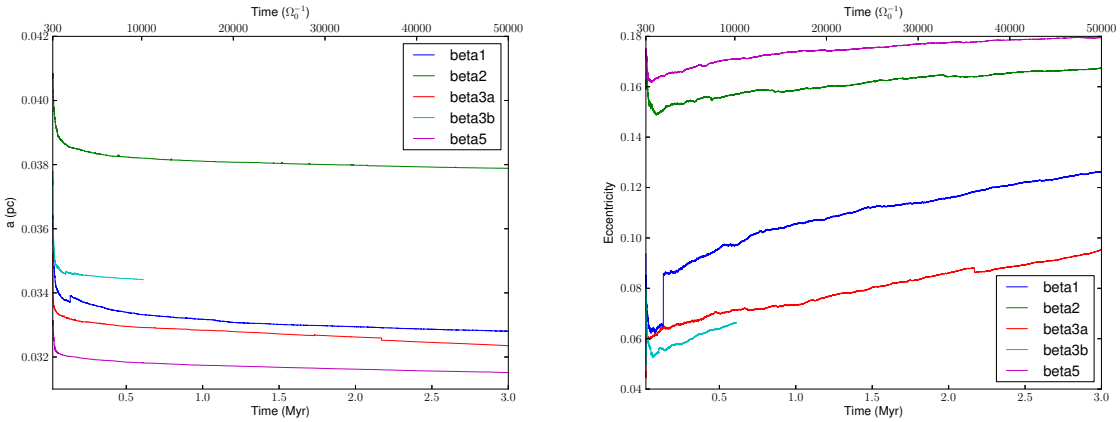

Figure 16: *Left panel:* Evolution of the binary semi-major axis for all cases in the $N-$body simulations in units of the initial orbital period Ω_0^{-1} and in Myrs. Case `beta3b` was not integrated for more than 10,000 orbits because of numerical issues due to the high number of stars in that simulation. *Right panel:* Same for the eccentricity.

In figure 16 we see the evolution of a and e for all cases, integrated with NBODY6 with the results of the SPH simulations as input parameter. After some 10,000 orbits the binaries reach a stagnation point from which the decay becomes much slower. The decay rates $(1/a)(\Delta a/\Delta t)$ averaged over the time period from 0.5 Myr to 3 Myr are: `beta1` : $7.2 \times 10^{-9}\,\mathrm{yr}^{-1}$, `beta2` : $4.0 \times 10^{-9}\,\mathrm{yr}^{-1}$, `beta3a` : $8.0 \times 10^{-9}\,\mathrm{yr}^{-1}$, and `beta5` : $4.0 \times 10^{-9}\,\mathrm{yr}^{-1}$ (although for this case we start at 1000 Ω_0^{-1}, which means actually from 0.56 to 3.06 Myr). In the first 0.1 Myr of the evolution, the significant drop in semi-major axis corresponds to decay rates of $6.7 \times 10^{-7}\,\mathrm{yr}^{-1}$ for `beta1`, $5.4 \times 10^{-7}\,\mathrm{yr}^{-1}$ for `beta2`, $5.4 \times 10^{-7}\,\mathrm{yr}^{-1}$ for `beta3a` and $3.2 \times 10^{-7}\,\mathrm{yr}^{-1}$ for `beta5`.

The early dynamical evolution (first few hundred Ω_0^{-1}) is dominated by close encounters between the MBH binary and stars on radial orbits (i.e. in the loss cone of the binary). This is naturally accompanied by a high rate of tidal disruptions (see figure 19) and a strong change in orbital binding energy of the binary. In the following long-term evolution, the loss cone has been depleted and the binary is subject to the secular effects of the disk as a non-spherical background potential. The effect of this type of mass distribution is a slow exchange of orbital energy but a rather efficient exchange of angular momentum (Merritt & Vasiliev 2010), which is consistent with the significant increase in eccentricity that we observe in this phase compared to the very slow decay rates in the semi-major axis.

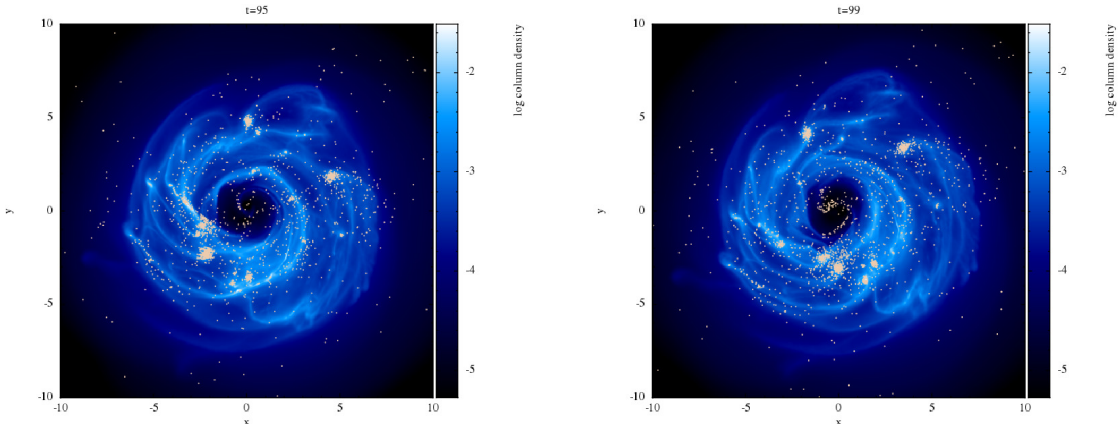

Figure 17: Same as figure 13 for the simulation `beta3b`. At the SPH time 95 the closest stellar cluster hurls itself on to the binary and leads to an enhancement in the TDEs. We take the position of stars and gas particles from the left panel to start a dedicated direct-summation $N-$body integration which we name after this instant of time, `beta3b95`.

6.4.1 *An infalling cluster of young stars*

In the SPH simulations modelling disc fragmentation we see large amounts of stars falling to the immediate vicinity of the MBH binary. In particular, in simulation `beta3b` we observe an infalling cluster [4] at $T = 95\,\Omega_0^{-1}$ (see figure 17).

Since this is quite interesting from the stellar dynamics point of view, we run a dedicated simulation for this particular situation with the direct-summation code. Nonetheless, at this early stage in the evolution of the disc, there is a significant mass in gas which has not yet transformed into stars. If we ran the simulation without taking into account the gas, the small stellar clusters would dissolve, as their potential wells would be abruptly much shallower and the stars could not be held together. We therefore have to include a prescription in the $N-$body simulations for the role of the gas, since including the gas particles directly is well outside the scope of our work.

In this dedicated $N-$body simulation we model each dense region that contains a non-negligible amount of mass as one particle with a big softening length. For this, we define a sphere at every region of interest. We then look at the SPH gas particle distribution and group together all particles within this region, compute their total mass, center-of-mass position and velocity and create one "cloud particle" with these properties (see Fig. 18). In the subsequent $N-$body simulation these particles are integrated separately, which required a modification in the code. In all gravitational

4 As in the former footnote about the movie, from $T = 95$ onwards in the simulation.

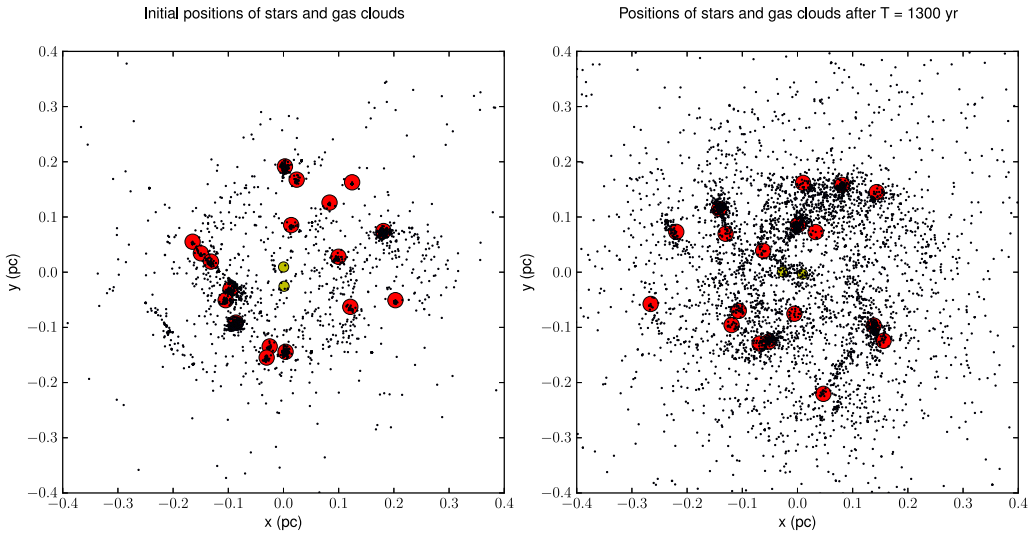

Figure 18: *Left panel:* Initial configuration in the x-y plane perpendicular to the angular momentum vector of the system for simulation `beta3b95` of table 1. Stars are shown with black dots, gas clouds with red circles. The MBHs are depicted with green circles. *Right panel:* The same system after the cluster falls on to the binary, after $\sim 1,300$ yrs. Note the enhanced number of stars in the vicinity of the binary. This translates in a larger number of TDEs.

interactions, the gravitational potential of the cloud particle seen by a regular star is then computed as

$$\Phi_c = -\frac{GM_c}{r_c + \epsilon}, \tag{57}$$

where M_c and r_c are the mass and distance to the cloud particle and ϵ denotes the softening length, taken to be of the order of the size of the corresponding sub-cluster. Although the concept of cloud particles is already implemented in the standard version of NBODY6, we modified it to integrate the cloud particles taking into account the gravitational potential of the other clouds, stars and MBHs in order to follow correctly the orbits around the central binary of MBHs.

The effect is that the particles in the sub-clusters now feel an additional gravitational force corresponding to the cloud and thus stay within their respective group for a longer time, which allows us to study their infall and to analyse TDEs. However, after one close encounter of a gas cloud with one of the MBHs, the cloud would suffer a stripping from the cluster and now float around as an unphysically big agglomeration of mass. This means that we can get only a meaningful result for the very first encounter of each sub-cluster with the binary. In this respect, when estimating the TDEs for the infalling cluster, we will be giving a *lower limit*, since we cannot simulate

Simulation	TDEs (yr^{-1})
beta1	$1.1 \cdot 10^{-4}$
beta2	$1.4 \cdot 10^{-4}$
beta3a	$6 \cdot 10^{-5}$
beta3b	$9 \cdot 10^{-5}$
beta5	$2 \cdot 10^{-5}$

Table 2: Tidal event rates for the simulations of table 1.

realistically further interactions of the cluster with the MBH binary. In the right panel of figure 18 we show the distribution of stars in the X–Y plane after the first interaction.

6.5 TIDAL DISRUPTION EVENTS

During the direct-summation $N-$body runs any star entering the tidal radius R_T of one of the MBHs is considered to be tidally disrupted and its mass is added to the mass of the hole. For a solar-type star, this radius is (see e.g. Amaro-Seoane 2012,for a derivation and examples)

$$R_T = R_\star \left(\frac{M_{BH}}{m}\right)^{1/3}. \tag{58}$$

In the last expression M_{BH} is the mass of *one* of the MBHs, $R_\star$ the radius of the star and m its mass. In order to estimate the radius of a star given its mass, we adopt the simple relation $R_\star \propto m^{0.6}$ (Demircan & Kahraman 1991; Gorda & Svechnikov 1998) with the normalization that a solar mass star has solar radius. Using this in Eq. 58, we can compute the tidal radius in solar radii:

$$R_{T,\odot} = 1.29\, m_\odot^{0.6} \left(\frac{M_{BH}}{m}\right)^{1/3}, \tag{59}$$

where $m_\odot$ is the mass of the star in solar masses and the pre-factor comes from an empirical fit for high-mass stars.

In figure 19 we show the accumulated stellar mass fraction in tidal disruptions for all simulations. Based on this figure and for a time interval of 0.1 Myr after the initialization of the simulations, we can convert the values in tidal disruption events, as shown in table 2. Notice that the rate is actually much higher at the beginning of the simulations, but that result is likely to be affected by our initialisation choices.

DISCUSSION

In this work we have presented the first realisations of fragmenting discs around a binary of two MBHs in SPH with star formation followed by direct-summation $N-$body simulations of the resulting systems. We have evaluated different fragmentation sce-

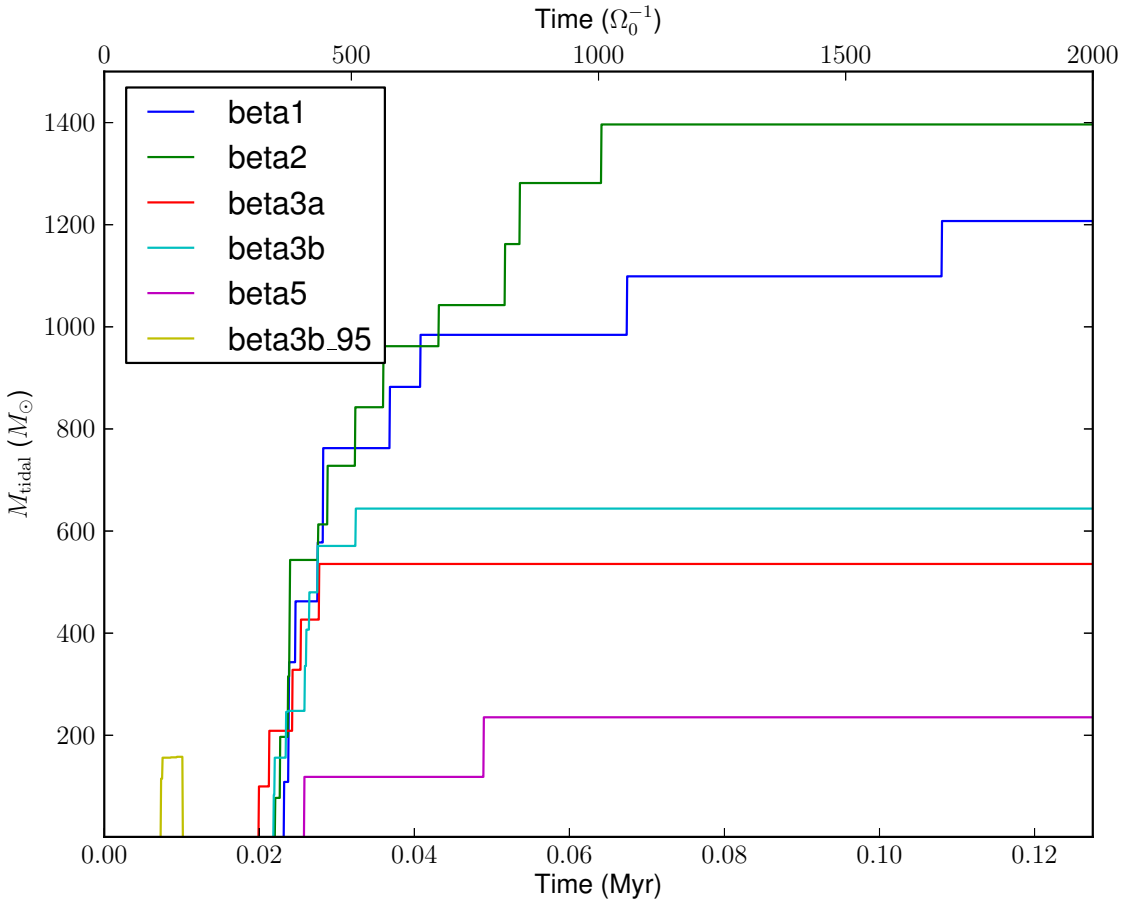

Figure 19: Accumulated stellar mass in tidal disruptions for the different simulations of table 1. Since we only track them in the $N-$body simulations, the curves start at $T = 300\,\Omega_0^{-1}$ but for model `beta3b95`, which as explained before, had a dedicated run. Because we cannot simulate realistically more than one infall of the cluster, we stop it after the first periapsis passage.

narios based on an approximation for the cooling rate of the gaseous discs and different prescriptions for the growth of protostars.

When the gas is almost completely depleted, we take the masses, positions and velocities of the newly formed stars and feed them to the direct-summation $N-$body integrations with the proviso that if the protostar has a mass above $120\,M_{\odot}$, we convert it into an agglomeration of stars following a Plummer profile of radius the Roche radius of the protostar to avoid artificially-created very massive stars.

We find that the rate of decay in our direct $N-$body simulations is slower than the $\approx 10^{-6}\,\mathrm{yr}^{-1}$ found in the SPH simulations of Cuadra et al. (2009), when scaling to the same masses and separations.

We simulate with a dedicated direct-summation integration the particular case of a simulation in which a cluster of stars that forms during the SPH simulation falls on to the binary, the case `beta3b95`. For this, we modify NBODY6 to include "gas cloud" particles that allow the infalling cluster to hold together in the dynamical simulation in which we cannot realistically simulate the gas.

Infalling clusters such as this and the scattering of isolated stars lead to a significant number of TDEs. To make an accurate estimation, we made a second modification of NBODY6 to implement stellar tidal disruptions, and we find that the event rates lie between $2\cdot 10^{-5}- \sim 10^{-4}$ per system per year, which lies on the high side of current (uncertain) estimates for the TDE rate in standard galaxies, which typically lie between $10^{-5}-10^{-6}\,\mathrm{yr}^{-1}$ (Phinney 1989; Magorrian & Tremaine 1999; Syer & Ulmer 1999), and lie well within the observed rates (Donley et al. 2002; van Velzen & Farrar 2012). A particular interesting signature of these TDEs is the "reverberation mapping" response of the circumbinary disc to a burst of emission produced by the TDEs. The light from the burst excites the gas in the disc, producing emission lines. The time-variability of the spectra, the *echo* of the TDE, during the months after the burst could in principle allow us to constrain the disc structure (Brem, Amaro-Seoane, Cuadra & Komossa; part II of this paper to be submitted).

While our simulations cannot follow the evolution of the binary for much longer times, it is interesting to ask the question whether the semi-major axis of the binary reaches distances that would lead it to coalesce within a Hubble time because of the emission of gravitational radiation, measurable in a LISA-like detector such as eLISA (Amaro-Seoane et al. 2012). For this, the binary has to shrink from an initial semi-major of $a \approx 0.04\,\mathrm{pc}$ down to $a \approx 0.003\,\mathrm{pc}$. This corresponds to an increase of orbital binding energy of about one order of magnitude. The net change in binding energy after an interaction with one bound star of mass $m_{\star}$ can be estimated as $\Delta E_{\star} = Gm_{\star}M_{\mathrm{bbh}}/a$. We start the direct-summation simulations with a ratio of stellar mass to MBH binary mass of $\approx 10\%$, so that ab definitio the stellar mass that is formed is not enough for the binary to shrink down to the phase in which the evolution is dominated by gravitational radiation. Indeed, if we consider all stars in the disc to be ejected, we estimate in the limit of this low mass ratio that the total effect of the stellar disc is of about $\delta E_{\mathrm{tot}} = GqM_{\mathrm{bbh}}^2/a$, where q is the mass ratio of stellar mass to BH mass. Following an argument similar to e.g. Quinlan (1996); Sesana et al. (2007), if we compare this to

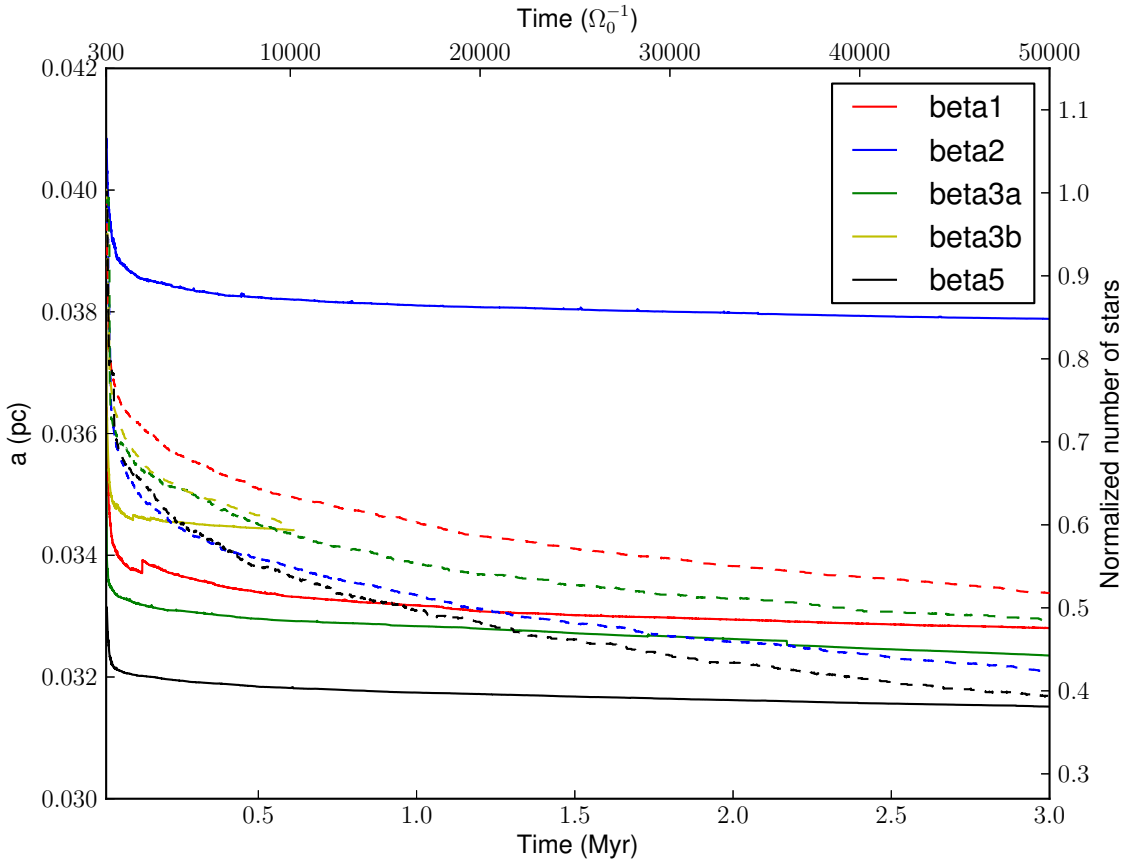

Figure 20: Same as the left panel of figure 16 but including the number of stars in each simulation, for the same colour but in dashed lines. By the end of our numerical treatment we have lost at least 50% in all cases.

the orbital energy at semi-major axis a, one finds that the relative change after ejecting all the stars is $\delta E_{\rm tot}/E \approx q/\nu$, where $\nu = 0.2$ is the symmetric mass ratio, well below what would be necessary to shrink the binary by one order of magnitude. We note that indeed ejecting half of the stellar mass only shrinks the binary semi-major axis by $< 25\%$, as we see in the first 3 Myr of our $N-$body simulations, in figure 20. While this is true for our specific scenario, we note that further episodes of gas inflow towards the centre could potentially trigger more episodes of star formation in the disc, which would lead to star scattering and a further skrinkage. Moreover, while we have focused on the effect of stars formed in-situ on the binary, but the system will be surrounded by a stellar cusp that constitutes an additional source of shrinkage for the binary. The supply of stars that will interact with it can be enhanced by additional mechanisms in a more realistic picture than that of an isolated, spherically symmetric galactic nucleus, as we discussed in the introduction.

BIBLIOGRAPHY

Aarseth, S. J. 1999, The Publications of the Astronomical Society of the Pacific, 111

——. 2003, Gravitational N-Body Simulations (ISBN 0521432723. Cambridge, UK: Cambridge University Press, November 2003.)

Alexander, R. D., Armitage, P. J., & Cuadra, J. 2008, MNRAS, 389, 1655

Amaro-Seoane, P. 2012, ArXiv e-prints

Amaro-Seoane, P. et al. 2012a, Accepted for publication at GW Notes

——. 2012b, Classical and Quantum Gravity, 29, 124016

Amaro-Seoane, P., Eichhorn, C., Porter, E. K., & Spurzem, R. 2010, MNRAS, 401, 2268

Amaro-Seoane, P., & Freitag, M. 2006, ApJ Lett., 653, L53

Amaro-Seoane, P., Miller, M. C., & Freitag, M. 2009, ApJ Lett., 692, L50

Begelman, M. C., Blandford, R. D., & Rees, M. J. 1980, Nat, 287

Berczik, P., Merritt, D., Spurzem, R., & Bischof, H.-P. 2006, ApJ Lett., 642, L21

Cuadra, J., Armitage, P. J., Alexander, R. D., & Begelman, M. C. 2009, MNRAS, 393, 1423

Cuadra, J., Nayakshin, S., Springel, V., & Di Matteo, T. 2006, MNRAS, 366, 358

Demircan, O., & Kahraman, G. 1991, Astrophysics and Space Science, 181

Donley, J. L., Brandt, W. N., Eracleous, M., & Boller, T. 2002, 124, 1308, arXiv:astro-ph/0206291

Dotti, M., Colpi, M., Haardt, F., & Mayer, L. 2007, MNRAS, 379, 956

Escala, A., Larson, R. B., Coppi, P. S., & Mardones, D. 2004, ApJ, 607, 765

——. 2005, ApJ, 630, 152

Gammie, C. F. 2001, ApJ, 553, 174

Gorda, S. Y., & Svechnikov, M. A. 1998, Astronomy Reports, 42

Hopman, C., & Alexander, T. 2006, ApJ, 645, 1152

Khan, F. M., Berentzen, I., Berczik, P., Just, A., Mayer, L., Nitadori, K., & Callegari, S. 2012, ApJ, 756, 30

Khan, F. M., Just, A., & Merritt, D. 2011, ApJ, 732, 89

Kustaanheimo, P. E., & Stiefel, E. L. 1965, J. Reine Angew. Math.

Levin, Y. 2007, MNRAS, 374, 515

Lodato, G. 2007, Nuovo Cimento Rivista Serie, 30, 293

Magorrian, J., & Tremaine, S. 1999, MNRAS, 309

Mayer, L., Kazantzidis, S., Madau, P., Colpi, M., Quinn, T., & Wadsley, J. 2007, Science, 316, 1874

McMillan, S. L. W., & Portegies Zwart, S. F. 2003, ApJ, 596, 314

Merritt, D., & Milosavljević, M. 2005, Living Reviews in Relativity, 8, 8

Merritt, D., & Vasiliev, E. 2011, ApJ, 726, 61

Milosavljević, M., & Merritt, D. 2003, ApJ, 596

Nayakshin, S., Cuadra, J., & Springel, V. 2007, MNRAS, 379, 21

Paardekooper, S.-J. 2012, MNRAS, 421, 3286

Perets, H. B., & Alexander, T. 2008, ApJ, 677, 146

Phinney, E. S. 1989, in IAU Symposium, Vol. 136, The Center of the Galaxy, ed. M. Morris, 543

Plummer, H. C. 1911, MNRAS, 71

Portegies Zwart, S. F., Baumgardt, H., McMillan, S. L. W., Makino, J., Hut, P., & Ebisuzaki, T. 2006, ApJ, 641, 319

Preto, M., Berentzen, I., Berczik, P., & Spurzem, R. 2011, ApJ Lett., 732, L26

Price, D. J. 2007, Publications of the Astronomical Society of Australia, 24, 159

Quinlan, G. D. 1996, New Astronomy, 1

Rice, W. K. M., Lodato, G., & Armitage, P. J. 2005, MNRAS, 364, L56

Roedig, C., Dotti, M., Sesana, A., Cuadra, J., & Colpi, M. 2011, MNRAS, 415, 3033

Roedig, C., Sesana, A., Dotti, M., Cuadra, J., Amaro-Seoane, P., & Haardt, F. 2012, A&A, 545, A127

Sesana, A., Haardt, F., & Madau, P. 2007, MNRAS, 379, L45

Springel, V. 2005, MNRAS, 364, 1105

Springel, V., Di Matteo, T., & Hernquist, L. 2005, MNRAS, 361, 776

Springel, V., Yoshida, N., & White, S. D. M. 2001, New Astronomy, 6, 79

Syer, D., & Ulmer, A. 1999, MNRAS, 306

van Velzen, S., & Farrar, G. R. 2012, European Physical Journal Web of Conferences, 39, 08002

7

A RAPID EVOLVING REGION IN THE GALACTIC CENTER: WHY S-STARS THERMALIZE AND MORE MASSIVE STARS ARE MISSING

Xian Chen[1] *&* **Pau Amaro-Seoane**[1]

Published in *The Astrophysical Journal Letters, Volume 786, Issue 2, article id. L14, 5 pp. (2014).*

Abstract: The existence of "S-stars" within a distance of 1″ from SgrA* contradicts our understanding of star formation, due to the forbiddingly violent environment. A suggested possibility is that they form far and have been brought in by some fast dynamical process, since they are young. Nonetheless, all conjectured mechanisms either fail to reproduce their eccentricities –without violating their young age– or cannot explain the problem of "inverse mass segregation": The fact that lighter stars (the S-stars) are closer to SgrA* and more massive ones, Wolf-Rayet (WR) and O-stars, are farther out. In this Letter we propose that the responsible for *both*, the distribution of the eccentricities and the paucity of massive stars, is the Kozai-Lidov-*like* resonance induced by a sub-parsec disk recently discovered in the Galactic center. Considering that the disk probably extended to smaller radius in the past, we show that in as short as (a few) 10^6 years, the stars populating the innermost 1″ region would redistribute in angular-momentum space and recover the observed "super-thermal" distribution. Meanwhile, WR and O-stars in the same region intermittently attain ample eccentricities that will lead to their tidal disruptions by the central massive black hole. Our results provide new evidences that SgrA* was powered several millions years ago by an accretion disk as well as by tidal stellar disruptions.

7.1 INTRODUCTION

Observations of the Galactic Center (GC) going back as far as 20 years (see Genzel et al. 2010, for a review) reveal three facts: (1) An isotropic cusp of young O/B and Wolf-Rayet (WR) stars, starting at a distance of 30″ from SgrA* and extending inward to about 1″ (1″ $\simeq$ 0.04 pc); (2) a mildly thick stellar *disk*, of about 100 WR and O-type stars, spanning from an inner radius of 1″ to an outer radius of about 10″; and (3) populating the innermost region, within 1″ from SgrA*, are a population of B stars, commonly referred to as the "S-stars", but *no* WR/O stars. A single star-formation (SF) episode

1 Max Planck Institut für Gravitationsphysik (Albert-Einstein-Institut), D-14476 Potsdam, Germany

may have explained the formation of disk and cusp stars (Lu et al. 2013), the S-stars, however, cannot have been born in this scenario, because the violent environmental conditions within $1''$ do not allow in-situ SF. One way of populating that region is by dynamical friction, but the associated timescale is too long. For this reason, the problem has the reputation of the "paradox of youth" (Ghez et al. 2003; Morris 1993).

This issue has led to the idea that S-stars could have formed at larger radii and brought in later by an efficient dynamical mechanism. One possibility is tidal separation of binaries (Ginsburg & Loeb 2006; Gould & Quillen 2003; Hills 1991). A binary, formed at larger radius, can be set in such an orbit that at periapsis it will be tidally separated by the central massive black hole (MBH), leaving one star, which could be a B star, bound to the MBH at a typical radius of $\lesssim 1''$. However, the captured stars would have very high eccentricities, typically about $0.93 - 0.99$ (see the original work of Hills 1991 and Amaro-Seoane 2012 for a review). It would require some $20 - 50$ Myr for them to achieve the observed near-thermal distribution (e.g. Antonini & Merritt 2013; Perets et al. 2009; Zhang et al. 2013), with the aid of a very dense cusp of segregated old stars which is in contradiction with current observations (Buchholz et al. 2009; Do et al. 2009). Even in the presence of a dense cusp, there are two additional issues: (1) the same process would work for WR/O stars, and we do *not* see them within $\lesssim 1''$ (Alexander 2011) and (2) the oldest O/WR stars are $\lesssim 10$ Myr, so there has to be at least two SF episodes, since S-stars inside $1''$ need ≥ 20 Myr to thermalize.

Since the stellar disk initially must be gaseous, it has been proposed as another possibility that B stars migrated in it towards the center (Griv 2010; Levin 2007). However, (1) this cannot explain the eccentricities of the S-stars because the migrating stars will remain on near-circular orbits (Antonini & Merritt 2013; Madigan et al. 2011; Perets et al. 2009), and (2) WR/O stars would have migrated towards the center due to the same mecahnism, but we do not observe them there. Once SF is over (no more gas), the stars in the disk, including the WR/O stars, would secularly torque each other and drift away from nearly-circular orbits to rather eccentric ones (Madigan et al. 2009), and hence at periapsis they would populate the central $1''$, but, still, we do not see WR/O-stars there either.

In this Letter we show that, provided the disk was heavier and more extended in the past (Alig et al. 2011; Bonnell & Rice 2008; Hobbs & Nayakshin 2009; Mapelli et al. 2012; Nayakshin et al. 2007; Wardle & Yusef-Zadeh 2008), it created a rapid evolving region (RER) inside $1''$, where the angular momenta of stars rapidly redistribute because of a Kozai-Lidov-like resonance. This RER can explain both the eccentricities of S-stars and the absence of WR/O-stars because the latter are tidally disrupted.

7.2 DISK-DRIVEN EVOLUTION

7.2.1 *Timescales*

To understand the effect of the disk, we first analyze the torque exerted by a wire of mass δm and radius R on a background star of semi-major axis a (Ivanov et al. 2005;

Löckmann et al. 2008; Šubr & Karas 2005). Chen et al. (2011) showed that the timescale for the wire to change the angular momentum of the star by a full cycle, i.e. to vary the eccentricity e of the star from its minimum value to the maximum and back, is

$$T_K = \begin{cases} \frac{2}{3\pi}\frac{M_\bullet}{\delta m}\left(\frac{a}{R}\right)^{-3} P(a), & \mathrm{Kozai-Lidov},\ a \leq R/2, \\ \frac{16\sqrt{2}}{3\pi}\frac{M_\bullet}{\delta m}\left(\frac{a}{R}\right)^{1/2} P(a), & \mathrm{Non-determ.},\ a > R/2, \end{cases} \tag{60}$$

where $M_\bullet = 4 \times 10^6\ M_\odot$ is the mass of the MBH, and $P(a) = 2\pi\left(a^3/GM_\bullet\right)^{3/2} \simeq 1.4 \times 10^3\ \ (a/[0.1\ \mathrm{pc}])^{3/2}$ yr is the orbital period of the star. The reason for $R/2$ is a requirement for having all orbits within the radius of the wire, including the most eccentric ones, $R_{\rm apo} = a\,(1+e) \sim 2\,a$, with $R_{\rm apo}$ the apocenter distance. Equation (60) is a generalization of the secular Kozai-Lidov (KL) timescale (see Naoz et al. 2013, and references therehin): (1) In the regime $a \leq R/2$ we recover this well-known secular phenomenon but (2) when $a \gtrsim R/2$, i.e. when stellar orbits *cross* a sphere with a radius of the wire, it provides good approximation to the non-deterministic (ND), but not necessarily chaotic, evolution of the stellar orbit.

Admitting that an extended disk is a superposition of wires, one can derive the corresponding timescale T'_K for the sum of torques to change the orbital elements of a star in a full cycle (Chang 2009):

$$1/T'_K = \int_{R_{\rm in}}^{R_{\rm out}} d(1/T_K), \tag{61}$$

where $R_{\rm in}$ and $R_{\rm out}$ denote the inner and outer radii of the disk, $d(1/T_K) \propto \delta m = 2\pi\Sigma_d(R)RdR$, and $\Sigma_d(R)$ is the surface density of the disk. During T'_K, when secular evolution predominates, a star typically oscillates a full cycle between the maximum and minimum eccentricities, which are predetermined by three orbital parameters, namely eccentricity, position angle of periapsis (ω), and inclination angle relative to the disk (θ). At any intermediate stage of that cycle, the "instantaneous" evolution timescale, defined as $t_K(l) \equiv l/|\dot{l}|$, can be derived from

$$t_K(l) \simeq l T'_K(a) \tag{62}$$

(e.g. Chang 2009; Chen et al. 2011), where $l \equiv \sqrt{1-e^2}$ is the dimensionless angular momentum and the dot denotes the time derivative. The linear dependence on l reflects the coherence of the disk torque during $t_K(l)$.

The MBH and cusp stars affect the KL-like evolution by perturbing the orbital parameters $(e,\ \omega,\ \theta)$. We must distinguish two regimes: (1) At *high* e, ω is significantly perturbed, because of the induced relativistic (GR) precession rate,

$$\dot{\omega}_{\rm GR} = 3(GM_\bullet)^{3/2}/\left(l^2 c^2 a^{5/2}\right), \tag{63}$$

with c the speed of light. It may even exceed the KL precession rate,

$$\dot{\omega}_K \simeq 2\pi / \left(T'_K\, l\right) \tag{64}$$

(e.g. Chang 2009). When this happens, the disk coherence is broken and the KL cycle quenched, hence it defines a boundary to the region in phase space where the evolution is driven by the disk. In some loose sense, this boundary is analogous to the Schwarzschild barrier in galactic nuclei (Brem et al. 2014; Merritt et al. 2011). (2) At *low e*, the perturbation on ω originates from the total stellar mass $M_*(a)$ enclosed by the orbit. The Newtonian precession rate

$$\dot{\omega}_M \simeq 2\pi l M_*(a)/[M_\bullet P(a)] \tag{65}$$

may exceed $\dot{\omega}_K$ in this regime, which imposes a second boundary (Chen et al. 2011).

Outside these boundaries, evolution of angular-momentum will be determined by either two-body relaxation, with a characteristic timescale of

$$t_{\rm 2b}(l) \equiv |l/\dot{l}| \simeq l^2 \left(M_\bullet/m_*\right)^2 P(a)/\left(N \ln\Lambda\right) \tag{66}$$

(e.g. Kocsis & Tremaine 2011), or (scalar) resonant relaxation (RR, Rauch & Tremaine 1996), on a timescale of

$$t_{\rm RR,s}(l) \equiv \left|\frac{l}{\dot{l}}\right| \simeq \frac{l^2}{1-l^2}\left(\frac{M_\bullet}{m_*}\right)^2 \frac{P^2(a)}{N t_\omega} \tag{67}$$

(Gürkan & Hopman 2007,who studied the dependence on e). In Equations (66) and (67), m_* denotes the average mass of one star, $N = M_*(a)/m_*$ is the number of stars enclosed by the stellar orbit, $\ln\Lambda = \ln(M_\bullet/m_*)$ is the Coulomb logarithm, and $t_\omega = 2\pi/|\dot{\omega}_M - \dot{\omega}_{\rm GR} - \dot{\omega}_K|$ is the joint precession timescale combining Newtonian, GR, and KL precessions (Chen & Liu 2013).

Between the two boundaries is the RER: Any star in it cycles between the maximum and minimum eccentricities predetermined by (e, ω, θ). Moreover, the two extrema are evolving. The corresponding timescale is given by vectorial RR (Rauch & Tremaine 1996), which changes θ on a timescale of

$$t_{\rm RR,v} \equiv \left|\frac{1}{\dot{\theta}}\right| \simeq \frac{0.3}{(0.5+e^2)^2}\frac{M_\bullet}{m_*}\frac{P(a)}{\sqrt{N}} \tag{68}$$

(Eilon et al. 2009; Gürkan & Hopman 2007). Inside RER, $t_{\rm RR,v}$ is longer than the Newtonian and GR precession timescales, so vectorial RR does not impact the boundaries. Its role is to characterize the required time for a star to explore in a random-walk-fashion the range of maxima and minima in eccentricities fenced in by the boundaries of the RER.

7.2.2 *A receding disk*

The boundaries of the RER are changing because the properties of the disk have changed during the past $(1-10)$ Myr. We can distinguish two stages in the evolution of the disk.

(1) An early phase in which the disk was mostly gaseous and its inner edge reached the innermost stable circular orbit (ISCO) at about $6GM_\bullet/c^2 \simeq 10^{-6}$ pc (Levin 2007; Nayakshin & Cuadra 2005). This disk contained at least $10^4\ M_\odot$ of gas, to trigger fragmentation and star formation (Nayakshin & Cuadra 2005), and it could have been as massive as $(3-10)\times 10^4\ M_\odot$ according to recent simulations (Bonnell & Rice 2008; Hobbs & Nayakshin 2009; Mapelli et al. 2012; Nayakshin et al. 2007). We will adopt a disk mass of $M_d = 3\times 10^4\ M_\odot$ for this phase. It is worth noting that stars formed in the outer disk may migrate inward (Griv 2010; Levin 2007), so the disk inside $R = 0.04$ pc could contain both gas and stars.

(2) Today, after some $(1-10)$ Myr, the central 0.04 pc of the disk is no longer present, because the gas is consumed by either star formation (Nayakshin & Cuadra 2005) or black-hole accretion (Alexander et al. 2012), and the stars have had time to be scattered out of the disk plane due to vectorial RR (Hopman & Alexander 2006; Kocsis & Tremaine 2011). For this reason, we say the inner edge of the disk has *receded* from the ISCO to the current location of $R_{\rm in} \simeq 1'' \simeq 0.04$ pc (e.g. Paumard et al. 2006), while the outer edge is still the same, at $R_{\rm out} \simeq 12'' \simeq 0.5$ pc. The present mass of the disk is $M_d = 10^4\ M_\odot$ (Bartko et al. 2010; Paumard et al. 2006).

In both situations, we modeled the disk surface density as a power-law of $\Sigma_d(R) \propto R^{-1.4}$ (Bartko et al. 2010), which leads to a mass of $6\times 10^3\ M_\odot$ at 10^{-6} pc $< R <$ 0.04 pc in the early phase. To derive $M_*(a)$ and N in Equations (65)-(68), we adopted the broken-power-law model from observations (Genzel et al. 2010), whose density slop is $\gamma = 1.3$ for the inner 0.25 pc. We assumed an average stellar mass of $m_* \simeq 10\ M_\odot$ (also see Kocsis & Tremaine 2011, for discussions). In this model, we have $t_{\rm RR,v} \simeq 1.5\times 10^6\ (0.5+e^2)^{-2}(a/1'')^{0.65}$ yr for stars in the central arcsec of the Galaxy.

7.3 SCULPTING THE GALACTIC CENTER

7.3.1 *Rapid Evolving Region*

In Figure 21 we display the boundaries of the RER. The left panel corresponds to $R_{\rm in} = 10^{-6}$ pc and the right one to $R_{\rm in} = 0.04$ pc. In this $(1-e)$ – a plane, at any location, we can estimate the instantaneous evolution timescale as:

$$\left|\frac{1-e}{\dot{e}}\right| = \frac{e(1-e)}{l^2}t_K(l) \simeq \frac{e(1-e)}{l}T'_K(a). \tag{69}$$

We can then identify the lines with constant evolution timescales, i.e. the contours. We call them "isochrones", and depict them as blue dotted curves. Outside the RER the isochrones are shown in grey and determined by either two-body scattering, $e\ (1-e)\ t_{\rm 2b}\ (l)/l^2$, or RR process, $e\ (1-e)\ t_{\rm RR,s}(l)/l^2$, whichever timescale is shorter.

Two striking conclusions from a first look at this figure are (1) stars in the RER evolve on very short timescales, of the order of $10^{3-5.5}$ yrs, to complete a full KL cycle. As discussed previously, after a time of $t_{\rm RR,v}$, any star at $a < 1''$ would have *fully* explored the angular-momentum range within the RER. (2) As the disk recedes, the boundaries come closer and the RER shrinks. Any star that finds itself out of the RER will be "frozen" from the point of view of another star which still is in it: The timescales outside RER are long.

Since short evolution timescale leads to low probability of stellar distribution, today (right panel of Figure 21), the absence of S-stars within the RER boundaries may be a plausible observational corroboration that the RER does exit at the GC. At present, the only measured object within the RER boundaries is G2 (red dots, Gillessen et al. 2013). From its nearby isochrones, we see that G2 must have been formed less than $10^{5.5}$ years ago.

7.3.2 *A close thermalization of the S-stars*

The two more successful scenarios of depositing B stars close to the GC, i.e. binary separation and disk migration, place these stars well within the RER (left panel of Figure 21). These stars are able to sufficiently mix in angular-momentum space, on a timescale of $t_{\rm RR,v} \simeq 0.7$ Myr in the binary-separation scenario and of $t_{\rm RR,v} \simeq 6$ Myr in the disk-migration one. The latter mechanism (disk migration) requires much longer time to reach the superthermal distribution in eccentricities becasue of the e dependence of Equation (68). We note that these timescales are at least 10 times shorter than those from the earlier models, which neglected the RER.

The fully-mixed eccentricities do not necessarily have a thermal distribution (Brem et al., in preparation). Following the argument that longer evolution timescale correlates with higher probability distribution, we will have $dN/de \propto dt/de$, and substituting Equation (69) for dt/de, we can derive $dN/de \propto dt/de \propto e/l$. This distribution function is steeper than a thermal one, $dN/de \propto e$. The steepness stems from the linear dependence of the evolution timescale ($l/\dot{l}$) on the orbital angular momentum l, whereas in the case of two-body relaxation and RR, the evolution time scales with $1-e^2$.

Figure 22 compares various cumulative probability distribution functions (CPDFs) for e, derived from two theoretical models –a thermal one and our RER model– as well as from observations. It is clear that compared to the thermal distribution, the RER one is in better agreement with the observations.

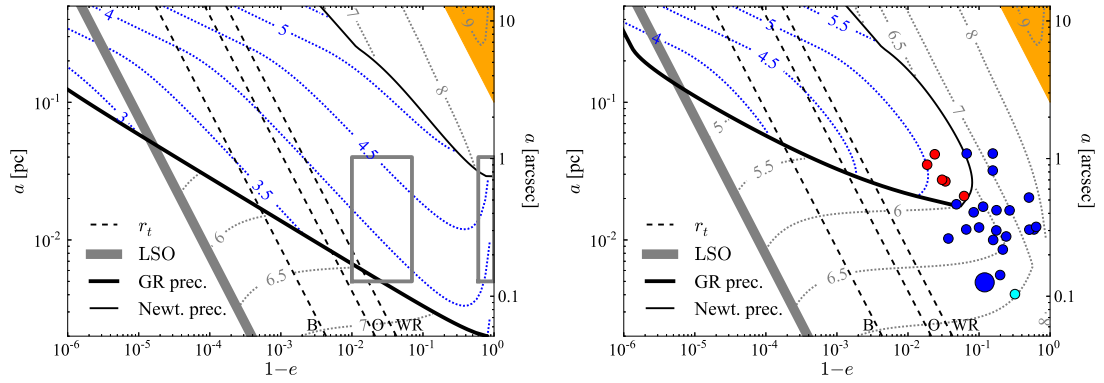

Figure 21: Mapping evolution timescales in the a – $(1-e)$ plane. The thick grey line on the left-hand-side corresponds to the last stable orbit (LSO) around SgrA*. The thick solid black curve is the result of equating the KL precession rate, $\dot{\omega}_K$, to its relativistic equivalent, $\dot{\omega}_{\rm GR}$. Above that curve, dynamical evolution is determined by KL effect up to the next solid black curve, which comes from equating $\dot{\omega}_K$ to $\dot{\omega}_M$, the precession rate induced by the enclosed stellar mass. The dashed black parallel lines crossing the figures from the top to the bottom indicate the typical tidal-disruption radii for B, O, and WR stars. The blue dotted isochrones, fenced in the region where the evolution is governed by the KL mechanism, are associated with the logarithms of the KL timescales given by Equation (69). The grey dotted isochrones are associated with the logarithms of the two-body-relaxation or RR timescales, whichever is shorter. The small orange triangles at the top-right corners depict the loci of the red giants in the GC. In the left panel, the two grey boxes depict the expected birth places of S-stars in the binary-separation and migration-in-disk models (also see Antonini & Merritt 2013). In the right panel, the dots correspond to: S-stars not associated with the young stellar disk (small-blue Gillessen et al. 2009), the infalling G2 object (also called DSO, see Eckart et al. 2013, for a different interpretation of its nature) measured at different times or different wavelengths (small-red Gillessen et al. 2013), S2/S0-2 (big-blue, the brightest S-star, Eisenhauer et al. 2003; Ghez et al. 2003), and S102/S0-102 (small-cyan, Meyer et al. 2012), the S-star with the shortest period known.

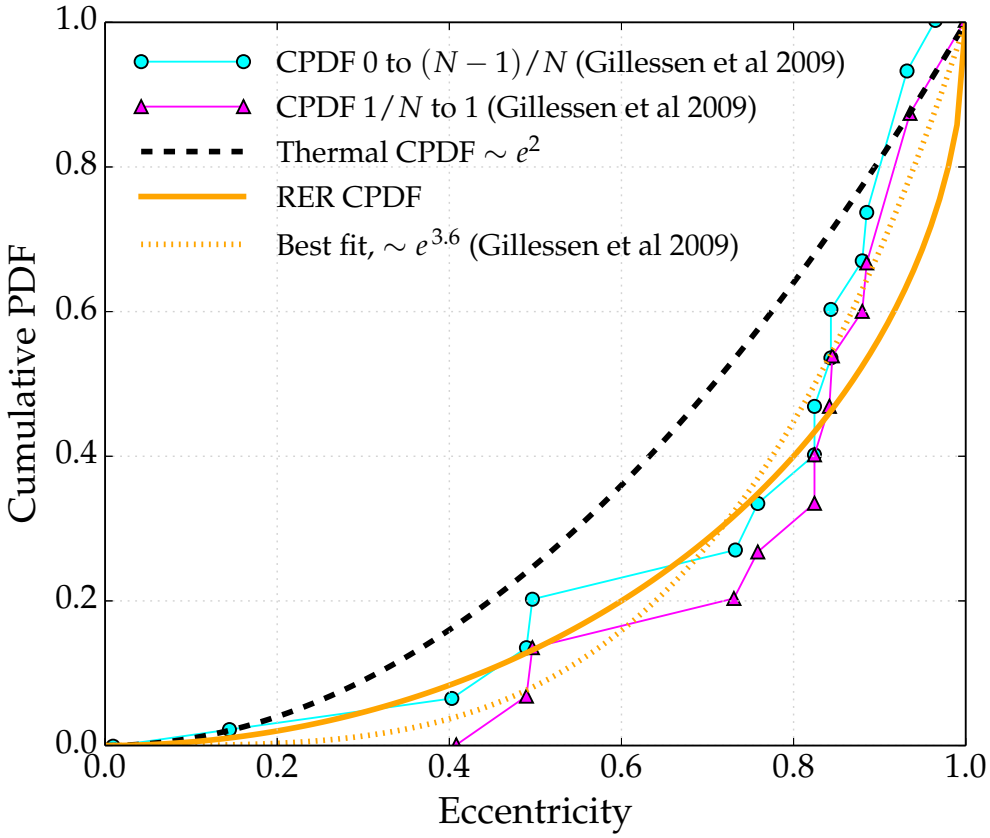

Figure 22: Cumulative probability distribution functions of the eccentricities of S-stars, derived from observations (cyan and purple), thermal distribution (e^2, black-dashed), our RER model ($1-\sqrt{1-e^2}$, orange-solid), and best fit to observational data (orange-dotted).

7.3.3 *Depleting WR/O stars*

For a star of mass m_* and radius r_*, if its eccentricity becomes so high that the orbital pericenter distance from SgrA* becomes smaller than the tidal radius

$$r_t \simeq r_* \left(\frac{M_\bullet}{m_*}\right)^{1/3} \simeq 4 \times 10^{-6}\ \mathrm{pc} \left(\frac{r_*}{R_\odot}\right) \left(\frac{m_*}{M_\odot}\right)^{-1/3}, \tag{70}$$

it will be tidally disrupted (Rees 1988). In Figure 21 we show typical r_t associated with B, O, and WR stars. Once stars cross it from the right to the left, they are lost. This drain is enhanced in the RER by the shorter and shorter timescales, as the stars progressively move to the left.

To calculate r_t, we assume $m_* = (7, 25, 60)\ M_\odot$ respectively for the three types of stars (Zinnecker & Yorke 2007). Main-sequence stars less massive than $7M_\odot$ are below the current detection limit of observations. Correspondingly, we have adopted $r_* = 4\ R_\odot$ for main-sequence B stars, and $r_* = 40\ R_\odot$ and $80\ R_\odot$ respectively for O- and WR stars. B stars can be envisaged as main-sequence stars, but O- and WR stars are more massive, and shorter-lived. We hence adopt larger radii for them, 3–4 times larger than typical radii on the main-sequence, since they have evolved off the main sequence (Bartko et al. 2010; Paumard et al. 2006).

We can see in the left panel of Figure 21 that any WR star in a stripe defined between $0.15'' \lesssim a \lesssim 0.8''$ and any O star in $0.2'' \lesssim a \lesssim 0.8''$ will be tidally disrupted, because it will have explored all the $(1-e)$ space in $\sim 10^6$ yrs. Similarly, for B stars, the corresponding stripe is delimited by the narrower zone $0.5'' \lesssim a \lesssim 0.8''$. In fact, this predicted gap (for B stars) does occur in the current distribution of S-stars (right panel of Figure 21). If we had assumed a disk mass of $M_d > 3 \times 10^4\ M_\odot$, this gap would have broadened to incorporat the region where $a < 0.5''$, and it would contradict current observations. Therefore, an upper limit to the disk mass can be derived, approximately $3 \times 10^4\ M_\odot$.

By looking at the left panel again, we realize that only WR/O stars with $a > 0.8''$ and low e can survive, because they are always outside of the RER and cannot drift quickly enough to higher e. Indeed, WR/O stars have been discovered only at $a \gtrsim 1''$ but not inside. In principle, our model cannot deplete WR/O stars at $a < 0.1''$, because at such small a the RER does not reach the tidal radii. Observations did not find any WR/O star there, maybe because the extrapolation of the disk density profile $\Sigma(R) \propto R^{-1.4}$ results in < 1 WR/O star at $R < 0.1''$.

7.4 DISCUSSIONS

In this Letter we have presented a picture that explains the distribution of the eccentricities of S-stars and the absence of more massive stars within $1''$ of SgrA*. Our *sole* hypothesis is that around $(1-10)$ Myr ago, the disk had extended down to $R \ll 0.04$ pc. We find that the torque exerted by the disk creates a region at the GC in which

the dynamical evolution is significantly accelerated as compared to other regions, by a factor ranging from 10 to 100 times, and we call it the "rapid evolving region".

Our scenario agrees with current observations about the nonexistence of an old segregated cusp in the GC (Buchholz et al. 2009; Do et al. 2009), contrary to other works, which crucially rely on the cusp to thermalize the S-stars (Antonini & Merritt 2013; Madigan et al. 2011; Perets et al. 2009; Zhang et al. 2013). Because the time that is needed to randomize angular momentum is now shortened to $(0.7-6)$ Myr, our model is able to accommodate various possibilities for the formation of S-stars, while other models rely heavily on when S-stars were brought to the GC (Antonini & Merritt 2013; Perets et al. 2009).

Moreover, our RER scenario unifies two observational facts that have been thought until now to be disconnected: We successfully populate the observed range of e for B stars and we can duplicate the observed discontinuity of WR/O stars above and below $1''$. Both of them will be established in as short as $(0.7-6)$ Myr, so we can even unify the origin of all the young stellar populations in the GC to *only one single SF episode*. This unification does pose a problem for earlier models: If all B stars formed simultaneously with WR/O stars, since this must be less than 6 Myr ago (because WR/O stars cannot be older), two-body relaxation and RR will fail to explain the distribution of e.

At this stage, it is crucial to theoretically understand the dynamical response of the old stellar population to the RER, and test it against the observations of dimmer (than B-type), older stars. If they match, it would be a robust evidence that the RER has indeed played a role in sculpting the GC.

BIBLIOGRAPHY

Alexander, T. 2011, The Galactic Center: a Window to the Nuclear Environment of Disk Galaxies, 439, 129

Alexander, R. D., Smedley, S. L., Nayakshin, S., & King, A. R. 2012, MNRAS, 419, 1970

Alig, C., Burkert, A., Johansson, P. H., & Schartmann, M. 2011, MNRAS, 412, 469

Amaro-Seoane, P. 2012, Submitted to Living Reviews in Relativity

Antonini, F., & Merritt, D. 2013, ApJ Letts., 763, L10

Bartko, H. 2010, ApJ, 708, 834

Bonnell, I. A., & Rice, W. K. M. 2008, Science, 321, 1060

Brem, P., Amaro-Seoane, P., & Sopuerta, C. F. 2014, MNRAS, 437, 1259

Buchholz, R. M., Schödel, R., & Eckart, A. 2009, A&A, 499, 483

Chang, P. 2009, MNRAS, 393, 224

Chen, X., & Liu, F. K. 2013, ApJ, 762, 95

Chen, X., Sesana, A., Madau, P., & Liu, F. K. 2011, ApJ, 729, 13

Do, T., Ghez, A. M., Morris, M. R., et al. 2009, ApJ, 703, 1323

Eilon, E., Kupi, G., & Alexander, T. 2009, ApJ, 698, 641

Eisenhauer, F., Schödel, R., Genzel, R., et al. 2003, ApJ Letts., 597, L121

Eckart, A., Mužić, K., Yazici, S., et al. 2013, A&A, 551, A18

Genzel, R., Eisenhauer, F., & Gillessen, S. 2010, RvMP, 82, 3121

Ghez, A. M., Duchêne, G., Matthews, K., et al. 2003, ApJ Letts., 586, L127

Gillessen, S., Eisenhauer, F., Trippe, S., et al. 2009, ApJ, 692, 1075

Gillessen, S. 2014, 40th COSPAR Scientific Assembly, 40, 992

Ginsburg, I., & Loeb, A. 2006, MNRAS, 368, 221

Gould, A., & Quillen, A. C. 2003, ApJ, 592, 935

Griv, E. 2010, ApJ, 709, 597

Gürkan, M. A., & Hopman, C. 2007, MNRAS, 379, 1083

Hills, J. G. 1991, AJ, 102,704

Hobbs, A., & Nayakshin, S. 2009, MNRAS, 394, 191

Hopman, C., & Alexander, T. 2006, ApJ Letts., 645, 1152

Ivanov, P. B., Polnarev, A. G., & Saha, P., 2005, MNRAS, 358, 1361

Kocsis, B., & Tremaine, S. 2011, MNRAS, 412, 187

Levin, Y. 2007, MNRAS, 374, 515

Levin, Y., & Beloborodov, A. M. 2003, ApJ Letts., 590, L33

Löckmann, U., Baumgardt, H., & Kroupa, P. 2008, ApJ Letts., 683, L151

Lu, J. R., Do, T., Ghez, A. M., et al. 2013, ApJ, 764, 155

Madigan, A.-M., Hopman, C., & Levin, Y. 2011, ApJ, 738, 99

Madigan, A.-M., Levin, Y., & Hopman, C. 2009, ApJ Letts., 697, L44

Mapelli, M., Hayfield, T., Mayer, L., & Wadsley, J. 2012, ApJ, 749, 168

Merritt, D., Alexander, T., Mikkola, S., & Will, C. M. 2011, Phys.Rev.D, 84, 044024

Meyer, L., Ghez, A. M., Schödel, R., et al. 2012, Science, 338, 84

Morris, M. 1993, ApJ, 408, 496

Naoz, S., Farr, W. M., Lithwick, Y., Rasio, F. A., & Teyssandier, J. 2013, MNRAS, 431, 2155

Nayakshin, S., & Cuadra, J. 2005, A&A, 437, 437

Nayakshin, S., Cuadra, J., & Springel, V. 2007, MNRAS, 379, 21

Paumard, T., et al. 2006, ApJ, 643, 1011

Perets, H. B., Gualandris, A., Kupi, G., Merritt, D., & Alexander, T. 2009, ApJ, 702, 884

Rauch, K. P., & Tremaine, S. 1996, NewA, 1, 149

Rees, M. J. 1988, Nature, 333, 523

Šubr, L., & Karas, V. 2005, A&A, 433, 405

Wardle, M., & Yusef-Zadeh, F. 2008, ApJ Letts., 683, L37

Zinnecker, H., & Yorke, H. W. 2007, Annual Review of Astronomy & Astrophysics, 45, 481

Zhang, F., Lu, Y., & Yu, Q. 2013, ApJ, 768, 153

8

TIDAL DISRUPTIONS OF SEPARATED BINARIES IN GALACTIC NUCLEI

Pau Amaro-Seoane[1], *M. Coleman Miller*[2], *& Gareth F. Kennedy*[3]

Published in *Monthly Notices of the Royal Astronomical Society*, Volume 425, Issue 4, pp. 2401-2406 (2012).

Abstract: Several galaxies have exhibited X-ray flares that are consistent with the tidal disruption of a star by a central supermassive black hole. In theoretical treatments of this process it is usually assumed that the star was initially on a nearly parabolic orbit relative to the black hole. Such an assumption leads in the simplest approximation to a $t^{-5/3}$ decay of the bolometric luminosity and this is indeed consistent with the relatively poorly sampled light curves of such flares. We point out that there is another regime in which the decay would be different: if a binary is tidally separated and the star that remains close to the hole is eventually tidally disrupted from a moderate eccentricity orbit, the decay is slower, typically $\sim t^{-1.2}$. As a result, careful sampling of the light curves of such flares could distinguish between these processes and yield insight into the dynamics of binaries as well as single stars in galactic centres. We explore this process using three-body simulations and analytic treatments and discuss the consequences for present-day X-ray detections and future gravitational wave observations.

8.1 INTRODUCTION

In the past few years, several galaxies have exhibited X-ray/UV flares consistent with the tidal disruption of a star by a supermassive black hole (SMBH; for flare observations see Dogiel et al. 2009; Donley et al. 2002; Gezari et al. 2009). These candidate disruptions are relevant to the fueling of some active galactic nuclei (particularly low-mass ones; see Wang & Merritt 2004) and contain important information about stellar dynamics in the centers of galaxies. In addition, they are related to one of the processes believed to lead to extreme mass ratio inspirals (EMRIs), in which a stellar-mass object spirals into a supermassive black hole; EMRIs are thought to be among the most

1 Max Planck Institut für Gravitationsphysik (Albert-Einstein-Institut), D-14476 Potsdam, Germany
2 University of Maryland Department of Astronomy and Joint Space-Science Institute, College Park, MD, 20742-2421, USA
3 Institut de Ciències del Cosmos, Facultat de Física Marti i Franquès, 1 E-08028 Barcelona, Spain

promising sources for milliHertz gravitational wave detectors such as the *Evolved Laser Interferometer Space Antenna* (LISA, see Amaro-Seoane et al. 2012, 2007).

Analyses of stellar tidal disruptions have focused on stars whose orbits are nearly parabolic relative to the SMBH (Rees 1988). In this case, roughly half the stellar material becomes unbound and the rest rains down on the SMBH with a rate that, for simplified stellar structure, scales with the time t since disruption as $\dot{M} \sim t^{-5/3}$ (this is expected at late times even for more realistic structure; see Lodato et al. 2009).

There is, however, another possible path to disruptions. Binaries that get close enough to a SMBH can be tidally separated without destroying either star. The result is that one star becomes relatively tightly bound to the SMBH whereas the other is flung out at high speed. The bound star will undergo dynamical interactions and its orbit will also shrink and circularise due to gravitational radiation. The star may eventually be tidally disrupted, but on an orbit that is much more bound than in the standard scenario. This will lead to a remnant disc of the type analyzed by Cannizzo et al. (1990), for which the accretion rate decreases more slowly than in the parabolic scenario: $\dot{M} \sim t^{-1.2}$ for reasonable opacities. If flare light curves are sampled sufficiently these decays could in principle be distinguished from each other, which would give us new insight into stellar dynamics and the prospects for EMRIs.

Here we present numerical and analytical analyses of binary tidal separation and subsequent tidal disruption of the remaining star. We note that there exist similar but not identical numerical studies. In particular Gould & Quillen (2003) use a mass for the black hole of $3.6 \times 10^6\,M_\odot$ but show results only for the subset that give captured stars with similar parameters to the observed stars S2-0. Their initial binary distributions are similar to ours, although they do not examine binaries with initial semi-major axis < 1 AU and focus on higher masses. Ginsburg & Loeb (2006) address a black hole mass of $4 \times 10^6\,M_\odot$ and their binaries are formed of two stars of masses $3\,M_\odot$. They present a few sample orbits of captured stars similar to the S-stars, but do not give a detailed distribution. Perets & Gualandris (2010) also focus on $4 \times 10^6\,M_\odot$ MBHs, and find as expected that the captured stars tend to have high eccentricities $e > 0.97$, but do not give a periapsis distribution for the stars. Madigan et al. (2009) present in their notable work direct-summation $N-$body simulations of small discs of stars with semi-major axes of 0.026 and 0.26 pc with $4\,10^6\,M_\odot$ MBHs, which produced stars with high eccentricities that did not, however, enter the region of greatest interest to us. Hence we have performed new numerical simulations to explore our scenario.

In § 2 we discuss tidal separations and present our three-body simulations of the process. In § 3 we use these results as initial conditions and analyze the competition between stellar dynamical processes (which can raise or lower the eccentricity) and gravitational radiation (which shrinks and circularises the orbit) to determine the mass ranges most likely to lead to moderate eccentricities at the point of disruption. In § 4 we discuss the tidal process itself, and argue that the small but nonzero residual eccentricities mean that for sufficiently low-mass SMBHs the star will typically be disrupted rather than settling into a phase of steady mass accretion onto the SMBH. We present our conclusions in § 5.

8.2 BINARY TIDAL SEPARATION

Tidal separation of binaries by SMBHs was first discussed by Hills (1988). He suggested that one member of the binary would be ejected with a velocity of $> 10^3\,\mathrm{km\,s^{-1}}$, a "hypervelocity star" (HVS); several such objects have now been observed (see Brown et al. 2009 for a discussion of their observed properties). The other member would settle into a fairly tightly bound orbit around the SMBH; see Miller et al. (2005) for a discussion in the context of extreme mass ratio inspirals into an SMBH.

To simulate this process we assume a uniform distribution of pericentre distances between 1 and 700 AU for the orbit of the binary around a $10^7\ M_\odot$ MBH. The initial orbit is also assumed to be parabolic and to have its relative inclination uniformly distributed over a sphere. In total 228,000 numerical simulations were conducted using a generalized three-body code described by Zare (1974) and Aarseth & Zare (1974). This numerical integrator is based on Kustaanheimo-Stiefel regularisation of a two-body system, which is described in Aarseth (2003); Kustaanheimo & Stiefel (1965). The total energy and angular momentum of the system are conserved to a high degree of accuracy and close encounters between bodies do not induce unphysical velocities.

The resulting distribution for the pericentre distance and eccentricity of the captured population, as well as the velocity distribution for the star re-ejected into the stellar system, are shown in Fig.(23) for an initial internal binary eccentricity of $e_i = 0.4$ and stellar mass of $1M_\odot$. To produce this figure we chose 10^7 sets of parameters for fixed eccentricities and drew the semimajor axis of the initial stellar binary from a log normal distribution between 0.05 and 10 AU. This is taken from observations of period distribution of binaries in local field stars (Duquennoy & Mayor 1991). The mean would be about 0.37 AU.

In the figure we show the resulting probabilities, where we plot the probability of finding a captured star with a particular pericentre and eccentricity bin given that a binary is scattered to within 700 AU of the MBH. The distribution of semimajor axes for captured stars is shown in Fig.(24) for a $1M_\odot$ star that was taken from an initial stellar binary with eccentricity $e_i = 0.0$, 0.4, 0.7 or 0.9.

We now discuss the evolution of the orbits of the stars after capture, under the combined influence of two-body relaxation and gravitational radiation.

8.3 COMPETITION BETWEEN STELLAR DYNAMICS AND GRAVITATIONAL RADIATION

Suppose that a binary has been tidally separated by a close passage to a supermassive black hole, but that the remaining object is outside the tidal radius (i.e., it is not torn apart yet). Gravitational radiation will circularise the orbit as it shrinks, but dynamical processes can increase the eccentricity. Eventually, the star will move inside the tidal radius and (as we argue in § 4) will probably be tidally disrupted if the SMBH is sufficiently low-mass.

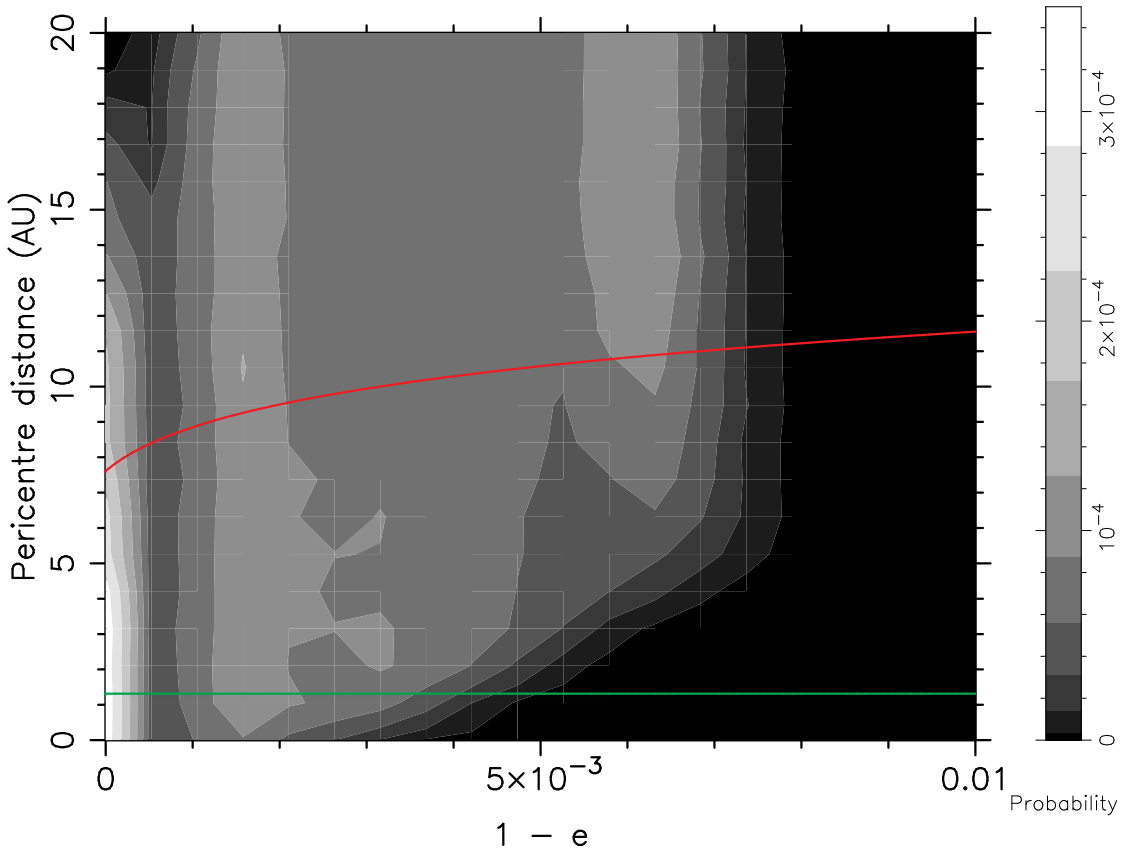

Figure 23: Distribution of the pericentre distance and eccentricity of the captured companion at the tidal separation radius for an initial eccentricity of $e_i = 0.4$ and stellar mass of $1M_\odot$. Other eccentricities do not change significantly the shape of the distribution. The red line indicates the maximum pericentre distance for which the tidal disruption happens within a Hubble time under the influence of gravitational radiation alone. In the limit $e \to 1$, r_p approaches the tidal disruption radius, which we display as a green line, at at 1.3 AU, although this cannot be seen directly in the figure because we are using a resolution of $\delta e = 10^{-4}$.

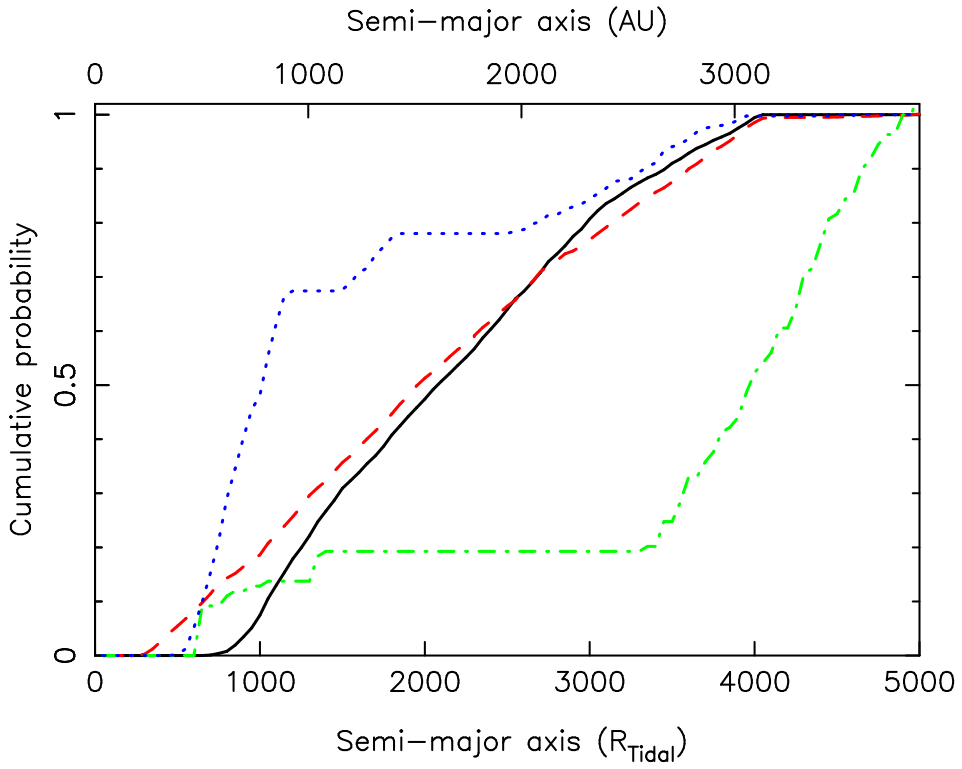

Figure 24: Cumulative probability distribution of the semimajor axis of the captured star after the tidal separation of the binary for a $1M_{\odot}$ star. The colours denote the initial eccentricity of the binary before being disrupted by the MBH, where black (solid line) is $e_i = 0.0$, red (dashed line) is $e_i = 0.4$, green (dot-dashed line) is $e_i = 0.7$ and blue (dotted line) is $e_i = 0.9$. The probabilities of captures are different in the different eccentricity cases, in particular the case $e_i = 0.9$ is easier to capture than the others.

In this section we discuss the dynamics subsequent to a tidal separation. We presume that the pericentre of the orbit of the remaining star is outside the tidal radius, so that there is no immediate tidal disruption. The star will then be subjected to two-body interactions that can change the semimajor axis and eccentricity of its orbit. In principle resonant relaxation (Rauch & Tremaine 1996) could also play a role, in particular due to the high eccentricity the orbit has, since the component of the torque is linearly proportional to eccentricity (Gürkan & Hopman 2007), but for the relevant tight orbits general relativistic pericentre precession essentially eliminates this effect (Merritt et al. 2011). We will therefore focus exclusively on two-body interactions.

The two-body energy relaxation time (during which the semimajor axis of the orbit will be roughly doubled or halved) for a star of mass m moving against a background of density ρ and velocity dispersion σ is (Spitzer 1987)

$$t_{\rm en} \approx \frac{0.3}{\ln\Lambda}\frac{\sigma^3}{G^2\rho m}\ . \tag{71}$$

Here $\ln\Lambda \sim 10$ is the Coulomb logarithm. For our purposes, however, it is not the semimajor axis but the pericentre distance that is important, because this is what determines whether the star enters the tidal region. It is therefore the angular momentum relaxation time that is more relevant. For a nearly circular orbit this time is comparable to the energy relaxation time, but as we saw in § 8.2 the initial eccentricity is close to unity in almost all cases. The angular momentum of an orbit scales as $\sqrt{a(1-e^2)}$, so an orbit with eccentricity e has an angular momentum a factor of $(1-e^2)^{1/2}$ less than a circular orbit with the same semimajor axis. Two-body relaxation is a diffusive process, hence the expected change in energy or angular momentum after time t scales as $t^{1/2}$. As a result, the angular momentum relaxation time is a factor of $[(1-e^2)^{1/2}]^2 = 1-e^2$ less than the energy relaxation time:

$$t_{\rm am} = \frac{0.3}{\ln\Lambda}\frac{\sigma^3}{G^2\rho m}(1-e^2)\ . \tag{72}$$

For $e \sim 1$ this is much shorter than the energy relaxation time, hence we will assume that a is fixed throughout. We also note that because angular momentum relaxation is a random walk process the angular momentum could go up or down; if it goes up then nothing interesting happens to the star, hence we will consider only the case in which the angular momentum and hence the pericenter distance decreases.

To be more quantitative, let us suppose that we have a galactic center with a supermassive black hole of mass M with a stellar mass density profile $\rho(r) = \rho_0(r/r_{\rm infl})^{-\alpha}$ inside the radius of influence $r_{\rm infl} \equiv 2GM/\sigma_0^2$, where σ_0 is the velocity dispersion in the bulge of the galaxy. The radius of influence is by definition the radius inside of which the total stellar mass equals the black hole mass, hence the normalization is $\rho_0 = \frac{3-\alpha}{4\pi}\frac{M}{r_{\rm infl}^3}$. Suppose we make the simplifying approximation that the velocity dispersion is $\sigma(r) = \sigma_0(r/r_{\rm infl})^{-1/2}$ (this scaling is accurate for $r \ll r_{\rm infl}$ but not for $r \sim r_{\rm infl}$ because of the mass contribution from stars). Let us assume in addition an

$M - \sigma_0$ relation of the form $M = 10^8\ M_\odot (\sigma_0/200\ \mathrm{km\ s^{-1}})^4$ (Tremaine et al. 2002). Then $r_{\rm infl} \approx 3 M_7^{1/2}$ pc, where $M = 10^7 M_7\ M_\odot$, and

$$t_{\rm am} \approx 7 \times 10^{11}\ \mathrm{yr} (3-\alpha)^{-1} M_7^{5/4} m_0^{-1} (r/r_{\rm infl})^{\alpha - 3/2} (1-e^2) \tag{73}$$

with $m_0 \equiv m/M_\odot$. $t_{\rm am}$ is the timescale on which two-body processes can raise or lower the pericentre distance significantly. Competing against this is the gravitational radiation timescale

$$t_{\rm GR} \approx 3 \times 10^{15}\ \mathrm{yr}\ m_0^{-1} M_7^{-2} \left(\frac{a}{1000\mathrm{AU}}\right)^4 (1-e^2)^{7/2}\ . \tag{74}$$

Over a time $t \approx t_{\rm GR}$, the orbit shrinks and circularises significantly. Setting the two timescales equal to each other and noting that the pericentre distance is $r_p = a(1-e)$ gives a critical pericentre distance of

$$r_{\rm p,crit} \approx 16\ \mathrm{AU}\ (8 \times 10^{-4})^{(2\alpha-3)/5} (3-\alpha)^{2/5} M_7^{(8-\alpha)/5} \left(\frac{a}{1000\mathrm{AU}}\right)^{(2\alpha-6)/5}\ . \tag{75}$$

Typical values for $r_{\rm p,crit}$ can be read directly off of the simulations. For one that can decay faster than a Hubble time it is < 10 AU, and for one that can decay faster than it would be disrupted by two-body relaxation it is more like 5 AU. At a smaller pericentre distance than is given by this expression, gravitational radiation dominates the evolution; conversely, at a larger pericentre distance, two-body relaxation dominates.

At the MBH masses $\sim 10^7\ M_\odot$ that we consider, there may or may not be time for the stars to relax dynamically, hence it is not clear which value of α to take. If strong mass segregation occurs then $\alpha = 2$ is likely (Alexander & Hopman 2009; Amaro-Seoane & Preto 2011; Preto & Amaro-Seoane 2010), but flatter slopes may also be relevant, particularly if there has been scouring by a previous massive black hole merger and the system has not yet readjusted. For a selection of slopes we find

$$\begin{aligned} r_{\rm p,crit} &\approx 14\ \mathrm{AU} M_7^{13/10} (a/1000\ \mathrm{AU})^{-3/5}, & \alpha &= 3/2 \\ r_{\rm p,crit} &\approx 7\ \mathrm{AU} M_7^{5/4} (a/1000\ \mathrm{AU})^{-1/2}, & \alpha &= 7/4 \\ r_{\rm p,crit} &\approx 4\ \mathrm{AU} M_7^{6/5} (a/1000\ \mathrm{AU})^{-2/5}, & \alpha &= 2\ . \end{aligned} \tag{76}$$

We will simplify by assuming that gravitational radiation is unimportant until $r_p = r_{\rm p,crit}$, at which point it takes over completely with no further influence from two-body effects. If this is true, then the next question is whether $r_{\rm p,crit}$ is greater than the tidal radius. If we focus on main sequence stars of mass $m \lesssim M_\odot$, then over a wide

range of masses their radii are reasonably fit by $R_\star \approx 0.85 R_\odot (m/M_\odot)^{2/3}$ (Demircan & Kahraman 1991) and the tidal radius is

$$r_T \approx R_\star \left(\frac{3M}{m}\right)^{1/3} \approx 1.3 \text{ AU} M_7^{1/3} m_0^{1/3} \,. \tag{77}$$

Thus we see that stars in this mass range will typically enter the gravitational radiation regime before they are tidally disrupted. Given that the critical pericenter is just a few times the tidal radius, and that many aspects of this calculation are uncertain, it is quite possible that although tidal effects drop off very sharply with distance they could have an impact on the orbit outside r_T. An exploration of this possibility would require careful hydrodynamic simulations, but for our purposes we will assume that they are not dominant.

Assuming that this is the case, we can compute the eccentricity of the orbit at the point that the pericentre distance equals r_T, when (as we show in the next section) the star is likely to be tidally disrupted instead of settling into a phase of steady accretion. We calculate the eccentricity by noting that to lowest (quadrupolar) order, pure evolution via gravitational radiation conserves the quantity

$$C = a e^{-12/19} (1 - e^2) \left(1 + \frac{121}{304} e^2\right)^{-870/2299} \tag{78}$$

(Peters 1964). We saw in § 8.2 that the initial eccentricity after tidal separation is nearly unity, so $1 + e \approx 2$. From our assumptions we also know that $r_p = a(1-e) = r_{\rm p,crit}$. Finally, if we assume that at the tidal radius the eccentricity is $e_T \ll 1$, so that $a_T \approx r_T$, we get

$$\begin{aligned} a_T e_T^{-12/19} &\approx 1.8 r_{\rm p,crit} \\ e_T &\approx 0.4 \left(\frac{r_{\rm p,crit}}{r_T}\right)^{-19/12} \,. \end{aligned} \tag{79}$$

For our three slopes the eccentricity at the tidal radius is thus

$$\begin{aligned} e_T &\approx 0.01 \; M_7^{-551/360} m_0^{19/36} (a/1000 \text{ AU})^{19/20}, && \alpha = 3/2 \\ e_T &\approx 0.03 \; M_7^{-209/144} m_0^{19/36} (a/1000 \text{ AU})^{19/24}, && \alpha = 7/4 \\ e_T &\approx 0.07 \; M_7^{-247/180} m_0^{19/36} (a/1000 \text{ AU})^{19/30}, && \alpha = 2 \end{aligned} \tag{80}$$

We now explore the consequences of the star sinking inside the tidal radius with this eccentricity, and argue that tidal disruption is the most likely outcome if the SMBH has sufficiently low mass. We then demonstrate that tidal disruption with a small eccentricity leads to a different light curve than the more commonly considered tidal disruption of a star on a parabolic orbit.

8.4 HYDRODYNAMICS NEAR AND INSIDE THE TIDAL RADIUS

Suppose that the star sinks gradually under the influence of gravitational radiation towards the tidal radius. The tidal stresses increase as $\sim (R_\star/r)^6$, where $R_\star$ is the stellar radius and r is the distance from the SMBH. Therefore the star will be flexed and distorted, and internal modes will be excited as it sinks (for a recent discussion and simple model of this complicated process, see Ogilvie 2009). If the energy from these modes could be dissipated then the orbit would undergo tidal circularisation and might end up in a stable mass transfer state. However, the energy that must be dissipated is significantly larger than the binding energy of the star. To see this, note that at the tidal radius r_T, we have $r_T = (3M/m)^{1/3} R_\star$. The binding energy of the star is $E_\star \approx Gm^2/R_\star$. The binding energy of the orbit is $E_{\rm orb} \approx GMm/r_T$. Circularisation of an orbit with eccentricity e at constant angular momentum releases an energy $e^2 E_{\rm orb}$, so the ratio of released energy to stellar binding energy is

$$e^2 \frac{E_{\rm orb}}{E_\star} \approx e^2 \left(\frac{M}{m}\right)\left(\frac{R_\star}{r_T}\right) \approx 3^{-1/3} e^2 \left(\frac{M}{m}\right)^{2/3} . \tag{81}$$

If $M \sim 10^7 m$ the ratio is therefore $\sim 3 \times 10^4 e^2$. From the previous section we found $e \sim 0.01 - 0.07$ for $M = 10^7\ M_\odot$, so the energy required to circularise the orbit would be $\sim 3 - 150$ times the binding energy of the star. If this energy could be released slowly this would cause no problems (note for comparison that in its lifetime the Sun will radiate a few hundred times its binding energy). However, the thermal (Kelvin-Helmholtz) time for solar-type stars is a few tens of millions of years, much longer than the inspiral time in our case and thus the tidal stresses will build up more rapidly than their mode energy can be radiated.

The competition is therefore between the time needed for gravitational radiation to move the star into the tidal radius (where mass transfer will ensue) and the time needed for circularisation due to tidal dissipation to deposit a stellar binding energy into the star and thus, presumably, to tidally disrupt the star. Note that Alexander & Morris (2003) discussed how tidal energy could produce “squeezars" with a different appearance from normal stars, without destroying the stars if the pericentre distance is sufficiently large. Here we are interested in the conditions for tidal destruction.

To evaluate this we adapt the expressions from Leconte et al. (2010) for the energy deposition rate of tidal dissipation in a planet due to its eccentric orbit around a star. They find

$$\dot{E}_{\rm tides} = 2K_p \left| N_a(e) - \frac{N^2(e)}{\Omega(e)} \right| \tag{82}$$

where

$$N(e) = \frac{1 + \frac{15}{2}e^2 + \frac{45}{8}e^4 + \frac{5}{16}e^6}{(1-e^2)^6} , \tag{83}$$

$$N_a(e) = \frac{1 + \frac{31}{2}e^2 + \frac{255}{8}e^4 + \frac{185}{16}e^6 + \frac{25}{64}e^8}{(1-e^2)^{15/2}} , \tag{84}$$

$$\Omega(e) = \frac{1 + \frac{3}{2}e^2 + \frac{1}{8}e^4}{(1-e^2)^5} \ , \tag{85}$$

and

$$K_p \approx \frac{9}{4} Q^{-1} \left(\frac{Gm^2}{R_*}\right) \left(\frac{M}{m}\right)^2 \left(\frac{R_*}{a}\right)^6 \left(\frac{GM}{a^3}\right)^{1/2} \tag{86}$$

In the last equation Q is the quality factor of the star, a standard parameterisation of the rate of tidal effects on to the star. The magnitude of Q is notoriously uncertain; values of $Q = 10^{5-6}$ are commonly used (see, e.g., Miller et al. 2009 for a recent example). If we use the expression $a_T = (3M/m)^{1/3} R_*$ for the tidal radius, this last expression reduces to

$$K_p \approx \frac{1}{4} Q^{-1} \left(\frac{Gm^2}{R_*}\right) \left(\frac{a}{a_T}\right)^{-6} \left(\frac{GM}{a^3}\right)^{1/2} \ . \tag{87}$$

In the limit $e \ll 1$ we find $N_a(e) \approx 1 + 23e^2$, $N^2(e) \approx 1 + 27e^2$, and $\Omega(e) \approx 1 + \frac{15}{2}e^2$. Thus

$$\dot{E}_{\rm tides} \approx \frac{7}{4} Q^{-1} e^2 \left(\frac{Gm^2}{R_*}\right) \left(\frac{a}{a_T}\right)^{-6} \left(\frac{GM}{a^3}\right)^{1/2} \ . \tag{88}$$

Thus the time needed to circularise the available energy $\sim e^2 (M/3m)^{2/3} (Gm^2/R_*)$ at $a = a_T$ is

$$\begin{aligned} T_{\rm circ,tide} &\approx e^2 (M/3m)^{1/3} (Gm^2/R_*) \\ &\quad \times [(7/4) Q^{-1} e^2 (Gm^2/R_*) (GM/a^3)^{1/2}]^{-1} \\ &= 3 \times 10^7 \text{ s } Q M_7^{2/3} m_0^{-1/6} \end{aligned} \tag{89}$$

where in the second line we have substituted $R_* = 0.85 R_\odot m_0^{2/3}$ and $a_T = (3M/m) R_*$. The circularisation time from gravitational radiation alone, at $e \ll 1$, is

$$\begin{aligned} T_{\rm circ,GW} &\approx (15/304) c^5 a^4 / (G^3 \mu M^2) \\ &\approx 6 \times 10^{11} \text{ s } M_7^{-2/3} m_0^{1/3} \end{aligned} \tag{90}$$

(Peters 1964), where in the last line we again substituted in $a = a_T$. Thus $T_{\rm circ,GW}/T_{\rm circ,tide} \approx 2 \times 10^4 Q^{-1} M_7^{-4/3} m_0^{1/2}$, which for $Q \sim 10^{5-6}$ is typically less than unity, hence only a fraction $T_{\rm circ,GW}/T_{\rm circ,tide}$ of the circularisation energy will go into tidal heating. Note, however, that for lower masses the eccentricity at the tidal radius is larger (scaling roughly as $M^{-3/2}$ for our three power laws) and that the ratio of circularisation energy to the internal binding energy scales as e^2, meaning that the total energy dissipated tidally scales as $\sim M^{-4}$, approximately. Thus even for $Q = 10^6$, several times the stellar binding energy will be dissipated for $M < 3 \times 10^6 \ M_\odot$.

If instead the SMBH mass is large, so that gravitational wave circularisation dominates over tidal circularisation, we expect that the star will settle into a period of steady mass transfer. The rate would be such that it balances the inward movement due to gravitational radiation, i.e., the characteristic time would be of order the grav-

itational radiation time. For our typical values, this is roughly 10^5 years, implying a rate of $\sim 10^{-5}\ M_\odot$ per year. Even if the luminosity is produced with an efficiency of 10%, this would produce a luminosity of only $\sim 10^{41}$ erg s^{-1}, weak enough and steady enough that it would not be distinguishable from a standard low-luminosity AGN. We therefore focus on the possibility that the star is tidally disrupted and that its debris is subsequently accreted by the SMBH.

If a star is disrupted from a low-eccentricity orbit the evolution of its tidal debris proceeds differently than if it is disrupted from a parabolic orbit. To see this, note that in the original argument of Rees (1988) it was demonstrated that the spread in the binding energy of the debris is comparable to the range in orbital binding energy from one side of the star to the other. If $m/M \sim 10^{-7}$, therefore, the fractional spread is $\sim (m/M)^{1/3} \sim 10^{-2}$. As a result, if an orbit with a pericentre $r \sim r_T$ has an eccentricity $e \gtrsim 0.99$, the debris semi-uniformly samples binding energies from zero to the binding energy of the original stellar center of mass. The assumption of exactly uniform sampling (equal mass for equal range in binding energy) leads to a mass accretion rate that scales with time t as $t^{-5/3}$; this law is more generally obtained at late times even for more realistic assumptions about stellar structure (e.g. Lodato et al. 2009). In contrast, if the spread in debris energies is much less than the average binding energy (corresponding to $e \ll 0.99$ in our example), then to lowest order the debris moves in a thin stream that intersects itself and settles within a few orbits into a remnant disc.

Such discs were studied by Cannizzo et al. (1990), who found that for plausible opacities the accretion rate would decay more gradually, e.g., $\dot{M} \propto t^{-1.2}$ for Thomson scattering. Moreover, because the debris would all be bound to the SMBH (unlike for the parabolic case, where roughly half the stellar mass escapes to infinity), the accretion rate could be quite substantial for comparatively low-mass SMBHs. For Thomson scattering, the expressions from Cannizzo et al. (1990) lead to

$$\dot{M} = 2 \times 10^{23}\ \mathrm{g\ s^{-1}} \left(\frac{\alpha}{0.1}\right)^{4/3} \bar{\rho}^{7/9} M_7^{-10/9} \left(\frac{\Delta M}{M_\odot}\right)^{5/3} . \tag{91}$$

Here $\bar{\rho}$ is the average density of the star in units of g cm^{-3}, ΔM is the mass of the remnant disc (which will initially be the mass of the star) and α is the Shakura & Sunyaev (1973) viscosity parameter. For $M_7 \lesssim 1$ this therefore has the possibility of shining at luminosities that are a significant fraction of the Eddington luminosity $L_E = 1.3 \times 10^{45} M_7$ erg s^{-1} assuming an efficiency $L/\dot{M}c^2 = 0.1$.

As pointed out to us by E. S. Phinney (2010, personal communication), depending on the very uncertain details of how tidal energy is deposited, is it possible that there will be a gravitational wave signature that attends the electromagnetic signature of disruption. In particular, it is not well established whether the tidal energy is deposited uniformly in the volume of the star or primarily where most of the matter is (both of which would lead to full disruption) or primarily in the envelope. If the last occurs, then the envelope would be stripped and lead to significant accretion with the characteristic decay discussed above, but the dense core would survive and could spiral

in further. This would lead to a coincident gravitational wave signal that could be detected with the proposed *LISA* if the source is close enough (Freitag 2003).

8.5 CONCLUSIONS

In his work, Hopman (2009) estimates that for a galactic nucleus such as ours, the tidal separation rate of binaries which start far away from the MBH is $\Gamma^{\rm GC}_{\rm tid\,sep} \sim 7 \times 10^{-7}(f_b|^{\rm GC}/0.05)\,{\rm yr}^{-1}$, where "GC" stands for Galactic Center and f_b is the fraction of stars in binaries. Fig.(6) of Hopman (2009) shows that the rate increases when we go to higher energies, because the loss-cone is depleted, allowing more binaries to "survive" in their way to the GC. Yu & Tremaine (2003) estimate that the number is enhanced by an order of magnitude by binaries *not* bound to the MBH. More remarkably, the event rates can be at least temporarily enhanced by *many orders of magnitude* if one considers the role of massive perturbers, such as giant molecular clouds or intermediate-mass black holes, which can accelerate relaxation by orders of magnitude as compared to two-body stellar relaxation (Perets et al. 2007). Another important potential boosting effect is the possibility that the potential is triaxial and not spherically symmetric (Merritt & Poon 2004; Poon & Merritt 2002, 2004). Taking these effects into account, we assume $\Gamma^{\rm GC}_{\rm tid\,sep} \sim 10^{-5}(f_b|^{\rm GC}/0.05)\,{\rm yr}^{-1}$. The fraction of main sequence stars that will eventually spiral into the SMBH after tidal separation is at least a few percent, so a plausible estimate of the total event rate for tidal disruptions of a single star originated by a separated binary in a Hubble time is $\Gamma^{\rm GC} \sim 10^{-7}(f_b|^{\rm GC}/0.05)\,{\rm yr}^{-1}$, and it could be higher. This rate is probably a subset of the rate at which single stars are likely to encounter SMBHs on parabolic orbits (see Amaro-Seoane et al. 2007,for a discussion of such extreme mass ratio inspirals). It is therefore possible that events with the $L \propto t^{-1.2}$ decay characteristic of low-eccentricity disruption may have rates smaller or similar to events with the $L \propto t^{-5/3}$ decay that is expected to be signatures of disruption of single stars in galactic nuclei and that is consistent with the initial decay of the recent Swift event Sw 1644+57 (Bloom et al. 2011).

BIBLIOGRAPHY

Aarseth S. J., 2003, Gravitational N-Body Simulations. ISBN 0521432723. Cambridge, UK: Cambridge University Press, November 2003.

Aarseth S. J., Zare K., 1974, Celestial Mechanics, 10, 185

Alexander T., Hopman C., 2009, ApJ, 697, 1861

Alexander T., Morris M., 2003, ApJ Lett., 590, L25

Amaro-Seoane P., Gair J. R., Freitag M., Miller M. C., Mandel I., Cutler C. J., Babak S., 2007, Classical and Quantum Gravity, 24, 113

Amaro-Seoane P., Preto M., 2011, Classical and Quantum Gravity, 28, 094017

Amaro-Seoane, P., Aoudia, S., Babak, S., et al. 2013, GW Notes, Vol. 6, p. 4-110, 6, 4

Bloom J. S., Giannios D., Metzger B. D., Cenko S. B., Perley D. A., Butler N. R., Tanvir N. R., Levan A. J., O'Brien P. T., Strubbe L. E., De Colle F., Ramirez-Ruiz E., Lee W. H., Nayakshin S., Quataert E., King A. R., Cucchiara A., Guillochon J., Bower G. C., Fruchter A. S., Morgan A. N., van der Horst A. J., 2011, Science, 333, 203

Brown W. R., Geller M. J., Kenyon S. J., Bromley B. C., 2009, ApJ Lett., 690, L69

Cannizzo J. K., Lee H. M., Goodman J., 1990, ApJ, 351, 38

Demircan O., Kahraman G., 1991, Astrophysics and Space Science, 181, 313

Dogiel V. A., Chernyshov D. O., Yuasa T., Prokhorov D., Cheng K.-S., Bamba A., Inoue H., Ko C.-M., Kokubun M., Maeda Y., Mitsuda K., Nakazawa K., Yamasaki N. Y., 2009, PASJ, 61, 1099

Donley J. L., Brandt W. N., Eracleous M., Boller T., 2002, 124, 1308

Duquennoy A., Mayor M., 1991, A&A, 248, 485

Freitag M., 2003, ApJ Lett., 583, L21

Gezari S., Heckman T., Cenko S. B., Eracleous M., Forster K., Gonçalves T. S., Martin D. C., Morrissey P., Neff S. G., Seibert M., Schiminovich D., Wyder T. K., 2009, ApJ, 698, 1367

Ginsburg I., Loeb A., 2006, MNRAS, 368, 221

Gould A., Quillen A. C., 2003, ApJ, 592, 935

Gürkan M. A., Hopman C., 2007, MNRAS, 379, 1083

Hills J. G., 1988, Nat, 331, 687

Hopman C., 2009, ApJ, 700, 1933

Kustaanheimo P. E., Stiefel E. L., 1965, J. Reine Angew. Math.

Leconte J., Chabrier G., Baraffe I., Levrard B., 2010, A&A, 516, A64+

Lodato G., King A. R., Pringle J. E., 2009, MNRAS, 392, 332

Madigan A.-M., Levin Y., Hopman C., 2009, ApJ Lett., 697, L44

Merritt D., Alexander T., Mikkola S., Will C., 2011, ArXiv e-prints

Merritt D., Poon M. Y., 2004, ApJ, 606, 788

Miller M. C., Freitag M., Hamilton D. P., Lauburg V. M., 2005, ApJ Lett., 631, L117

Miller N., Fortney J. J., Jackson B., 2009, ApJ, 702, 1413

Ogilvie G. I., 2009, MNRAS, 396, 794

Perets H. B., Gualandris A., 2010, ApJ, 719, 220

Perets H. B., Hopman C., Alexander T., 2007, ApJ, 656, 709

Peters P. C., 1964, Physical Review, 136, 1224

Poon M. Y., Merritt D., 2002, ApJ Lett., 568, 89

—, 2004, ApJ, 606, 774

Preto M., Amaro-Seoane P., 2010, ApJ Lett., 708, L42

Rauch K. P., Tremaine S., 1996, New Astronomy, 1, 149

Rees M. J., 1988, Nat, 333, 523

Shakura N. I., Sunyaev R. A., 1973, A&A, 24, 337

Spitzer L., 1987, Dynamical evolution of globular clusters. Princeton, NJ, Princeton University Press, 1987, 191 p.

Tremaine S., Gebhardt K., Bender R., Bower G., Dressler A., Faber S. M., Filippenko A. V., Green R., Grillmair C., Ho L. C., Kormendy J., Lauer T. R., Magorrian J., Pinkney J., Richstone D., 2002, ApJ, 574, 740

Wang J., Merritt D., 2004, ApJ, 600, 149

Yu Q., Tremaine S., 2003, ApJ, 599, 1129

Zare K., 1974, Celestial Mechanics, 10, 207

9

THE IMPACT OF REALISTIC MODELS OF MASS SEGREGATION ON THE EVENT RATE OF EXTREME-MASS RATIO INSPIRALS AND CUSP RE-GROWTH

Pau Amaro-Seoane[1] *& Miguel Preto*[2]

published in *Classical and Quantum Gravity, Volume 28, Issue 9, id. 094017 (2011)*

Abstract: One of the most interesting sources of gravitational waves (GWs) for *LISA* is the inspiral of compact objects on to a massive black hole (MBH), commonly referred to as an "extreme-mass ratio inspiral" (EMRI). The small object, typically a stellar black hole (bh), emits significant amounts of GW along each orbit in the detector bandwidth. The slowly, adiabatic inspiral of these sources will allow us to map space-time around MBHs in detail, as well as to test our current conception of gravitation in the strong regime. The event rate of this kind of source has been addressed many times in the literature and the numbers reported fluctuate by orders of magnitude. On the other hand, recent observations of the Galactic center revealed a dearth of giant stars inside the inner parsec relative to the numbers theoretically expected for a fully relaxed stellar cusp. The possibility of unrelaxed nuclei (or, equivalently, with no or only a very shallow cusp, or core) adds substantial uncertainty to the estimates. Having this timely question in mind, we run a significant number of direct-summation $N-$body simulations with up to half a million particles to calibrate a much faster orbit-averaged Fokker-Planck code. We show that, under quite generic initial conditions, the time required for the growth of a relaxed, mass segregated stellar cusp is shorter than a Hubble time for MBHs with $M_\bullet \lesssim 5 \times 10^6 M_\odot$ (i.e. nuclei in the range of *LISA*). We then investigate the regime of strong mass segregation (SMS) for models with two different stellar mass components. Given the most recent stellar mass normalization for the inner parsec of the Galactic center, SMS has the significant impact of boosting the EMRI rates by a factor of ~ 10 in comparison to what would result from a $7/4-$Bahcall & Wolf cusp resulting in ~ 250 events per Gyr per Milky Way type galaxy. Such intrinsic rate should translate roughly into $\sim 10^2 - 7 \times 10^2$ sbh's EMRIs detected by LISA over a mission lifetime of 2 or 5 years, respectively), depending on the detailed assumptions regarding LISA detection capabilities.

1 Max Planck Institut für Gravitationsphysik (Albert-Einstein-Institut), D-14476 Potsdam, Germany
2 Astronomisches Rechen-Institut, Mönchhofstr. 12-14, D-69120 Heidelberg, Germany

9.1 INTRODUCTION

Nowadays it is well-established that a massive dark object, very possibly a massive black hole (MBH) with a mass of about $4 \times 10^6 M_\odot$, is lurking in the centre of the Milky Way (Ghez et al. 2008; Eisenhauer et al. 2005; Ghez et al. 2005; Gillessen et al. 2009). While there is an emerging consensus about the origin and growth of supermassive black holes (SMBH, with masses about or larger than $10^8 M_\odot$) (DiMatteo et al. 2008; Ferrarese & Ford 2005; Volonteri 2010), MBHs with smaller masses such as the one in the Galactic centre remain a (relatively) understudied enigma. One of the keys to understanding the growth and evolution of MBHs in this lower mass range resides in the dynamics of stars in their vicinity. This is the case mainly because relaxation times there are low enough that the surrounding stellar systems should have had enough time—through two-body relaxation *alone*—to evolve towards a steady-state which is independent of the particular initial conditions at the time of formation. The Galactic center is thought to fulfill such condition. It is the universality of such relaxed stellar nuclei that gives us a crucial predictive power on the expected properties of the MBH environment, on the stellar candidates for close interaction with the central MBH and on the resulting gravitational wave (GW) signatures. If, on the contrary, non-relaxed systems were generic, then one would need to resort to *case-by-case modelling of each galactic nucleus*.

The ideal probe for these innermost regions of galaxies is the GW radiation that is emitted by stellar bhs and other compact objects that come very close to the MBH. One of the main channels for interaction between stars and a central MBH is the adiabatic, slow inspiral of compact remnants (CR) into the MBH due to the emission of GWs—an EMRI. During such an event, the small body effectively acts as a probe of spacetime close to the MBH as its orbit slowly shrinks due to the energy and angular momentum lost in the form of GW radiation. In case of $10^5 - 10^6 M_\odot$ MBHs, after some $\sim 10^4 - 10^5$ orbits in the LISA band ($f_{\rm orb} \gtrsim 10^{-4}$ Hz and a periapsis $a \lesssim$ few $\times$ $R_{\rm Schw}$, since we only consider sources which are completely embedded in the band, and not bursting sources), the small body eventually merges with the MBH. The information contained in the waves will allow us to determine the parameters of these binary system with an unprecedented accuracy (see for instance Babak et al. 2010; Barack and Cutler 2004), corroborate the existence of MBHs and maybe even provide the first direct detection of an intermediate MBH (in case the primary is $\sim 10^{3-4} M_\odot$).

LISA will thus scrutinize exactly the mass range about which electromagnetic observational information is currently lacking. In its most general form, the EMRI problem—the astrophysical modelling of event rates and parameters for EMRIs—spans many orders of magnitude. From the bulge regions at few$\times$10 pc, where the dynamics is essentially collisionless –but from where single stellar bhs and binaries with CRs originate; down to the parsec scale of the nucleus itself which evolves secularly over (local) relaxation timescales; and then further down to milliparsec scales where relativistic effects start to dominate the evolution. But, however, once a steady state configuration establishes itself in the central parsec region, the EMRI rates are rather

expected to depend strongly on the (universal) density distribution of CRs within (in order of magnitude) $\mathcal{O}(0.01\mathrm{pc})$ from the hole. This is indeed the region from which these inspiralling sources are expected to originate (Hopman & Alexander 2005). The dynamics in this tiny volume has been rather unexplored until the relevance of EMRIs and sub-parsec observations of the Galactic center have raised its interest. Since then, many authors have devoted a number of works to the analysis of this peculiar regime (Alexander & Hopman 2003; Freitag 2003; Hopman & Alexander 2006; Sigurdsson and Rees 1997).

We discuss in this work the stellar distribution of dense stellar systems around MBHs in the LISA mass range. Realistic modeling of mass segregation—which is the natural outcome for any realistic stellar population—will strongly impact the expected EMRI rates, since it favors the accumulation of heavier objects towards the center (Alexander and Hopman 2009; Preto and Amaro-Seoane 2010a; Hopman & Alexander 2006). In Section 2, we begin by summarizing the results obtained by Preto and Amaro-Seoane (2010a) that show how to calibrate the FP calculations with direct N-body simulations[1]; then, still in the same section, we present new results concerning the robustness of N-body realisations of stellar cusp growth with respect to the total particle number N. In section 3, we present new results on the growth of stellar cusps from a variety of initial conditions resulting from carving a cavity in the star's phase space distribution function. This is motivated from a variety of astrophysical mechanisms that may lead to cusp destruction; and these mechanisms are critically assessed in the end of the section. We show that, under very generic circumstances, the time required for the growth of a cusp is shorter than a Hubble time. Therefore, quasi-steady, mass segregated, stellar cusps are expected to be common around MBHs in the LISA mass range. But see Merritt (2010) and Madigan et al. (2010) for different perspectives. EMRI detection rates for *LISA* are expected to peak for $M_\bullet \sim 10^5 - 10^6 M_\odot$ (Gair 2009) leading us to conclude that at least a sizeable fraction of these events should originate from strongly segregated cusps. Finally, in Section 4 we present new estimates on the expected EMRI rates in mass segregated nuclei and conclude that our realistic modeling of mass segregation has a significant impact on these rates.

9.2 MASS SEGREGATION

The distribution of stars around a massive black hole is a classical problem in stellar dynamics (Bahcall and Wolf 1976; Lightman and Shapiro 1977). Bahcall and Wolf (1976) have shown, through a kinetic treatment that, within the radius of gravitational influence of the hole r_h, in case all stars are of the same mass, this quasi-steady distribution takes the form of power laws, $\rho(r) \sim r^{-\gamma}$, in physical space with $\rho(r)$ the stellar density at a radius r and $f(E) \sim E^p$ in energy space (with E the energy and $\gamma = 7/4$

1 Direct N-body simulations compute the gravitational accelerations between particles using the exact Newton's law, without introducing any approximations to compute the gravitational potential (Binney and Tremaine 2008).

and $p = \gamma - 3/2 = 1/4$)[2]. This is the so-called *zero-flow solution* for which the net flux of stars in energy space is *precisely* zero. Preto et al. (2004) and Baumgardt et al. (2004) were the first to demonstrate the robustness of the corresponding direct-summation N-body realizations, and have therefore validated the assumptions inherent to the Fokker-Planck (FP) approximation—namely, that scattering is dominated by uncorrelated, 2-body encounters and, in particular, dense stellar cusps[3] populated with stars of the *same mass* are robust against ejection of stars from the cusp. The latter result is not trivial as for a BW $\gamma = 7/4$ cusp stellar densities are extremely high at the center and the fraction of stars with speeds close to the escape velocity from the cusp is quite high at all radii $r \lesssim r_h$, with r_h the influence radius of the MBH (Preto 2010).

Single mass models are very poor approximations of real stellar populations. To first order of approximation, an evolved stellar population can be represented by two (well-separated) mass scales: one in the range $\mathcal{O}(1M_\odot)$ corresponding to low mass main-sequence stars, white dwarfs (WDs) and neutron stars (NSs); another with $\mathcal{O}(10M_\odot)$ representing stellar bhs. Therefore, for simplicity, here we restrict our discussion to models with two mass components and leave the more general case to another work in preparation (Preto and Amaro-Seoane 2010b).

When stars of two different masses are present, there is mass segregation which is a process by which the heavy stars accumulate near the center while the lighter ones float outward (Khalisi et al. 2007; Spitzer 1987). Accordingly, stars with different mass get distributed with different density profiles. Bahcall and Wolf (1977), henceforth BW77, have argued heuristically that a scaling relation $p_i = m_i/m_j \times p_j$ (where the subindices i, j refer to the light or heavy components) establishes itself and depends only on the mass ratio. Here, as in the single-mass case, the crucial assumption is that all components are abundant enough that they undergo enough scattering among themselves and with the other components as to stabilize into an approximate *zero-flow* solution. Obviously, this cannot happen independently of the number fraction of the different stellar masses (Alexander and Hopman 2009; Preto and Amaro-Seoane 2010a). In the realistic situation where the number fraction of heavy objects (in our case, stellar bhs) is small, a new solution coined by Alexander and Hopman (2009) as *strong mass segregation* (SMS) obtains with density of heavy objects scaling as $\rho_H(r) \sim r^{-\alpha}$, where $\alpha \gtrsim 2$. The solution has two branches and can be parametrized by the parameter

$$\Delta = \frac{D^{(1)}_{HH} + D^{(2)}_{HH}}{D^{(1)}_{LH} + D^{(2)}_{LH}} \approx \frac{N_H m_H^2}{N_L m_L^2} \frac{4}{3 + m_H/m_L}, \tag{92}$$

where N_L and N_H are the total number of light and heavy stars, m_L and m_H are the corresponding individual masses. Δ provides a measure of the importance of the heavy star's self-coupling relative to the light-heavy coupling (in terms of the 1st and

2 We note that 12 years *before* the work of BW, Gurevich (1964) derived a similar solution for how electrons distribute around a positively charged Coulomb center, which is the equivalent of the MBH in our case.

3 In this work, a nucleus is said to be a *core* if $\gamma < 1$; it is said to be a *cusp* if $\gamma > 1$.

2nd order diffusion coefficients); and it depends essentially on the mass *and* number ratios, which is one parameter more than proposed by BW77. The *weak* branch, for $\Delta > 1$ corresponds to the scaling relations found by BW77; while the *strong* branch, for $\Delta < 1$, generalizes the BW77 solution[4]. Stellar populations with continuous star formation and an initial mass function (IMF) given by $dN/dM \propto M^{-\alpha}$ will be characterized by $\Delta < 1$ if $\alpha \gtrsim 1.8$ and $\Delta < 1$ otherwise; and, in particular, Salpeter and Kroupa's IMF generate evolved stellar populations with $\Delta < 1$ (Alexander and Hopman 2009).

There is a straightforward physical interpretation for the strong branch of mass segregation. In the limit where heavy stars are very scarce, they barely interact with each other and instead sink to the center due to dynamical friction against the sea of light stars. Therefore, a quasi-steady state develops in which the heavy star's current is *not* nearly zero and thus the BW77 solution does not hold exactly anymore. Indeed, in the limit where the number fraction f_H of heavy stars is vanishingly small, as is the case of nuclei with realistic IMFs, the stellar potential is dominated by the light component. In this case, the light stars should evolve as if in isolation and develop a $\gamma_L \sim 7/4$ density cusp. The scarce heavy stars sink to the center due to dynamical friction against the background of light stars, and will not exert any significant back-reaction on them (Preto 2010).

Figure 1 displays the FP and NB evolutions of the spatial density $\rho_L(r)$ and $\rho_H(r)$ for models with two mass components corresponding to different initial profiles, MBH masses and total particle number N. The starting models are either $\gamma = 1$ or $\gamma = 1/2$ Dehnen profiles for both components with a MBH of 1% or 5% of the total mass of the cluster. Dehnen density profiles are defined by $\rho(r) = (3-\gamma)M_{TOT}/4\pi r^{\gamma}(r_b + r)^{4-\gamma}$, have total stellar mass M_{TOT}, an inner (outer) logarithmic slope γ $(4-\gamma)$ and a break radius $r_b = 1$ (which is larger than r_h in all cases). We adopt units where $G = M_{TOT} = 1$. The density of both components reaches a quasi-steady state within $\sim 0.2T_{\rm rlx}(r_h)$, where $T_{\rm rlx}(r_h)$ relaxation time measured at the influence radius (Preto and Amaro-Seoane 2010a). The top and middle panels display the strong mass segregation solution with $\gamma_H \sim 2.1$ as expected for $\Delta = 0.08$ ($f_H = 2.5 \times 10^{-3}$); while, in the bottom panel, $\Delta = 13.2$ ($f_H = 0.429$) displays the weak solution for which $\gamma_H \sim 7/4$. The former value was chosen to be close to the number fraction of stellar bhs to be expected from a standard Salpeter or Kroupa's IMF; the latter value is chosen to be representative of the regime of weak segregation studied by BW77. One can see from Figure 1 that in the case of weak segregation $\rho_H > \rho_L$ everywhere due to the extremely high number of heavy objects; in contrast, in the SMS regime $\rho_H > \rho_L$ only for $r \lesssim 0.01r_h$ (and the light objects dominate in number almost everywhere). In all cases the asymptotic slopes are valid within $\sim 0.1r_h$ and are totally predictable once Δ is known. These results agree pretty well with the predictions for the SMS regime (Alexander and Hopman 2009).

The particle number in our direct-summation $N-$body simulations sample ranges from $N = 124,000$ to $N = 512,000$; our results do not show evidence of any depen-

4 The choice of the names is based upon the resulting slopes in the density profiles, which are steeper (*stronger*) or shallower (*weaker*)

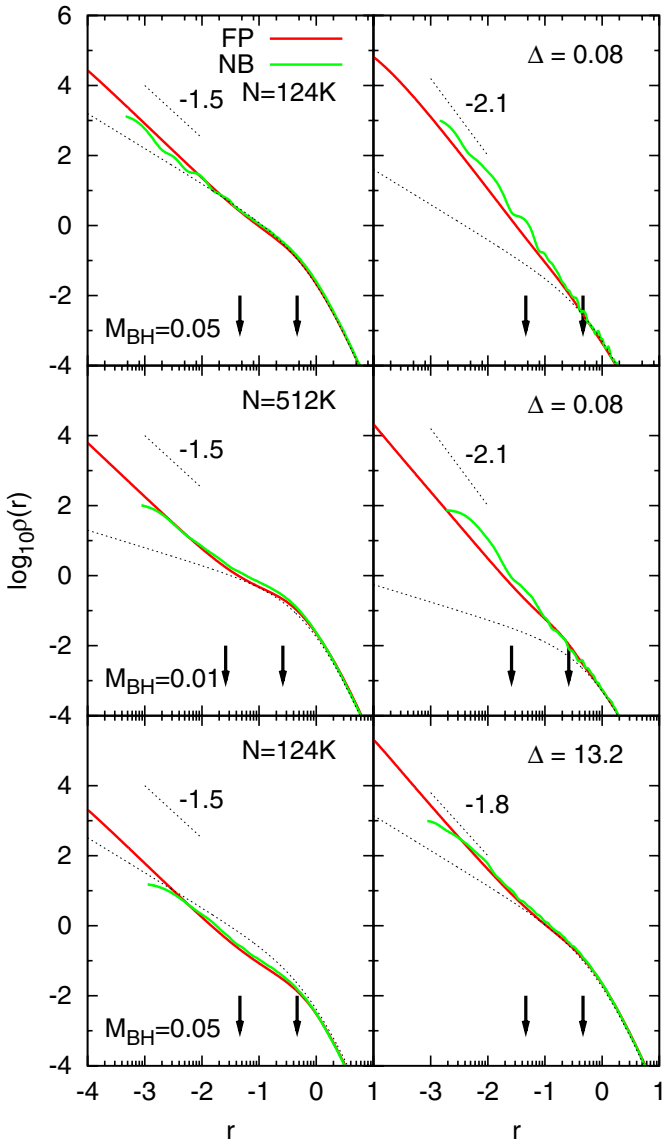

Figure 25: Evolution of density profiles. Mass density profiles, $\rho_L(r)$ (left panels) and $\rho_H(r)$ (right panels) at the end of the integrations, after $\approx 0.2T_{\rm rlx}(r_{\rm h})$. Red curves are from FP calculations, green curves are from NB simulations. The agreement between both methods is quite good. The mass ratio between heavy and light stars is $R = 10$, representing the expected typical mass ratio between light stars (MS stars, WDs and NSs) and stellar bhs, as explained in the text; the number fraction of heavy stars $f_H = 2.5 \times 10^{-3}$ (top and middle panels) and $f_H = 0.429$ (lower panels), corresponding to the strong and weak segregation regimes respectively. The initial condition is a Dehnen profile with central slope $\gamma = 1$ for the top and bottom panels (Preto and Amaro-Seoane 2010a), $\gamma = 1/2$ in the middle panel; a central MBH with 5% of the total mass of the cluster and 1% likewise. The particle number is $N = 124,000$ (top and bottom) and $N = 512,000$ (middle). The asymptotic slope γ_H decreases from $\gtrsim 2$ to $\approx 7/4$ when moving from the strong to the weak branch of the solution. The asymptotic slope $\gamma_H \approx 3/2$ throughout, or just slightly below this value. The arrows point to radii r_h and $0.1r_h$.

dence on total N, nor on the initial value of γ, once the results are re-scaled appropriately (*i.e.* measured in terms of the relaxation time). The agreement between NB and FP methods is quite good in all cases.

9.3 CUSP RE-GROWTH

9.3.1 *Current observations: A missing cusp*

We have seen that theory predicts a steady state cusp that reaches extremely high densities in the center near the MBH. Furthermore, given a normalization at, say, r_h and a knowledge of the stellar mass function (and thus of Δ), the density profile inside r_h becomes completely determined. But observations are much more complicated to interpret. First, one must realize that there are very few galaxies for which the influence radius r_h can be resolved. In fact, except for the nearest galaxies, r_h covers an angular region in the sky which is too small to be resolved even with the HST. The HST has an angular resolution of $\sim 0.1''$. In the case of galaxies in the Virgo cluster, at ~ 17 Mpc of distance, it can only resolve regions with linear sizes $\gtrsim 8.25$ pc. Therefore, HST would not be able to resolve SgrA*'s radius of influence if it were at the distance of Virgo. Since $r_h \propto M_\bullet^{1/2}$, it can only start to resolve the influence radius of Virgo's MBHs that have masses $M_\bullet \gtrsim 4 \times 10^7 M_\odot$. Second, even in the few cases for which r_h can be resolved to some extent, it still is necessary to assess whether the observed stars (only those that are bright enough to be detected) really trace the underlying (dynamically dominant) invisible population. Third, given the fact that, as we have seen, stars tend to segregate by mass, there is an extra uncertainty related to the unknown stellar mass function. Moreover, there are indications that star formation events are common in galactic nuclei and furthermore that the resulting IMF in these sub-parsec regions may be substantially different from that of the field stars and biased towards heavy masses (Bartko et al. 2010). Finally, it is necessary to deproject the observations and, in the (inevitable) absence of complete knowledge of phase space coordinates, one must rely on kinematic assumptions regarding the (an-)isotropy of stellar velocities and on the three dimensional shape of the stellar system.

Nevertheless, it has come as a surprise that very recent spectroscopic observations of the Galactic center revealed a core (or even a dip) in the surface distribution of the old stellar population (essentially red giants) which should have had time to relax into a cuspy density profile (Buchholz et al. 2009; Do et al. 2009). The caveat is that the detected stars are still a small fraction, of about 5%, of the stellar population as a whole and therefore do not exclude the presence of an extended dark cluster (presumably made of stellar bhs and other CRs)—which would indeed agree with our theoretical expectations.

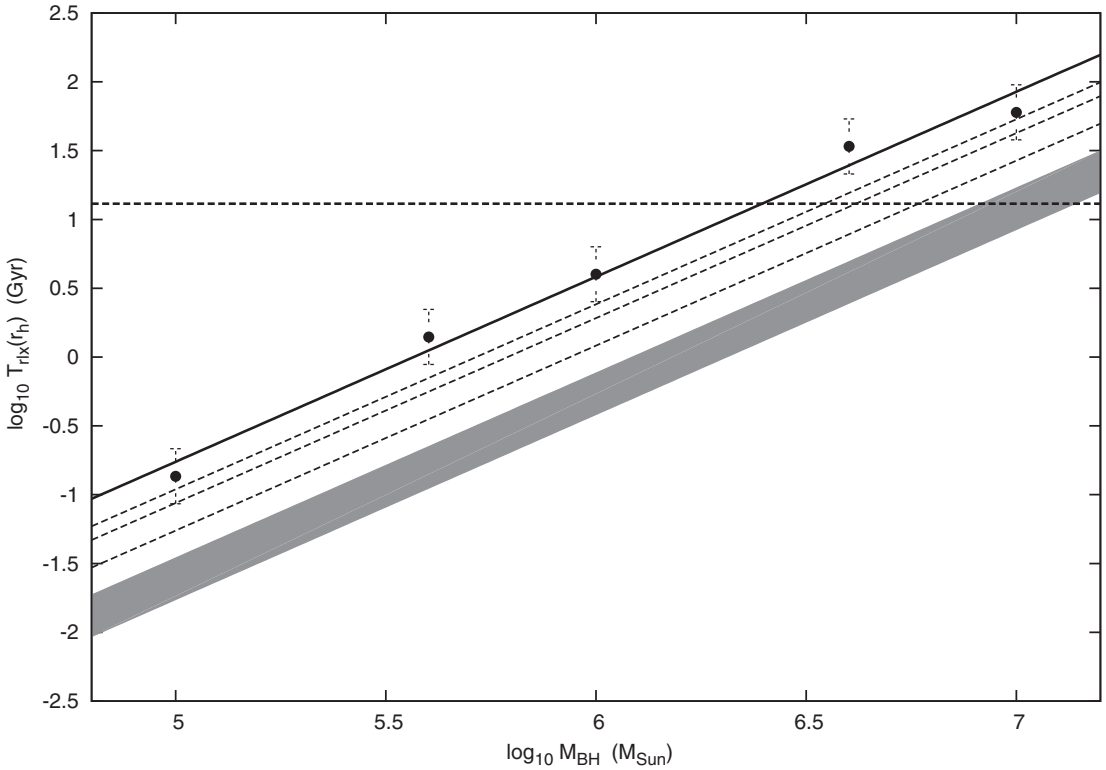

Figure 26: Time for cusp re-growth. Single-mass relaxation time at r_h for single-mass cored models as a function of MBH mass. The shaded area covers $[0.1T_{\rm rlx}, 0.2T_{\rm rlx}]$—the time for cusp re-growth if there is no hole in the initial DF. The three dashed lines above the shaded region represent the average time needed for the cusp re-growth in case one imposes an initial cavity with size $R_{\rm cav} = 0.5, 1$ or 2 pc. The horizontal dashed curve represents 13 Gyr. It can be seen that the time needed to re-grow a cusp around MBH with masses $M_\bullet \lesssim 5 \times 10^6 M_\odot$ is below a Hubble time so long as the initial cavity is smaller than $\lesssim 2$ pc.

9.3.2 *Carving a hole in the stellar distribution*

To assess the likelihood that the Galactic center is indeed unrelaxed, it is natural to ask: how long does it take to re-grow a cusp if, at some point, it has been destroyed? A complete answer will, of course, depend on the extent to which the cusp was destroyed, *i.e.* how much mass was expelled from the original cusp and over which radial range. At this level, it does not matter very much which mechanism led to the destruction of the cusp. We discuss briefly possible scenarios for cusp destruction at the end of the section.

In order to investigate this question, we have concocted a set of initial conditions purported to mimic the outcome of a destroying cusp event—such as the carving of a cavity in phase space through the ejection of stars by, say, an infalling IMBH or, following a major merger, by a MBH. We model the outcome of such an event by imposing that all stars with binding energies larger than some E_0 or almost equivalently, with semimajor axis smaller than $GM_\bullet/2E_0$, are not present in the initial DF. In fact, inside r_h the MBH dominates the gravitational potential and $E \sim GM_\bullet/2a$. We thus set up an initial Dehnen model with $f(E) = 0$ for $E > E_0$—in other words, there is an initial cavity in the phase space DF, but not in physical space as the stars with lower energy still entail $\rho(r) \sim r^{-1/2}$ at the center, although with a smaller amplitude than the original model. The values of E_0 were chosen to represent cavities of size $R_c = 0.5, 1, 2$ pc resulting from the inspiral of an IMBH/MBH. Note that these models are, by construction, isotropic in the velocity distribution. [5] Our fiducial model is a Milky Way type nucleus with $M_\bullet = 4 \times 10^6 M_\odot$, some $10^6 M_\odot$ in total stellar mass inside 1 pc distributed according to an initial central density slope $\gamma = 1/2$, two components with masses $m_L = 1 M_\odot$ and $m_H = 10 M_\odot$, and 0.1% of stellar bhs by number. When the stellar distribution has no phase space cavity, this translates into having stars down to roughly 10^{-5} pc. Having validated the FP models with detailed N-body simulations, we now proceed in the rest of the paper to describe results obtained with the (much faster) FP approach.

Figure 2 shows the times for cusp re-growth computed with FP for different galactic nuclei models. The time for cusp re-growth is defined as the time it takes for a given initial density profile ($\rho(r)$ in space or $f(E)$ in phase space, with or without an initial cavity) to reach its asymptotic slope, which depends on Δ, down to $r \sim 0.01 r_h$. This is indeed the scale which is resolved by recent observations of the Galactic center (Schödel et al. 2009). The shaded region represents the time of cusp re-growth for a range of R and f_H (all in the SMS regime, $\Delta < 1$) for the case where $f(E)$ extends to high E without any cut. It can be seen that, for $M_\bullet \lesssim 10^7 M_\odot$, cusps grow in less than a Hubble time; in the particular case of the Milky Way nucleus with $M_\bullet \sim 4 \times 10^6 M_\odot$, it takes no longer than ~ 4.8 Gyr to fully re-grow a steady-state, mass segregated, stellar cusp and only ~ 2.4 Gyr to have it grown down to $0.01 r_h$. If, instead, an initial cavity is imposed at the center with size $R_{\rm cav} = 0.5, 1$ or 2 pc in case of the Milky Way

5 We assume that the timescale for isotropization of velocities is much shorter than that associated with the cusp re-growth; in any event this should not affect our estimates by more than 10% or 20% maximum.

(or $R_{\rm cav} = 0.2r_h, 0.4r_h$ or $0.8r_h$ in case of a generic nucleus), times for re-growth are represented by the dashed curves above the shaded region. In this case, times for cusp re-growth increase; in the Milky Way case, it becomes $\sim 4.8, 7.2$ or 12 Gyr, respectively. Note that, in the mass range $10^5 - 10^6 M_\odot$, the times for cusp re-growth are definitely *much shorter* than a Hubble time—even if a fairly large cavity of size comparablee to r_h is hypothesized. The full curve represents the relaxation times computed at the radius of influence r_h, while the dashed curves represent the *actual* times for cusp re-growth as measured from FP calculations (Preto and Amaro-Seoane 2010a).

It is difficult to devise plausible mechanisms for the formation of such large cores in the stellar distribution. For instance, the inspiral of an IMBH of mass $M_\bullet \sim 10^{3-4} M_\odot$ that forms an unequal-mass binary with the MBH and ejects stars through three body encounters would tend to progressively wipe out the stellar cusp. However, the core radius carved by such an event is $r_c \sim 0.02 - 0.04$ pc (Baumgardt et al. 2006) and thus a steady inflow of such IMBHs (one every 10^7 years for a Hubble time) would be required in order to carve a large core 50 or 100 larger. Such large inflow of IMBHs have been proposed by Portegies Zwart et al. (2006). This does not seem very likely anymore in light of the fact that such IMBHs were hypothesized to be formed by run-away mergers of stars in the center of globular clusters. However, at solar metallicities, such mechanism seems very inneficient. Mass loss due to very strong winds severely limits the growth of the stellar object being formed and the likely end result of a run-away merger is a $\sim 100 M_\odot$ Wolf-Rayet star. At lower metallicities, mass loss is lower and the remnant can be more massive $\sim 260 M_\odot$, but in any case it will not form an IMBH (Glebbek et al. 2009). In sum, it looks very unlikely that sufficient IMBHs can be formed in order to generate such steady inflow to the Galactic center. Another possibility would be that SgrA* is a binary MBH, but this would most likely imply that there has been a, more or less recent, major merger involving the Milky Way. This would contradict the apparent pure-disk nature of the Galaxy, as theoretical interpretations of stellar kinematic data of the Galactic Bulge seem to favor that the Bulge is part of the disk and not a separate component resulting from a merger Shen et al. (2010)y—aside from the fact that there are strong constraints from the SgrA* proper motion (Reid and Brunthaler 2004).

Stars in a Keplerian potential, $GM_\bullet/r$, do not precess because of the $1:1$ resonance between their radial and azimuthal frequencies. Resonant relaxation (RR) results from the coherent torques that such stars exert on each other leading to a fast evolution of their orbital angular momenta over timescales $\lesssim T_{pr}$, where T_{pr} is the precession timescale due to departures from an exact Kepler potential (Rauch and Tremaine 1996). Madigan et al. (2010) suggest that RR, by increasing the rate of angular momentum diffusion in the near-Keplerian gravitational potential around the MBH, may boost the tidal disruption rate of stars and could thus create a near-cavity (out to ~ 0.1 pc) in the stellar distribution. It is certain that RR operates to some extent in the inner parsec, but we doubt it can completetly explain the dearth of red giant stars there or,

more generally, the full destruction of a cusp—including CRs such as stellar bhs[6] First, their final density distribution does not show a cavity, nor a shallow cusp profile, for $r \gtrsim 0.1$ pc; instead, they get final slopes $\gamma \sim 1.5$ for $r \gtrsim 0.1$ pc. This is in contrast with observations which show a decaying density for $r \lesssim 0.24$ pc (Buchholz et al. 2009). Second, we believe that their Monte-Carlo calculations severely underestimate the rate at which the cusp re-grows; in fact, they obtain a timescale which is $\sim 10 - 30$ times longer than that obtained with our N-body simulations (which are free from any simplifying dynamical assumptions), and also from ours and their own recent FP calculations (Hopman and Madigan 2010). Third, were they to use the latter rates, and given that the time RR takes to deplete the cusp is of the same order as the time we obtain for cusp re-growth, the net effect of RR on the cusp would likely be minute. Moreover, stellar bhs cannot be tidally disrupted, and this makes them less susceptible to be extracted from the cusp than $10M_\odot$ stars.

9.4 EMRIS RATES

9.4.1 *Adiabatic and abrupt EMRIs: Estimation of the rates*

Given a steady state stellar bhs continue to diffuse in (E, J)-space and some of them eventually come into close interaction with the MBH. During a close interaction, a stellar bh can either be promptly scattered into the MBH, accompanied by a single or a few brief bursts of GWs in the *LISA* band—the so-called "direct-plunges"—, though they are not likely detectable unless if emitted from the Galactic center (Hopman et al. 2007), or scattered outwards in the cusp. In either case, it does not live enough to become an EMRI. Alternatively, it may undergo a very slow, adiabatic, inspiral without being appreciably disturbed by other stars and, in this case, it will eventually become an EMRI detectable by LISA. An EMRI object thus has to spend very many orbits without being significantly scattered by the gravitational tugs of the other stars. In other words, they must fullfill the following *inspiralling criterion*: the time $T_{\rm GW}$ it takes for the inspiral, due to orbital energy lost by GW emission only, must be shorter than the typical time T_J it takes on average to drift in angular momentum by an amount J which equals its orbital angular momentum. Otherwise, they will be promptly captured by the MBH before entering the LISA band. The inspiral criterion can be stated in terms of the parameter s being smaller than unity, $s = T_{\rm GW}/T_J < 1$. For $T_{\rm GW} > T_J$, it is almost certain that this object has either taken an almost radial orbit and fallen into the MBH as a direct plunge or has been scattered outwards. [7] It turns out that this parameter simply scales with orbital's semimajor axis: $s \propto a^{3/2-p}$ (Hopman & Alexander 2005), which means that it is a decreasing function of a so long as $p < 3/2$.

6 Resonant relaxation is, nevertheless, very likely to have a significant impact on the EMRI event rates (Hopman and Alexander 2006).

7 In steady state, on average each star that drifts outward by an amount J will be compensated by another that drifts inward by the same amount. This balance only breaks down for those orbits that fall on to the hole, since there are obviously no stars coming out of it to keep detailed balancing.

This is indeed the case in both regimes of mass segregation. Furthermore, Hopman & Alexander (2005) have shown that the probability for a successful inspiral as a function of orbital semimajor axis (or energy) is almost a step function of semimajor axis. If $a < a_{\rm GW}$, it is almost certain that the stellar bh will become an EMRI; it will almost certainly not become one in case the inequality sign is reversed (and the width of the "transition region" is very small). This crucial threshold quantity demarcates the orbits which are close enough to the MBH to sucessfully decouple from the rest of the cluster and undergo the slow, adiabatic inspiral that defines an EMRI from those more weakly bound orbits that will be perturbed out of the EMRI tracks due to scattering with other stars.

Therefore, in order to estimate the EMRI event rate, given a steady state $f(E)$, obtained via the FP equation, one essentially counts the number of stars that populate the region of phase space for which the inspiralling criterion above is satisfied and divide it by the local relaxation time. Note that here, for simplicity, we ignore other driving mechanisms—in particular, we ignore resonant relaxation. Under these assumptions, the EMRI rate for stellar bhs is approximately given by

$$\Gamma_{\rm EMRI} = f_\bullet \int_{E_{\rm GW}}^{+\infty} dE \, \frac{n(E)}{\ln(J_c(E)/J_{\rm lc}) \; T_{\rm rlx}(E)}, \tag{93}$$

where $f_\bullet$ is the number fraction of SBHs in the stellar population, $n(E)$ is the total number of stars per unit energy($n(E) \propto f(E)$, see Preto (2010)), $J_c(E) = \sqrt{GM_\bullet/2E}$ is the specific angular momentum of a circular orbit of energy E, $J_{\rm lc} = 4\,GM_\bullet/c$ is the loss-cone angular momentum and $T_{\rm rlx} = 0.34\ \sigma^3/[G^2(m_\bullet\rho_\bullet + m_*\rho_*)\ln\Lambda]$ is the relaxation time. The log term in the denominator in (93) arises from the phase space (partial) depletion resulting from the presence of the loss cone. The conversion between r and E is, for $r \ll r_h$, $\langle E(r)\rangle = GM_\bullet/2r$ or $E = GM_\bullet/2a$. The critical radius $a_{\rm GW}$, or energy $E_{\rm GW}$, for EMRIs is approximately $a_{\rm GW} = 0.01 r_h$; and, to first order, $a_{\rm GW}$ is independent of $M_\bullet$ (Hopman & Alexander 2005).

9.4.2 *The relevance of realistic models of mass segregation for the rates*

The weak regime of SMS, and corresponding BW solution, would lead to a fairly high intrinsic rate, per galaxy, of EMRIs. In fact, Figure 3 shows that, for a Milky Way nucleus, in case $\Delta > 1$, the intrinsic EMRI rate is $\gtrsim 10^3$ per Gyr. This is, however, unrealistic as such scenario pressuposes an unrealistically high number fraction of bhs ($f_\bullet \gtrsim 0.0325$ for $\Delta > 1$). In the more realistic case, when $\Delta \sim 0.03$ the BW solution would entail a strong supression of the EMRI rate to—at best—a few tens of events per Gyr. This is where SMS solution appears to rescue us. SMS implies a higher density of bhs inside r_h as compared with the $\gamma = 7/4$ solution, and in this way—by decreasing the local T_{rlx} and increasing $n(E)$ close to the MBH—it partially, but not completely, compensates for the small number fraction of bhs entailed by realistic mass functions.

In order to quantitatively evaluate the boost $\Gamma_{\rm SMS}/\Gamma_{\rm BW}$ to the EMRI rates from SMS, for a given Δ and a fixed mass normalization at r_h, one needs to estimate what would

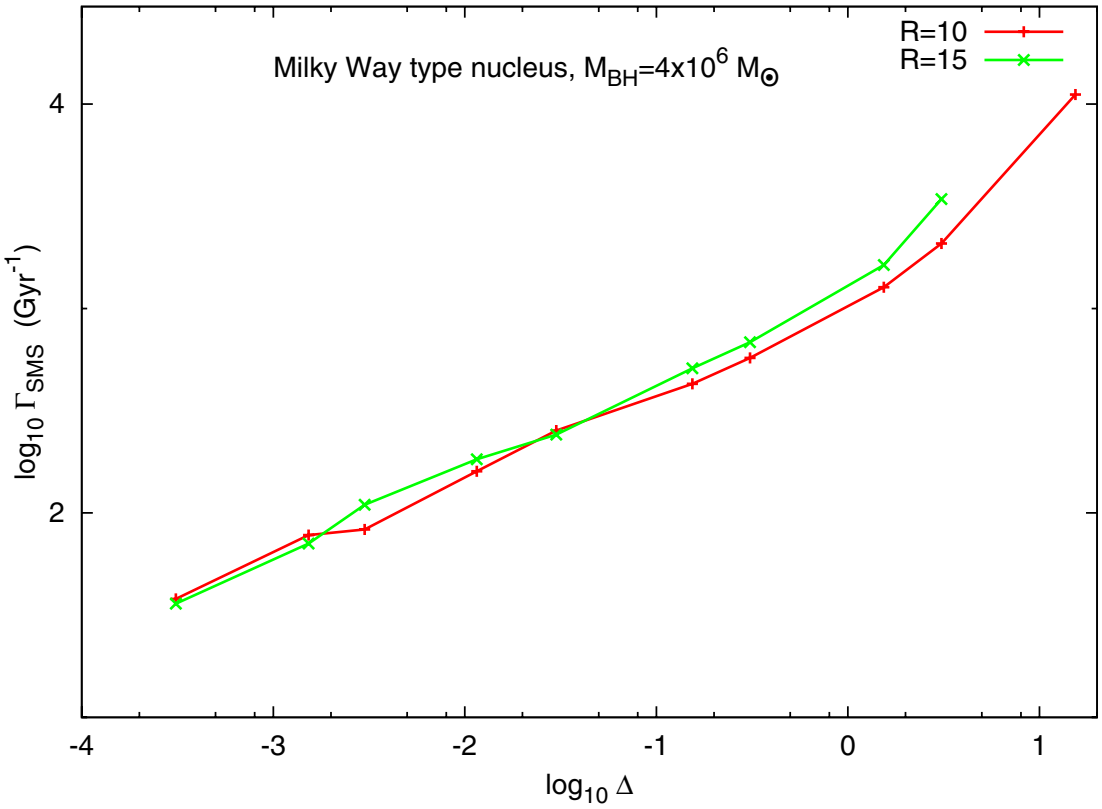

Figure 27: EMRI rate as a function of Δ. The number of stellar bh EMRI events per Gyr in a Milky Way type nucleus ($M_\bullet = 4 \times 10^6 M_\odot$ and $M_*(< 1\mathrm{pc}) = 10^6 \mathrm{M}_\odot$) as a function of the parameter Δ. This is computed from a two-component mass segregated stellar cusp ($\gamma_H \approx 2.1$ and $\gamma_L \approx 1.5$) with mass ratios $R = 10$ and 15 obtained from FP calculations. In the case of the fiducial value $f_\bullet = 10^{-3}$, $\Delta \approx 0.03$; in those circumstances, each Milky Way like nucleus will produce on average ~ 250 stellar bh EMRIs per Gyr.

be the rate if the spatial and phase space densities were determined by the $\gamma = 7/4$ cusp for $r \lesssim 0.1 r_h$. This is done as follows: we define analytically both $\rho(r)$ and $f(E)$ that would result from a $\gamma = 7/4$ inside $0.1 r_h$

$$\begin{aligned} \rho(r) &= \rho_{FP}(r), \qquad r > r_L \\ \rho(r) &= \rho_{FP}(r_L) \times \left(\frac{r_L}{r}\right)^{7/4}, \quad r \leq r_L, \end{aligned} \tag{94}$$

and

$$\begin{aligned} f(E) &= f_{FP}(E), \qquad E < E_L \\ f(E) &= f_{FP}(E_L) \times \left(\frac{E}{E_L}\right)^{1/4}, \quad E \geq E_L, \end{aligned} \tag{95}$$

where the indices FP mean that the profile is taken from the Fokker-Planck calculation. r_L (and E_L) is a reference radius (energy) chosen according to $r_L \sim 0.1 r_h$.

Figure 4 shows the boost to the EMRI rates due to SMS relative to what would be obtained from a BW profile. Going from an unrealistically high $f_\bullet$, as adopted by BW77 (say $\Delta = 3$), to a more realistic $f_\bullet$ (say $\Delta = 0.03$), while neglecting the existence of SMS, one supresses the EMRI rate by factors of $\sim 100 - 150$ (the former would lead to $\sim$ few $\times 10^3$ EMRIs per Gyr; the latter is reduced to $\sim$ few tens per Gyr). However, by taking into account the SMS solution, for this low $\Delta = 0.03$, we boost again the rates by a factor close to 10, thus partially compensating the reduction of EMRIs (from few tens to a few hundred per Gyr; in fact, there are ~ 250 per Gyr in case $\Delta = 0.03$ for a Milky Way nucleus). We conclude that the apparently inocuous and tiny change of the logarithmic slope from $\gamma_H = 7/4$ to $\gamma_H \sim 2$ can have a substantial effect (a factor of ~ 10) on the expected EMRI rate.

Figure 5 shows the dependence of the intrinsic EMRI rate on the mass of the central MBH, where the validity of the $M_\bullet - \sigma$ relation was assumed (Ferrarese & Ford 2005). We see that the EMRI rate for stellar bhs scales as $\propto M_\bullet^{-0.19}$, independently of R and $f_\bullet$. Its absolute normalization depends obviously on the number fraction $f_\bullet$ of sbhs, in agreement with Figures 3 and 4.

One can make a rough conversion of the estimated intrinsic rate into LISA detection rates. Following Gair (2009), who made a number of assumptions regarding the local density of MBHs and its spin distribution, plus on the LISA detection capabilities, we find that according to its equation (7), LISA will see around $\sim 10^2 - 7 \times 10^2$ EMRI events during a 2-year or 5-year mission, respectively. Note that these rates may change by factors of $\sim 2 - 3$ as a function of corrections to the local MBH mass density (Graham and Driver 2007); moreover, the uncertainties regarding the efficiency of RR and other channels may still affect the rate predictions by one or two orders of magnitude. A lot of work still remains to be done; nevertheless, the consequences regarding the SMS regime are significant and under control.

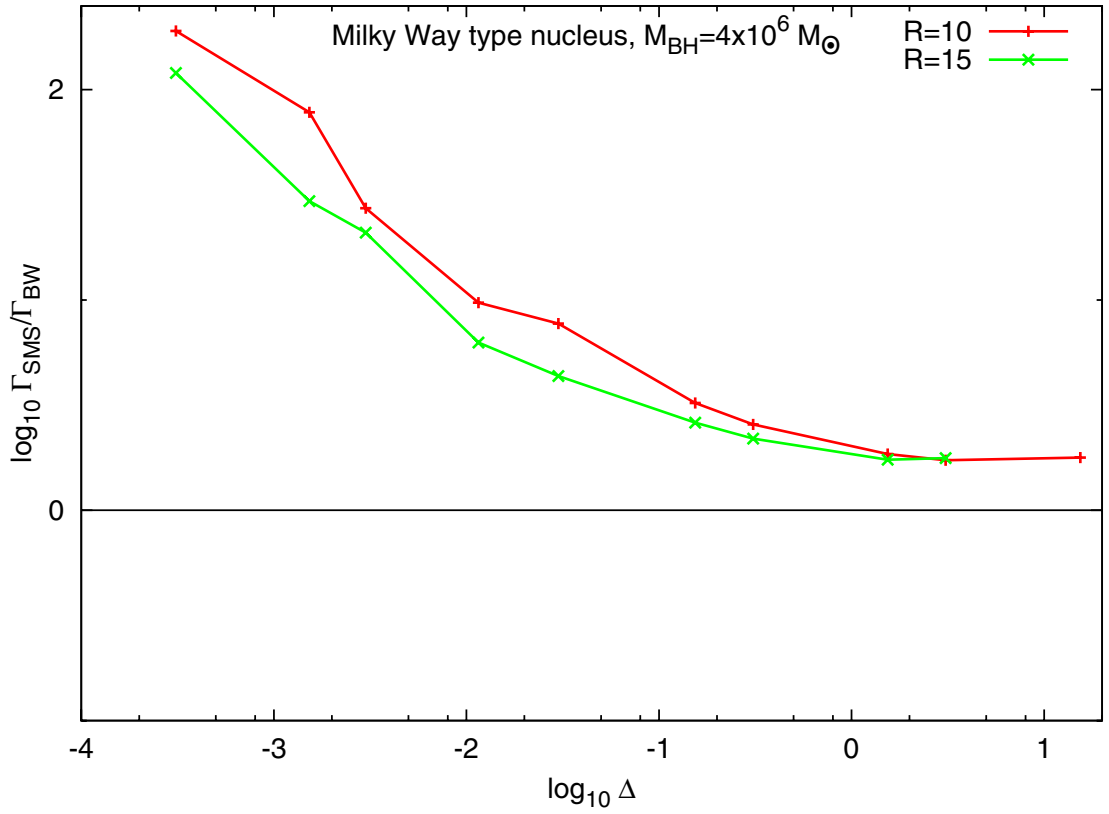

Figure 28: Boost on the EMRI rates from strong segregation. One can see that, for values of $\Delta < 1$, there is a significant boost to the EMRI rates in comparison to which it would result in the case of a $\gamma = 7/4$ BW cusp. In particular, for our fiducial value $\Delta \sim 0.03$ ($f_\bullet \sim 10^{-3}$), the boost is of order of a factor 10 with respect to a 7/4-BW cusp with the same mass normalization at $r = 1$ pc.

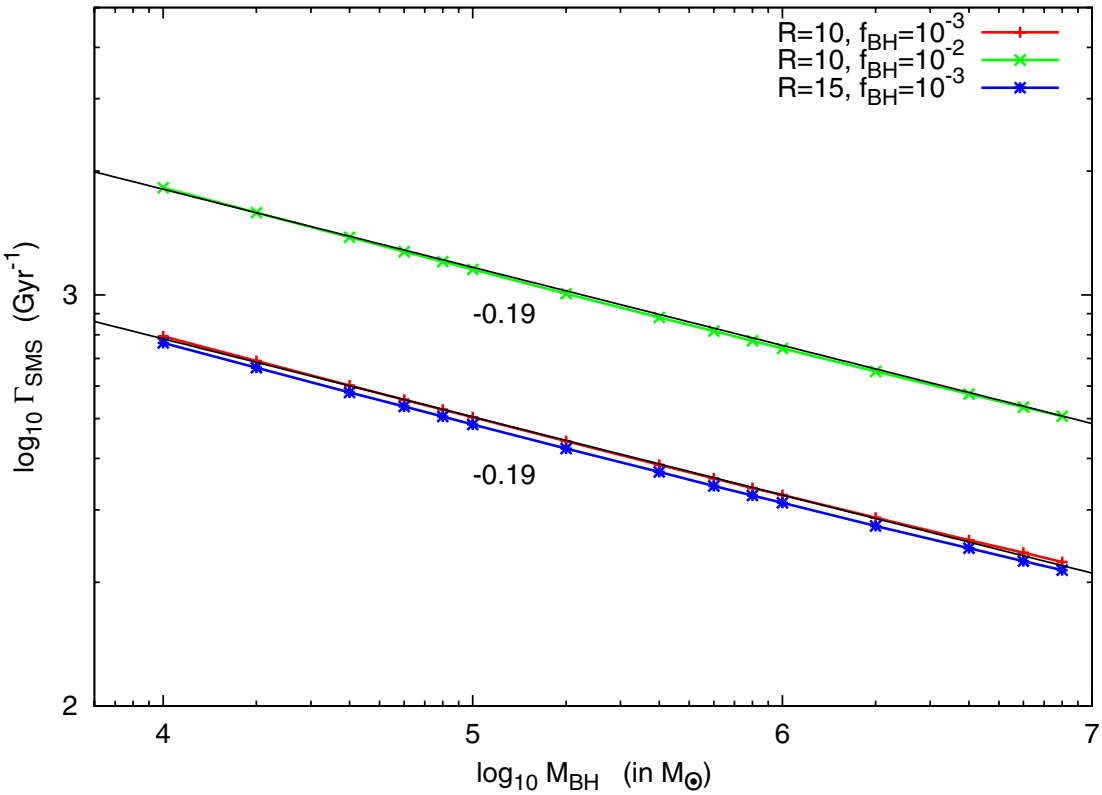

Figure 29: EMRI rates as a function of MBH mass in strongly segregated nuclei. The EMRI rate depends on the MBH mass, $\Gamma_{SMS} \propto M_\bullet^{-0.19}$. Shown are curves for $\Delta = 0.03$ ($f_\bullet = 10^{-3}$ and 10^{-2}) and three different mass ratios between heavy and light stars, $R = 10$ and 15.

9.5 CONCLUSIONS

We have considered simplified stellar models of galactic nuclei, with only two mass components, which harbor MBHs that fall into the LISA detection bandwidth. For quite generic initial conditions, such stellar clusters are expected to have reached a relaxed, mass segregated, steady state which is independent of initial conditions at the time of formation. Strong (realistic) mass segregation is a robust outcome from the growth and evolution of stellar cusps around MBHs in the mass range $10^4 - 10^7 M_\odot$ to which LISA will be sensitive. Our N-body results validate the Fokker-Planck description of the *bulk* properties of the stellar distribution. SMS boosts the EMRI event rates with respect to what would be implied by a shallower stellar density profile (*e.g.* $\gamma = 7/4$, which has been the working assumption of almost all event rate estimates in the literature so far) that also respect the mass normalization obtained from observations of the Galactic center at 1 pc from the hole. In particular, our fiducial models of the Galactic center are enhanced by a factor of ~ 10—leading to a predicted value of ~ 250 stellar bh EMRIs per Gyr. The FP formalism assumes two-body relaxation as the only dynamical driver present—this could be a severe restriction at radii $\lesssim 0.01 r_h$, inside which even the NB simulations with higher N in our sample start to run out of particles and where RR could play an important role (Hopman and Alexander 2006; Madigan et al. 2010). Other crucial mechanisms are resonant relaxation, (small) triaxiality of the galactic potential, tidal separation of binaries and massive perturbers (see e.g. Amaro-Seoane et al. 2007, for a review). These are the subject of our current research work, and the extent to which they can significantly affect the EMRI rates is still an open question.

BIBLIOGRAPHY

Alexander T and Hopman C 2003 *ApJ Lett.* **590**, 29–32.

Alexander T and Hopman C 2009 *ApJ* **697**, 1861–1869.

Amaro-Seoane P, Gair J R, Freitag M, Miller M C, Mandel I, Cutler C J and Babak S 2007 *Classical and Quantum Gravity* **24**, 113–+.

Babak S, Baker J G, Benacquista M J, Cornish N J, Larson S L, Mandel I, McWilliams S T, Petiteau A, Porter E K, Robinson E L, Vallisneri M, Vecchio A, Data Challenge Task Force t M L, Adams M, Arnaud K A, Błaut A, Bridges M, Cohen M, Cutler C, Feroz F, Gair J R, Graff P, Hobson M, Shapiro Key J, Królak A, Lasenby A, Prix R, Shang Y, Trias M, Veitch J, Whelan J T and participants 2010 *Classical and Quantum Gravity* **27**(8), 084009–+.

Bahcall J and Wolf R 1976 *ApJ* **209**, 214–232.

Bahcall J and Wolf R 1977 *ApJ* **216**, 883–907 (BW77).

Barack L and Cutler C. 2004 *Phys Rev D* **69**, 082005.

Bartko, H.; Martins, F.; Trippe, S.; Fritz, T. K.; Genzel, R.; Ott, T.; Eisenhauer, F.; Gillessen, S.; Paumard, T.; Alexander, T.; Dodds-Eden, K.; Gerhard, O.; Levin, Y.; Mascetti, L.; Nayakshin, S.; Perets, H. B.; Perrin, G.; Pfuhl, O.; Reid, M. J.; Rouan, D.; Zilka, M.; Sternberg, A. 2010 *ApJ* **708**, 34–840

Baumgardt H, Makino J and Ebisuzaki T 2004 *ApJ* **613**, 1133–1142.

Baumgardt H, Gualandris A and Portegies Zwart S T 2006 *MNRAS* **372**, 174–182.

Binney, J. andTremaine, S. Galactic Dynamics (Princeton, US: Princeton University Press, 2008.)

Buchholz R., Schödel, R. and Eckart, A. 2009 *A&A*, **499**, 483

Di Matteo, T., Colberg, J., Springel, V., Hernquist, L. andSijacki, D. 2008 *ApJ* **676**, 33.

Do, T., Ghez, A. M., Morris, M. R., Lu, J. R., Matthews, Keith andYelda, S., andLarkin 2009 *ApJ* **703**, 1323.

Eisenhauer F, Genzel R, Alexander T, Abuter R, Paumard T, Ott T, Gilbert A, Gillessen S, Horrobin M, Trippe S, Bonnet H, Dumas C, Hubin N, Kaufer A, Kissler-Patig M, Monnet G, Ströbele S, Szeifert T, Eckart A, Schödel R and Zucker S 2005 *ApJ* **628**, 246–259.

Ferrarese, L. & Ford, H. 2005, *Space Sci. Rev.*, **116**, 523

Freitag M 2003 *ApJ Lett.* **583**, 21–24.

Gair J 2009 *Classical and Quantum Gravity* **26**, 094034.

Ghez A M, Salim S, Hornstein S D, Tanner A, Lu J R, Morris M, Becklin E E and Duchêne G 2005 *ApJ* **620**, 744–757.

Ghez A M, Salim S, Weinberg N N, Lu J R, Do T, Dunn J K, Matthews K, Morris M R, Yelda S, Becklin E E, Kremenek T, Milosavljevic M and Naiman J 2008 *ApJ* **689**, 1044–1062.

Gillessen S, Eisenhauer F, Trippe S, Alexander T, Genzel R, Martins F and Ott T 2009 *ApJ* **692**, 1075–1109.

Glebbeek, E.; Gaburov, E.; de Mink, S. E.; Pols, O. R.; Portegies Zwart, S. F. 2009 *A&A* **497**, 255–264

Graham A.W. and Driver S.P. 2007 *MNRAS* **380**, L15–L19.

Gurevich A. 1964, *Geomag. Aeronom.*, **4**, 247

Hopman C and Alexander T 2005 *ApJ* **629**, 362–372.

Hopman C and Alexander T 2006 *ApJ* **645**, 1152–1163.

Hopman C and Alexander T 2006 *ApJL* **645**, 133–136.

Hopman C and Freitag M and Larson S L 2007 *MNRAS* **378**, 129-136.

Hopman C and Madigan A.-M. 2011, The Galactic Center: a Window to the Nuclear Environment of Disk Galaxies, 439, 180

Khalisi E, Amaro-Seoane P and Spurzem R 2007 *MNRAS* **374**, 703-720.

Kroupa P 2001 *MNRAS* **322**, 231–246.

Lightman A and Shapiro S 1977 *ApJ* **211**, 244–262.

Madigan A.-M., Hopman, C. and Levin Y. 2011, *ApJ* **738**, 99

Merritt D 2010 *ApJ* **718**, 739–761.

Preto M 2010 *GW Notes* **3**, 3–27.

Preto M, Merritt D and Spurzem R 2004 *ApJL* **613**, 109–113.

Preto M and Amaro-Seoane P 2010 *ApJL* **708**, 42–46.

Preto M and Amaro-Seoane P 2011, to be submitted to *ApJ*

Portegies Zwart, Simon F.; Baumgardt, Holger; McMillan, Stephen L. W.; Makino, Junichiro; Hut, Piet; Ebisuzaki, Toshi 2006 *ApJ* **641**, 319–326

Rauch K and Tremaine S 1996 *New Astronomy* **1**, 149–170.

Reid M J and Brunthaler A 2004, *ApJ*, **616**, 872–884

Schödel R, Merritt D andEckart A 2009, *A&A*, **502**, 91

Shen, Juntai; Rich, R. Michael; Kormendy, John; Howard, Christian D.; De Propris, Roberto; Kunder, Andrea 2010 *ApJL*,**720**, L72-L76

Sigurdsson S and Rees M J 1997 *MNRAS* **284**, 318–326.

Spitzer L 1987 *Dynamical evolution of globular clusters* Princeton, NJ, Princeton University Press, 1987, 191 p.

Volonteri, M. 2010, *A&A Rev* , **18**, 279

10

THE ROLE OF THE SUPERMASSIVE BLACK HOLE SPIN IN THE ESTIMATION OF THE EMRI EVENT RATE

Pau Amaro-Seoane[1], *Carlos F. Sopuerta*[2], *& Marc Dewi Freitag*[3]

Published in *Monthly Notices of the Royal Astronomical Society*, Volume 429, Issue 4, p.3155-3165 (2013).

Abstract: One of the main channels of interactions in galactic nuclei between stars and the central massive black hole (MBH) is the gradual inspiral of compact remnants into the MBH due to the emission of gravitational radiation. This process is known as an "Extreme Mass Ratio Inspiral" (EMRI). Previous works about the estimation of how many events space observatories such as LISA will be able to observe during its operational time differ in orders of magnitude, due to the complexity of the problem. Nevertheless, a common result to all investigations is that the possibility that a compact object merges with the MBH after only one intense burst of GWs is much more likely than a slow adiabatic inspiral, an EMRI. The later is referred to as a "plunge" because the compact object dives into the MBH, crosses the horizon and is lost as a probe of strong gravity for eLISA. The event rates for plunges are orders of magnitude larger than slow inspirals. On the other hand, nature MBH's are most likely Kerr and the magnitude of the spin has been sized up to be high. We calculate the number of periapsis passages that a compact object set on to an extremely radial orbit goes through before being actually swallowed by the Kerr MBH and we then translate it into an event rate for a LISA-like observatory, such as the proposed ESA mission eLISA/NGO. We prove that a "plunging" compact object is conceptually indistinguishable from an adiabatic, slow inspiral; plunges spend on average up to hundred of thousands of cycles in the bandwidth of the detector for a two years mission. This has an important impact on the event rate, enhancing in some cases significantly, depending on the spin of the MBH and the inclination: If the orbit of the EMRI is prograde, the effective size of the MBH becomes smaller the larger the spin is, whilst if retrograde, it becomes bigger. However, this situation is not symmetric, resulting in an effective enhancement of the rates. The effect of vectorial resonant relaxation on the sense of the orbit does not affect the enhancement. Moreover, it has been recently proved that the production of low-eccentricity EMRIs is severely blocked by the presence of a blockade in the rate at which orbital angular momenta change takes place. This is the result of relativistic precession on to the stellar potential torques and hence affects EMRIs originating via resonant relaxation at distances of about $\sim 10^{-2}$ pc from the MBH. Since high-eccentricity EMRIs

1 Max Planck Institut für Gravitationsphysik (Albert-Einstein-Institut), D-14476 Potsdam, Germany
2 Institut de Ciències de l'Espai (CSIC-IEEC), Campus UAB, Bellaterra, Spain
3 Institute of Astronomy, Madingley Road, Cambridge, CB3 0HA, UK

are a result of two-body relaxation, they are not affected by this phenomenon. Therefore we predict that eLISA EMRI event rates will be dominated by high-eccentricity binaries, as we present here.

10.1 MOTIVATION

We know, mostly through high-resolution observations of the kinematics of stars and gas, that most, if not all, nearby bright galaxies harbour a dark, massive, compact object at their centres. (Ferrarese & Ford 2005; Kormendy 2004). The most spectacular case is our own galaxy, the Milky Way. By tracking and interpreting the stellar dynamics at the centre of our galaxy, we have the most well-established evidence for the existence of a massive black hole (MBH) (Ghez et al. 2008; Eisenhauer et al. 2005; Ghez et al. 2005; Gillessen et al. 2009). Observations of other galaxies indicate that the masses of MBH can reach a few billion solar masses ($M_\odot$). The existence of such a MBH population in the present-day universe is strongly supported by Sołtan's argument that the average mass density of these MBHs agrees with expectations from integrated luminosity of quasars (Sołtan 1982; Yu & Tremaine 2002). Many correlations linking the MBH's mass and overall properties of its host spheroid (bulge or elliptical galaxy) have been discovered. The tightest are with the spheroid mass (Häring & Rix 2004), its velocity dispersion ($M-\sigma$ relation, Tremaine et al. 2002) and degree of concentration (Erwin et al. 2004). Consequently, understanding the origin and evolution of these MBHs necessitates their study in the context of their surrounding stellar systems.

The ideal probe of these regions is the gravitational radiation (GWs) that is emitted by some compact stars very close to the black holes, and which will be surveyed by eLISA/NGO (evolved Laser Interferometer Space Antenna / New Gravitational Wave Observatory Amaro-Seoane et al. 2012; Amaro-Seoane et al. 2012b). This mission will scrutinise the range of masses fundamental to the understanding of the origin and growth of supermassive black holes; i.e. MBHs with masses below $10^7\,M_\odot$.

10.2 EMRIS AND DIRECT PLUNGES

For a binary of a MBH and a stellar black hole to be in a LISA-like band, it has to have a frequency of between roughly 1 and 10^{-5} Hz. The emission of GWs is more efficient as they approach the LSO, so that the observatory will detect the sources when they are close to the LSO line. The total mass required to observe systems with frequencies between 0.1 Hz and 10^{-4} Hz is of $10^4-10^7\,M_\odot$. For masses larger than $10^7\,M_\odot$ the frequencies close to the LSO will be too low, so that their detection will be very difficult. On the other hand, for a total mass of less than $10^3\,M_\odot$ we could in principal detect them at an early stage, but then the amplitude of the GW would be rather low.

To interact closely with the central MBH, stars have to find themselves on "loss-cone" orbits, which are orbits elongated enough to have a very close-in periapsis (Amaro-Seoane & Spurzem 2001; Frank & Rees 1976; Lightman & Shapiro 1977). The rate of

tidal disruptions can be established semi-/analytically if the phase space distribution of stars around the MBH is known (Magorrian & Tremaine 1999; Syer & Ulmer 1999; Wang & Merritt 2004, for estimates in models of observed nearby nuclei). To account for the complex influence of mass segregation, collisions and the evolution of the nucleus over billions of years, detailed numerical simulations are required, however (Amaro-Seoane 2004; Amaro-Seoane & Preto 2011; Freitag et al. 2006; Baumgardt et al. 2004; David et al. 1987a,b; Preto & Amaro-Seoane 2010; Freitag & Benz 2002; Khalisi et al. 2007; Murphy et al. 1991).

As the star spirals down towards the MBH, it has many opportunities to be deflected back by two-body encounters onto a "safer orbit" (Alexander & Hopman 2003; Amaro-Seoane et al. 2007), hence even the definition of a loss cone is not straightforward. Once again, the problem is compounded by the effects of mass segregation and resonant relaxation, to mention two main complications. As a result, considerable uncertainties are attached to the (semi-)analytical predictions of capture rates and orbital parameters of EMRIs.

Naively one could assume that the inspiral time is dominated by GW emission and that if this is shorter than a Hubble time, the compact object will become an EMRI. This is wrong, because one has to take into account the relaxation of the stellar system. Whilst it certainly can increase the eccentricity of the compact object, it can also perturb the orbit and circularise it, so that the required time to inspiral in, $t_{\rm GW}$, becomes larger than a Hubble time. The condition for the small compact object to be an EMRI is that it is on an orbit for which $t_{\rm GW} \ll (1-e)\, t_{\rm r}$ (Amaro-Seoane et al. 2007), with $t_{\rm r}$ the *local* relaxation time. When the binary has a semi-major axis for which the condition is not fulfilled, the small compact object will have to be already on a so-called "plunging orbit", with $e \geq e_{\rm plunge} \equiv 1 - 4\, R_{\rm Schw}/a$, where $R_{\rm Schw}$ is the Schwarzschild radius of the MBH, i.e. $R_{\rm Schw} = 2GM_\bullet/c^2$, with $M_\bullet$ being the MBH mass. It has been claimed a number of times by different authors that this would result in a too short burst of gravitational radiation which could only be detected if it was originated in our own Galactic Center (Hopman et al. 2007), because one needs a coherent integration of some few thousands repeated passages through the periapsis in the eLISA bandwidth.

Therefore, such "plunging" objects would then be lost for the GW signal, since they would be plunging "directly" through the horizon of the MBH and only a final burst of GWs would be emitted, and such burst would be (i) very difficult to recover, since the very short signal would be buried in a sea of instrumental and confusion noise and (ii) the information contained in the signal would be practically nil. There has been some work on the detectability of such bursts (Berry & Gair 2012; Hopman et al. 2007; Rubbo et al. 2006; Yunes et al. 2008), but they would only be detectable in our galaxy or in the close neighborhood, but the event rates are rather low, even in the most optimistic scenarios.

The typical size of the central MBH can be associated with the gravitational radius (radial horizon location) of the MBH, which in the case of the Milky Way MBH corresponds to approximately $R_{\rm Schw} \sim 1.3 \times 10^7$ km $\approx 4.1 \times 10^{-7}$ pc (neglecting spin contributions). This number gives a good indication of how small are these MBHs in

size, which means they have a small cross section and hence, the chances a star has to "plunge" through the horizon of the MBH directly are very small.

To quantify the probability for star absorption by a MBH it is crucial to take into account the location of the Last Stable Orbit (LSO) of a test massive body in terms of the MBH parameters. According to General Relativity, these are the mass $M_\bullet$ and its intrinsic angular momentum or spin $S_\bullet = a_\bullet M_\bullet c$, where $a_\bullet$ is the spin parameter with length dimension and subject to the constraints $0 \leq a_\bullet c^2/(GM_\bullet) \leq 1$. The LSO location is given by a surface in the orbital configuration space that can be described in terms of the parameters (p, e, ι), where p is the dimensionless semilatus rectum, e is the eccentricity, and ι is the orbital inclination (with respect to the MBH spin axis) of the orbit. Equivalently one can also use the semimajor axis a, or the periapsis location $r_{\rm peri}$, instead of p. The periapsis and apoapsis radii are given then by:

$$r_{\rm peri} = \frac{GM_\bullet\, p}{c^2(1+e)}\,,$$
$$r_{\rm apo} = \frac{GM_\bullet\, p}{c^2(1-e)}\,. \tag{96}$$

It is well-known (see e.g. Bardeen 1970) that the LSO, for the case of circular orbits, lies at $3\,R_{\rm Schw}$ for non-spinning MBHs, while it is shifted out to $9GM_\bullet/c^2$ for retrograde orbits and down to $GM_\bullet/c^2$ for prograde orbits, and these values correspond to the case of "extremal" MBHs, characterized by maximal spins, i.e. $a_\bullet c^2/(GM_\bullet) = 1$. Despite this fact, traditional EMRI event rate estimations are based on considerations that neglect the spin of the MBH. Taking into account the spin one would expect (considering the asymmetry between prograde and retrograde orbits) an *increase* of the number of EMRIs since some of the traditionally neglected "direct plunges" can actually be disguised EMRIs.

10.3 ORBITAL GEODESIC MOTION AROUND A KERR MBH

In order to show the importance of the effect of the spin in the estimation of the number of EMRIs that will produce a significant amount of GW cycles in the band of eLISA, we present here two types of calculations. The first one is to adapt known results about the stability of orbits of massive objects around a MBH to our discussion. The second is an estimation of the number of cycles for for orbits which would be plunging orbits for a Schwarzschild MBH, or orbits with no sufficient cycles when the MBH was assumed to be non-spinning for the case with spin. We show that a significant fraction of them are actually EMRIs with sufficient cycles to be detected by a space-based observatory like eLISA. Parts of these calculations, mainly due to the high eccentricities involved, require numerical computations.

At this point it is useful to review some basic characteristics of the orbital geodesic motion of massive bodies around a Kerr MBH. First of all, the geometry of a Kerr MBH is axisymmetric (with respect to the spin axis) instead of spherically-symmetric

as in the case of Schwarzschild MBHs, and this means that the inclination of the orbit with respect to the spin axis, ι, plays an important role in the dynamics. Actually, orbits outside the equatorial plane are not planar, like in Keplerian motion or orbits around a Schwarzschild MBH, but instead they would precess around a plane with a certain inclination ι with a frequency that we call f_θ, where θ refers to the polar Boyer-Lindquist coordinate of the MBH (Boyer & Lindquist 1967; Misner et al. 1973). In addition, relativistic effects cause precession of the periapsis, and this already happens for Schwarzschild MBHs, so that we have to consider two more frequencies, f_r and f_φ. The first one, f_r, is associated with the radial motion and the time to go from periapsis, $r_{\rm peri}$, to apoapsis, $r_{\rm apo}$, and back. The second one, f_φ, is associated with the azimuthal motion around the spin axis and the time to complete a full turn ($2\,\pi$) around this axis, or in other words, the time for the azimuthal angle φ to increase 2π radians.

In summary, generic bound motion around a Kerr MBH exhibits three fundamental frequencies, $(f_r,\, f_\theta,\, f_\varphi)$ and this implies that the GW emission of an EMRI will be quite rich in structure (not only these GWs will contain features with these frequencies but also with a number of harmonics of them), encoding the detailed geometry of the central Kerr MBH. The GW emission will back react on to the system and this translates in particular in a change of the orbital parameters $(p,\, e,\, \iota)$ of the orbit. These changes can be estimated by considering the energy and angular momentum carried away from the extreme-mass-ratio binary by the GWs emitted. More specifically, the GW emission changes the constants of motion of the geodesic motion, namely the energy per unit mass (normalized with respect to the star mass, m), E, the angular momentum along the spin axis per unit mass, L_z, and the so-called Carter constant per unit mass square, C, which is associated with an extra symmetry of the Kerr geometry, similar to what happens in certain axisymmetric Newtonian potentials (Binney & Tremaine 1987). Actually, the set of constants (E, L_z, C) parametrizes the geodesic orbit in the same way as the set of orbital parameters (p, e, ι) does. Therefore, there is a mapping between these two sets (see Schmidt 2002) which is going to be crucial in the calculations that we present here. The explicit form of this mapping is quite complex and we do not include it here, we just mention that we used the implementation described in Sopuerta & Yunes (2011).

In the case of a non-spinning Schwarzschild MBH, where ι and C do not play any role, the mapping is much more simple and is given by:

$$\frac{E^2}{c^2} = \frac{(p-2-2e)(p-2+2e)}{p\,(p-3-e^2)}\,, \tag{97}$$

$$L_z^2 = \frac{G^2 M_\bullet^2\, p^2}{c^2 (p-3-e^2)}\,. \tag{98}$$

Using the symmetries of the geometry of a Kerr MBH we can separate the equations for geodesic orbital motion so that the trajectory of a massive body, described in terms of Boyer-Lindquist coordinates $\{t, r, \theta, \varphi\}$, can be written as follows

$$\rho^2 \frac{dt}{d\tau} = \frac{1}{\Delta}\left(\Sigma^2 \frac{E}{c} - 2a_\bullet r_\bullet \frac{L_z}{c} r\right) \tag{99}$$

$$\rho^4 \left(\frac{dr}{d\tau}\right)^2 = \left[\left(r^2 + a_\bullet^2\right)\frac{E}{c} - a_\bullet \frac{L_z}{c}\right]^2 - \left(\frac{Q}{c^2} + r^2\right)\Delta \equiv R(r) \tag{100}$$

$$\rho^4 \left(\frac{d\theta}{d\tau}\right)^2 = \frac{C}{c^2} - \frac{L_z^2}{c^2}\cot^2\theta - a_\bullet^2\left(1 - \frac{E^2}{c^2}\right)\cos^2\theta \tag{101}$$

$$\rho^2 \frac{d\varphi}{d\tau} = \frac{1}{\Delta}\left[2a_\bullet r_\bullet \frac{E}{c} r + \frac{L_z}{c}\frac{\Delta - a_\bullet^2 \sin^2\theta}{\sin^2\theta}\right]. \tag{102}$$

In the last set of equations we have introduced the following definitions:

$$\begin{aligned} r_\bullet &\equiv \frac{GM_\bullet}{c^2}, \\ Q &\equiv C + (L_z - a_\bullet E)^2, \\ \rho^2 &\equiv r^2 + a_\bullet^2 \cos^2\theta \\ \Delta &\equiv r^2 - 2r_\bullet r + a_\bullet^2 = r^2 f + a_\bullet^2, \text{ with } f \equiv 1 - \frac{2r_\bullet}{r}. \end{aligned} \tag{103}$$

For convenience, we also define the quantity $\Sigma^2 \equiv (r^2 + a_\bullet^2)^2 - a_\bullet^2 \Delta \sin^2\theta$. The first equation tells us how the coordinate time t changes with respect to the proper time τ and the other three describe the trajectory in space. One can combine the four equations to obtain the spatial trajectory in terms of coordinate time t, the time of observers at infinity, i.e. $(r(t), \theta(t), \varphi(t))$.

10.4 KERR AND SCHWARZSCHILD SEPARATRICES

In figures 30 and 31 we show plots of the location of the LSO in the plane a (pc) - $(1 - e)$, including the Schwarzschild separatrix between stable and unstable orbits, $p - 6 - 2e = 0$[1], for both prograde and retrograde orbits and for different values of the inclination ι. Each plot corresponds to a different value of the spin, showing how increasing the spin makes a difference in shifting the location of the separatrix between stable and unstable orbits, pushing prograde orbits near $GM_\bullet/c^2$ while retrograde orbits are pushed out towards $9GM_\bullet/c^2$. The procedure we have used to build these plots is a standard one. Briefly, given a value of the dimensionless spin parameter $s \equiv a_\bullet c^2/(GM_\bullet)$ and a value of the eccentricity e and inclination angle ι we apply the following algorithm:

1 The relation between p and a is $a = (GM_\bullet/c^2)(p/(1 - e^2))$.

1. We start from an initial value of the semilatus rectum p which, together with the value of the eccentricity fixes the apoapsis and periapsis radii through the equations in (96). On the other hand, the inclination of the orbital plane can also be described in terms of the polar angle θ, so that $\theta_{\rm inc}$ represents the inclination angle and is closely related to ι (see e.g., Drasco & Hughes 2004). The advantage of using $\theta_{\rm inc}$ is that it is related in a simple way to the extrema of θ, $\theta_{\rm min}$ satisfying –see equation (101)

$$\left(\frac{d\theta}{d\tau}\right)_{\theta=\theta_{\rm min}} = 0\,, \tag{104}$$

by $\theta_{\rm inc} = {\rm sign}(L_z)\left(\frac{\pi}{2} - \theta_{\rm min}\right)$, with

$${\rm sign}(L_z) = \begin{cases} +1 & \text{for prograde orbits}\,, \\ -1 & \text{for retrograde orbits}\,. \end{cases} \tag{105}$$

Then, from the condition of extrema of $\theta_{\rm min}$ and its relation to $\theta_{\rm inc}$, we can find the value of the Carter constant C in terms of the energy E and angular momentum along the spin axis L_z.

2. From the conditions of extrema of periapsis and apoapsis,

$$\left(\frac{dr}{d\tau}\right)_{r=r_{\rm peri}} = \left(\frac{dr}{d\tau}\right)_{r=r_{\rm apo}} = 0, \tag{106}$$

[see equation (100)], and using the expression of C in terms of (E, L_z) from the previous point, we find the values of (E, L_z) (and hence of C too).

3. The radial motion for geodesic orbits around Kerr has four extrema, the periapsis and apoapsis locations and two more radii, r_3 and r_4, such that

$$r_{\rm apo} \geq r_{\rm peri} \geq r_3 > r_4. \tag{107}$$

Actually, r_4 always lies inside the horizon radius,

$$r_{\rm H} = \left(\frac{GM_\bullet}{c^2}\right)\left(1 + \sqrt{1 - s^2}\right), \tag{108}$$

i.e. $r_4 < r_{\rm H}$. For any stable orbit, it is obvious that the radial motion happens inside the interval $[r_{\rm peri}, r_{\rm apo}]$. However, for orbital configurations with $r_{\rm peri} =$

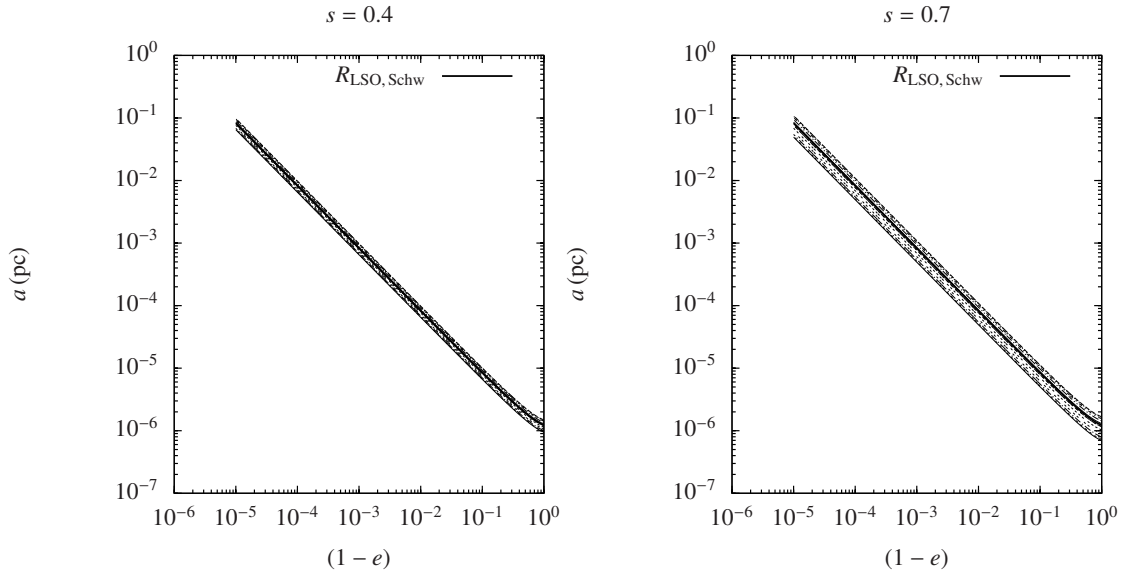

Figure 30: LSO for a MBH of mass $4 \times 10^4\, M_\odot$ and a SBH of mass $m_\bullet = 10\, M_\odot$ for a Kerr MBH of spin $s = 0.4$ (left) and $s = 0.7$ (right). The Schwarzschild separatrix is given as a solid black line. Curves above it correspond to retrograde orbits and inclinations of $\iota = 5.72$, 22.91, 40.10, 57.29, 74.48 and 89.95° starting from the last value (89.95°). In the left panel we can barely see any difference from the different inclinations due to the low value of the spin.

r_3, the potential of the MBH changes its shape and the orbits become unstable, marking the location of the LSO. In this case, we have that

$$\left(\frac{dR(r)}{dr}\right)_{r=r_3} = 0, \tag{109}$$

where $R(r)$ denotes the right-hand side of the evolution equation for the radial position r (see equation 100).

The calculations in this algorithm are done numerically, so we check whether this condition is satisfied to some tolerance level. In the case it is not satisfied, we use this information to prescribe the next value of p and come back to the first point in the algorithm. The process is repeated until we identify the LSO with the desired accuracy.

10.5 NUMBER OF CYCLES

The second type of relativistic computations that we have performed concerns the estimation of the number of cycles that certain EMRI orbital configurations that were

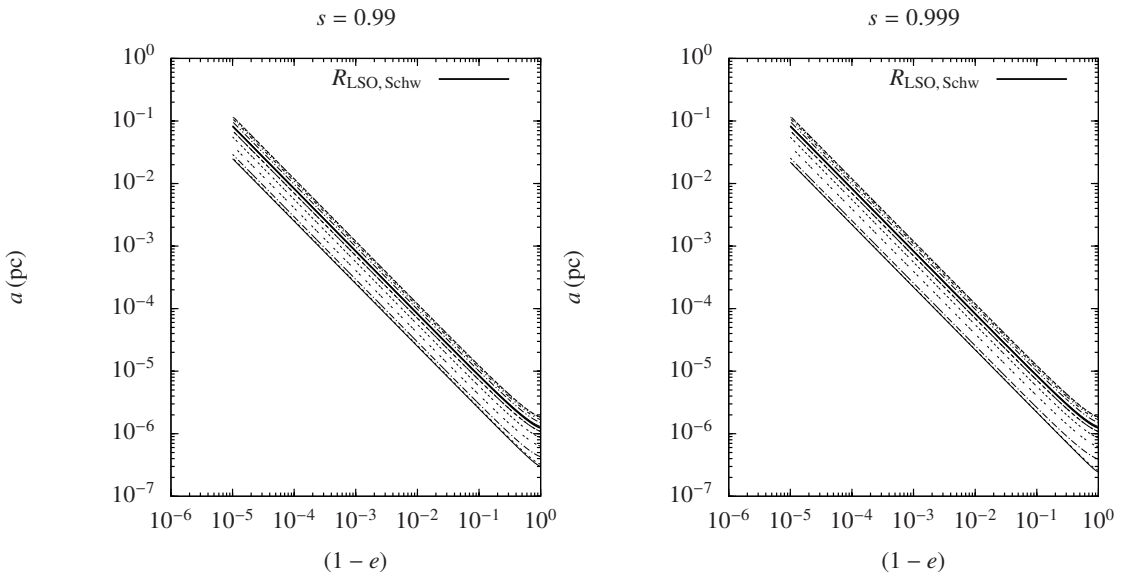

Figure 31: As in figure 30 but for a spin of $s = 0.99$ (left) and $s = 0.999$ (right panel). The larger the spin, the "further away" the Kerr LSO gets from the Schwarzschild LSO.

thought to be plunging orbits (or orbits with no sufficient cycles) in the case of non-spinning MBHs can spend in a frequency regime of $f \in [10^{-4}, 1]$ Hz during their last year(s) of inspiral before plunging into the MBH. This is important to assess how many of these EMRIs will have sufficient Signal-to-Noise Ratio (SNR) to be detectable. The way in which these estimations have been done is the following. We start with a certain orbital configuration characterized by the orbital parameters $(p_{(0)}, e_{(0)}, \iota_{(0)})$. Equivalently, we can characterise the initial orbital configuration by the constant of motions $(E_{(0)}, L_{z(0)}, C_{(0)})$. Hence, the idea is to track the inspiral without actually integrating the equations of geodesic motion of section 10.3 or any other type of equations that follow the trajectory. Instead, we picture the inspiral as a sequence of geodesic orbits, each of them characterized by orbital parameters $(p_{(i)}, e_{(i)}, \iota_{(i)})$ (or equivalently, constants of motion $(E_{(i)}, L_{z(i)}, C_{(i)})$) with $i = 0, \ldots, N_{\rm plunge}$, being $N_{\rm plunge}$ the final plunging configuration. The transition between each orbital configuration is governed by the GW emission. Our particular algorithm to follow the inspiral goes as follows (our implementation uses the formulæ in the appendices of Sopuerta & Yunes 2011 and the formulae derived by Gair & Glampedakis 2006):

1. Given an orbital configuration $(p_{(i)}, e_{(i)}, \iota_{(i)})$ and its associated constants of motion $(E_{(i)}, L_{z(i)}, C_{(i)})$, we compute the averaged evolution of the constants of motion, $(\dot{E}, \dot{L}_z, \dot{C})$, using the formulæ of (Gair & Glampedakis 2006), which combine post-Newtonian calculations at the 2PN order with fits to results for the GW emission based on the Teukolsky formalism (Teukolsky 1973) (for details

see Drasco & Hughes (2006); Glampedakis et al. (2002); Hughes (2000, 2001); Hughes et al. (2005)).

2. For the given orbital parameters we estimate the radial period T_r, that is the time to go from apoapsis to periapsis and back to apoapsis (see Fujita & Hikida 2009; Schmidt 2002 for details of this computation. In Fujita & Hikida 2009 there is a typo in one of the relevant formulae for our computations fixed in the appendices of Sopuerta & Yunes 2011).

3. We compute the change in the constants of motion. To that end, due to the fact that the GW emission by an EMRI is relatively weak, we do not consider in general just one passage through periapsis, but several of them, say $N^{\rm peri}_{(i)}$. Thus, the change in the constants of motion is:

$$(\Delta E_{(i)}, \Delta L_{z(i)}, \Delta C_{(i)}) = (\dot{E}_{(i)}, \dot{L}_{z(i)}, \dot{C}_{(i)}) \times N^{\rm peri}_{(i)} \times T_r. \tag{110}$$

And from here,

$$(E_{(i+1)}, L_{z(i+1)}, C_{(i+1)}) = (E_{(i)}, L_{z(i)}, C_{(i)}) + (\Delta E_{(i)}, \Delta L_{z(i)}, \Delta C_{(i)}). \tag{111}$$

4. From these new constants of motion and using similar techniques to the ones described above for the LSO computation we can find the new orbital parameters $(p_{(i+1)}, e_{(i+1)}, \iota_{(i+1)})$. We then go back to the first step and follow the inspiral until we detect that the new configuration corresponds to an unstable orbit corresponding to the plunge. We estimate the number of cycles as the number of times that the stellar object turned around the spin axis, $N^{\rm cycles}_{\varphi}$.

In Table 3 we show some results for a series of inspirals whose initial orbital parameters are such that the pair (e, p) lies on the separatrix between stable and unstable orbits in the case of non-spinning MBHs (i.e. $p = 6 + 2e$). Therefore, these are inspirals that under the assumption that spin can be neglected would have no cycles in the eLISA band. However, we can see from the values for the number of cycles in the table that many of those systems actually perform a significant number of cycles, more than sufficient to be detectable with good SNR. The number of cycles has been associated with N_φ (the number of times that the azimuthal angle φ advances 2π) which is usual for binary systems. However, as we have discussed above the structure of the waveforms from EMRIs is quite rich since they contain harmonics of three different frequencies. Therefore the waveforms have cycles associated with the three

frequencies $(f_r, f_\theta, f_\varphi)$ which makes them quite complex and in principle this is good for detectability (assuming we have the correct waveform templates). Another fact that is worth mentioning is that the cycles quoted in Table 3 happen just before plunge and take place in the strong field region very near the MBH horizon. Then, these cycles should contribute more to the SNR than cycles taking place farther away from the MBH horizon. Regarding the accuracy of these estimations, the main sources of error are the approximations made for the radiation-reaction effects, which are based on a post-Newtonian expansions and fits to results from black hole perturbation theory. Corrections from higher-order terms will introduce corrections to these results that depend on the EMRI configuration, but those corrections should not affect the magnitude of these numbers. In the Table we quote the integers that are closer to the numerical result.

10.6 IMPACT ON EVENT RATES

Only a certain fraction of stars in phase space will come close enough to interact with the MBH. These stars are said to belong to the "loss-cone" (see e.g. Amaro-Seoane & Spurzem 2001; Frank & Rees 1976).

For radii larger than 0.01 pc the main leading mechanism for producing EMRIs is two-body relaxation (Amaro-Seoane et al. 2007; Amaro-Seoane 2012; Hopman & Alexander 2005), and this is the region of phase-space in which our analysis is applied with priority, since for a Schwarzschild MBH one has just direct plunges. For radii below 0.01 pc we note that the enhancement in the EMRI event rate due to resonant relaxation predicted by Hopman & Alexander (2005) is severely affected by the presence of a blockade in the rate at which orbital angular momenta change takes place. This so-called "Schwarzschild barrier" is a result of the impact of relativistic precession on to the stellar potential torques, as recently shown by Merritt et al. (2011) with a few direct-summation $N-$body simulations expanded with a statistical Monte-Carlo study. Indeed, this "Schwarzschild barrier" has been corroborated in an independent work with a statistical study based on a sample of *some 2,500* direct-summation $N-$body simulations by Brem et al. (2012) in which the authors include post-Newtonian corrections and also, for the first time, the implementation of a solver of geodesic equations in the same code. This barrier poses a real problem for the production of low-eccentricity EMRIs. However, high-eccentricity EMRIs, which had been classified until now wrongly of "plunges" do not have this problem, since they are a product of pure two-body relaxation. This is why we will only focus on two-body relaxation for the estimation of the rates.

The event rate can be hence approximately calculated as

$$\dot{N}_{\rm EMRI} \simeq \int_0^{a_{\rm EMRI}} \frac{dN_\bullet(a)}{\ln\left(\theta_{\rm LC}^{-2}\right) t_r(a)}\,, \tag{112}$$

with $\theta_{\rm LC}$ the loss-cone angle, $N_\bullet(a)$ the number of stellar black holes (SBHs) within a semi-major axis a and $a_{\rm EMRI}$ a maximum radius within which we estimate the event

MBH mass $M_\bullet$ $(M_\odot)$	MBH Spin s	Semimajor axis $a_{(0)}$ (pc)	Eccentricity $1-e_{(0)}$	Inclination $\iota_{(0)}$ (rad)	Time to plunge $T_{\rm plunge}$ (yrs)	Time in band $T_{\rm band}$ (yrs)	Cycles in band N_φ
$5.0\cdot10^4$	0.30	$9.57\cdot10^{-3}$	10^{-6}	0.00	$3.92\cdot10^2$	0.06	914
$5.0\cdot10^4$	0.30	$9.57\cdot10^{-3}$	10^{-6}	0.70	$3.92\cdot10^2$	0.06	625
$5.0\cdot10^4$	0.90	$9.57\cdot10^{-3}$	10^{-6}	0.00	$3.92\cdot10^2$	0.11	4174
$5.0\cdot10^4$	0.90	$9.57\cdot10^{-3}$	10^{-6}	1.00	$3.92\cdot10^2$	0.08	2646
$1.0\cdot10^5$	0.70	$1.91\cdot10^{-2}$	10^{-6}	0.00	$7.87\cdot10^2$	0.29	6968
$1.0\cdot10^5$	0.70	$1.91\cdot10^{-2}$	10^{-6}	1.00	$7.86\cdot10^2$	0.23	3411
$1.0\cdot10^5$	0.99	$1.91\cdot10^{-2}$	10^{-6}	0.00	$4.70\cdot10^3$	0.38	8938
$1.0\cdot10^5$	0.99	$1.91\cdot10^{-2}$	10^{-6}	0.70	$3.92\cdot10^3$	0.32	7892
$5.0\cdot10^5$	0.30	$9.57\cdot10^{-2}$	10^{-6}	0.00	$4.31\cdot10^4$	1.98	8246
$5.0\cdot10^5$	0.30	$9.57\cdot10^{-2}$	10^{-6}	1.00	$4.31\cdot10^4$	1.61	3061
$5.0\cdot10^5$	0.95	$9.57\cdot10^{-2}$	10^{-6}	0.00	$5.10\cdot10^4$	2.00	40093
$5.0\cdot10^5$	0.95	$9.57\cdot10^{-2}$	10^{-6}	1.00	$4.31\cdot10^4$	2.00	27600
$1.0\cdot10^6$	0.30	$1.91\cdot10^{-2}$	10^{-5}	0.00	$1.27\cdot10^4$	1.98	10943
$1.0\cdot10^6$	0.30	$1.91\cdot10^{-2}$	10^{-5}	1.00	$1.19\cdot10^4$	1.91	3552
$1.0\cdot10^6$	0.70	$1.91\cdot10^{-2}$	10^{-5}	0.00	$1.35\cdot10^4$	1.99	51308
$1.0\cdot10^6$	0.70	$1.91\cdot10^{-2}$	10^{-5}	1.00	$1.20\cdot10^4$	1.99	23291
$1.0\cdot10^6$	0.90	$1.91\cdot10^{-2}$	10^{-5}	0.00	$1.40\cdot10^4$	1.99	58841
$1.0\cdot10^6$	0.90	$1.91\cdot10^{-2}$	10^{-5}	1.00	$1.17\cdot10^4$	2.00	38245
$1.0\cdot10^6$	0.99	$1.91\cdot10^{-2}$	10^{-5}	0.00	$1.43\cdot10^4$	2.00	61726
$1.0\cdot10^6$	0.99	$1.91\cdot10^{-2}$	10^{-5}	1.00	$1.17\cdot10^4$	2.00	47678
$5.0\cdot10^6$	0.30	$9.57\cdot10^{-2}$	10^{-5}	0.00	$1.44\cdot10^5$	1.93	5258
$5.0\cdot10^6$	0.30	$9.57\cdot10^{-2}$	10^{-5}	1.00	$1.36\cdot10^5$	0.00	0
$5.0\cdot10^6$	0.70	$9.57\cdot10^{-2}$	10^{-5}	0.00	$1.55\cdot10^5$	2.00	40687
$5.0\cdot10^6$	0.70	$9.57\cdot10^{-2}$	10^{-5}	1.00	$1.36\cdot10^5$	2.00	14936
$5.0\cdot10^6$	0.90	$9.57\cdot10^{-2}$	10^{-5}	0.00	$1.61\cdot10^5$	2.00	41369
$5.0\cdot10^6$	0.90	$9.57\cdot10^{-2}$	10^{-5}	1.00	$1.35\cdot10^5$	1.99	30695
$1.0\cdot10^7$	0.30	1.91	10^{-6}	0.00	$4.02\cdot10^6$	1.99	3089
$1.0\cdot10^7$	0.30	1.91	10^{-6}	1.00	$3.78\cdot10^6$	0.00	0
$1.0\cdot10^7$	0.70	1.91	10^{-6}	0.00	$4.27\cdot10^6$	2.00	23425
$1.0\cdot10^7$	0.70	1.91	10^{-6}	1.00	$3.79\cdot10^6$	1.98	8747
$1.0\cdot10^7$	0.99	$1.91\cdot10^{-1}$	10^{-5}	0.00	$1.44\cdot10^6$	1.98	22455
$1.0\cdot10^7$	0.99	$1.91\cdot10^{-1}$	10^{-5}	1.00	$1.18\cdot10^6$	1.99	28589
$5.0\cdot10^7$	0.30	$9.57\cdot10^{-1}$	10^{-5}	0.00	$1.44\cdot10^7$	0.00	0
$5.0\cdot10^7$	0.30	$9.57\cdot10^{-1}$	10^{-5}	1.00	$1.36\cdot10^7$	0.00	0
$5.0\cdot10^7$	0.70	$9.57\cdot10^{-1}$	10^{-5}	0.00	$1.55\cdot10^7$	1.72	4247
$5.0\cdot10^7$	0.70	$9.57\cdot10^{-1}$	10^{-5}	1.00	$1.35\cdot10^7$	0.00	0
$5.0\cdot10^7$	0.99	$9.57\cdot10^{-1}$	10^{-5}	0.00	$1.65\cdot10^7$	1.88	4422
$5.0\cdot10^7$	0.99	$9.57\cdot10^{-1}$	10^{-5}	1.00	$1.35\cdot10^7$	1.52	4625

Table 3: This table shows the main properties of some (prograde) inspirals that initially lie on the separatrix (LSO) of non-spinning MBHs and hence they would not be detectable in the eLISA band. The numbers in the first five columns have been already introduced in the text. The sixth column gives the time it takes for each inspiral to get to plunge. The seventh column shows how much time it spends in band assuming the plunge occurs at the end of the eLISA mission time (assumed to be 2 yrs here). The last column show the number of orbital cycles in band (during $T_{\rm band}$), defined as the number of times that the azimuthal angle φ advances 2π during the last two years before plunge. The number of GW cycles can be then defined as twice this number.

rate $\dot{N}_{\rm EMRI}$. We assume that the SBHs distribute around the central MBH following a power-law cusp of exponent γ, i.e. that the density profile follows $\rho \propto r^{-\gamma}$ within the region where the gravity of the MBH dominates the gravity of the stars, with γ ranging between 1.75 and 2 for the heavy stellar components (Alexander & Hopman 2009; Amaro-Seoane et al. 2004; Amaro-Seoane & Preto 2011; Bahcall & Wolf 1976, 1977; Preto et al. 2004; Preto & Amaro-Seoane 2010; Peebles 1972) and see Gurevich (1964) for an interesting first idea of this concept[2]. We then have that the number of stars within a radius r is

$$n(r) = \frac{(3-\gamma)}{4\,\pi}\left(\frac{M_\bullet}{m_\star}\right)\left(\frac{1}{R^3_{\rm infl}}\right)\left(\frac{r}{R_{\rm infl}}\right)^{-\gamma}. \tag{113}$$

Hence, the number of SBHs within a is

$$N_\bullet(a) \simeq N_0\left(\frac{a}{R_0}\right)^{3-\gamma}. \tag{114}$$

Hence, we have that

$$dN_\bullet(a) = (3-\gamma)\frac{N_0}{R_0}\left(\frac{a}{R_0}\right)^{2-\gamma} da\,. \tag{115}$$

10.6.1 *The Schwarzschild case*

We know that (see e.g. Alexander & Livio 2001; Amaro-Seoane & Spurzem 2001) $\theta^{-2}_{\rm LC} \simeq J_{\rm max}/J_{\rm LC}$. Since the loss-cone angular momentum can be approximated as $J_{\rm LC} \simeq 4\,GM_\bullet/c$ and $J_{\rm max} = \sqrt{GM_\bullet a}$, we have that

$$\theta^{-2}_{\rm LC} \simeq \sqrt{\frac{a}{8\,R_{\rm Schw}}}, \tag{116}$$

We assume also that relaxation is dominated by a single stellar black hole (SBH) population, since because of mass segregation the most massive objects sink down to the centre and the light stars are pushed out from the centre. The relaxation time at a distance a is

$$t_r(a) = t_0\left(\frac{a}{R_0}\right)^{\gamma-3/2}, \tag{117}$$

with

$$t_0 = 0.3389\,\frac{\sigma_0^3}{\ln\Lambda\, G^2 m_\bullet^2\, n_0}\,. \tag{118}$$

2 The authors obtained a similar solution for how electrons distribute around a positively charged Coulomb centre.

Since (see e.g. Amaro-Seoane et al. 2007)

$$n_0 = \frac{3-\gamma}{4\pi} N_0 R_0^3 \tag{119}$$

$$\sigma_0^2 = \frac{1}{1+\gamma}\frac{GM_\bullet}{R_0}, \tag{120}$$

we have that equation (118) becomes

$$t_0 \simeq 4.26\, \frac{1}{(3-\gamma)(1+\gamma)^{3/2}} \frac{\sqrt{R_0^3 (GM_\bullet)^{-1}}}{\ln\Lambda\, N_0} \left(\frac{M_\bullet}{m_\bullet}\right)^2 . \tag{121}$$

We now define a *critical* radius at which the two regimes that lead the evolution of the EMRI decouple. The first evolution is dominated by relaxational processes, via exchange of E and J between SBHs on a capture orbit with stars from the surrounding stellar system, while in the second regime the evolution of the EMRI is totally dominated by the emission of gravitational waves. This is given in figure 1 of Amaro-Seoane et al. (2007) with their red curve. In other words, the line gives us the radius as a function of a at which the relaxational time at periapsis is approximately equal to the timescale defined by the approximation of Peters (1964). Hence, we have to solve

$$\begin{aligned} t_{\rm r}(a)(1-e) &= K\, t_{\rm GW}(a,\, e) \\ J(a,\, e) &= J_{\rm LC} \\ (1-e)\, a &= \frac{8\, G\mathcal{M}_\bullet}{c^2} \end{aligned} \tag{122}$$

In the first equality, K is a factor of order unity. In the last equality we assume a Schwarzschild radius and we assume that the LSO is at $4 \times R_{\rm Schw}$ Approximating $e \sim 1$, the function $f(e)$ from Peters (1964) $f(e) = 425/(768\sqrt{2})$. Hence

$$t_{\rm GW}(a,\, e) \cong \sqrt{2}\, \frac{24}{85} \frac{c^5}{G^3} \frac{a^4}{M_\bullet^2\, m_\bullet} (1-e)^{7/2} . \tag{123}$$

And so, finally from equations (122), (117) and (121) and solving for $a_{\rm EMRI}$, we have that

$$a_{\rm EMRI} \simeq R_0 \left[16.97\, K\, (3-\gamma)\, (1+\gamma)^{3/2} \ln\Lambda\, N_\bullet \frac{m_\bullet}{M_\bullet}\right]^{\frac{1}{\gamma-3}} . \tag{124}$$

Or, absorbing some constants into a newly defined K_γ,

$$a_{\rm EMRI} = K_\gamma \, R_0 \left(\frac{1}{\ln \Lambda} \frac{M_\bullet}{N_\bullet \, m_\bullet} \right)^{\frac{1}{3-\gamma}}$$
$$K_\gamma := \left[16.97 \, K \, (3-\gamma) \, (1+\gamma)^{3/2} \right] . \tag{125}$$

We can then derive the event rate for the Schwarzschild case, based on 112,

$$\dot{N}^{\rm Schw}_{\rm EMRI} \cong 0.235 \, \frac{4 \, (3-\gamma)^2 \, (1+\gamma)^{3/2}}{9-4\gamma} \, K_\gamma^{\frac{9-4\gamma}{2}}$$
$$\frac{\ln \Lambda^{\frac{2\gamma-3}{6-2\gamma}}}{\ln \left(\frac{a_{\rm EMRI}}{8 \, R_{\rm Schw}} \right)} \left(\frac{N_\bullet m_\bullet}{M_\bullet} \right)^{\frac{3}{6-2\gamma}} \sqrt{\frac{G M_\bullet}{R_0^3}} \, . \tag{126}$$

The last equation is based on the assumption that equation (122) holds, and the last equality, $(1-e)a = 8\,GM_\bullet/c^2$, is the "effective" value of the periapsis for the last parabolic stable orbit (LSO from now onwards) for a Schwarzschild MBH. I.e. if the star is on an orbit that in Newtonian dynamics leads to a periapsis smaller than this value, the star disappears if we take into account relativistic dynamics.

10.6.2 *The Kerr case*

In the Kerr case we simply have to recalculate where this LSO is by taking into account the value of the spin of the MBH. We then have to either shrink or enlarge it by a certain factor function of the inclination and spin, $\mathcal{W}(\iota, s)$, so that the effective pericentre of LSO is

$$(1-e)\, a = \mathcal{W}(\iota, s) \times \frac{8\, G M_\bullet}{c^2} \, . \tag{127}$$

This quantity can be derived from the separatrices of the figures in section 10.3. If the orbit can get closer to the MBH in the Kerr case, then $\mathcal{W}(\iota, s) < 1$; otherwise $\mathcal{W}(\iota, s) > 1$. Since the separatrices are nearly parallel, we hence can define $\mathcal{W}(\iota, s)$ like

$$\mathcal{W}(\iota, s) := \left\langle \frac{a_{\rm LSO,\,Kerr}}{a_{\rm LSO,\,Schw}} \right\rangle = \frac{1}{N} \sum_i \frac{a_{\rm LSO,\,Kerr}(e_i)}{a_{\rm LSO,\,Schw}(e_i)} \, . \tag{128}$$

That is, given a spin and an inclination, we take for N values of the eccentricity the semimajor axis corresponding to the Kerr value, $a_{\rm LSO,\,Kerr}(e)$ and to the Schwarzschild case, $a_{\rm LSO,\,Schw}$ and we sum for the ratio of the two semi-majors over all eccentricities. This allows us to calculate by how much the LSO has been "shifted".

Spin (s)	Inclination (ι, rad)	$\mathcal{W}(\iota, s)$
0.900	0.100	0.429452
0.900	0.400	0.448093
0.900	0.700	0.499450
0.900	1.000	0.598278
0.900	1.300	0.739339
0.900	1.570	0.883679
0.900	-0.100	1.415955
0.900	-0.400	1.377239
0.900	-0.700	1.295011
0.900	-1.000	1.175760
0.950	0.100	0.370036
0.950	0.400	0.386009
0.950	0.700	0.436921
0.950	1.000	0.548352
0.950	1.300	0.708257
0.950	1.570	0.867320
0.950	-0.400	1.396449
0.950	-0.700	1.309052
0.950	-1.000	1.181942
0.950	-1.300	1.024866
0.990	0.100	0.297301
0.990	0.400	0.306924
0.990	0.700	0.354716
0.990	1.000	0.494738
0.990	1.300	0.679468
0.990	1.570	0.852821
0.990	-0.100	1.454732
0.990	-0.400	1.411720
0.990	-0.700	1.320145
0.990	-1.000	1.186631
0.990	-1.300	1.020814
0.999	0.100	0.260205
0.999	0.400	0.264063
0.999	0.700	0.310302
0.999	1.000	0.479038
0.999	1.300	0.672349
0.999	1.570	0.849364
0.999	-0.100	1.458589
0.999	-0.400	1.415145
0.999	-0.700	1.322624
0.999	-1.000	1.187655
0.999	-1.300	1.019828

Table 4: Values for $\mathcal{W}$.

If we redo the derivation of (126) taking into account equation 127, we can obtain $\dot{N}_{\rm EMRI}$ in function of $\mathcal{W}$, $\dot{N}^{\rm Kerr}_{\rm EMRI}$ and, hence, we can calculate the ratio of the rates as a function of the inclination ι and spin s:

$$a^{\rm Kerr}_{\rm EMRI} = a^{\rm Schw}_{\rm EMRI} \times \mathcal{W}^{\frac{-5}{6-2\gamma}}(\iota, s) \tag{129}$$

$$\dot{N}^{\rm Kerr}_{\rm EMRI} = \dot{N}^{\rm Schw}_{\rm EMRI} \times \mathcal{W}^{\frac{20\gamma-45}{12-4\gamma}}(\iota, s)\,. \tag{130}$$

For instance, for a spin of $s = 0.999$ and an inclination of $\iota = 0.4\,\mathrm{rad}$, we estimate that $\mathcal{W} \sim 0.26$ and, thus, $\dot{N}^{\rm Kerr}_{\rm EMRI} \sim 30$. I.e. *we boost the event rates by a factor of 30* in comparison to a non-rotating MBH.

10.7 NET EFFECT OF RESONANT RELAXATION ON EMRI RATES

10.7.1 *The role of vectorial resonant relaxation*

To understand the impact of the previous calculation on event rates for EMRIs we have to elaborate on prograde and retrograde orbits. We have seen that retrograde EMRI orbits see the central MBH as an effectively "larger" MBH; i.e. it is easier to plunge through the horizon. Contrary, prograde EMRI orbits "see" the effective size of the MBH shrink and, thus, have a harder time in hitting the central MBH. It is therefore important to assess the orientation of orbits in the regime of interest. It takes on average (vectorial) resonant relaxation (RR) a time $t_{\rm RR,\,v}$ to rotate coherently the orbital plane of an orbit by an angle $\pi/2$ (Hopman & Alexander 2006). To change a prograde (retrograde) orbit to a retrograde (prograde) orbit, it takes four times longer: The $\pi/2$ rotation is the maximum that can be obtained over the self-quenching time; the rest to get up to a full π rotation is done non-coherently over 4 coherence times (see Bregman & Alexander 2011,for a discussion of the numeric prefactors).

It should be noted that vector RR is invariant under precession (see e.g. Hopman & Alexander 2006). We must note also that the change in the inclination of the orbit with respect to the spin axis due to GW emission is relatively rather small (see Hughes (2000, 2001)), so small that frequently it has been assumed to be constant, which provides an extra equation for the evolution of the Carter constant in the inspiral process, making things significantly simpler.

The dependence of the transverse RR torque (i.e. direction-changing torque) on the eccentricity has been measured from simulations by Gürkan & Hopman (2007). In their work, the authors derive that it grows quadratically by a factor 3 in total from 0 to 1.

The radius of the sphere of influence is

$$r_{\rm infl} = \frac{1}{1+\gamma}\frac{GM_\bullet}{\sigma_0^2} \approx 1\ \mathrm{pc}\frac{1}{1+\gamma}\left(\frac{M_\bullet}{10^6\,M_\odot}\right)\left(\frac{60\ \mathrm{km/s}}{\sigma_0}\right)^2\,, \tag{131}$$

for a given exponent γ. Within this radius the relaxation time is

$$t_{\rm r}(r) \propto (1+\gamma)^{-3/2} \frac{\ln\Lambda\,\sigma^3(r)}{G^2\langle m\rangle m_{\rm CO} n(r)} \simeq 2\times10^8\,{\rm yr}\,(1+\gamma)^{-3/2}\left(\frac{\sigma}{100\,{\rm km\,s^{-1}}}\right)^3\left(\frac{10\,M_\odot}{m_{\rm CO}}\right) \left(\frac{10^6\,M_\odot{\rm pc}^{-3}}{\langle m\rangle n}\right). \quad (132)$$

In this equation we follow the usual notation: $\sigma(r)$ is the local velocity dispersion; for $r < r_{\rm infl}$ it is approximately the Keplerian orbital speed $\sqrt{GM_\bullet r^{-1}}$; $n(r)$ is the *local* density of stars, $\langle m\rangle$ is the average stellar mass, $m_{\rm CO}$ is the individual mass of the compact object, which we assume to be all SBHs, and take a mass of $m_{\rm CO} = 10\,M_\odot$ for all of them. In the vicinity of a MBH, ($r < r_{\rm infl}$), $\Lambda \approx M_\bullet/m_\star$ (Bahcall & Wolf 1976; Lightman & Shapiro 1977), and typically $\ln\Lambda \sim 11$.

Relaxation redistributes orbital energy amongst stellar-mass objects until SBHs form a power-law density cusp, $n(r) \propto r^{-\gamma}$ with $\gamma \simeq 1.75$ around the MBH, while less massive species arrange themselves into a shallower profile, with $\alpha \simeq 1.4-1.5$ as we have mentioned earlier, although recent studies have found a general solution to the problem of mass segregation around MBH in galactic nuclei, with a more efficient diffusion for the heavy stars, reaching a $\gamma \sim -2$ in the "strong mass-segregation" regime (Alexander & Hopman 2009; Amaro-Seoane & Preto 2011; Preto & Amaro-Seoane 2010).
Since $\sigma(r)^2 = GM_\bullet/r$ and we take that $\langle m\rangle = 0.7\,M_\odot$ and, as mentioned, $m_{\rm CO} = 10\,M_\odot$, we have all information to derive $t_{\rm r,\,peri}(r) := (1-e)\,t_{\rm r}$ from Equation (132) and (113).

As regards the explicit expression for the characteristic timescale for *vectorial* resonant relaxation, from Hopman & Alexander (2006) we have that

$$t_{\rm RR,\,v} = P(a)\frac{M_\bullet}{m_\star}\frac{\beta_v(e)^2}{\sqrt{N(a)}}, \quad (133)$$

where we have taken into account the corrections for high values of e as given in Gürkan & Hopman (2007), $\beta_v(e) = 0.28\,(e^2+0.5)$ and $P(a) = a^{3/2}/(GM_\bullet)^{1/2}$. This allows us to follow the dependence with the radius (and eccentricity) of the ratio $t_{\rm r,\,peri}/t_{\rm RR,\,v}$.

If we now equate the timescales of interest, the gravitational radiation driven time $t_{\rm GW}$, defined as in the approximation of Peters (1964), to the two-body relaxation time at periapsis, $t_{\rm r,\,peri}$, we obtain the short-dashed curve of figure 32 on the left of this line, the contribution of GW radiation to orbital evolution dominates over two-body relaxation. In the absence of resonant relaxation, if a SBH crosses this line from the right (lower eccentricities), it will become an EMRI, provided, of course, that it is still on a stable orbit, i.e. above the separatrix corresponding to its orbital orientation.

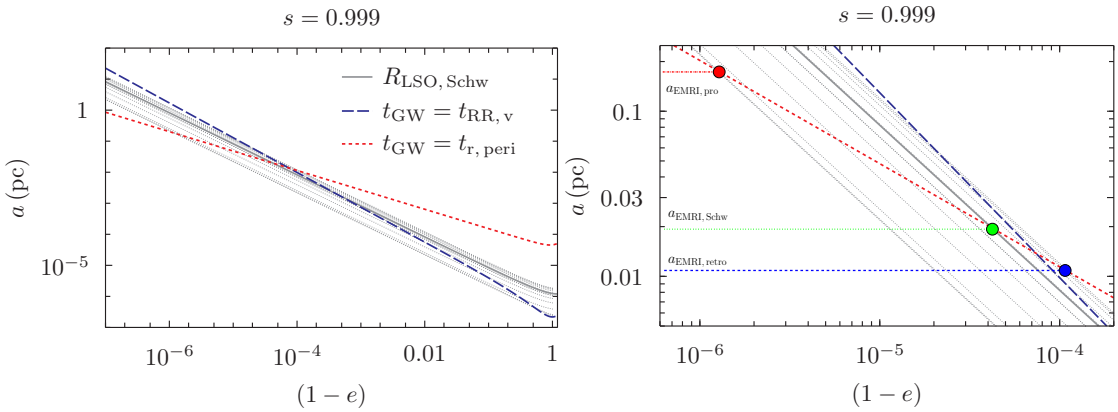

Figure 32: *Left panel:* Relation between different timescales in the $s = 0.999$ case. As in the prior section, we display the Schwarzschild separatrix as a solid, black line and the separatrices for different inclinations with different curves in light grey. The dashed, blue line shows the value of a and $1-e$ for which the vectorial resonant relaxation timescale ($t_{\rm RR,\,v}$) is equal to the gravitational loss timescale ($t_{\rm GW}$). The dashed, dotted line corresponds to the values of a and $1-e$ for which the relaxation time at periapsis ($t_{\rm r,\,peri}$) equals the gravitational loss timescale. *Right panel:* Same as the left panel but zoomed to see where the dashed, red curve intersects the last one of the retrograde, Schwarzschild and prograde separatrices. We show this with a blue dot and a long-dashed curve for the retrograde case which yields the last separatrix, with a green dot and a green, short-dashed curve for the Schwarzschild separatrix and with a red dot and a dash-dotted curve for the last separatrix of the prograde case. These lines give us $a_{\rm EMRI,\,retro}$, $a_{\rm EMRI,\,Schw}$ and $a_{\rm EMRI,\,pro}$, correspondingly.

For a Schwarzschild MBH, all separatrices are the same and there is a unique critical point (PS). A SBH with a semi-major axis larger that the value at PS will experience a direct plunge if relaxation brings its eccentricity to a high value because it will cross the separatrix (and be swallowed in less than an orbital time) before it has a chance to enter into the GW-dominated regime. Conversely, objects with smaller semi-major axis values are much more likely to end up as EMRIs rather than plunges.

For a fast spinning SMBH, the separatrix for prograde orbits is shifted to significantly lower a values, with a corresponding higher value of the critical semi-major axis, corresponding to the point PP in figure 32. As we have explained above, it is this effect which can lead to a significant increase in the EMRI rate, combined with the fact that the critical point for retrograde orbits (PR) is much less affected and that an isotropic orbit distribution is expected, thanks to relaxational processes. However this increase in EMRI rate would can be thwarted by vector RR if this process can change the orbital orientation of a SBH after it has crossed the "$t_{\rm GW} = t_{\rm r,\,peri}$" line and before it has completed its GW-driven inspiral, i.e. on a timescale shorter than $t_{\rm GW}$. Indeed, if

the orbit becomes significantly less prograde as the the inspiral takes place, due to RR, the separatrix moves up and the SBH might suddenly find itself on a plunge orbit.

To check for this possibility, we also plot, in figure 32, a long-dashed line corresponding to the condition $t_{\rm GW} = t_{\rm RR,\,v}$, with $t_{\rm GW} < t_{\rm RR,\,v}$ on the left of this line. SBHs that cross the "$t_{\rm GW} = t_{\rm r,\,peri}$" line while on the left side of the "$t_{\rm GW} = t_{\rm RR,\,v}$" line keep their orbital orientation during their inspiral and complete it without abrupt plunge. One can see that, for our choice of parameters, this is the case for all prograde orbits. On the other hand, retrograde orbits can cross the "$t_{\rm GW} = t_{\rm r,\,peri}$" line while RR is still effective enough to change their orientation during inspiral. However, the effect of RR on retrograde orbits cannot reduce significantly the total EMRI rate and may even increase it slightly because (1) these orbits contribute less that the prograde ones (and more to the plunge rate) and (2) statistically, RR is more likely to make the orbit become less retrograde which pushes down the separatrix.

Finally, we also note that for the other proposed mechanism to produce EMRIs, the tidal separation of a binary containing a compact object (Amaro-Seoane et al. 2007; Miller et al. 2005), the captured objects typically have much lower eccentricities and smaller semi-major axis. Therefore, they cross "$t_{\rm GW} = t_{\rm r,\,peri}$" line and start their inspiral, with orbital parameters well above the uppermost separatrix (for retrograde orbits). As the GW-driven trajectory in the $e - a$ plane is basically parallel to the separatrices, there is no danger of a premature plunge, even though RR has ample time to flip the orbital orientation during inspiral.

10.8 CONCLUSIONS

In this article we have addressed the problem of direct plunges and MBHs. If this is a Schwarzschild MBH, the compact object will plunge through the horizon and will hence not contribute to the mapping of space and time around the MBH, contrary to an EMRI, which describes thousands of cycles before it merges with the central MBH. On the other hand, the event rate of plunges is much larger than that of EMRIs, as a number of different studies by different authors using different methods find.

Up to now spin effects of the central MBH have been always ignored. Hence, the question arises, whether a plunge is really a plunge when the central MBH is spinning. This consideration has been so far always ignored.

So as to estimate EMRI event rates, one needs to know whether the orbital configuration of the compact object is stable or not, because this is the kernel of the difference between an EMRI and a plunge. In this paper we take into account the fact that the spin makes the LSO to be much closer to the horizon in the case of prograde orbits but it pushes it away for retrograde orbits. Since the modifications introduced by the spin are not symmetric with respect to the non-spinning case, and they are more dramatic for prograde orbits, we prove that the inclusion of spin increases the number of EMRI events by a significant factor. The exact factor of this enhancement depends on the spin, but the effect is already quite important for spins around $s \sim 0.7$.

We also prove that these fake plunges, "our" EMRIs, do spend enough cycles inside the band of eLISA to be detectable, i.e. they are to be envisaged as typical EMRIs. We note here that whilst it is true that EMRIs very near the new separatrix shifted by the spin effect will probably contribute not enough cycles to be detected, it is equally true for the old separatrix (Schwarzschild, without spin). In this sense, we find that the spin increases generically the number of cycles inside the band for prograde EMRIs in such a way that EMRIs very near to the non-spin separatrix, which contributed few cycles, become detectable EMRIs. In summary, spin increases the area, in configuration space of detectable EMRIs. We predict thus that EMRIs will be highly dominated by prograde orbits.

Moreover, because spin allows for stable orbits very near the horizon in the prograde case, the contribution of each cycle to the SNR is significantly bigger than each cycle of an EMRI around a non-spinning MBH.

We then show that vectorial resonant relaxation will not be efficient enough to change prograde orbits into retrogrades once GW evolution dominates (which would make the EMRIs plunge instantaneously, as they would be in a non-allowed region of phase space).

These new kind of EMRIs we describe here, high-eccentric EMRIs, are produced by two-body relaxation and, as such, they are ignorant of the Schwarschild barrier. While low-eccentricity EMRIs run into the problem of having to find a way to travers this barrier, our "plunge-EMRIs" do not. We predict that EMRI rates will be dominated by high-eccentricity binaries, with the proviso that the central MBH is Kerr.

BIBLIOGRAPHY

Alexander T., Hopman C., 2003, ApJ Lett., 590, 29

Alexander T., Hopman C., 2009, ApJ, 697, 1861

Alexander T., Livio M., 2001, ApJ Lett., 560, 143

Amaro-Seoane P., 2004, PhD thesis, PhD Thesis, Combined Faculties for the Natural Sciences and for Mathematics of the University of Heidelberg, Germany. VII + 174 pp. (2004), http://www.ub.uni-heidelberg.de/archiv/4826

—, 2012, ArXiv e-prints

Amaro-Seoane P., Aoudia S., Babak S., Binétruy P., Berti E., Bohé A., Caprini C., Colpi M., Cornish N. J., Danzmann K., Dufaux J.-F., Gair J., Jennrich O., Jetzer P., Klein A., Lang R. N., Lobo A., Littenberg T., McWilliams S. T., Nelemans G., Petiteau A., Porter E. K., Schutz B. F., Sesana A., Stebbins R., Sumner T., Vallisneri M., Vitale S., Volonteri M., Ward H., 2012a, Accepted for publication at GW Notes

—, 2012b, Classical and Quantum Gravity, 29, 124016

Amaro-Seoane P., Freitag M., Spurzem R., 2004, MNRAS

Amaro-Seoane P., Gair J. R., Freitag M., Miller M. C., Mandel I., Cutler C. J., Babak S., 2007, Classical and Quantum Gravity, 24, 113

Amaro-Seoane P., Preto M., 2011, Classical and Quantum Gravity, 28, 094017

Amaro-Seoane P., Spurzem R., 2001, MNRAS, 327, 995

Bahcall J. N., Wolf R. A., 1976, ApJ, 209, 214

—, 1977, ApJ, 216, 883

Bardeen J. M., 1970, Nat, 226, 64

Baumgardt H., Makino J., Ebisuzaki T., 2004, ApJ, 613, 1143

Berry C. P. L., Gair J. R., 2013, MNRAS, 433, 3572

Binney J., Tremaine S., 1987, Galactic Dynamics. Princeton University Press

Boyer R. H., Lindquist R. W., 1967, Journal of Mathematical Physics, 8, 265

Bregman M., Alexander T., 2012, ApJ, 748, 63

Brem P., Amaro-Seoane P., Sopuerta C., 2014, MNRAS 437, 1259

David L. P., Durisen R. H., Cohn H. N., 1987a, ApJ, 313, 556

—, 1987b, ApJ, 316, 505

Drasco S., Hughes S. A., 2004, Phys. Rev. D, 69, 044015

—, 2006, Phys. Rev. D, 73, 024027

Eisenhauer F., Genzel R., Alexander T., Abuter R., Paumard T., Ott T., Gilbert A., Gillessen S., Horrobin M., Trippe S., Bonnet H., Dumas C., Hubin N., Kaufer A., Kissler-Patig M., Monnet G., Ströbele S., Szeifert T., Eckart A., Schödel R., Zucker S., 2005, ApJ, 628, 246

Erwin P., Graham A. W., Caon N., 2004, in Coevolution of Black Holes and Galaxies, L. C. Ho, ed.

Ferrarese L., Ford H., 2005, Supermassive Black Holes in Galactic Nuclei: Past, Present and Future Research

Frank J., Rees M. J., 1976, MNRAS, 176, 633

Freitag M., Amaro-Seoane P., Kalogera V., 2006, ApJ, 649, 91

Freitag M., Benz W., 2002, A&A, 394, 345

Fujita R., Hikida W., 2009, Classical and Quantum Gravity, 26, 135002

Gair J. R., Glampedakis K., 2006, Ph. Rev. D, 73, 064037

Ghez A. M., Salim S., Hornstein S. D., Tanner A., Lu J. R., Morris M., Becklin E. E., Duchêne G., 2005, ApJ, 620, 744

Ghez A. M., Salim S., Weinberg N. N., Lu J. R., Do T., Dunn J. K., Matthews K., Morris M. R., Yelda S., Becklin E. E., Kremenek T., Milosavljevic M., Naiman J., 2008, ApJ, 689, 1044

Gillessen S., Eisenhauer F., Trippe S., Alexander T., Genzel R., Martins F., Ott T., 2009, ApJ, 692, 1075

Glampedakis K., Hughes S. A., Kennefick D., 2002, Phys. Rev. D, 66, 064005

Gurevich A., 1964, Geomag. Aeronom., 4, 247

Gürkan M. A., Hopman C., 2007, MNRAS, 379, 1083

Häring N., Rix H.-W., 2004, ApJ Lett., 604, L89

Hopman C., Alexander T., 2005, ApJ, 629, 362

—, 2006, ApJ, 645, 1152

Hopman C., Freitag M., Larson S. L., 2007, MNRAS, 378, 129

Hughes S. A., 2000, Ph. Rev. D, 61, 084004

—, 2001, Ph. Rev. D, 64, 064004

Hughes S. A., Drasco S., Flanagan É. É., Franklin J., 2005, Physical Review Letters, 94, 221101

Khalisi E., Amaro-Seoane P., Spurzem R., 2007, MNRAS

Kormendy J., 2004, in Coevolution of Black Holes and Galaxies, from the Carnegie Observatories Centennial Symposia., Ho L., ed., Cambridge University Press, p. 1

Lightman A. P., Shapiro S. L., 1977, ApJ, 211, 244

Magorrian J., Tremaine S., 1999, MNRAS, 309, 447

Merritt D., Alexander T., Mikkola S., Will C. M., 2011, Phys. Rev. D, 84, 044024

Miller M. C., Freitag M., Hamilton D. P., Lauburg V. M., 2005, ApJ Lett., 631, L117

Misner C. W., Thorne K. S., Wheeler J. A., 1973, Gravitation

Murphy B. W., Cohn H. N., Durisen R. H., 1991, ApJ, 370, 60

Peebles P. J. E., 1972, ApJ, 178, 371

Peters P. C., 1964, Physical Review, 136, 1224

Preto M., Amaro-Seoane P., 2010, ApJ Lett., 708, L42

Preto M., Merritt D., Spurzem R., 2004, ApJ Lett., 613, L109

Rubbo L. J., Holley-Bockelmann K., Finn L. S., 2006, ApJ Lett., 649, L25

Schmidt W., 2002, Classical and Quantum Gravity, 19, 2743

Sołtan A., 1982, MNRAS, 200, 115

Sopuerta C. F., Yunes N., 2011, Phys. Rev. D, 84, 124060

Syer D., Ulmer A., 1999, MNRAS, 306, 35

Teukolsky S. A., 1973, ApJ, 185, 635

Tremaine S., Gebhardt K., Bender R., Bower G., Dressler A., Faber S. M., Filippenko A. V., Green R., Grillmair C., Ho L. C., Kormendy J., Lauer T. R., Magorrian J., Pinkney J., Richstone D., 2002, ApJ, 574, 740

Wang J., Merritt D., 2004, ApJ, 600, 149

Yu Q., Tremaine S., 2002, MNRAS, 335, 965

Yunes N., Sopuerta C. F., Rubbo L. J., Holley-Bockelmann K., 2008, ApJ, 675, 604

11

THE BUTTERFLY EFFECT IN THE EXTREME-MASS RATIO INSPIRAL PROBLEM

Pau Amaro-Seoane[1], *Patrick Brem*[1], *Jorge Cuadra*[2] *& Philip J. Armitage*[3]

Published in *The Astrophysical Journal Letters, Volume 744, Issue 2, article id. L20, 6 pp. (2012).*

Abstract: Measurements of gravitational waves from the inspiral of a stellar-mass compact object into a massive black hole are unique probes to test General Relativity (GR) and MBH properties, as well as the stellar distribution about these holes in galactic nuclei. Current data analysis techniques can provide us with parameter estimation with very narrow errors. However, an EMRI is not a two-body problem, since other stellar bodies orbiting nearby will influence the capture orbit. Any deviation from the isolated inspiral will induce a small, though observable deviation from the idealised waveform which could be misinterpreted as a failure of GR. Based on conservative analysis of mass segregation in a Milky Way like nucleus, we estimate that the possibility that another star has a semi-major axis comparable to that of the EMRI is non-negligible, although probably very small. This star introduces an observable perturbation in the orbit in the case in which we consider only loss of energy via gravitational radiation. When considering the two first-order non-dissipative post-Newtonian contributions (the periapsis shift of the orbit), the evolution of the orbital elements of the EMRI turns out to be chaotic in nature. The implications of this study are twofold. From the one side, the application to testing GR and measuring MBHs parameters with the detection of EMRIs in galactic nuclei with a millihertz mission will be even more challenging than believed. From the other side, this behaviour could in principle be used as a signature of mass segregation in galactic nuclei.

11.1 MOTIVATION

A stellar mass black hole or neutron star executes $\sim 10^{5-6}$ orbits during the final year of inspiral toward a $\sim 10^6\ M_\odot$ supermassive black hole (MBH). The large number of cycles implies that a phase-coherent measurement of the inspiral, achievable through detection of low frequency gravitational waves, would be a tremendously powerful probe of the spacetime near a black hole (Amaro-Seoane et al. 2007; Hughes 2009).

1 Max Planck Institut für Gravitationsphysik (Albert-Einstein-Institut), D-14476 Potsdam, Germany
2 Departamento de Astronomía y Astrofísica, Pontificia Universidad Católica de Chile, Santiago, Chile
3 JILA, University of Colorado and NIST, at Boulder, 440 UCB, Boulder, CO 80309-0440, USA

Among other things, it would enable a precise determination of the spin of the supermassive black hole, and a test of General Relativity that is independent of current constraints derived from pulsar timing data.

There is no foreseeable instrument sensitive enough to detect gravitational waves from extreme mass ratio inspirals (EMRIs) over time scales comparable to the orbital period. As a consequence, realizing the astrophysical and gravitational physics promise of EMRIs requires an assurance that the inspiral can be accurately modeled over many orbits using templates calculated by solving the 2-body problem in General Relativity (for a review, see e.g., Barack 2009). It is therefore necessary to assess whether gas, stars or other compact objects in the vicinity, could significantly perturb EMRI trajectories. In the case of gas, perturbations to stellar mass black holes or neutron stars[1] are securely negligible provided that accretion on to the black hole occurs in a low density, radiatively inefficient flow (Narayan 2000). Such flows are much more common than dense accretion discs, which *would* yield observable phase shifts during inspiral (Kocsis et al. 2011), at least at the relatively low redshifts where EMRIs may be observed.

In this Letter, we quantify the nature and strength of possible perturbations from point mass perturbers: low mass stars or compact objects in tight orbits around the supermassive black hole. Any perturbers are unlikely to orbit close enough to the EMRI to undergo strong interactions, so the regime of interest is one where the third body is relatively distant and the interaction weak. The Newtonian analog of this problem has been studied extensively in the context both of Solar System satellite evolution, and for transit timing variations of extrasolar planets (Agol et al. 2005; Dermott, Malhotra & Murray 1988; Holman & Murray 2005; Veras, Ford & Payne 2011). In Newtonian gravity, perturbations are strong only at the location of mean motion resonances, and these have the effect of inducing small jumps in eccentricity upon divergent resonance crossing. This would already be interesting for the EMRI problem, since the jumps in eccentricity would result in a perturbation to the gravitational wave decay rate, and an eventual dephasing of the waveform. However, as we will see, the inclusion of post-Newtonian corrections changes the evolution qualitatively. Computing trajectories that include the two first-order non-dissipative post-Newtonian corrections, we find evidence of dependence on initial conditions in the evolution of the perturbed inner binary, such that arbitrarily small variations in the initial orbit lead to significantly different future behaviour.

11.2 ASTROPHYSICAL LIMITS ON PERTURBERS

Is it likely that a star or compact object will be present close enough to perturb the orbit of an EMRI? Excluding low mass MBHs ($M_\bullet < 10^6\ M_\odot$), where the stellar tidal disruption limit comes into play, the existence of perturbers is not excluded by elementary

1 White dwarf EMRIs are excluded here, because mass loss from the compact object itself could form a dynamically significant disc even if the background accretion flow is of low density(Zalamea, Menou & Beloborodov 2010).

arguments. Neither, however, is it easy to calculate the probability distribution of perturbers, whose proximity will depend upon the details of discreteness and relativistic effects very close to the MBH, and mass segregation and EMRI injection mechanisms in galactic nuclei (Amaro-Seoane et al. 2004; Freitag et al. 2006; Preto et al. 2004).

Rather than face these difficulties, we limit ourselves here to order of magnitude estimates for the likely location of the nearest star and compact object. For stars, assumed to be of a single mass M_*, we assume a cusp-like distribution with density profile $\rho \propto R^{-\gamma}$, extending from the MBH to its radius of influence $R_{\rm BH} = GM_\bullet/\sigma^2$. Here σ is the velocity dispersion of the galaxy. Using the fact that the enclosed mass, $M(R) \simeq M_\bullet$ at $R = R_{\rm BH}$, we find that the expected radius of the innermost star, R_1, is,

$$\frac{R_1}{R_g} = \left(\frac{M_*}{M_\bullet}\right)^{1/(3-\gamma)} \left(\frac{c}{\sigma}\right)^2, \tag{134}$$

where $R_g = GM_\bullet/c^2$. This formula yields an explicit estimate for R_1 once we adopt a relation between $M_\bullet$ and σ (Gültekin et al. 2009). For the location of the next nearest compact object (or EMRI), we use an even simpler approach. We calculate the expected semi-major axis for uncorrelated inspirals due to gravitational radiation (Peters 1964), assuming near-circular orbits and rate $\dot{N}_{\rm EMRI}$. Finally, we plot the tidal limit (e.g. Rees 1988) for 0.3 $M_\odot$ main-sequence stars.

Figure 33 shows these estimates as a function of $M_\bullet$. For a standard cusp slope $\gamma = 1.75$, there is likely to be a low mass stellar perturber within a few hundred R_g for $M_\bullet > 10^6\ M_\odot$. Similarly, if the EMRI rate is as high as 10^{-6} yr^{-1}, there is a significant chance (at least a few percent) that a second compact object will be present between $10 - 10^2\ R_g$ for $10^6\ M_\odot < M_\bullet < 10^7\ M_\odot$. Clearly, these crude estimates do not demonstrate that *most* EMRIs will be perturbed by third bodies, but they do suggest that perturbers may be close enough in some galaxies to motivate detailed consideration of their dynamical effects.

11.3 METHODS

We are interested in the secular effect of a star acting on an EMRI which will describe thousands of orbits in the detector bandwidth and slowly decay. The kind of effects on the wave that we are looking at are tiny, though detectable, and the mass difference between the two binaries (the MBH-EMRI and the MBH-star systems) is huge. We need therefore a numerical tool capable of integrating the plunging orbit of the EMRI while inducing a minimal error in the integration, since data analysis techniques can detect e.g. eccentricity differences of the order $\Delta e \sim 10^{-3}$ (Amaro-Seoane et al. 2010; Key & Cornish 2011; Porter & Sesana 2010). We hence have chosen to use a direct $N-$body approach (Aarseth 1999, 2003), the `planet` code, written by Aarseth[2]. This is the most expensive method because it involves integrating all gravitational forces for

2 who, as is his admirable custom, has made the code publicly available `http://www.ast.cam.ac.uk/~sverre/web/pages/nbody.htm`

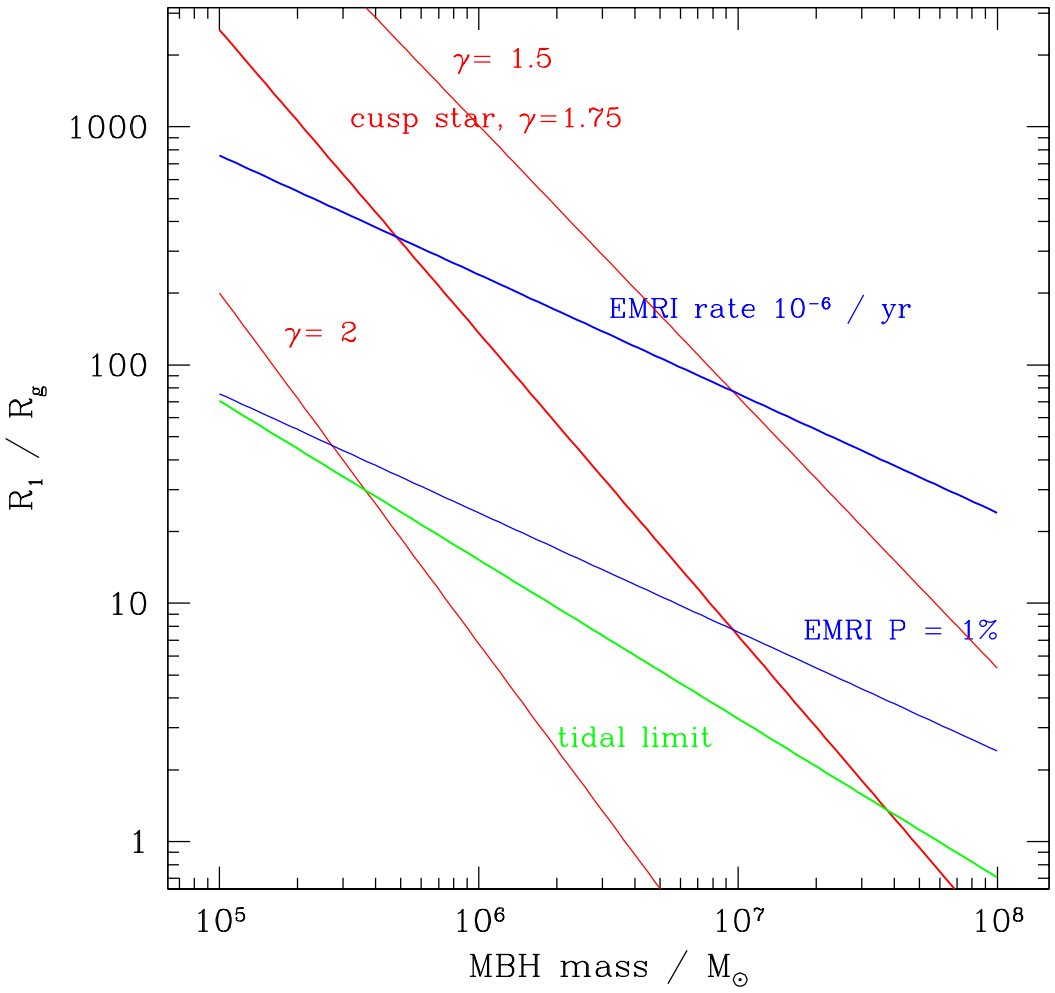

Figure 33: Estimates for the semi-major axis of the innermost perturbing body around a massive black hole, scaled to the hole's gravitational radius $R_g = GM_\bullet/c^2$. The red lines show the location of the innermost star, estimated assuming that stars of mass 0.3 $M_\odot$ follow a single power-law cusp of index γ in a galaxy on the $M_\bullet$-σ relation. The green line shows the tidal disruption limit for such stars. The blue lines show the average (upper) and 1% probability (lower) location of the next nearest EMRI, assuming uncorrelated inspirals at a rate of 10^{-6} yr^{-1}.

all three bodies at every time step, without making any a priori assumptions about the system. Our approach employs the improved Hermite integration scheme, which requires computation of not only the accelerations but also their time derivatives. Since we are simply integrating Newton's equations directly, all gravitational effects are included. For the purpose of our study, nonetheless, we have included relativistic corrections to the Newtonian forces (the forces can be found in the same page in the `toy` code[3]). This was first implemented in a direct-summation $N-$body code by Kupi et al. (2006). For this, one has to add perturbations in the integration, so that the forces are modified by

$$F = \overbrace{F_0}^{\text{Newt.}} + \overbrace{\underbrace{c^{-2}F_2}_{\text{1PN}} + \underbrace{c^{-4}F_4}_{\text{2PN}}}^{\text{periapsis shift}} + \overbrace{\underbrace{c^{-5}F_5}_{\text{2.5PN}}}^{\text{energy loss}} + \overbrace{\mathcal{O}(c^{-6})}^{\text{neglected}} \tag{135}$$

In the last equation "PN" stands for post-Newtonian. We note that the perturbations do not need to be small compared to the two-body force (Mikkola 1997). The expressions for F_2, F_4 and F_5 can be found in Blanchet & Faye (2001), their equation 7.16.

11.4 DISSIPATION OF ENERGY AND RESONANCES

We first analyse the system by contemplating only the relativistic effect of dissipation of energy; i.e. our simulations only incorporate the 2.5 PN correction term. We stop the integration when the separation between the stellar BH and the MBH is $a_\bullet = 5\,R_{\rm Schw}$, which approximately corresponds to the limit where the PN approximation is not valid anymore. The inspiral down to this distance takes typically in our simulations some 440,000 orbits.

In Fig.(34) the test stellar black hole of mass $m_\bullet = 10\,M_\odot$ has been initially set in such an orbit that it is totally embedded in a LISA-like detector band (i.e. with an orbital period $< 10^5$ secs, namely $P_\bullet = 6 \times 10^3$ secs) and is hence an EMRI; its initial semi-major axis is $a_{\bullet,\rm i} \simeq 1.45 \times 10^{-6}$ pc and its eccentricity $e_{\bullet,\rm i} = 0.05$. The perturber, a star of mass $m_\star = 10\,M_\odot$ is initially on an orbit in which the semi-major axis has the value $a_{\star,\rm i} \simeq 4.1 \times 10^{-6}$ pc and the eccentricity at $T = 0$ is $e_{\star,\rm i} = 0.5$. The inclination of the system EMRI – star was set to 30° initially in the upper panel. This constitutes our reference system.

In the figure, the straight lines mark the condition $P_\star/P_\bullet = A$, with A an integer, $P_\star$ the period of the star around the MBH and $P_\bullet$ the period of the EMRI around the MBH; i.e. where the resonances occur. The first three resonances have an impact on $e_\bullet$ which can be seen on the plot; later resonances do also affect $e_\bullet$, with $\Delta e_\bullet \sim 10^{-3}$. We also note that in the upper panel one can see in-between smaller jumps; they correspond to higher-order resonances, $P_\star/P_\bullet$ = 5.5, 6.5 and 7.5.

We made the choice for an initial inclination of 30° to avoid another effect that introduces a change in the eccentricity. In the lower panel we have *exactly* the same

3 `ftp://ftp.ast.cam.ac.uk/pub/sverre/toy/README`

system but for $i_\star = 45^\circ$. With this value, and the fact that the orbit is prograde, the Kozai oscillation of eccentricity is present (Kozai 1962). Even if the eccentricity of the EMRI $e_\bullet$ suffers the characteristic Kozai oscillations, the loci for the resonances still fulfill the condition $P_\star / P_\bullet =$ integer.

11.5 DOES THE FLAP OF THE STAR AT APOAPSIS SET OFF A TORNADO AT PERIAPSIS?

In this subsection we address numerically the effect of including the relativistic periapsis shift along with the dissipation of energy; i.e. the set of corrections as specified in Eq.(135). As we show below, the effect of the periapsis shift changes completely the evolution of the system. In Fig.(35) we show four cases. One of them corresponds to the reference system but taking into account the periapsis shift. We only display these examples but note that the behaviour is also chaotic[4] for other nearby choices of $i_\star$. When using an initial inclination of $i_\star = 45^\circ$, which corresponds to the same situation as in the lower panel of Fig.(34) but taking into account the periapsis shift, along with another case which is identical but for $i_\star = 45.0000000001^\circ$, we find also a chaotic result which moreover eliminates the secular Kozai oscillation of e.

We have systematically studied this chaotic behaviour by running hundreds of simulations in which we methodically increase in minimal differences an initial dynamical orbital parameter such as the inclination, semi-major axis or eccentricity. In all cases and parameters the evolution corroborates the chaotic behaviour of the system. We have also tested a mass for the perturbing star of 5 and $1.44\,M_\odot$, as well as different values of $e_\star$ (0.1, 0.3, 0.7 and 0.9), with similar results.

In order to fence in the region within which the system is chaotic, we systematically increase the semi-major axis of the star and run the same experiment. We start with the same difference in inclination at a slightly larger semi-major axis, and then regularly increase it until we reach one order of magnitude over the fiducial case, as we depict in Fig.(36). The chaotic behaviour ceases at about one order of magnitude of the initial value of $a_\star$ in the reference case.

11.6 QUANTIFYING THE DEPENDENCE ON INITIAL CONDITIONS OF THE SYSTEM

In this section we present a way of characterizing the rate of separation of infinitesimally close trajectories systematically. To achieve this we compare our fiducial model with another case in which we set up the EMRI in an (almost) imperceptibly different initial orbit (the initial difference is 2×10^{-10} pc, while the objects are moving on the same ellipse) and keep the same initial conditions of the MBH and the perturber. Hence EMRI in the second case differs only from the reference case slightly and has

4 When we use the word, we do not follow the rigorous mathematical definition of chaos. We mean a strong dependence on the initial conditions.

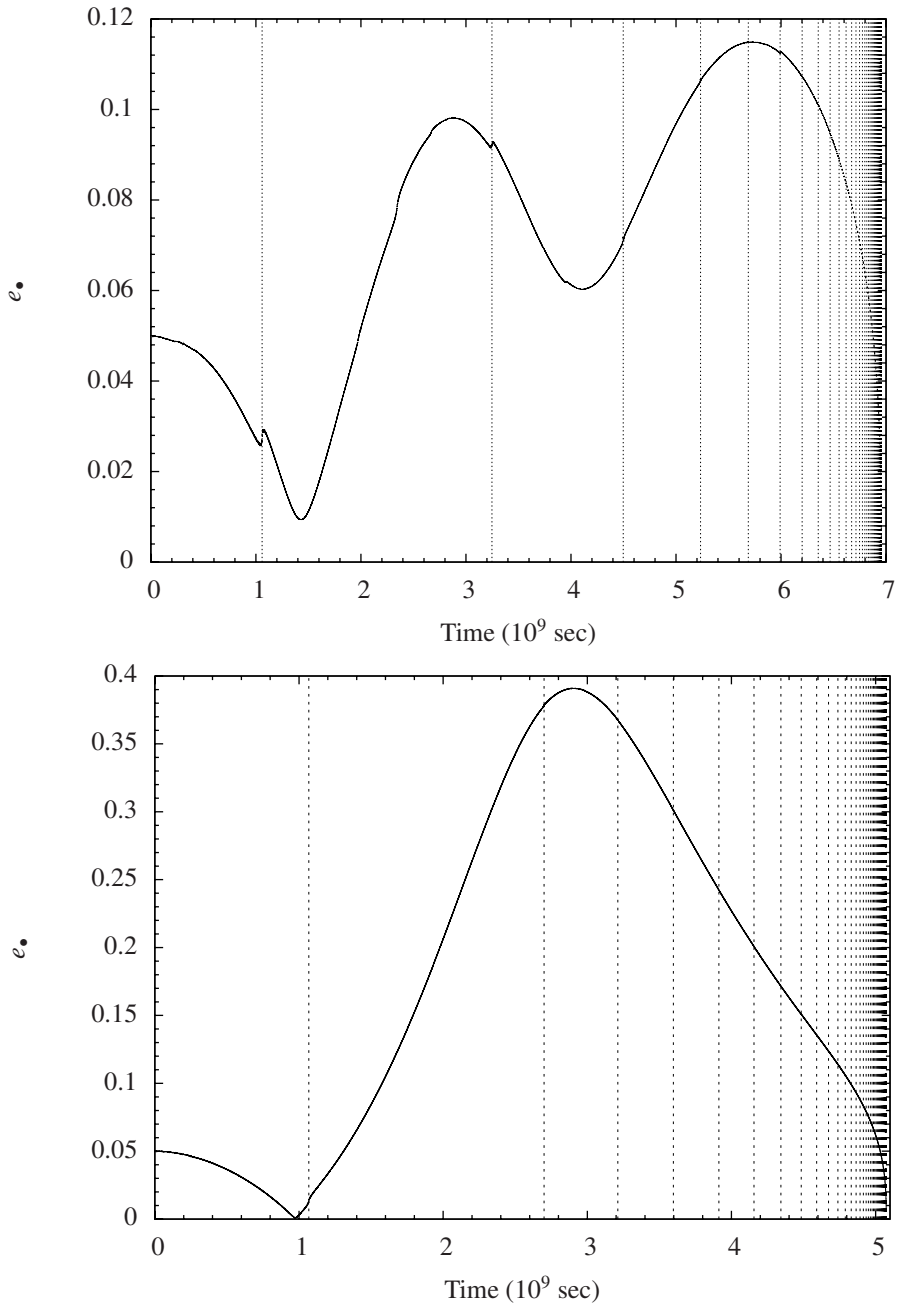

Figure 34: *Upper panel:* Results for the fiducial case using the direct-summation $N-$body integrator. The mass of the MBH is $\mathcal{M}_\bullet = 10^6\,M_\odot$, the mass of the stellar black hole is $m_\bullet = 10\,M_\odot$. See text for more details. *Lower panel:* Same configuration but with an initial inclination of the star of $i_\star = 45^\circ$ instead of 30°, i.e. the inclination triggers the Kozai mechanism, since $i_\star > 39.2^\circ$ *and* the orbit is prograde. As mentioned in the previous case, even if the changes in eccentricity cannot be directly seen in the curve, they are of the order $\Delta\, e_\bullet \sim 10^{-3}$.

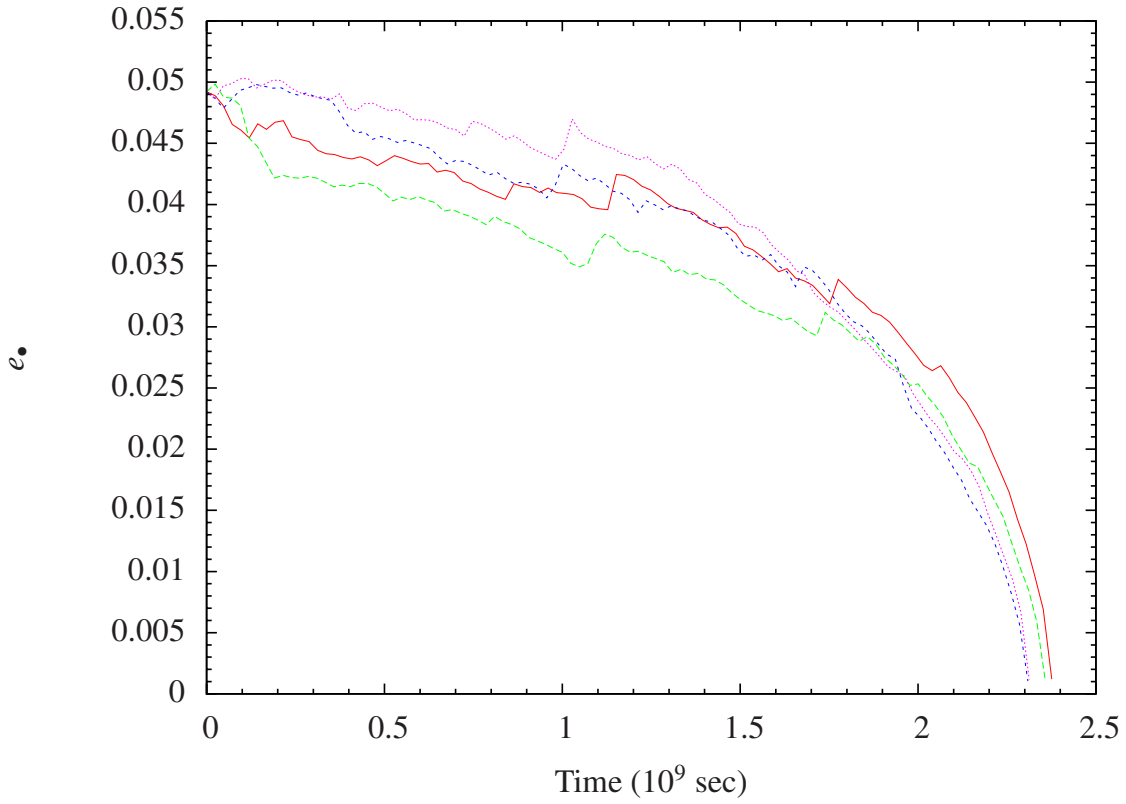

Figure 35: Fiducial case with energy dissipation and periapsis shift correcting terms for different initial inclinations of the perturber. The solid (red) curve corresponds to $i_\star = 30°$, the long-dashed (green) to $i_\star = 30.001°$, the short-dashed (blue) corresponds to the fiducial case plus a *billionth* of a degree, $i_\star = 30.0000000001°$ and the dotted (magenta) to the reference plus a 10^{-13} of a degree, $i_\star = 30.0000000000001°$.

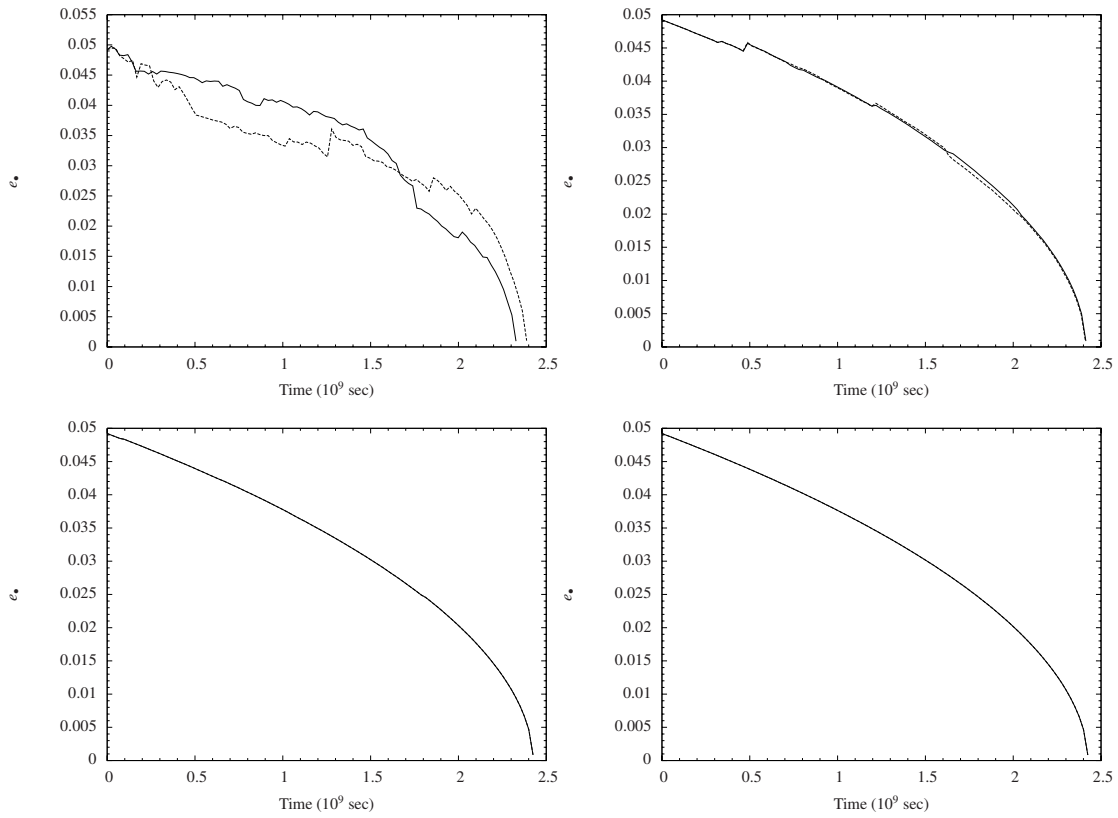

Figure 36: Same as in Fig.(35) but we set initially the perturber at a larger and larger initial semi-major axis. From the top to bottom and from the left to the right, the semi-major axis of the perturber is $a_\star = 4 \times 10^{-6}$ pc, 6×10^{-6} pc, 9×10^{-6} pc and 4.07243×10^{-5} pc. Solid lines correspond to $i_\star = 30^\circ$ and dashed lines to $i_\star = 30.0000000001^\circ$.

an initial distance separation of r_0. We say that the two models are in phase provided that

$$r \approx r_0. \tag{136}$$

If the two different realizations reach a separation

$$r \approx 2\,a_\bullet \tag{137}$$

the EMRI bodies are moving out of phase, on entirely unrelated orbits. We thence are able to estimate a characteristic timescale $\tau_{\rm deph}$ for the system to become out of phase. In Fig.(37) we display the separation of the two systems for different distances to the perturber. From these figures we can measure the value of a characteristic timescale $\tau_{\rm deph}$ for a given $a_\star$.

From the data points obtained in the upper panels of Fig.(37) we can then derive the relation displayed in the lower panel. For large enough distances, of the order of $\sim 10^{-5}$ pc the two timescales converge and the system becomes deterministic.

11.7 CONCLUSIONS

In this paper we have addressed the role of a perturbation on an EMRI by a nearby star. The system depends extremely on *minimal* changes in the initial conditions (as small as a 10^{-9} part in the inclination) lead to a very different dynamical evolution. In all cases, however, the Kozai mechanism is washed out by the periapsis shift, as one can expect (see e.g. Blaes et al. 2002; Holman et al. 1997). For distances of the order of $a_\star \sim 10^{-5}$ pc the system enters the chaotic regime, for perturbing masses as small as $1.44\,M_\odot$. While we cannot state clearly whether this will be a common feature for EMRIs, since the different dynamical and relativistic phenomena involved in the problem are many and not straightforward (see for a review Amaro-Seoane et al. 2007 and also Amaro-Seoane 2011 for a dedicated review of the dynamics), it seems plausible that for a Milky Way-like galaxy a star can be at such a radius from the EMRI system that it will significantly perturb it. From the standpoint of detection and data analysis, this is yet another complication of the problem and could even lead to the misinterpretation that nature's GR is not what we believe it to be. On the other hand, from the point of view of stellar dynamics, the detection of one of these systems would shed light on our current understanding of galactic dynamics in general and mass segregation in particular.

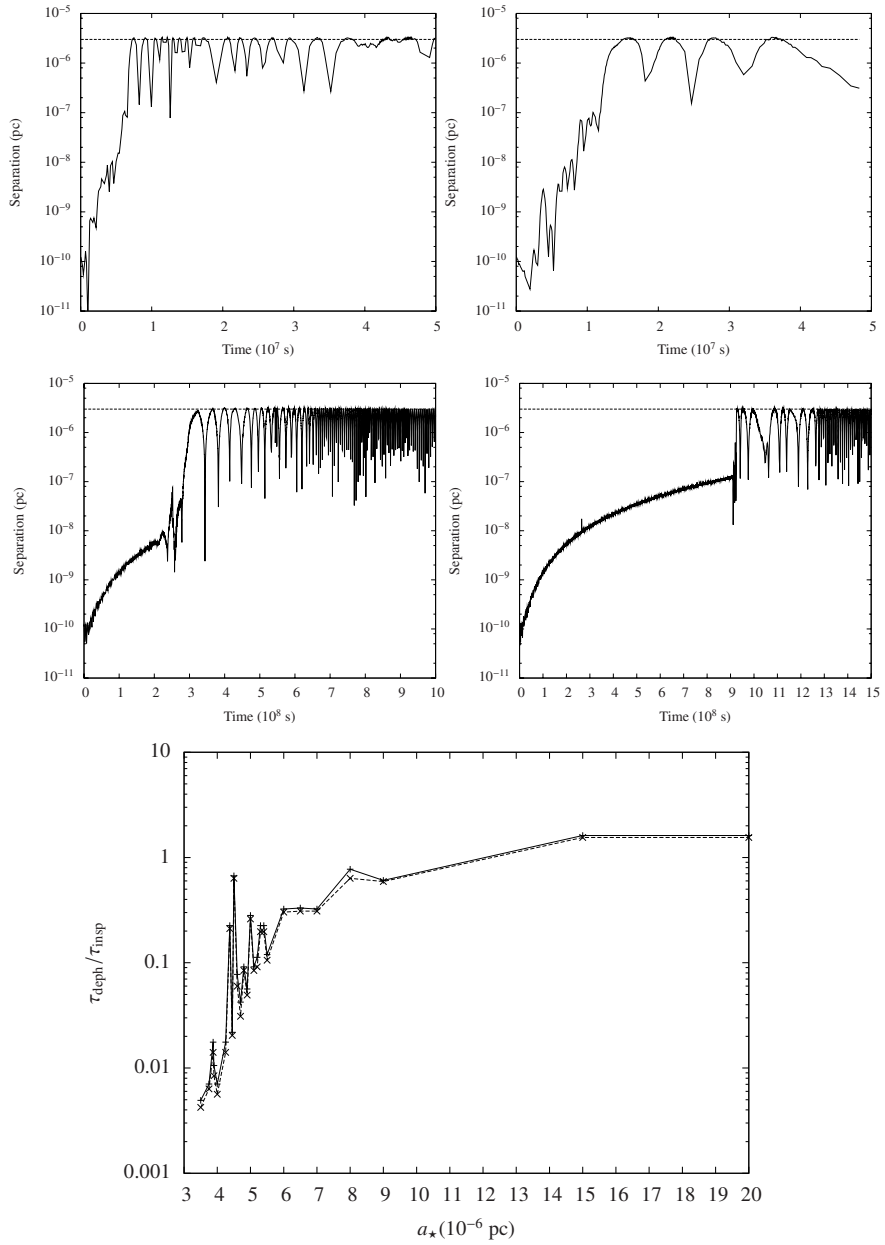

Figure 37: *Upper panels:* From the left to the right and from the top to the bottom we show the separation r for a increasing separation of the perturbing star of 3.5×10^{-6}, 3.9×10^{-6}, 4.375×10^{-6}, and 4.5×10^{-6} pc. The dashed line shows the critical distance $2\,a_\bullet$. Note the different timescales in the lower panels. *Lower panel:* $\tau_{\rm deph}$ against distance to the perturber normalized to the gravitational radiation timescale of the isolated system $\tau_{\rm insp}$; i.e. the merger timescale without the perturber acting onto the binary MBH-EMRI.

BIBLIOGRAPHY

Aarseth, S. J. 1999, The Publications of the Astronomical Society of the Pacific, 111

——. 2003, Gravitational N-Body Simulations (ISBN 0521432723. Cambridge, UK: Cambridge University Press, November 2003.)

Agol E., Steffen J., Sari R., Clarkson W., 2005, MNRAS, 359, 567

Amaro-Seoane, P., Freitag, M., & Spurzem, R. 2004, MNRAS

Amaro-Seoane P., Gair J. R., Freitag M., Miller M. C., Mandel I., Cutler C. J., Babak S., 2007, Classical and Quantum Gravity, Vol. 24, Issue 17, R113

Amaro-Seoane P., 2011 Living Reviews in Relativity (to be submitted soon)

Amaro-Seoane, P., Eichhorn, C., Porter, E. K., & Spurzem, R. 2010, MNRAS, 401, 2268

Amaro-Seoane, P., & Preto, M. 2011, Classical and Quantum Gravity, 28, 094017

Barack L., 2009, Classical and Quantum Gravity, Vol. 26, Issue 21, pp. 213001

Blaes, O., Lee, M. H., & Socrates, A. 2002, ApJ, 578, 775

Blanchet, L., & Faye, G. 2001, Phys. Rev. D, 63, 062005

Dermott S. F., Malhotra R., Murray C. D., 1988, Icarus, 76, 295

Freitag, M., Amaro-Seoane, P., & Kalogera, V. 2006, ApJ, 649, 91

Ghez, A. M. et al. 2008, ApJ, 689, 1044

Gültekin K., et al., 2009, ApJ,698, 198

Holman M. J., Murray N. W., 2005, Science, 307, 1288

Holman, M., Touma, J., & Tremaine, S. 1997, Nature, 386

Hughes S. A., 2009, ARA&A, 47, 107

Key, J. S., & Cornish, N. J. 2011, Phys Rev D, 83

Kocsis, B., Yunes, N., & Loeb, A. 2011, Phys. Rev. D, 84, 024032

Kozai, Y. 1962, AJ, 67

Kupi, G., Amaro-Seoane, P., & Spurzem, R. 2006, MNRAS, L77+

Mikkola, S. 1997, Celestial Mechanics and Dynamical Astronomy, 68

Narayan R., 2000, ApJ, 536, 663

Peters P. C., 1964, Physical Review, 136, 1224

Porter, E. K., & Sesana, A. 2010, ArXiv e-prints, arXiv:1005.5296

Preto, M., Merritt, D., & Spurzem, R. 2004, ApJ Lett., 613

Preto, M., & Amaro-Seoane, P. 2010, ApJ Lett., 708, L42

Rees, M. J. 1988, Nature, 333, 523

Veras D., Ford E. B., Payne M. J., 2011, MNRAS, 727, 74

Zalamea I., Menou K., Beloborodov A. M., 2010, MNRAS, 409, L25

12

INVESTIGATING THE RETENTION OF INTERMEDIATE-MASS BLACK HOLES IN STAR CLUSTERS USING *N*-BODY SIMULATIONS

Symeon Konstantinidis[1], **Pau Amaro-Seoane**[2], *& Kostas D. Kokkotas*[3]

Published in *Astronomy & Astrophysics, Volume 557, id.A135, 8 pp. (2013).*

Abstract: Contrary to supermassive and stellar-mass black holes (SBHs), the existence of intermediate-mass black holes (IMBHs) with masses ranging between $10^{2-5}\,M_{\odot}$ has not yet been confirmed. The main problem in the detection is that the innermost stellar kinematics of globular clusters (GCs) or small galaxies, the possible natural loci to IMBHs, are very difficult to resolve. However, if IMBHs reside in the centre of GCs, a possibility is that they interact dynamically with their environment. A binary formed with the IMBH and a compact object of the GC would naturally lead to a prominent source of gravitational radiation, detectable with future observatories. We use *N*-body simulations to study the evolution of GCs containing an IMBH and calculate the gravitational radiation emitted from dynamically formed IMBH-SBH binaries and the possibility that the IMBH escapes the GC after an IMBH-SBH merger. We run for the first time direct-summation integrations of GCs with an IMBH including the dynamical evolution of the IMBH with the stellar system and relativistic effects, such as energy loss in gravitational waves (GWs) and periapsis shift, and gravitational recoil. We find in one of our models an intermediate mass-ratio inspiral (IMRI), which leads to a merger with a recoiling velocity higher than the escape velocity of the GC. The GWs emitted fall in the range of frequencies that a LISA-like observatory could detect, like the European eLISA or in mission options considered in the recent preliminary mission study conducted in China. The merger has an impact on the global dynamics of the cluster, as an important heating source is removed when the merged system leaves the GC. The detection of one IMRI would constitute a test of GR, as well as an irrefutable proof of the existence of IMBHs.

12.1 MOTIVATION

Intermediate-mass black holes (IMBHs), with masses $M \sim 10^{2-5}$ $M_{\odot}$ possibly exist at the centres of globular clusters (GCs) or small galaxies, if we assume that they follow the observed correlations between super-massive BHs (SMBHs) and their stellar surroundings (see Gültekin et al. 2009; Miller 2009; Miller & Colbert 2004; Tremaine et al. 2002, and references therein). Due to their mass, these objects cannot form via

1 Astronomisches Rechen-Institut, Mönchhofstraße 12-14, 69120, Zentrum für Astronomie, Universität Heidelberg, Germany

2 Max Planck Institut für Gravitationsphysik (Albert-Einstein-Institut), D-14476 Potsdam, Germany

3 Theoretical Astrophysics (TAT), IAAT, Eberhard Karls University of Tübingen, Auf der Morgenstelle 10, 72076 Tübingen, Germany, and Department of Physics, Aristotle University of Thessaloniki, Thessaloniki 54124 Greece

the formation scenarios of stellar-mass black holes, which are the final results of stellar evolution of massive stars (Belczynski et al. 2010; Fryer 1999; Fryer & Kalogera 2001) or SMBHs with masses $M \sim 10^{6-9}\,M_\odot$, that exist at the centres of galaxies (Gillessen et al. 2009; Rees 1978, 1984) and for which there exists an emerging consensus about their formation (Madau & Rees 2001; Volonteri & Rees 2005).

There have been proposed several scenarios for the formation of IMBHs most of which require extremely dense environments, similar to the centers of GCs, for the IMBHs to form and grow in mass (Miller & Colbert 2004; van der Marel 2004). Miller & Hamilton (2002) suggest in their work that such massive black holes (BHs) can form from repeated mergers of a $\sim 50\,M_\odot$ BH, located at the center of a GC, with other SBH of lower mass. The $\sim 50\,M_\odot$ threshold is required to ensure that the BH will not receive large recoil velocities after each merger and so will remain bound to the GC. According to (Miller & Hamilton 2002) the initial $\sim 50\,M_\odot$ BH could be formed either directly from the collapse of a massive star, or from a large number of SBH-SBH mergers, which would produce mostly escaping SBHs, but also a minority of large BHs, bound to the GC.

An interesting scenario for the formation of IMBHs in the early evolution of GCs, has been studied by Freitag et al. (2006a); Gürkan et al. (2004); Portegies Zwart et al. (2004); Portegies Zwart & McMillan (2000, 2002); Quinlan & Shapiro (1990). According to this scenario, the most massive stars sink to the centre of a GC even before they become BHs and thus the cluster experiences an early core collapse during which the central density of stars becomes large enough, that massive stars start to rapidly and continuously merge with each other (see also Goswami et al. 2012; Portegies Zwart et al. 2004). This runaway process very soon leads to the formation of a very massive star (VMS), located close to the centre of the GC. It is unknown how stellar evolution proceeds in such a VMS (Glebbeek et al. 2009), but if it is assumed that the star directly collapses to a BH, without significant mass-loss, this could form an IMBH. Accretion of stars and gas during the next Myrs could increase its mass up to two orders of magnitude (Vesperini et al. 2010). Finally, as in SMBHs, Population III stars have been proposed as possible progenitors of IMBHs (see van der Marel 2004; Whalen & Fryer 2012, and references therein), but there are still many uncertainties in the evolution of such a star (Heger & Woosley 2002).

Although the formation of IMBHs has been studied extensively during the last decades and their existence has been proposed in the early 70s (Bahcall & Ostriker 1975; Frank & Rees 1976; Wyller 1970), there is still no direct proof of their existence. However, there is an increasing number of favouring evidences that suggest that they should exist. The most prominent evidence is from the observations of ultra-luminous X-ray sources (ULXs, Feng & Soria 2011), which are usually associated to IMBHs. The brightest known ULX, known as HLX-1, is located in the outskirts of the edge-on Soa type galaxy ESO243-49 and is currently the strongest IMBH candidate. Based on the extreme luminosity of the X-ray source, which has a maximum of up to $1.1 \times 10^{42}\,\mathrm{erg\,s^{-1}}$ in the $0.2 - 10$ keV band, Farrell et al. (2009) derive a conservative lower limit of $500\,M_\odot$ for the potential IMBH (see also Farrell et al. 2010; Godet et al. 2009). More recent ob-

servations measured a peak luminosity of 1.3×10^{42} erg s^{-1} (Godet et al. 2011) and a possible period of variability of $\sim$ 1yr (Godet et al. 2012; Servillat et al. 2011). X-ray luminosities up to $\sim 10^{41}$ erg s^{-1} can be explained by super-Eddington accretion to $\sim 20\,M_\odot$ SBHs (Begelman 2002) and/or beaming (King 2008). However, larger BH masses are needed for explaining luminosities $> 10^{41}$ erg s^{-1}. For HLX-1 the most recent estimate for the mass of the potential IMBH is $\sim 3 \times 10^3 - 10^5\,M_\odot$ (Davis et al. 2011; Godet et al. 2012; Servillat et al. 2011), very well in the range of masses of IMBHs. Further investigations of HLX-1 confirmed its extraordinary luminosity by proving its association with galaxy ESO243-49 at a distance of 95 Mpc (Wiersema et al. 2010), and thus made the evidence of an IMBH even stronger. Interestingly, the X-ray source is not located at the center of the host galaxy, but it lies at a distance ~ 3.3 kpc from its center and ~ 0.8 kpc out of the galactic plane, possibly associated with a star cluster which appears to be in the same area. According to Farrell et al. (2012) this cluster has a mass of $\sim 4 \times 10^6\,M_\odot$ and is either a massive young star cluster or an old GC. Optical observations of HLX-1 with VLT seem to rule out the case of a massive star cluster and favour the presence of a ~ 10 Gyr old globular cluster with mass $< 10^6\,M_\odot$ or a < 10 Myr small star cluster with mass $\sim 10^4\,M_\odot$ (Soria et al. 2012, 2010).

Other recent interesting observational examples that point to the existence of these objects can be found in the work of Sutton et al. (2012), which evaluates a sample of eight extreme luminosity ultra-luminous X-ray source candidates and state that the observed luminosities can be explained in terms of IMBHs with masses in the range of $10^3 - 10^4\,M_\odot$. Another X-ray source that might be associated with an IMBH is found at the center of the nearby (d $= 3.1$ Mpc, Karachentsev et al. (2004)) dwarf lenticular galaxy NGC 404 (Binder et al. 2011). Using both stellar and gas dynamical mass estimates, Seth et al. (2010) estimated the mass of the potential IMBH to be $\sim 10^5\,M_\odot$, which agrees with recent estimates from Expanded Very Large Array observations (Nyland et al. 2012) and from X-ray observations (Binder et al. 2011). Finally, Nyland et al. (2012) confirmed the location of the source at the center of the nuclear star cluster hosted by NGC 404 and ruled out other possible scenarios such as an X-ray binary, stellar formation or a supernova remnant.

The above observational examples provide strong evidence of the existence of IMBHs, but do not indisputably prove that they exist. A direct proof would come from detailed kinematical observations of stars moving under the influence of the IMBH at the centers of GCs. Unfortunately, the radius of influence of an IMBH is only of a few arc seconds (Chanamé et al. 2010; Miller & Colbert 2004; Peebles 1972), so it is very difficult, if not impossible, to accurately determine its mass by measuring the velocities of stars moving under its influence, with the currently available instruments. This technique has been successfully used for determining the mass of the SMBH at the centre of the Milky Way galaxy, where the stellar environment is less dense than the core of GCs and also there exists a number of young and bright stars, moving under the gravitational influence of the SMBH which have been followed by observations for

more than 15 years (Gillessen et al. 2009). The radius of influence R of an IMBH of mass $M_\bullet$ can be defined as:

$$R = \frac{GM_\bullet}{\sigma^2}, \tag{138}$$

where σ the velocity dispersion at the center of the cluster. At a distance d this translates to an angular radius of influence (Bender 2005):

$$\alpha = 1''\Big(\frac{M_\bullet}{10^3\ \mathrm{M}_\odot}\Big)\Big(\frac{\sigma}{10\ \mathrm{km\ s^{-1}}}\Big)^{-2}\Big(\frac{d}{10\ \mathrm{kpc}}\Big)^{-1} \tag{139}$$

For a $10^4\,\mathrm{M}_\odot$ IMBH the influence radius is of $\sim 5''$, assuming a central velocity dispersion of $\sigma = 20\ \mathrm{km\,s^{-1}}$ and a distance of ~ 5 kpc (see also Miller & Colbert 2004, for a similar example). Also, since GCs are old systems, this small sphere of influence contains mainly massive stellar remnants and old, dim stars that could not be easily observed and traced. For the above reasons, kinematical techniques can currently only give upper limits on the mass of the potential IMBHs at the centers of galactic GCs (Anderson & van der Marel 2010; Lützgendorf et al. 2012; Noyola et al. 2010; van der Marel & Anderson 2010) (see also Kirsten & Vlemmings 2012; Strader et al. 2012, for observations that do not support the IMBH scenario). Since such limits are based on measurements of proper motions, velocity dispersion or line of sight motions away of the sphere of influence of the potential IMBH, alternative to IMBH explanations cannot be ruled out (Baumgardt et al. 2003, 2005). Hence, we would need the Very Large Telescope Interferometer (VLTI) and one of the next-generation near-infrared instruments, the VSI or GRAVITY (Eisenhauer et al. 2008; Gillessen et al. 2006). In that case we could improve the astrometric accuracy by an order of magnitude and thus we would possibly be in the position of detecting the innermost kinematics of a GC around a potential IMBH and thus measure accurately its mass.

An interesting avenue towards the *direct* detection of an IMBH, which would not require future optical or infrared telescopes and several years of observations, is GW astronomy. Additionally, IMBH-SBH binaries that might form in GCs represent an excellent test of GR, since they are similar to extreme mass-ratio inspirals (Amaro-Seoane et al. 2007). In particular, space-borne detectors such as the ESA-led eLISA (Amaro-Seoane et al. 2012) or Chinese mission study options ("ALIA" from now onwards, see Bender et al. 2005; Crowder & Cornish 2005; Gong et al. 2011) will be able to catch these systems (which might also be referred as intermediate mass-ratio inspirals, IMRIs) with good signal-to-noise ratios (SNR) if the GC is not further than $z \sim 0.7$ (Amaro-Seoane et al. 2012; Miller 2006; Miller & Hamilton 2002). According to Miller & Hamilton (2002), LISA will be able to detect around 10 IMBH-SBH binaries at any given time, while the merger of the BHs might be detectable by LIGO-II (and Advanced LIGO should see many of them Amaro-Seoane & Santamaría 2010; Fregeau et al. 2006).

If an IMRI forms in a GC, it is undoubted that sooner or later it will lead to an IMBH-SBH merger. Recent studies from numerical relativity (Lousto et al. 2010; Lousto & Zlochower 2011a,b; Koppitz et al. 2007; Pollney et al. 2007; Rezzolla 2009; Rezzolla et al.

2008) show that BH-BH mergers result to a gravitational wave recoil which, depending on the mass-ratio and spins of the merging BHs, might be as large as ~ 5000 km s^{-1} (Lousto & Zlochower 2011a). The mass-ratio of an IMRI in a GC is large enough to avoid such large recoils, but it is still possible for an IMBH of mass up to $\sim 10^3$ M$_\odot$ to receive a kick greater than the escape velocity of the GC and therefore leave the system (Holley-Bockelmann et al. 2008).

In this work we use N-body simulations to study the interactions of an IMBH with SBHs in young star clusters and describe, for the first time, the production on an IMRI with our direct-summation code in one of our integrations. In Section 12.2 we describe the numerical tool and choice of the initial data used for the simulations. In Section 12.3 we describe the interactions of the IMBH with SBHs in the simulation we observed an IMRI, and we discuss the possibility that the gravitational recoil velocity assigned to the IMBH after the merger, kicks the IMBH out of the GC. In Section 12.4 we calculate the gravitational radiation from such an IMRI in an approximate way. Finally, in Section 12.5 we conclude our work showing that an IMRI would be detectable by future space-based GW detectors, such as LISA, we discuss the effects of the ejection of the IMBH on the GC, their possible connection with ULXs not associated with GCs and we present our future plans for a statistical study of IMBH-SBH interactions in GCs.

12.2 NUMERICAL TOOL AND INITIAL CONDITIONS

We integrate the dynamical evolution of a globular cluster containing a $500-1000$ M$_\odot$ IMBH with `Myriad` (Konstantinidis & Kokkotas 2010), a direct-summation $N-$body code that integrates all gravitational forces for all particles at every time step. The programme uses the Hermite integration scheme (Aarseth 1999, 2003). This requires computation of not only the accelerations, but also their time derivatives. Particles that are tightly bound or with very small separation are integrated using the time-symmetric Hermite scheme (Kokubo et al. 1998), which is a symplectic integrator that makes the numerical errors oscillate between two limits that can be controlled by the choice of the time step. The code uses post-Newtonian correcting terms to the Newtonian forces, including 1, 2 and 2.5 order, as described for the first time in an $N-$body code by Kupi et al. (2006) (their equations 1, 2 and 3), as well as a recipe for gravitational recoil. The recoil velocity depends strongly on the mass ratio of the two holes, on the magnitude of their spins and on their directions with respect to the plane of the orbit (see e.g. Rezzolla 2009, and references therein). The equation that we have implemented in the code is taken from Lousto et al. (2010),

$$\vec{v} = (v_m + v_\perp \cos\xi)\ \hat{e}_1 + v_\perp \sin\xi\, \hat{e}_2 + v_\parallel\, \hat{e}_3. \tag{140}$$

In the last equation, the indices $\perp$ and $\parallel$ stand for perpendicular and parallel directions with respect to the orbital angular momentum vector $\vec{L}$ of the binary. $\hat{e}_1$ is a unit vector and lies on the plane of the orbit connecting the two MBHs, with direction from the

heavier to the lighter one. $\hat{e}_2$ is also on the plane of the orbit, but perpendicular to $\hat{e}_1$, with direction such that $\hat{e}_1$, $\hat{e}_2$ and $\hat{e}_3$ construct an orthonormal system, with $\hat{e}_3$ defined such that it is the unit vector parallel to $\vec{L}$. ξ is the angle between the unequal contributions of mass and spin to the recoil velocity. We assign random, maximal spins to the stars of the GC, and in particular we initially give the IMBH a spin $a = S/M^2$ (see e.g. Lousto et al. 2010) of 0.998.

We assume that the IMBH forms at the center of the cluster when the GC is 10 Myr old. This agrees with the formation scenario of runaway stellar mergers (Portegies Zwart & McMillan 2002) and also of the repeated SBH-SBH mergers (Miller & Hamilton 2002). For our study the number and masses of SBHs are of particular importance. Therefore, before creating the initial data for our simulations, we studied the number of SBHs and their masses assuming different initial mass functions (IMF) and metallicities. For the initial mass function (IMF) we use Kroupa-like distributions (see Kroupa 2001a; Kroupa et al. 1993) and also simple power law distributions with different values for the slope α (see Salpeter 1955). We fix the total number of stars to $N = 32768$, the lower stellar mass limit to $m_{\rm low} = 0.2\ {\rm M}_\odot$ and the upper mass limit to $m_{\rm upper} = 150\ {\rm M}_\odot$. Finally, we use values for the metallicity Z ranging from 0.0001 to 0.02. We investigate in total 15 models with different slopes of the IMF and metallicities and for each one of them we create a set of 100 random realisations. We evolve the stars of each realisation to 10 Myr using the stellar evolution code `sse` (Hurley et al. 2000) and we calculate averages for the number of SBH created and also for their higher and lower masses. The results are described in Table 5. Assuming no supernova kicks, the number of SBHs created depends strongly on the choice of the IMF slopes and ranges from ~ 20 to ~ 70 in our models. On the other hand the masses of the SBHs depend on the metallicity and range from $\sim 3\ {\rm M}_\odot$ (for Z = 0.02) to $\sim 27\ {\rm M}_\odot$ (for Z < 0.001).

For the initial data of our simulations, we picked 4 representative cases from our investigation that produce low and high numbers of SBHs. We also picked a value Z = 0.001 for the metallicity as typical for a GC which resulted in the formation of SBHs with masses between $\sim 13\ {\rm M}_\odot$ and $27\ {\rm M}_\odot$. In those models all stars with masses above $20\ {\rm M}_\odot$ have evolved off the main sequence at 10 Myr.

For our fiducial simulation A, we choose slopes $\alpha_1 = 1.3$ and $\alpha_2 = 2.4$, which, after stellar evolution until $t = 10$ Myr, result in 62 stellar-mass BHs in the system, close to the highest number of SBHs created in our models. For the distribution of stars and BHs in the cluster, we use a King profile (King 1966) with concentration parameter $W_0 = 7$. The initial escape velocity at the centre of the cluster is $\sim 17\,{\rm km\,s^{-1}}$. At the centre of the cluster we introduce an IMBH of mass $M_\bullet = 500\,{\rm M}_\odot$ and correct the velocities of all stars and BHs of the GC to reach dynamical equilibrium. We created also three additional initial data changing the IMF, the mass of the IMBH and/or the initial concentration of the clusters. Case B is like A but with $M_\bullet = 1,000\,{\rm M}_\odot$ and $\alpha_2 = 2.5$, which results in 52 SBHs; case C is like B but with a King parameter of 6 and 48 SBHs. Finally, case D is like A but with a King parameter of 6 and $\alpha_1 = 1.2$ and

IMF	Z	$N_{\rm BHs}$	$M_{\rm BH\,max}$	$M_{\rm BH\,min}$
Kroupa '93	0.02	26 ± 4	14.11 ± 0.90	3.33 ± 0.28
Kroupa '93	0.001	22 ± 5	25.58 ± 2.60	14.50 ± 0.22
Kroupa '93	0.0001	23 ± 4	26.46 ± 0.64	15.35 ± 1.54
Kroupa '01	0.02	71 ± 9	15.00 ± 0.26	3.14 ± 0.15
Kroupa '01	0.001	68 ± 9	26.19 ± 0.16	13.88 ± 0.08
Kroupa '01	0.0001	69 ± 9	26.88 ± 0.23	14.13 ± 1.24
Salpeter	0.02	54 ± 6	14.77 ± 0.47	3.19 ± 0.17
Salpeter	0.001	50 ± 6	26.05 ± 0.30	13.38 ± 0.01
Salpeter	0.0001	51 ± 6	26.74 ± 0.40	14.12 ± 1.51
Power Law ($\alpha = 2.5$)	0.02	29 ± 5	14.21 ± 0.85	3.38 ± 0.32
Power Law ($\alpha = 2.5$)	0.001	26 ± 4	25.86 ± 0.52	14.88 ± 0.22
Power Law ($\alpha = 2.5$)	0.0001	27 ± 4	26.38 ± 0.62	15.66 ± 2.06
Power Law ($\alpha = 2.4$)	0.02	45 ± 6	14.60 ± 0.68	3.25 ± 0.24
Power Law ($\alpha = 2.4$)	0.001	41 ± 6	26.03 ± 0.28	13.11 ± 1.70
Power Law ($\alpha = 2.4$)	0.0001	42 ± 6	26.77 ± 0.32	14.47 ± 1.67

Table 5: Description of the full set of initial data created for the investigation of the BH number and masses using different IMFs. We use a Kroupa '93 (Kroupa et al. 1993), a Kroupa '01 (Kroupa 2001b), a Salpeter (Salpeter 1955) and two simple power law mass functions with slopes $\alpha = -2.5, -2.4$. For each IMF we use three different values for the metallicity (Z), 0.0001, 0.001 and 0.02 and we create 100 realisations for each IMF-Z combination. We then evolve the stars up to 10 Myr using the stellar evolution code `sse`. Finally, we find averages for the number of BHs (third column) and their minimum (fourth column) and maximum (fifth column) masses. In all data sets the total number of stars is 32768 and their initial masses range from $0.2 M_\odot$ to $150 M_\odot$.

Case	α_1	α_2	$N_{\rm BHs}$	W_0	$M_{\rm IMBH}\ [M_\odot]$
A	1.3	2.4	62	7	500
B	1.3	2.5	52	7	1000
C	1.3	2.5	48	6	1000
D	1.2	2.7	17	6	500

Table 6: Initial data for the 4 simulations.

$\alpha_2 = 2.7$, which result in only 17 SBHs, close to the lower number of SBHs created in our test models. The initial data for the 4 simulations are described in Table 6.

We performed the dynamical evolution of each of the 4 models using `Myriad`, which treats the stars and stellar remnants as point particles, but takes into account their sizes in the case of collisions. No primordial mass segregation is taken into account, so the BHs are formed in all the distances from the centre of the cluster. The absence of initial mass-segregation leads to an underestimate of the initial frequency of IMBH-SBH interactions, but, as we will show below, most of the most massive SBHs sink to the center and interact with the IMBH very soon. Stellar evolution is only used for creating the initial data for our models. During the N-body simulations stellar evolution is turned off, so the masses of stars and the masses and the number of remnants remain constant in time. This is a simplification, which does dot have a significant impact on the dynamics of the IMBH and therefore on our results. Further (i.e. after the 10 Myr of the initial data) stellar evolution would create a number of SBHs with very low mass ($< 10\ \mathrm{M}_\odot$), which would have a negligible influence on the dynamics of the IMBH and on a possible binary that the IMBH would form with one of the higher-mass SBHs. Low-mass SBHs are expected not to be able to replace higher-mass SBH as companions of the IMBH. Instead, they are expected to be ejected easily through natal kicks and interactions with the IMBH and other higher-mass SBHs (Baumgardt et al. 2004).

From our set of simulations, only case A had an IMRI; we will therefore focus on this case in the remainder of the article. As of now, `Myriad` runs only with the assistance of the special-purpose GRAPE system (Makino et al. 2003), so that we are subjected to the the availability and performance of GRAPE systems.

12.3 DYNAMICS OF THE SYSTEM

Initially, the IMBH interacts strongly with a sub-group of stars and SBHs that contains approximately 20 members. As the system evolves, the members of this sub-group change. Soon, most of the stellar-mass BHs of the system sink towards the centre and start to interact with the IMBH and its environment. During this process, some of them receive big kicks due to 3-body interactions and are slingshot away from the centre of the cluster or GC itself. After $T \sim 3$ Myr the first stable IMBH-SBH binary forms. The companion of the IMBH is a SBH with mass $m_{\bullet,11} = 23.9\,\mathrm{M}_\odot$ and the initial semi-major

axis of this binary is $a \sim 88$ AU. At $T \sim 9.2$ Myr this binary has a strong interaction with another SBH of the system. The interaction leads to a change of companion for the IMBH, which now builds a binary with a SBH of mass $m_{\bullet,18} = 20.1\,M_\odot$. The initial semi-major axis of the new binary is $a \sim 17.6$ AU. This binary survives for nearly 40 Myr, but its characteristics vary significantly. At $T \sim 49$ Myr the semi-major axis changes to $a \sim 5$ AU, while the eccentricity increases to $e = 0.965$. At this point in the simulation, this binary interacts strongly with the second most massive SBH, which leads to a companion exchange. The new binary has an initial semi-major axis of $a \sim 6.55$ AU and a very high eccentricity, of $e = 0.999$. The mass of the new companion SBH is $m_{\bullet,2} = 26.54\,M_\odot$. In Fig.(38) we show the evolution of the semi-major axis and eccentricity for all of these binaries combined into a single curve. After some $T \sim 13,000$ yr the binary merges and the resulting IMBH receives a random recoil velocity that depends on the mass ratio of the two members of the system and on the random spins that the code assigned to them. This "gravitational rocket" or recoil is such that the resulting velocity exceeds the escape velocity and the merged system leaves the GC. This is due to the fact that we are using a low number of stars for the clusters; more realistic clusters will have larger escape velocities, so that the retained fraction of recoiling IMBH is larger and not well-represented by our case. We studied the distribution of recoil velocities for a merger of a binary similar to that of simulation A. We ran a two-body interaction 10^7 times and calculated the recoil using equation (140) with different spin orientations and magnitudes for the two black holes. We found that the most probable recoil velocity for a binary such as the one of case A peaks around 25 $\mathrm{km\,s^{-1}}$, with a probability of 21% that the merged system achieves velocities greater than 50 $\mathrm{km\,s^{-1}}$, of the order of realistic GC escape velocities.

In Fig. (39) we show the evolution of the distances of the 10 most massive SBHs from the center. The SBHs inspiral the center very rapidly, as long as the IMBH exists in the cluster. Some of them escape the system, after passing very close to the central binary. After the IMBH merges with its binary companion SBH, the coalesced system leaves the GC and the trajectories of the remaining SBHs are not as steep, because they orbit the center of density of the GC without sinking rapidly into it.

In Fig. (40) we show the Lagrange radii of the cluster during the simulation. We stop the simulation at ~ 10 Myr after the ejection of the IMBH. From t=0 until the ejection of the IMBH, which happened at $t \sim 49$ Myr, the Lagrange radii increase constantly. This agrees with other results of other N-body (Baumgardt et al. 2004) and recent Monte Carlo (Umbreit et al. 2012) simulations of GCs containing IMBHs, and it happens because the central IMBH and the IMBH-SBH binary that forms almost instantly after the beginning of the simulation, act as a heating source for the cluster. Kinetic energy is transferred from the IMBH-SBH binary to the stars and SBHs that pass close from the density center making the binary constantly harder and the stars more energetic and thus expanding the cluster. When the IMBH is removed from the cluster, the heating source is absent, so the cluster starts contracting slowly as is obviously shown in the Lagrange radii. The shrinkage of the cluster would continue until the central number density of stars becomes high enough that another heating

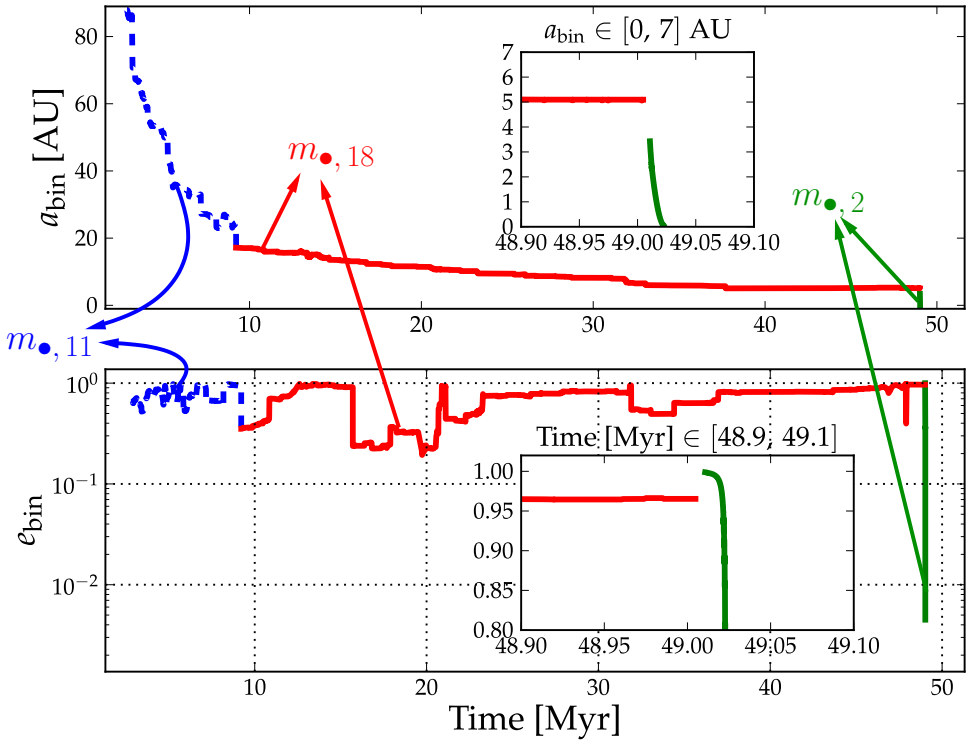

Figure 38: Evolution of the semi-major axis and eccentricity of the different three binaries formed with the IMBH. Shortly after the beginning of the simulation, the IMBH builds a binary with the SBH with the 11th most massive mass, $m_{\bullet,11}$. This corresponds to the first part of the curve (dashed blue curve). Later there is an interaction which leads to a companion exchange for the binary, the SBH with the 18th most massive mass, $m_{\bullet,18}$. This binary lives for about 40 Myr. We can see that the two first binaries have phases of very high eccentricity, $e_{\rm bin} \sim 1$, but not high enough to lead to a coalescence. The jumps in $e_{\rm bin}$ indicate that the IMBH-SBH is still in a regime in which interactions with other stars play an important role. The system shrinks further and further until there is a three-body interaction. The binary is unbound and for a short period of time the IMBH has no companion, as indicated in the zoom-in subplots embedded in both, the upper and lower panels. Then the final binary forms, with the second most massive SBH. This binary is very hard and quickly losses energy via GWs radiation, which very efficiently leads to circularization and the final merger.

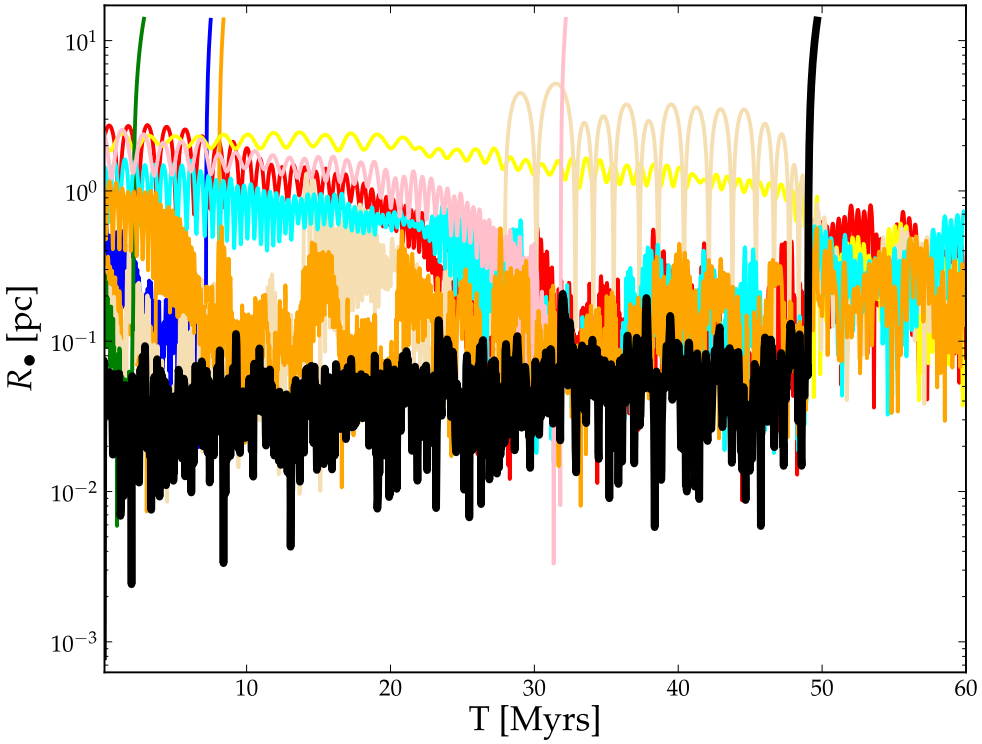

Figure 39: Distance $R_\bullet$ to the density center of the GC of the ten most massive SBHs and the IMBH (solid black line). Strong interactions of the SBHs lead to ejection of four of them before the IMBH merges. They are removed from the simulation when $R_\bullet > 10$ pc and they are unbound with the GC. At $T \sim 47.7$ Myr the IMRI leads to a coalescence that kicks the resulting merged system off the GC.

source (i.e. a new binary) is formed at the center. Even though we integrated the system for another ~ 10 Myr after the ejection, no such source formed.

In all simulations the IMBH had as a companion a SBH, which was replaced several times with another SBH usually of greater mass. In the end, the companion of the IMBH was one of the most massive SBHs of the cluster. Most of the lower-mass SBHs after sinking to the center and interacting with the central IMBH-SBH binary, were kicked out of the GC. Also, in none of the simulations we find a main-sequence or giant star tidally disrupted by the IMBH. This is in agreement with the models of (Baumgardt et al. 2004) which contain a number of massive SBHs. In our models, apart from the IMBH, SBHs are the most massive objects in the GC and therefore sink to the center faster than any other star. As a result a IMBH-SBH binary forms very soon with the companion of the IMBH being more massive than any other non-SBH object of the cluster. Thus, only interactions of the binary with another SBH of comparable or higher mass than the current companion of the IMBH may lead to a companion exchange, so it is almost impossible for a normal star to come too close to the IMBH to get tidally disrupted. Therefore, tidal disruptions of stars are not favoured in our models.

After the merger, the IMBH leaves the GC without any companion. This may be an artifact of the low number of stars used in the simulation. In real clusters a small number of stars or remnants are expected to be bound to the IMBH, so if the IMBH receives a large kick, they will follow it outside the GC. In this case, and if there are no massive SBHs among the IMBH companions, some stars might be tidally disrupted by the IMBH, and thus the system might become a ULX not associated with a GC.

12.4 GRAVITATIONAL WAVES FROM AN IMRI

In this section we follow the binary IMBH-SBH from the standpoint of emission of GWs. In Fig.(41) we can see the evolution of the IMRI in a semi-major axis and orbital period – eccentricity plane. The binary enters the plot from the top with a high eccentricity, which places it very close to the innermost stable circular orbit, but the loss of energy quickly circularises it and drives it to lower eccentricities. As we discussed in the previous section, the binary forms with a very small initial semi-major axis, so that it hardens very efficiently. Hence, the binary follows closely what we can expect from the approach of Peters (1964), since the post-Newtonian terms lead the evolution of the system, which can be regarded as dynamically decoupled from the GC. It then enters the band of a LISA-like or ALIA detector with a significant eccentricity and the simulation is stopped when the semi-major axis is $a = 5\,R_{Schw}$, the Schwarzschild radius of the IMBH. That is the moment at which the code assigns a recoil velocity to the merged system based on the spins of the two compact objects.

In Fig.(42) we can see the same from the perspective of the characteristic amplitude and frequency of the waves. We display the first harmonics in the approximation of Keplerian ellipses of Peters & Mathews (1963).

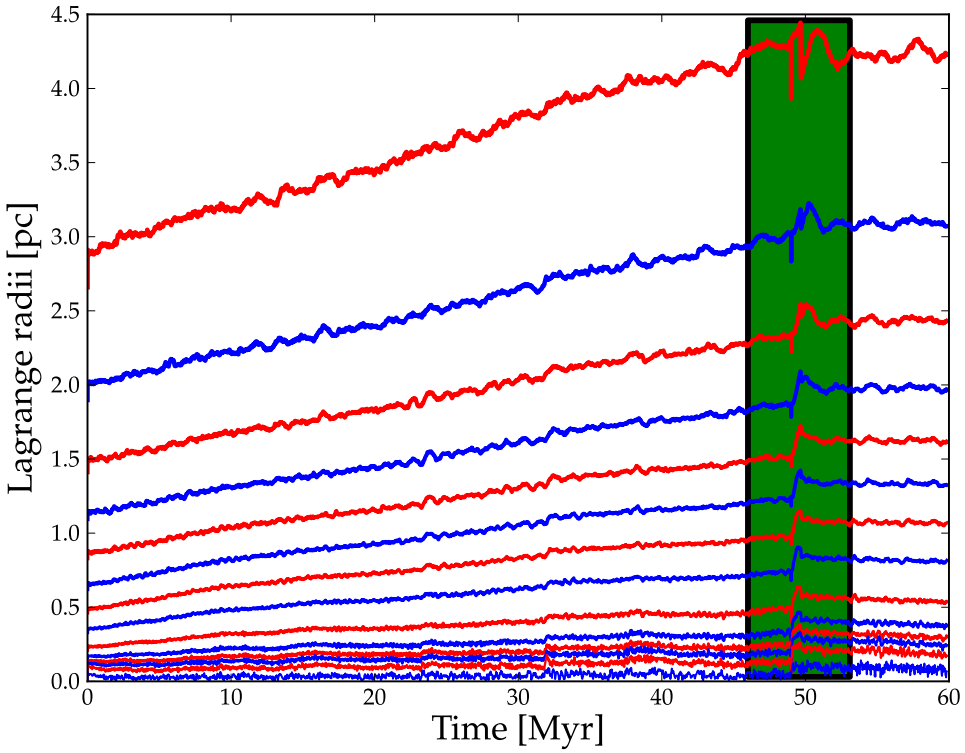

Figure 40: Lagrangian radii showing the evolution of different mass fractions in the cluster: from the top to the bottom 90, 80 ... 20, 10, 5, 3, 2, 1 and 0.1% of the total mass. The green rectangle shows the interval of time before and after the kick of the IMBH off the cluster. All mass curves suffer a jump at the moment of ejection. After the removal of the heating source from the center, the curves are flatter and their slopes start to decrease.

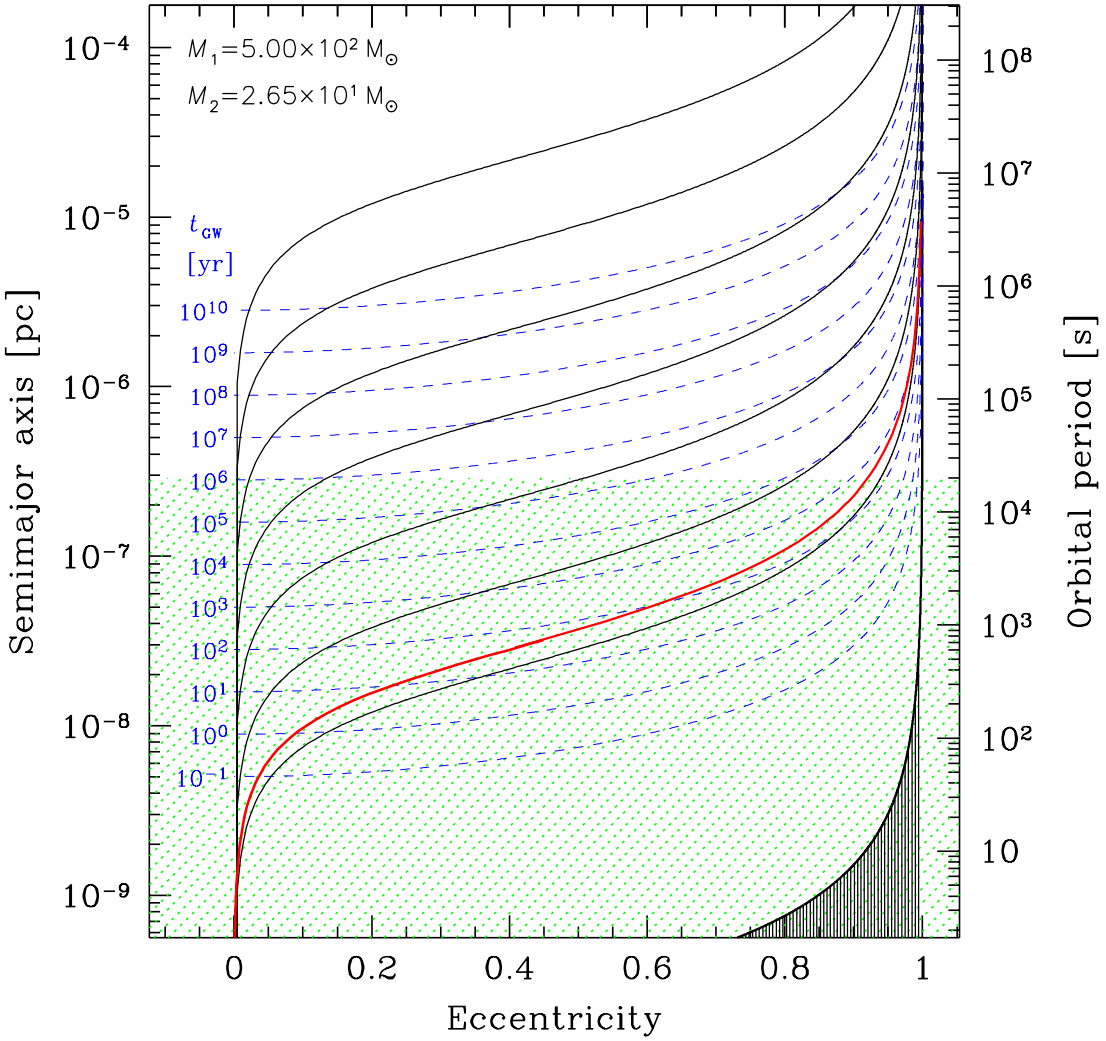

Figure 41: Inspiral of the SBH into the IMBH from the top to the bottom and from the left to the right in the eccentricity–semi-major axis plane. The red, solid curve starting at a very eccentric orbit shows the results of the NBODY simulation. The dashed, green region corresponds to the band of a LISA-like mission. Dashed, blue curves correspond to the trajectories due only to the emission of GWs in the Peters & Mathews (1963) approximation. We also plot the corresponding merger timescales in the same approximation in dashed, blue lines starting at 10^{10} years, and in solid, black lines the corresponding trajectories for evolution by GW emission Peters (1964) approximation. The black-shaded region on the right corresponds to the last stable circular orbit. Since the binary starts at a very high eccentricity, it basically follows one of the solid black lines, because it merges quickly and does not interact with other stars in the system.

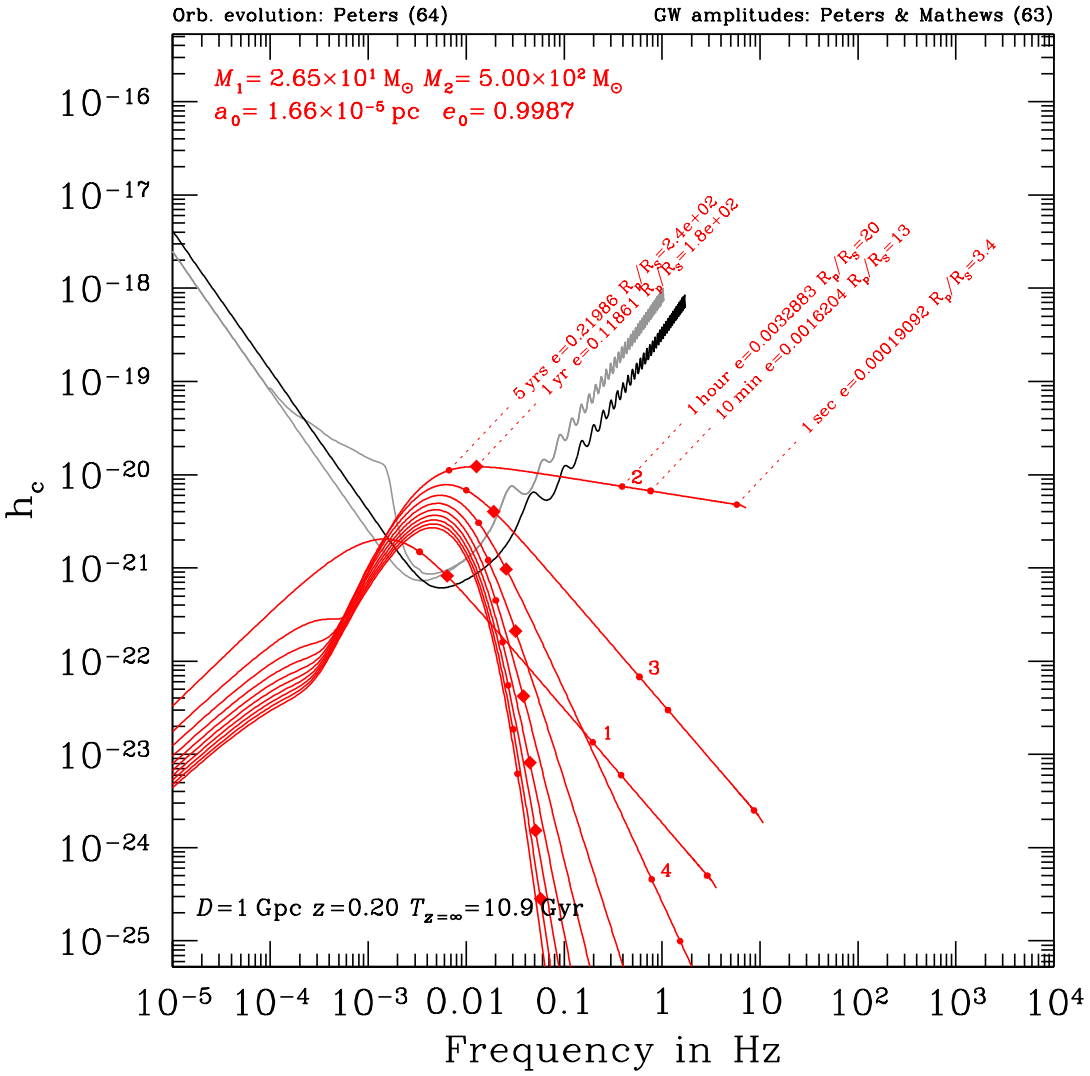

Figure 42: Characteristic amplitude h_c of the first harmonics of the quadruple gravitational radiation emitted during the inspiral of the IMRI. The numbers show the first four of the harmonics. The orbital evolution is calculated in the Peters (1964) approximation and the amplitudes as in Peters & Mathews (1963). We assume the source is at a distance D = 1 Gpc. We indicate with a solid curve the noise curve $\sqrt{f\,S_h(f)}$ for the ALIA detector with an arm-length of 3×10^9 m, a telescope diameter of 0.58 m, and a 1-way position noise of $8/\sqrt{\text{Hz}}$ pm; i.e. the 3H configuration of Gong et al. (2011). We also add the noise curve for a LISA-like detector (in grey, Larson et al. 2000), with the Galactic binary white dwarf confusion background (Bender & Hils 1997). Note that the SNR is not given by the height above the curve, but by the area below it. For each panel we show the ratio $R_{\rm p}^0/R_{\rm s}$, the initial periapsis distance over the Schwarzschild radius of the system. We indicate the moments in the evolution for which the time to coalescence is 5, 1 yr, 1 hour, 10 minutes and 1 sec.

12.5 CONCLUSIONS

In this work we have investigated with a direct-summation code the evolution of GCs that harbour an IMBH in their center. The code uses relativistic corrections and a prescription for gravitational recoil. For one of the cases we find that an IMRI forms with a SBH due to close interactions, which leads to the ejection of IMBH after coalescence. We follow the properties of the IMRI from a standpoint of the global evolution of the cluster and of GW.

Before the formation of the IMRI and the subsequent ejection of the IMBH, the cluster experiences strong expansion as a result of two-body relaxation in the presence of an IMBH. The IMBH-SBH binaries that are formed transfer kinetic energy to the stars that sink to the center and as a result the GC expands significantly. Some of the inner Lagrange radii of the cluster almost double in size during the first ~ 50 Myr of dynamical evolution. Also, most of the massive SBHs sink to the center very rapidly and after interacting with the IMBH, if they do not become its companions, they receive large kicks and get ejected violently from the GC. After the ejection of the IMBH, the GC slowly starts to contract as a result of the absence of the heating source at the center. This might lead to another core collapse of the GC, something we do not observe in the simulation in the first 10 Myr after the ejection if the IMBH.

In our simulations, the IMBH forms a binary with a SBH very early and then exchanges its companion several times. In the simulation we observed an IMRI, the IMBH formed a binary with the second most massive SBH of the system. The initial high eccentricity of the IMBH-SBH binary lead to an IMRI and a subsequent merger. We showed that for $z \leqslant 0.7$ the energy loss of the binary in GWs is easily detectable by space-borne missions such as a LISA-like observatory (Amaro-Seoane et al. 2012) or ALIA in its 8 pc configuration. Moreover, the IMRI enters the bandwidth of the detectors with a very high eccentricity, $e = 0.9987$, as with the EMRIs. One year before the final coalescence, the system still retains a residual eccentricity of $e \sim 0.12$, and ten minutes before merger of $e \sim 10^{-3}$, which is detectable by data-analysis techniques (Amaro-Seoane et al. 2010; Key & Cornish 2011; Porter & Sesana 2010).

IMRIs represent a test of GR, as well as a probe of space and time around massive black holes and also of the innermost kinematics of GCs to very large distances, of the order of a few Gpc. On the top of that, a successful detection would represent very robust proof for the existence of IMBHs. The fact that the kick is making the merged system leave the GC is possibly an artifact of the low particle number we used in the simulations, though in principle recoiling velocities can be much higher than the escape velocity of a cluster, of the order of $\sim 50\ \mathrm{km\,s^{-1}}$ (see e.g. Holley-Bockelmann et al. 2008; Rezzolla 2009). However, we have also demonstrated that there is a non-negligible statistical probability that a similar case leads to a kick of the IMBH off a realistic GC.

In our simulations we do not observe any tidal disruption of stars and also in the simulation in which we had an IMRI, the IMBH left the system without any companion. This is probably also an artifact of the low number of stars used in the simulations.

In real clusters normally there is a small number of stars bound to the IMBH, so after all the SBHs are ejected and probably after some IMBH-SBH mergers, the IMBH will be followed by a number of main-sequence or giant stars, even if it is ejected from the GC. Therefore, if after the IMBH-SBH merger the IMBH remains in the GC, it might soon become an X-ray source at the center of the cluster, similar to the ULXs that are located at the centers of GCs (e.g. the ULX at NGC 404 Binder et al. 2011; Nyland et al. 2012). On the other hand, if it escapes the GC, followed by the stars bound to it, it might soon become a ULX outside of the GC. In this context, HLX-1 might be an escaping IMBH that originated at the center of ESO243-49 and received a large recoil velocity after a merger with a massive SBH. The kick is responsible for the escape if the IMBH, which is followed by a number of stars gravitationally bound to it. This scenario supports one of the possible scenarios for HLX-1 suggested by Soria et al. (2012) according to which the HLX-1 is an IMBH embedded in a young population of stars with ages < 10 Myr and total mass with upper bound of $\sim 10^4$ $M_\odot$. A larger number of simulations of escaping IMBHs using a realistic number of stars would be appropriate for testing this scenario.

In spite of the code been ported to run on a PC with special-purpose hardware GRAPE, we can not cover a broader parameter space, nor study cases with a larger number of stars, or study the global dynamical evolution of the GC after the kick for a longer time. We plan on performing a better parameter space exploration thanks to the availability of GPUs, which will allow us to address the limitations we described above. This will allow us to investigate the potential global structure of the GC after the kick, since the impact on the cluster could in principle be a signature for the process. Also, it will allow us to study also the properties and detectability of the escaping IMBHs and their possible companions.

BIBLIOGRAPHY

Aarseth S. J., 1999, The Publications of the Astronomical Society of the Pacific, 111, 1333

Aarseth S. J., 2003, Gravitational N-Body Simulations. ISBN 0521432723. Cambridge, UK: Cambridge University Press, November 2003.

Amaro-Seoane P., Aoudia S., Babak S., Binétruy P., et. al 2013, GW Notes.

Amaro-Seoane P., Eichhorn C., Porter E. K., Spurzem R., 2010, MNRAS, 401, 2268

Amaro-Seoane P., Gair J. R., Freitag M., Miller M. C., Mandel I., Cutler C. J., Babak S., 2007, Classical and Quantum Gravity, 24, 113

Amaro-Seoane P., Santamaria L., 2009, ApJ in press

Anderson J., van der Marel R. P., 2010, ApJ, 710, 1032

Bahcall J. N., Ostriker J. P., 1975, Nature, 256, 23

Baumgardt H., Hut P., Makino J., McMillan S., Portegies Zwart S., 2003, ApJ Lett., 582, L21

Baumgardt H., Makino J., Ebisuzaki T., 2004, ApJ, 613, 1143

Baumgardt H., Makino J., Hut P., 2005, ApJ, 620, 238

Baumgardt H., Makino J., Hut P., McMillan S., Portegies Zwart S., 2003, ApJ Lett., 589, L25

Begelman M. C., 2002, ApJ Lett., 568, L97

Belczynski K., Bulik T., Fryer C. L., Ruiter A., Valsecchi F., Vink J. S., Hurley J. R., 2010, ApJ, 714, 1217

Bender P. L., Armitage P. J., Begelman M. C., Pema R., 2005, White Paper submitted to the NASA SEU Roadmap Committee

Bender P. L., Hils D., 1997, Classical and Quantum Gravity, 14, 1439

Bender R., 2005, in Merloni A., Nayakshin S., Sunyaev R. A., eds, Growing Black Holes: Accretion in a Cosmological Context Supermassive Black Holes in Nearby Galaxy Centers. pp 147–153

Binder B., Williams B. F., Eracleous M., Seth A. C., Dalcanton J. J., Skillman E. D., Weisz D. R., Anderson S. F., Gaetz T. J., Plucinsky P. P., 2011, ApJ, 737, 77

Chanamé J., Bruursema J., Chandar R., Anderson J., van der Marel R., Ford H., 2010, in de Grijs R., Lépine J. R. D., eds, IAU Symposium Vol. 266 of IAU Symposium, HST's hunt for intermediate-mass black holes in star clusters. pp 231–237

Crowder J., Cornish N. J., 2005, Physical Review D, 72, 083005

Davis S. W., Narayan R., Zhu Y., Barret D., Farrell S. A., Godet O., Servillat M., Webb N. A., 2011, ApJ, 734, 111

Eisenhauer F., Perrin G., Brandner W., Straubmeier C., et al. 2008, in Society of Photo-Optical Instrumentation Engineers (SPIE) Conference Series Vol. 7013 of Society of Photo-Optical Instrumentation Engineers (SPIE) Conference Series, GRAVITY: getting to the event horizon of Sgr A*

Farrell S. A., Servillat M., Oates S. R., Heywood I., Godet O., Webb N. A., Barret D., 2010, X-ray Astronomy 2009; Present Status, Multi-Wavelength Approach and Future Perspectives, 1248, 93

Farrell S. A., Servillat M., Pforr J., Maccarone T. J., Knigge C., Godet O., Maraston C., Webb N. A., Barret D., Gosling A. J., Belmont R., Wiersema K., 2012, ApJ Lett., 747, L13

Farrell S. A., Webb N. A., Barret D., Godet O., Rodrigues J. M., 2009, Nat, 460, 73

Feng H., Soria R., 2011, NAR, 55, 166

Frank J., Rees M. J., 1976, MNRAS, 176, 633

Fregeau J. M., Larson S. L., Miller M. C., O'Shaughnessy R., Rasio F. A., 2006, ApJ Lett., 646, L135

Freitag M., Gürkan M. A., Rasio F. A., 2006, MNRAS, 368, 141

Fryer C. L., 1999, ApJ, 522, 413

Fryer C. L., Kalogera V., 2001, ApJ, 554, 548

Gürkan M. A., Freitag M., Rasio F. A., 2004, ApJ, 604, 632

Gillessen S., Eisenhauer F., Trippe S., Alexander T., Genzel R., Martins F., Ott T., 2009, ApJ, 692, 1075

Gillessen S., Perrin G., Brandner W., Straubmeier C., Eisenhauer F., Rabien S., Eckart A., Lena P., Genzel R., Paumard T., Hippler S., 2006, in Society of Photo-Optical Instrumentation Engineers (SPIE) Conference Series Vol. 6268 of Society of Photo-Optical Instrumentation Engineers (SPIE) Conference Series, GRAVITY: the adaptive-optics-assisted two-object beam combiner instrument for the VLTI

Glebbeek E., Gaburov E., de Mink S. E., Pols O. R., Portegies Zwart S. F., 2009, AA, 497, 255

Godet O., Barret D., Webb N. A., Farrell S. A., Gehrels N., 2009, ApJ Lett., 705, L109

Godet O., Farrell S., Barret D., Webb N., Servillat M., 2011, The Astronomer's Telegram, 3569, 1

Godet O., Plazolles B., Kawaguchi T., Lasota J.-P., Barret D., Farrell S. A., Braito V., Servillat M., Webb N., Gehrels N., 2012, ApJ, 752, 34

Gong X., Xu S., Bai S., Cao Z., Chen G., Chen Y., He X., Heinzel G., Lau Y.-K., Liu C., Luo J., Luo Z., Pulido Patón A., Rüdiger A., Shao M., Spurzem R., Wang Y., Xu P., Yeh H.-C., Yuan Y., Zhou Z., 2011, Classical and Quantum Gravity, 28, 094012

Goswami S., Umbreit S., Bierbaum M., Rasio F. A., 2012, ApJ, 752, 43

Gültekin K., Richstone D. O., Gebhardt K., Lauer T. R., Tremaine S., Aller M. C., Bender R., Dressler A., Faber S. M., Filippenko A. V., Green R., Ho L. C., Kormendy J., Magorrian J., Pinkney J., Siopis C., 2009, ApJ, 698, 198

Heger A., Woosley S. E., 2002, ApJ, 567, 532

Holley-Bockelmann K., Gültekin K., Shoemaker D., Yunes N., 2008, ApJ, 686, 829

Hurley J. R., Pols O. R., Tout C. A., 2000, MNRAS, 315, 543

Karachentsev I. D., Karachentseva V. E., Huchtmeier W. K., Makarov D. I., 2004, AJ, 127, 2031

Key J. S., Cornish N. J., 2011, Phys Rev D, 83, 083001

King A. R., 2008, MNRAS, 385, L113

King I. R., 1966, AJ, 71, 64

Kirsten F., Vlemmings W. H. T., 2012, AA, 542, A44

Kokubo E., Yoshinaga K., Makino J., 1998, MNRAS, 297, 1067

Konstantinidis S., Kokkotas K. D., 2010, AA, 522, A70+

Koppitz M., Pollney D., Reisswig C., Rezzolla L., Thornburg J., Diener P., Schnetter E., 2007, Physical Review Letters, 99, 041102

Kroupa P., 2001a, MNRAS, 322, 231

Kroupa P., 2001b, MNRAS, 322, 231

Kroupa P., Tout C. A., Gilmore G., 1993, MNRAS, 262, 545

Kupi G., Amaro-Seoane P., Spurzem R., 2006, MNRAS, pp L77+

Larson S. L., Hiscock W. A., Hellings R. W., 2000, Physical Review D, 62, 062001

Lousto C. O., Campanelli M., Zlochower Y., Nakano H., 2010, Classical and Quantum Gravity, 27, 114006

Lousto C. O., Zlochower Y., 2011a, Physical Review Letters, 107, 231102

Lousto C. O., Zlochower Y., 2011b, Phys. Rev. D, 83, 024003

Lützgendorf N., Kissler-Patig M., Gebhardt K., Baumgardt H., Noyola E., Jalali B., de Zeeuw P. T., Neumayer N., 2012, AA, 542, A129

Madau P., Rees M. J., 2001, ApJ Lett., 551, L27

Makino J., Fukushige T., Koga M., Namura K., 2003, PASJ, 55, 1163

Miller C., 2006, in APS April Meeting Abstracts Gravitational Radiation from Intermediate-Mass Black Holes. p. 4003P

Miller M. C., 2009, Classical and Quantum Gravity, 26, 094031

Miller M. C., Colbert E. J. M., 2004, International Journal of Modern Physics D, 13, 1

Miller M. C., Hamilton D. P., 2002, MNRAS, 330, 232

Noyola E., Gebhardt K., Kissler-Patig M., Lützgendorf N., Jalali B., de Zeeuw P. T., Baumgardt H., 2010, ApJ Lett., 719, L60

Nyland, K., Marvil, J., Wrobel, J. M., Young, L. M., & Zauderer, B. A. 2012, ApJ, 753, 103

Peebles P. J. E., 1972, ApJ, 178, 371

Peters P. C., 1964, Physical Review, 136, 1224

Peters P. C., Mathews J., 1963, Physical Review, 131, 435

Pollney D., Reisswig C., Rezzolla L., Szilágyi B., Ansorg M., Deris B., Diener P., Dorband E. N., Koppitz M., Nagar A., Schnetter E., 2007, Phys.Rev.D, 76, 124002

Portegies Zwart S. F., Baumgardt H., Hut P., Makino J., McMillan S. L. W., 2004, Nature, 428, 724

Portegies Zwart S. F., McMillan S. L. W., 2000, ApJ Lett., 528, L17

Portegies Zwart S. F., McMillan S. L. W., 2002, ApJ, 576, 899

Porter E. K., Sesana A., 2010, ArXiv e-prints

Quinlan G. D., Shapiro S. L., 1990, ApJ, 356, 483

Rees M. J., 1978, in E. M. Berkhuijsen & R. Wielebinski ed., Structure and Properties of Nearby Galaxies Vol. 77 of IAU Symposium, Emission from the nuclei of nearby galaxies - Evidence for massive black holes. pp 237–242

Rees M. J., 1984, ARA&A, 22, 471

Rezzolla L., 2009, Classical and Quantum Gravity, 26, 094023

Rezzolla L., Dorband E. N., Reisswig C., Diener P., Pollney D., Schnetter E., Szilágyi B., 2008, ApJ, 679, 1422

Salpeter E. E., 1955, ApJ, 121, 161

Servillat M., Farrell S. A., Lin D., Godet O., Barret D., Webb N. A., 2011, ApJ, 743, 6

Seth A. C., Cappellari M., Neumayer N., Caldwell N., Bastian N., Olsen K., Blum R. D., Debattista V. P., McDermid R., Puzia T., Stephens A., 2010, ApJ, 714, 713

Soria R., Hakala P. J., Hau G. K. T., Gladstone J. C., Kong A. K. H., 2012, MNRAS, 420, 3599

Soria R., Hau G. K. T., Graham A. W., Kong A. K. H., Kuin N. P. M., Li I.-H., Liu J.-F., Wu K., 2010, MNRAS, 405, 870

Strader J., Chomiuk L., Maccarone T. J., Miller-Jones J. C. A., Seth A. C., 2012, Nature, 490, 71

Sutton A. D., Roberts T. P., Walton D. J., Gladstone J. C., Scott A. E., 2012, MNRAS, 423, 1154

Tremaine S., Gebhardt K., Bender R., Bower G., Dressler A., Faber S. M., Filippenko A. V., Green R., Grillmair C., Ho L. C., Kormendy J., Lauer T. R., Magorrian J., Pinkney J., Richstone D., 2002, ApJ, 574, 740

Umbreit S., Fregeau J. M., Chatterjee S., Rasio F. A., 2012, ApJ, 750, 31

van der Marel R. P., 2004, Coevolution of Black Holes and Galaxies, p. 37

van der Marel R. P., Anderson J., 2010, ApJ, 710, 1063

Vesperini E., McMillan S. L. W., D'Ercole A., D'Antona F., 2010, ApJ Lett., 713, L41

Volonteri M., Rees M. J., 2005, ApJ, 633, 624

Whalen D. J., Fryer C. L., 2012, ApJ Lett., 756, L19

Wiersema K., Farrell S. A., Webb N. A., Servillat M., Maccarone T. J., Barret D., Godet O., 2010, ApJ Lett., 721, L102

Wyller A. A., 1970, ApJ, 160, 443

13

SOWING THE SEEDS OF MASSIVE BLACK HOLES IN SMALL GALAXIES: YOUNG CLUSTERS AS THE BUILDING BLOCKS OF ULTRA-COMPACT-DWARF GALAXIES

Pau Amaro-Seoane[1], *Symeon Konstantinidis*[2], *Marc Dewi Freitag*[3], *M. Coleman Miller*[4] *& Frederic A. Rasio*[5]

Published in *The Astrophysical Journal*, Volume 782, Issue 2, article id. 97, 14 pp. (2014).

Abstract: Interacting galaxies often have complexes of hundreds of young stellar clusters of individual masses $\sim 10^{4-6}\ M_\odot$ in regions that are a few hundred parsecs across. These cluster complexes interact dynamically, and their coalescence is a candidate for the origin of some ultracompact dwarf galaxies (UCDs). Individual clusters with short relaxation times are candidates for the production of intermediate-mass black holes of a few hundred solar masses, via runaway stellar collisions prior to the first supernovae in a cluster. It is therefore possible that a cluster complex hosts multiple intermediate-mass black holes that may be ejected from their individual clusters due to mergers or binary processes, but bound to the complex as a whole. Here we explore the dynamical interaction between initially free-flying massive black holes and clusters in an evolving cluster complex. We find that, after hitting some clusters, it is plausible that the massive black hole will be captured in an ultracompact dwarf forming near the center of the complex. In the process, the hole typically triggers electromagnetic flares via stellar disruptions, and is also likely to be a prominent source of gravitational radiation for the advanced ground-based detectors LIGO and VIRGO. We also discuss other implications of this scenario, notably that the central black hole could be considerably larger than expected in other formation scenarios for ultracompact dwarfs.

13.1 INTRODUCTION

Several bound systems of young, massive clusters in colliding galaxies have been observed using the Hubble Space Telescope (HST). The best studied case is the Antennæ

2 Astronomisches Rechen-Institut, Mönchhofstraße 12-14, 69120, Zentrum für Astronomie, Universität Heidelberg, Germany
3 Institute of Astronomy, Madingley Road, CB3 0HA Cambridge, UK
4 Department of Astronomy and Joint Space-Science Institute, University of Maryland, College Park, MD 20742-2421, USA
5 Department of Physics and Astronomy, and Center for Interdisciplinary Exploration and Research in Astrophysics (CIERA),Northwestern University, Evanston, IL 60208, USA

galaxies (NGC 4038/4039), the nearest example of two colliding disc galaxies listed in the Toomre (1977) sequence. HST observations reveal in this system the existence of relatively small regions (compared with the size of the galaxies) harbouring hundreds or thousands of young clusters (Whitmore 2006; Whitmore et al. 2010, 1999). In particular, Whitmore et al. (2010) observed 18 areas ("knots") of sizes spanning $100-600$ pc which contain hundreds of clusters. The mass function of those systems, which we will henceforth refer to as "Cluster Complexes" (CCs), is

$$dN/dM \propto M^{\beta}, \tag{141}$$

with $\beta = -2.10 \pm 0.20$ in the range $M \sim 10^{4-5}\ M_{\odot}$ (see also Zhang & Fall 1999). Bastian et al. (2006) found in the same system low-mass CCs with masses around $10^{6}\mathrm{M}_{\odot}$ and diameters of some $100-200$ pc. One of the best studied CCs in the Antennæ galaxy is "knot S", with a total mass of $10^{8}\mathrm{M}_{\odot}$ and a total radius of ~ 450pc (Whitmore et al. 1999). Other galaxies with recently discovered CCs include NGC 7673 (Homeier et al. 2002), M82 (Konstantopoulos et al. 2009), NGC 6745 (de Grijs et al. 2003), Stephan's Quintet (Gallagher et al. 2001) and NGC 922 (Pellerin et al. 2010).

CCs are bound systems (Bruens et al. 2011; Fellhauer & Kroupa 2005; Kroupa 1998; Whitmore et al. 2010) and on relatively short time-scales at least some of their member clusters will merge to form a single object. Kroupa (1998) and Fellhauer & Kroupa (2005) have postulated CCs as the breeding ground of Ultra-Compact Dwarf Galaxies (UCDs). Following this idea, Bruens et al. (2011) performed $N-$body simulations of CCs with different total masses ($10^{5.5}-10^{8}\ M_{\odot}$) and initial Plummer radii $10-160$ pc. They conclude that UCDs, Extended Clusters (ECs) or even large Globular Clusters (GCs) might be the product of an agglomeration of clusters in CCs. They find in their simulations that almost all members of a CC merge in less than 1 Gyr. In some cases this timescale can be as short as 10 Myr. By the end of their simulations a very massive cluster forms in the centre of the CC, with a mass of $26-97\%$ the mass of the initial CC and a radius of ~ 50 pc.

Theoretical and numerical studies show that at least a fraction of young star clusters could host intermediate-mass black holes (IMBHs, black holes with masses ranging between $10^{2-4}\,M_{\odot}$) at their centres. A possible formation path is that in a young cluster, the most massive stars sink to the centre due to mass segregation. After a high-density stellar region forms, stars start to collide and merge with each other. A number of numerical studies with rather different approaches show that, under these circumstances, at least one of the stars increases its mass rapidly in a process of runaway collisions (Freitag et al. 2006a,b; Gürkan et al. 2004; Portegies Zwart et al. 2004; Portegies Zwart & McMillan 2000). Nonetheless, there are a number of open questions regarding this process. One of the main uncertainties is the role of stellar winds. In principle at approximately solar metallicity winds may limit the mass of this very massive star (VMS) to a few hundreds of solar masses rather than a few thousands (Belkus et al. 2007). Nevertheless we note that this requires a substantial extrapolation of already uncertain wind loss rates to stellar masses an order of magnitude beyond what is observed. Also, the collision process might lead to lumpy bags of stellar cores

in an extended envelope rather than to relaxed stars near the end of the runaway collision (M. Davies, private communication). In addition, when Suzuki et al. (2007) combined direct $N-$body simulations with smooth particle hydrodynamics (SPH) they found that stellar winds would not hinder the formation of the VMS. It is thus possible but not certain that IMBHs can form in young clusters. We will assume their existence as a working hypothesis.

Apart from the obvious interesting implications for models of galaxy formation and, in particular, of UCDs, mergers of clusters in CCs are a powerful source of gravitational waves if these harbour central IMBHs in their respective centres (Amaro-Seoane et al. 2010; Amaro-Seoane & Freitag 2006; Amaro-Seoane et al. 2009; Amaro-Seoane & Santamaría 2010). In particular, Amaro-Seoane & Freitag (2006) showed that such mergers would lead to the formation of an IMBH binary, which would merge in a time scale as short as ~ 7 Myr. Such a merger would be easily detected with space-borne observatories and also with ground-based detectors such as Advanced LIGO or Advanced VIRGO (AdLIGO/AdVIRGO) if it occurs within ~ 2 Gpc (Fregeau et al. 2006). Using more realistic waveforms including spins, Amaro-Seoane & Santamaría (2010) find that the detection distance is increased significantly, up to an orientation-averaged distance of $\sim 5-12$ Gpc, depending on the spin configuration and mass ratios. In the case of the Einstein Telescope (ET), the same authors find that the maximum redshifts for ET are $z \sim 10$, which implies that binaries of IMBHs will be a cosmological probe.

Numerical relativity simulations show that during the merger of the holes, gravitational radiation is emitted asymmetrically with the size of asymmetry depending on the mass ratio of the two black holes and on their spin magnitude and orientation (Baker et al. 2008; Boyle & Kesden 2008; Campanelli et al. 2007a,b; Gonzalez et al. 2007; Healy et al. 2009; Herrmann et al. 2007a,b; Lousto & Zlochower 2008; Lousto et al. 2010; Lousto & Zlochower 2011b; Pretorius 2005; Sopuerta et al. 2006; van Meter et al. 2010; Zlochower et al. 2010) If this recoiling velocity exceeds a few times the velocity dispersion of the merged cluster, then the IMBH leaves the host cluster. There is a massive black hole at large in the CC. Even if an IMBH escapes from one cluster, it might still be bound to the CC as a whole, which means that it has the possibility of interacting with other clusters and, perhaps, their IMBHs.

In this article we address the formation of ultra-compact dwarf galaxies by the agglomeration of young clusters in CCs, along with the role of one or more recoiling IMBHs, using direct-summation $N-$body simulations. For this, we run a set of ~ 200 individual experiments in which we vary mass ratios, relative speeds, and impact parameter to study in detail the interaction between a single IMBH and a cluster. We then study the interaction of one or more IMBHs at large in a CC with individual clusters with an additional set of $N-$body simulations. We correct for the trajectory of the IMBH, based on point dynamics and the mass loss in the individual clusters, by using the previous 200 experiments. We also follow the growth of a seed UCD in a CC and record all stellar disruptions triggered by the presence of the IMBH(s). For realistic models of CCs we find that the IMBH(s) end up captured by the seed UCD or by a smaller cluster which is close to the UCD. Thus, if the fraction of IMBHs in

the CC ($f_\bullet$ from now onwards) is not zero, this is a process of allocating one or more IMBH at the very centre of a UCD.

13.2 INTERACTIONS BETWEEN A RECOILING IMBH AND AN INDIVIDUAL YOUNG CLUSTER

In this section we make a study of the parameter space for a collision between a recoiling IMBH and an individual young cluster in a CC. We run a set of ~ 200 direct $N-$body simulations to build a grid which we will later use in our simulations of the IMBH in the CC, as explained in the introduction. Initially we set the IMBH and the cluster on an orbit with positive relative speed and thus positive total energy in the initial state, i.e. a hyperbolic orbit, as described in Amaro-Seoane (2006). We schematically show this for reference in Fig. (43) and follow a similar notation. The initial trajectory of the IMBH would bring it within a minimum distance $d_{\rm min}$ of the cluster centre if the cluster was replaced by a point particle. In the centre-of-mass reference frame (COM),

$$\begin{aligned}
\mathbf{x}_\bullet &= \lambda_{\rm cl}\,\mathbf{d},\\
\mathbf{x}_{\rm cl} &= -\lambda_\bullet\,\mathbf{d},\\
\mathbf{v}_\bullet &= \lambda_{\rm cl}\,v_{\rm rel},\\
\mathbf{v}_{\rm cl} &= -\lambda_\bullet\,\mathbf{v}_{\rm rel}
\end{aligned} \tag{142}$$

where $\mathbf{v}_{\rm rel}$ is the relative velocity of the two objects $\mathbf{d}$ is their separation vector, $\mathbf{x}_{\bullet,{\rm cl}}$ are the positions of their centres, and $\lambda_{\bullet,{\rm cl}} = m_{\bullet,{\rm cl}}/(\mathcal{M}_\bullet + M_{\rm cl})$.

The number of stars in the cluster is always $\mathrm{N}_\star = 3\times10^4$ and we use for their initial distribution a King model of concentration $W_0 = 7$ (King 1966; Peterson & King 1975), and all stars have the same mass, to simplify the interpretation of the results, although we note that a mass function could have an impact in the outcome of individual hits. Stellar evolution is not taken into account for the same reason. Although the number of stars we simulate is still below of what we can expect from a real cluster, we deem the dynamical interaction to be correct but for probably the most extreme mass ratios in which the mass ratio between the IMBH and the total mass in the cluster is one and two. We include these cases for completness but note that in those cases the stars in those clusters do not represent a single star but a set of them. I.e. the IMBH will hit lighter clusters with those mass ratios, and the orbital evolution of the IMBH will be correctly estimated in our simulations, but the trajectory of a single star in such clusters does not trace one single star, but a set of them. The simulations are performed with the direct-summation NBODY4 programme of Aarseth (2003). This choice was made for the sake of the accuracy of the study of the orbital parameter evolution of the IMBH and mass loss in the cluster; this numerical tool includes both the KS regularisation (Kustaanheimo & Stiefel 1965) and chain regularisation, which means that when two or more particles are tightly bound to each other or the separation is very small during

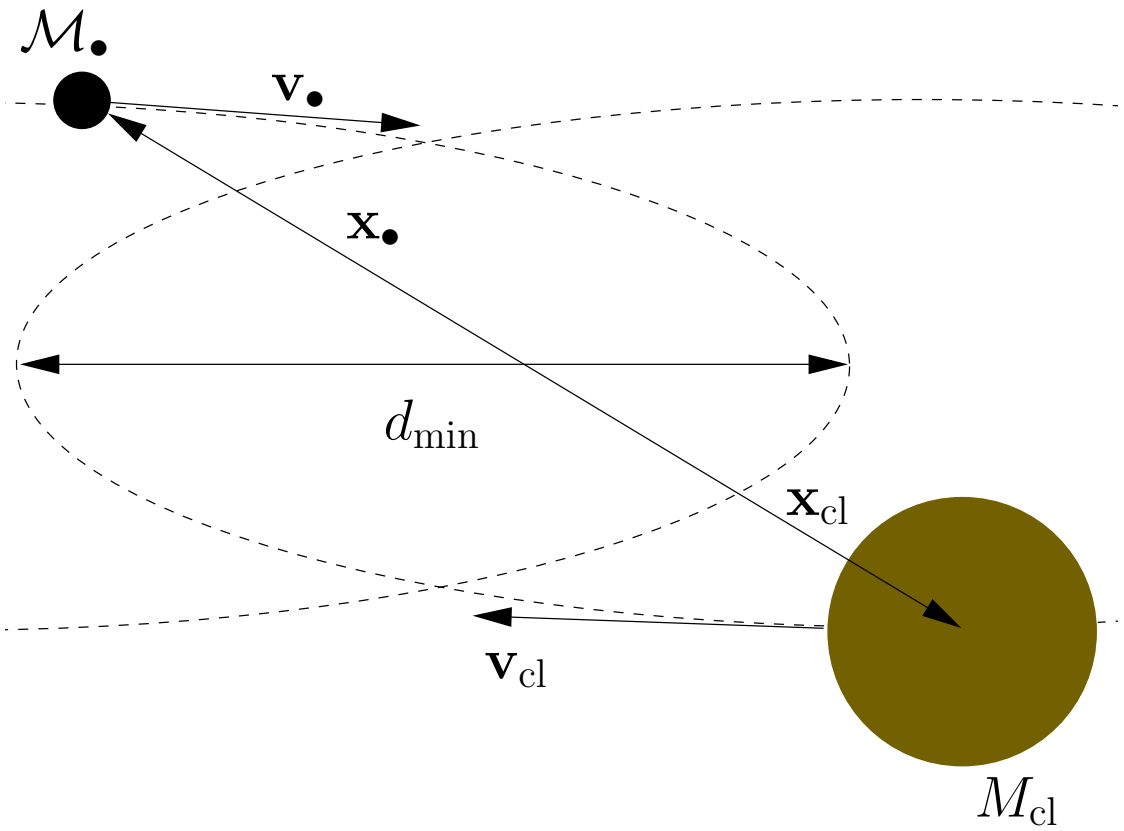

Figure 43: Geometry for the initial conditions of the parabolic collision, in the COM of the IMBH–cluster system. To obtain the grid displayed in Fig.(44), we systematically vary $d_{\rm min}$, the relative velocity and the mass ratio between the IMBH and the cluster.

a hyperbolic encounter, the system becomes a candidate to be regularised in order to avoid problematical small individual time steps. The basis of direct $N-$body codes relies on a Hermite integrator scheme (Aarseth 1999, 2003) for which we need not only the accelerations but also their time derivatives. This extra computational overhead is necessary for us to follow reliably the orbital evolution of *every* single star (or IMBH) in our system. While the code was not meant to integrate clusters in which a particle is significantly much more massive than the rest of them, a mass ratio of the order of what we have considered in this study leads to an accurate integration, with individual time integration errors of the order of 10^{-10} in energy.

At the end of an N-body run, we need to identify the particles that are still forming a bound cluster, the particles that are bound to the IMBH, and the particles that have become unbound. We also need to know whether the IMBH has been captured by the stellar cluster. We have therefore developed an iterative algorithm. To initialize the procedure, we make a (computationally) quick guess of which particles are bound to the cluster and which ones form a bound group including the IMBH (the "IMBH group"). Note that a given particle can be in both groups, for instance if the IMBH has been captured by the cluster and has sunk to its centre or is orbiting it. For this first guess, stellar particles are considered bound to the IMBH group if they are bound to the IMBH (i.e., we do not take into account the self-gravity of the bound stars themselves).

For the first-guess cluster, one assumes that its centre corresponds to the median position of all stellar particles, i.e. the x, y and z components of the "centre" are taken to be the medians of the corresponding components of the positions of all the stellar particles. The median turns out to be a much more robust estimate of where the bulk of the particles is, compared to the average position or the centre of mass (i.e. the mass-weighted average position) as those quantities are very sensitive to the the positions of a few particles ejected at large distances from the rest. For this first guess, the 90 % of the particles closest to this median position are assumed to be part of the cluster.

For the first iteration, we have to compute the binding energy of a particle relative to the cluster group, hence we need to know the velocity of that group. To estimate the velocity of the cluster in the first-guess attribution, we take the average velocity of the 10 % of the particles closest to the assumed centre. This number is sufficient to avoid large fluctuations due to individual particle velocities ("random velocities"). On the other hand, taking a significantly larger fraction of particles is neither necessary nor advisable as it is not yet known which particles are actually bound together as a cluster. We have to make sure that the velocity defined in the procedure is a good estimate of that of the actual bound cluster. Otherwise, the kinetic energies relative to this first-guess cluster are biased towards high values and the iterative procedure fails at identifying a bound cluster. The iterations proceed as follows: For each particle, the binding energies relative to the cluster and the IMBH group are computed. For this, we have to estimate the position of the centre of each group and its velocity. For the IMBH group, they are fixed to the values of the IMBH itself. For the cluster, the centre position and velocity are defined to be the mass-weighted mean values for all

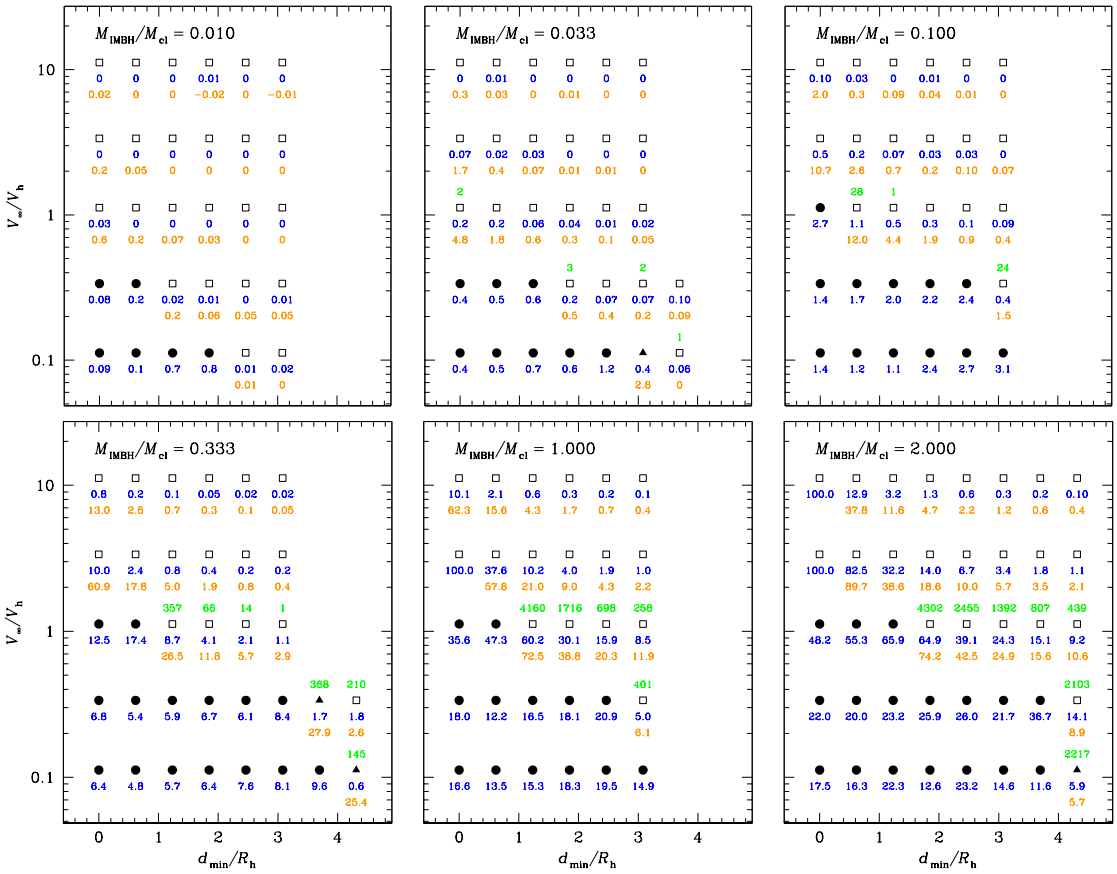

Figure 44: Outcomes of all 196 simulations of encounters between a cluster with King parameter $W_0 = 7$ and an IMBH. Each panel shows the results for a given mass ratio $M_{BH}/\mathcal{M}_{cl}$. The abscissa of each plot is the minimum distance d_{min}, computed assuming 2-body dynamics, in units of the half-mass radius R_h. The ordinate is the relative velocity at infinity V_∞, in units of $V_h \equiv (G\mathcal{M}_{cl}/R_h)^{1/2}$, a typical velocity dispersion for the cluster. Solid round dots show "mergers", i.e., cases where the IMBH has been captured by the cluster and has settled at its centre. Solid triangles are cases in which the IMBH is orbiting the cluster (a merger is likely to be the long-term outcome). Open squares are "fly-throughs". The number just below a symbol (in blue in the on-line colour version) is fractional mass loss from the cluster in percent. The second, lower number (in orange in the on-line colour version) is the fractional reduction in specific binding energy of the cluster, also in percent. A number above a symbol indicates how many stellar particles are bound to the IMBH (when it has not merged with the cluster).

particles within half a "typical size" of the previous estimate of the centre. The typical size of the cluster is the harmonic mean of the distance to its centre (for all particles considered bound to it):

$$R_{\rm typ} = R_{\rm harm} \equiv M_{\rm cl} \left(\sum \frac{m_i}{R_i} \right)^{-1} . \tag{143}$$

One advantage of defining $R_{\rm typ}$ using the harmonic mean, instead of using the half-mass radius or some other Lagrangian radius, is that this does not require a sorting of the particles. The gravitational energy is computed assuming a spherical mass distribution, i.e., as if each particle bound to a group (cluster or IMBH group) was a spherical shell of matter, of radius R_i centred on either the IMBH position or the estimated centre of the cluster. Typically, the attributions of the particles to either or both groups converge after fewer than ten iterations.

At the end, the attributions are cleaned up in the following way. If a stellar particle belongs to both the cluster and the IMBH group, the binding energies to both structures are compared. It will be kept as member of the IMBH group only if the binding energy to the IMBH group is larger than to the cluster group. In that case, it will also be kept as member of the cluster only if the IMBH itself is bound to the cluster. This reduces the number of double-members in a reasonable way, still allowing for situations such as the IMBH having captured some stars while being itself on a bound orbit around the (main) cluster.

Finally, to interpret the results, we allow for three different outcomes. A *merger* is when the IMBH group is bound to the cluster (as determined assuming each group is a point mass) and the distance between the centres of the groups is smaller than the sum of the $R_{\rm typ}$'s. A *satellite* situation arises when the two groups are bound but the distance between their centre is larger than twice the sum of the $R_{\rm typ}$'s. A *flyby* is when the groups are unbound and the distance between their centres is larger than either the sum of the total extent of each group or five times the sum of the $R_{\rm typ}$'s. Any other situation would be considered as *unknown* but does not occur if the $N-$body simulation has been carried out for a sufficient duration.

In Fig.(45) and 46 we show two particular cases for the IMBH – cluster interaction in the COM frame which, although not representative for the whole sample displayed in Fig.(44), are interesting in terms of the dynamics of the system [1] . In the first case $d_{\rm min} = 1$, which leads to an almost head-on collision between the IMBH and the cluster. Nonetheless, because of the low relative velocity and mass ratio, the interaction does not lead to a huge mass loss from the cluster. Even if at $T = 45.60$ Myr the IMBH and cluster seen to be unbound, the IMBH is still forming a binary with the COM of

1 The interested reader can visit
`http://members.aei.mpg.de/amaro-seoane/ultra-compact-dwarf-galaxies`,
for movies based on the results of the figures (the last URL is a 3D version of the second movie). The encoding of the movies is the free OGG Theora format and should stream automatically with a gecko-based browser (such as mozilla or firefox) or with chromium or opera. Otherwise please see e.g.
`http://en.wikipedia.org/wiki/Wikipedia:Media_help_(Ogg)`
for an explanation on how to play the movies.

the cluster and, hence, the semi-major axis decays again. After some 154 Myrs the IMBH settles down to the centre and is captured. In the second figure, the larger mass ratio has a significant impact in terms of mass loss. Already after 11.62 Myr the IMBH has captured some stars from the cluster, which remain bound to the trajectory of the hole and follow its trajectory. This satellite and the IMBH are nevertheless still gravitationally bound to the cluster and hence fall back again. The higher mass in the IMBH–satellite system leads to a rather large mass loss from the original cluster. After 80.50 Myrs the IMBH is at the centre of the remaining cluster.

13.3 INTERACTIONS BETWEEN A SINGLE RECOILING IMBH AND CLUSTERS IN A CC

13.3.1 *Integrator and first considerations*

Now that we have completed the grid of individual IMBH-cluster interactions, we can explore the scenario in which one IMBH is at large in a CC, interacting with many different IMBH on its way, either to an eventual escape from the CC, or down to the very centre, where the seed of a UCD is forming by the mergers of clusters. In this section we will assume $f_\bullet = 2/N_{\rm tot}$, where $N_{\rm tot}$ is the total number of clusters in the CC; that is, only two clusters in the whole CC harbour an IMBH and we also assume that they have coalesced and the merged hole escaped from the host cluster. As we will see, the presence of the IMBH triggers stellar disruptions in individual clusters of the CC, which could potentially represent a fingerprint of this process. In next section we will look at larger values of $f_\bullet$.

The numerical code that we use for the simulations of the CC and the IMBH is `Myriad` (Konstantinidis & Kokkotas 2010), which uses the Hermite fourth-order predictor-corrector scheme with block time steps (Makino & Aarseth 1992) for advancing the particles in time, while the accelerations and their derivatives are computed using GRAPE-6 (Makino et al. 2003) special purpose computers. Close encounters between particles (i.e. between clusters or between the IMBH and a cluster) are detected using the GRAPE-6 and evolved with a time-symmetric Hermite fourth-order integrator (Kokubo et al. 1998). Even though the code was originally designed for dynamical simulations of stars in star clusters, its flexible modularity made it easy to adapt to our particular problem. In particular, we assigned a radius to each particle representing a cluster, and we allowed clusters to merge with each other whenever the distance was smaller than the sum of the radii. In the simulations the IMBH is also a particle with a radius set to its Schwarzschild radius.

From the individual IMBH-cluster simulations presented previously we have data for the outcomes based on the mass ratio $\mathcal{M}_\bullet/\mathcal{M}_{\rm cl}$, the distance of closest approach between IMBH and cluster, and the relative velocity of the two objects and, thus, the change in kinetic energy of the IMBH. We use these results to correct the position and velocity of the IMBH after each interaction with a cluster in the simulation of the CC. This also provides us with information about the number of stellar disruptions

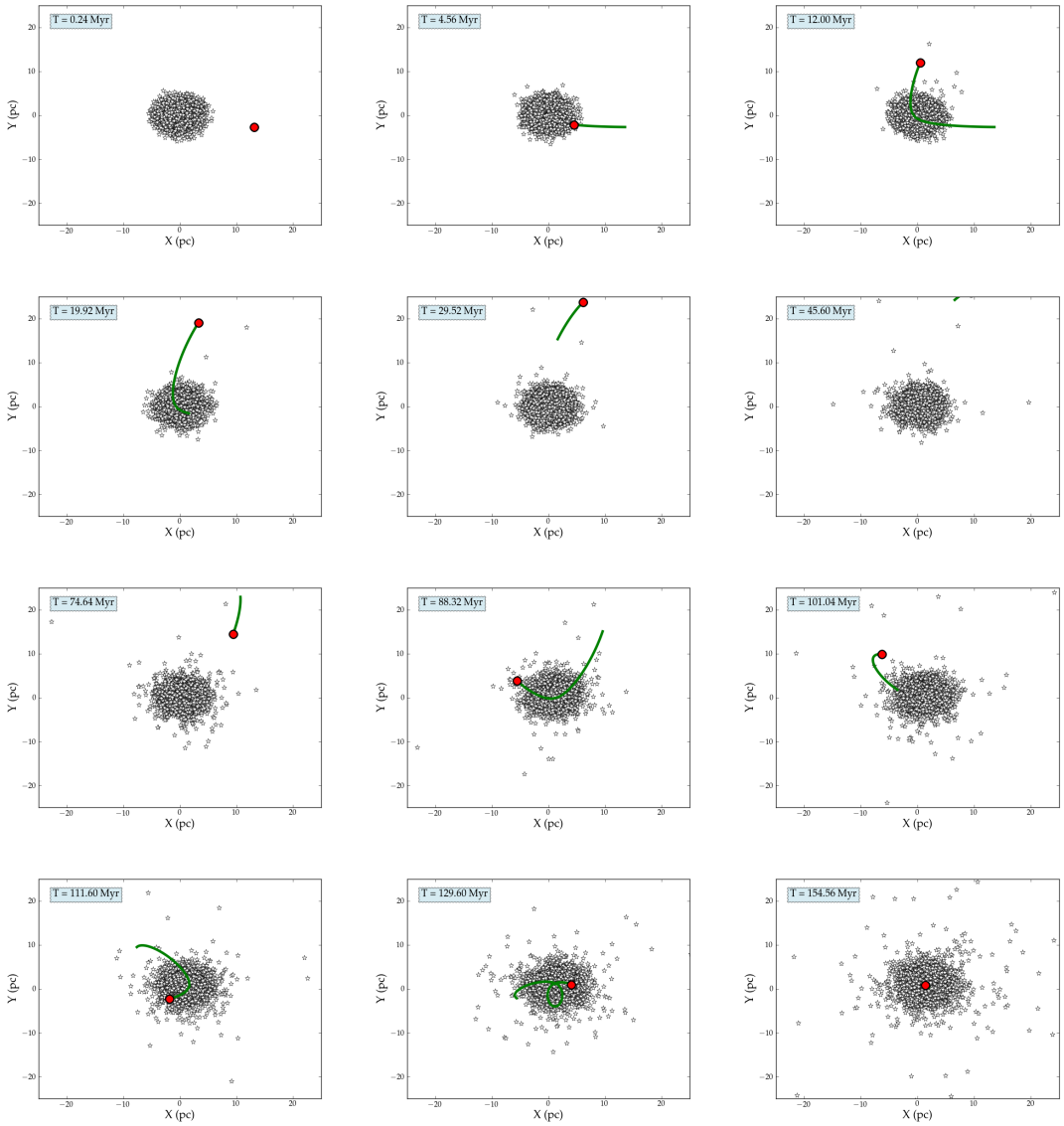

Figure 45: Projection in the X–Y plane of all trajectories of the stars (star symbols) in a cluster and the IMBH (red circle) for 12 different moments in the interaction. In this particular case, the process leads to the capture of the IMBH. For visibility, the radius of the IMBH and the stars has been artificially magnified. We also depict the previous 60 positions of the IMBH with a solid, green line. The mass ratio between the IMBH and the cluster is 0.01, the minimum distance of approach of the COM of the cluster and the IMBH is $d_{\rm min} = 1$ and $V_\infty = 1 {\rm km\,s^{-1}}$.

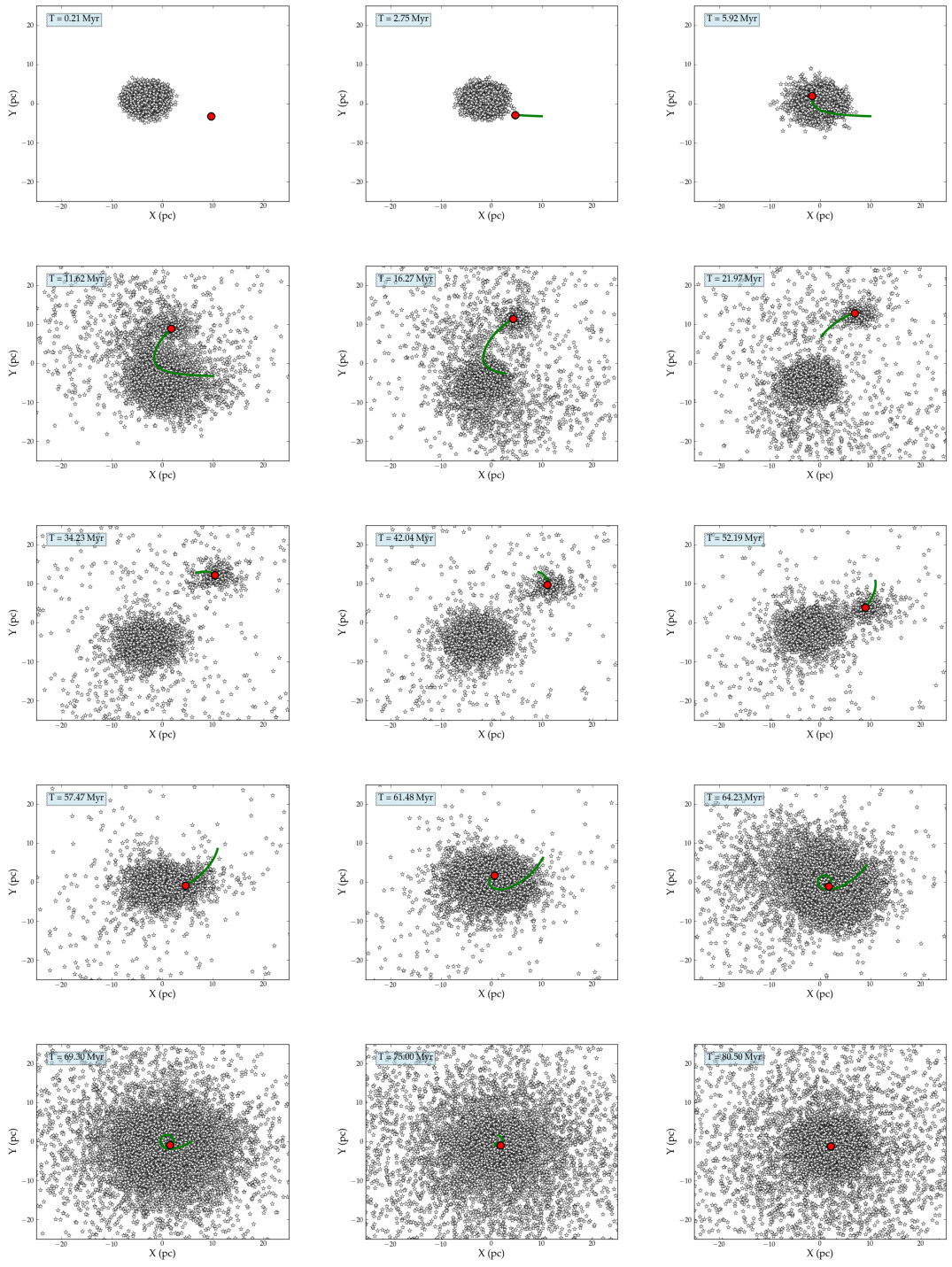

Figure 46: Same as in Fig.(45) for 15 different times. The mass ratio in this case is 0.333, $d_{\rm min} = 5$ and $V_\infty = 3 {\rm km\,s^{-1}}$.

triggered by the IMBH, as well as the characteristics of the cluster which captures the IMBH (if any). If a capture does occur, the simulation finishes and then we record the position of the "trapping" cluster in the CC. Another possible termination of the simulation is if the IMBH leaves the CC, because its speed is high enough to escape the complex.

13.3.2 *Assumptions for the initial conditions of the CC and the IMBH*

Initially we fix the radius of the CC, $R_{\rm CC}$, to a typical value coming from observational data and populate it with individual clusters following equation 141. In particular, in the "knots" of the Antennæ galaxy one observes a mass distribution with $n = -2$. The number of *observed* individual clusters in CCs is of the order of 100, but the actual number might actually be thousands, most of which are simply too faint to be observed (as discussed in e.g. Fellhauer & Kroupa 2005). We set the total mass of the CC to a typical observed value, $M_{\rm CC} \sim 10^6 - 10^8\,M_\odot$. The individual clusters have half-mass radii ranging between 0.5 and 4 pc and are distributed initially in the CC following a Plummer model (Plummer 1911) with a cut off radius (see table 7). The masses of the clusters are discrete and come from the $\mathcal{M}_\bullet/\mathcal{M}_{\rm cl}$ ratios that were used in the IMBH–cluster $N-$body simulations. Then, for $\mathcal{M}_\bullet = 5\times10^3 M_\odot$ and $\mathcal{M}_\bullet/\mathcal{M}_{\rm cl} = 0.01, 0.033, 0.1, 0.33, 1, 2$, the discrete masses of the clusters in the CC are $5\times10^5{\rm M}_\odot, 1.51515\times10^5{\rm M}_\odot, 5\times10^4{\rm M}_\odot, 1.51515\times10^4{\rm M}_\odot, 5\times10^3{\rm M}_\odot$ and $2.5\times10^3{\rm M}_\odot$. When two clusters collide in the CC simulation, we assume a 20% mass loss, based on the simulations of the collisions of two clusters of Amaro-Seoane et al. (2009); Amaro-Seoane & Freitag (2006), so the cluster product of the merger of two individual clusters has a mass which is 80% of the sum of the masses and a new radius, equal to the radius of the more massive cluster plus the 20% of the sum of the radii of the two clusters.

The IMBH in the merged cluster is assumed to be the product of a merger of two IMBHs that were located at the centres of two merging star clusters. We assume that this happened close to the centre of the CC, where most of the individual cluster-cluster collisions take place, because this is where the numerical density of clusters is highest. Hence, we initially place the IMBH at the centre of the CC. We choose a mass of $\mathcal{M}_\bullet = 5\times10^3\ M_\odot$, which determines the masses of individual clusters from the grid given in the previous section. The recoil speed of the merged IMBH could in principle be up to ~ 5000 km s^{-1} (Boyle & Kesden 2008; Herrmann et al. 2007a,b; Lousto & Zlochower 2011a,b)for optimal mass ratios, spins, and spin orientations. The recoils of greatest interest to our present study are in the ~ 100 km s^{-1} range, because the merged IMBH will then escape from its host cluster but be bound to the CC as a whole. It is difficult to judge how representative this will be for the mergers of actual IMBHs in CCs. Assuming the spin orientations are random, speeds in this range are characteristic of mass ratios $q \sim 0.1$ for substantial spins, or spins $a/M \sim 0.1$ for mass ratios comparable to unity (Lousto et al. 2010; van Meter et al. 2010). For our purposes we will study the case of $v_{\rm recoil} = 100$ km s^{-1}. At this speed, the escape time from a cluster of total radius ~ 10pc is ~ 0.1Myr. Hence we simply place the IMBH initially

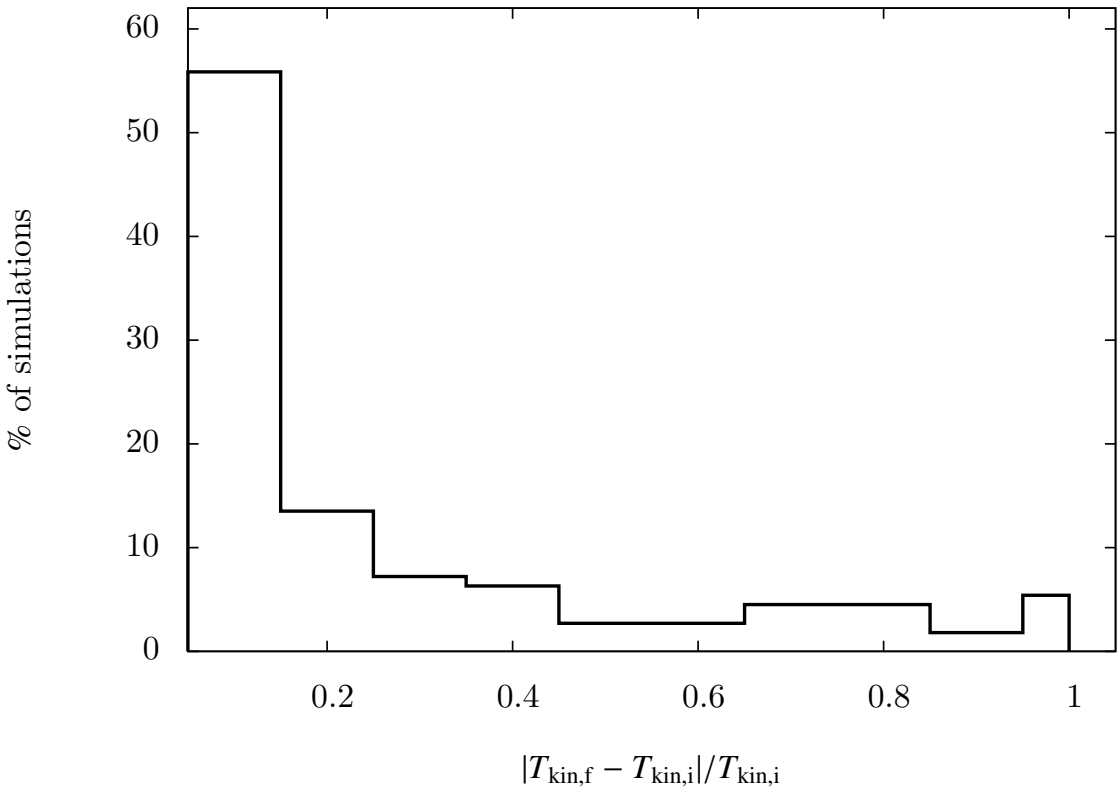

Figure 47: Kinetic energy difference between the initial and final kinetic energy ($T_{\mathrm{kinf,i}}$ and $T_{\mathrm{kinf,f}}$ respectively) normalized to the initial energy for all collisions between the IMBH and the clusters resulting in a fly-through for all $N-$body simulations.

ID	N	M_{CC} ($M_\odot$)	R_{CC} (pc)	ID	N	M_{CC} ($M_\odot$)	R_{CC} (pc)
A1	5×10^2	1.522×10^7	45	E1	3×10^3	4.32×10^7	122
A2	5×10^2	1.522×10^7	90	E2	4×10^3	5.75×10^7	165
A3	5×10^2	1.522×10^7	132	E3	4×10^3	5.75×10^7	246
A4	5×10^2	1.522×10^7	168	E4	4×10^3	5.75×10^7	329
A5	5×10^2	1.522×10^7	255				
B1	1×10^3	1.522×10^7	90	F1	5×10^3	7.18×10^7	122
B2	1×10^3	1.522×10^7	128	F2	5×10^3	7.18×10^7	165
B3	1×10^3	1.522×10^7	169	F3	5×10^3	7.18×10^7	248
B4	1×10^3	1.522×10^7	252	F4	5×10^3	7.18×10^7	330
B5	1×10^3	1.522×10^7	333				
C1	2×10^3	2.9×10^7	126	G1	6×10^3	8.6×10^7	122
C2	2×10^3	2.9×10^7	167	G2	6×10^3	8.6×10^7	165
C3	2×10^3	2.9×10^7	252	G3	6×10^3	8.6×10^7	248
C4	2×10^3	2.9×10^7	336	G4	6×10^3	8.6×10^7	330
D1	3×10^3	4.32×10^7	124	H1	8×10^3	1.14×10^8	122
D2	3×10^3	4.32×10^7	166	H2	8×10^3	1.14×10^8	165
D3	3×10^3	4.32×10^7	249	H3	8×10^3	1.14×10^8	248
D4	3×10^3	4.32×10^7	332	H4	8×10^3	1.14×10^8	330

Table 7: Simulation ID, number of clusters, total mass and cut-off radius of the CC. Note that the table is vertically split in two subtables.

at the centre of the CC, not bound to any cluster, and assume that it recoils in a random direction.

For the evolution of the recoiling IMBH we must take into account the loss of kinetic energy every time it hits a cluster. In figure (47) we can see the distribution of the resulting kinetic energy after a hit for all fly-by simulations of figure (44). While there is a spread in the distribution, there is a strong spike around 10% of loss for about 50% of all simulations. We have therefore adopted a slightly larger value, of 20%. This loss of energy will result into a rather negligible deacceleration of the IMBH, so that it will have more chances to escape the CC, and it will also lead to a lower number of stellar tidal disruptions. On the other hand, a bit less than 50% of all "fly-throughs" have *at least* over $\sim$ 5% of relative loss after one hit. This situation is more appealing from a dynamical standpoint, and therefore we will first address it. In the next sections we will assume an average loss of 20% for the "fly-throughs" hits, and in section 13.5 we will briefly explore the other situation.

Our parameter space consists of the number of clusters N and the initial radius of the CC, R_{CC}. The total mass M_{CC} of the CC is a consequence of N, because the masses of the clusters are assumed to follow a power law. The total radius that we use varies from 45 pc to 330 pc. Given the mass and the size of the CCs, the initial escape speeds

at the centres of the CCs are between $27 - 137 \mathrm{km\,s^{-1}}$. All details for all simulations are given in table 7.

13.3.3 *Results of the simulations*

In figure 50 we present the results of our 34 CC simulations. In simulations A1-A5, B1-B5, C1-C4, D1-D4, E3-E4, F4, G4 and H4 the IMBH escapes the CC after between zero and a few interactions with clusters. These cases correspond to smaller-mass CCs or to low initial concentrations. In simulations E1-E2, F1-F3, G1-G3, and H1-H4, which are more representative of observed CCs, the IMBH is captured in the CC after a significant number of interactions and ends up being trapped by an individual cluster, which can be the UCD seed (cases E1, E2, F2, F3, and H2). We show two particular cases which led to the capture of the IMBH in figures 48 and 49.

The IMBH goes through a very large number of interactions with individual clusters until it is eventually trapped. This number depends on the density of clusters in the CC. In 6 simulations, the IMBH gets captured by a cluster that has not yet merged with other clusters. In 5 simulations, the cluster that captures the IMBH is the central cluster of the CC, the seed UCD. We show in table 8 the details about the cluster that captures the IMBH, the distance from the centre where this takes place, and the mass of the most massive cluster in the system at the time of the IMBH-capture, i.e., the mass of the UCD seed. An interesting process in the dynamical evolution of the system is that the IMBH triggers stellar collisions, i.e., stars are set on such an orbit that they collide and disappear from the system. We note that only in one case, in simulation F1, one star was torn apart by the tidal forces of the IMBH acting on a star. The middle number next to each circle of figure 50 corresponds to star-star *collisions triggered by the IMBH* in the clusters. We can conclude that one should expect a star-star collision in a CC every $5 - 8$Myr. In figure 51 we show the accumulated number of stellar collisions that led to a disruption in function of the time for simulation G3, as well as the accumulated number of hits between the IMBH and a cluster.

The third number next to each circle of Figure 50 is the initial escape velocity at the centre of the CC. As it is obvious, CCs with values $< 100 \mathrm{km\,s^{-1}}$ retain the IMBH due to our choice of the initial recoiling speed. An interesting case is simulation H4 in which the escape velocity is $84 \mathrm{km\,s^{-1}}$, but the IMBH escapes because the system is initially not very concentrated and the IMBH has only 2 interactions with clusters. In this case, the energy of the IMBH did not decrease enough to be trapped in the CC. Simulation G3 corresponds to the opposite situation. Even though the escape speed is the same as in H4, the IMBH remains in the system because the CC is denser, so that the IMBH has a chance of interacting significantly with clusters and, hence, of decreasing its kinetic energy below the threshold. In figure 52 we have the evolution of the velocity of the IMBH in simulation G3 compared with the escape velocity at the radius of the CC where the IMBH is. Initially, the escape velocity is lower than the velocity of the IMBH, ensuring the escape of the IMBH from the system, but the IMBH loses energy rapidly during the first few Myr because of its interactions with clusters.

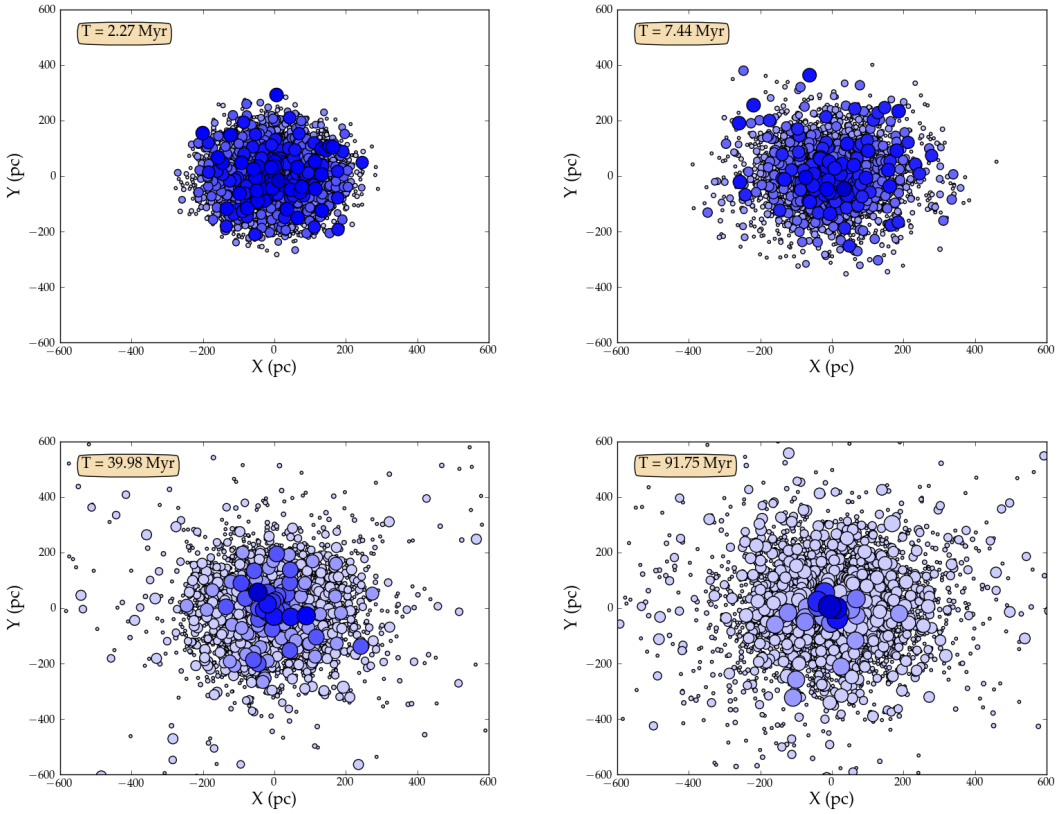

Figure 48: Formation of the UCD seed at the centre of the CC. We show a projection in the X–Y plane of all individual clusters for the simulation F3. The radii of the clusters have been artificially magnified, heavier members have larger sizes and darker colours *relative to every panel for the sake of visibility*. This means that even if the colours of the heaviest clusters in the last panel are as dark as the most massive ones in the first panel, the clusters in the last panel are heavier and larger. After 7.44 Mys we can already see how the more massive clusters start to agglomerate at the centre of the CC. Later, at $T \sim 40$ Myr, all of them are confined to the central part of the CC and in the last panel we can see that only a handful of clusters are heavy and a very massive cluster is sitting at the very centre, while lighter clusters occupy all of the remaining space. The mass of this very massive cluster is $2.9 \times 10^6 M_\odot$ and constitutes the seed of the UCD. See `http://members.aei.mpg.de/amaro-seoane/ultra-compact-dwarf-galaxies`, model F3 for an animation of the process.

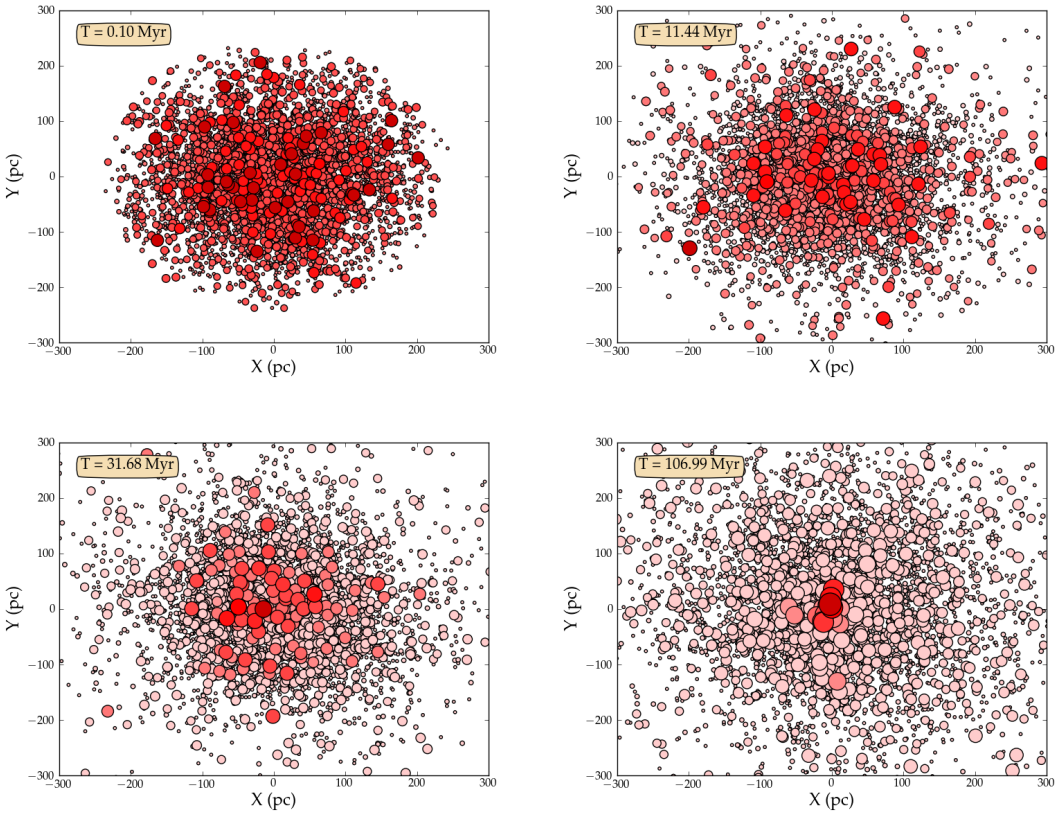

Figure 49: Same as in Fig.(48) but for simulation G3. In this case we show a zoom of diameter 600 pc. As in the first figure, after some $\sim$ 100 Myr we have a very massive cluster at the centre and all other clusters are much lighter. The heaviest cluster at this time has a mass of $5.5 \times 10^5\,M_\odot$, while clusters with masses $5.2 \times 10^5\,M_\odot$, $5.0 \times 10^5\,M_\odot$, $1.9 \times 10^5\,M_\odot$, $1.4 \times 10^5\,M_\odot$ and $6.5 \times 10^4\,M_\odot$ lie very close to the centre of the CC. See `http://members.aei.mpg.de/amaro-seoane/ultra-compact-dwarf-galaxies`, model G3 for a movie of the figure.

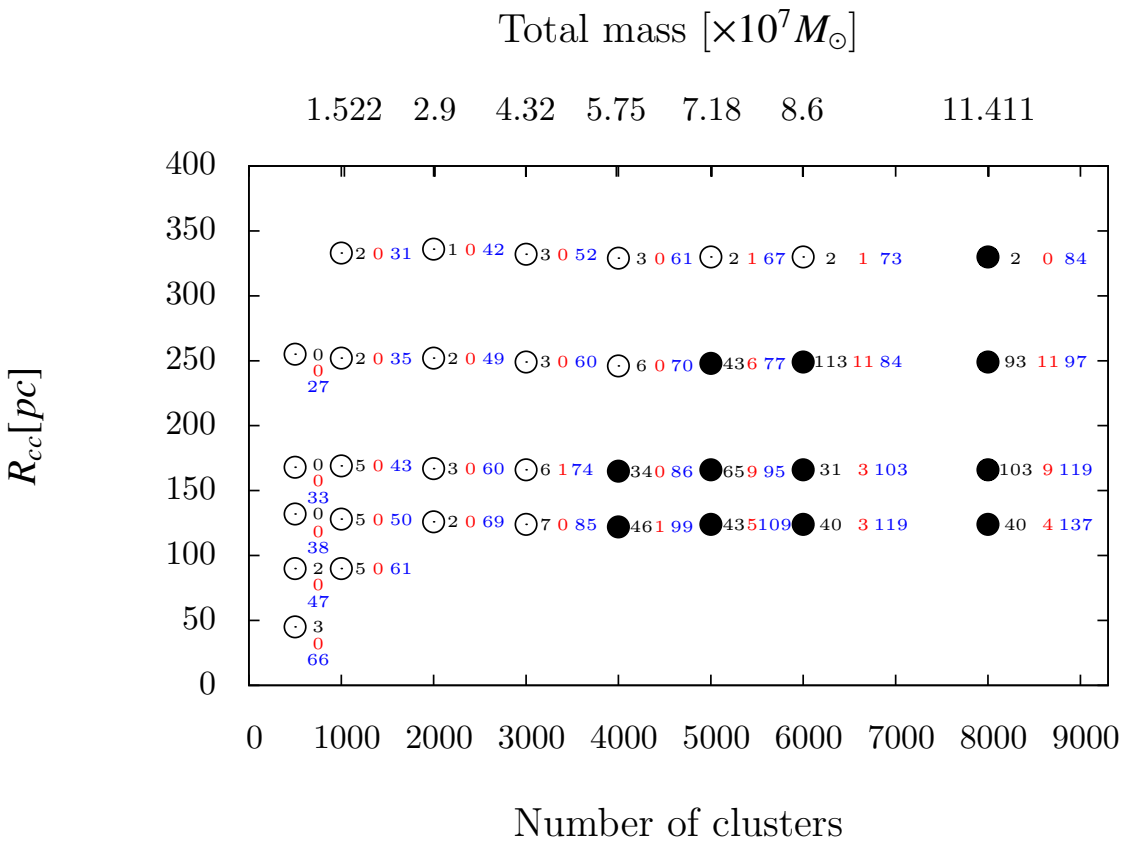

Figure 50: Outcome of the CC simulations. The x-axis shows the number of clusters in each simulation, while the y-axis shows the initial radius of the CC. The upper x-axis shows the total mass of the system in $M_\odot$. Every circle corresponds to a single entry of Table 7 in a way such that the circle at the bottom left corresponds to the simulation with ID A1 and the circle at the top right corresponds to the simulation with ID H4. An open circle indicates a simulation where the IMBH finally escaped the CC. On the other hand, a filled circle represents a simulation where the IMBH remained bound to the system. Next to every circle there are three numbers. The first (black) shows the number of clusters hit by the IMBH until either it escapes the CC or it is captured by a cluster. The second (red) number is the number of stars that are tidally disrupted by the IMBH and the number of star-star collisions triggered by the IMBH in the clusters. The third number indicates the initial escape velocity at the centre of the CC in $\mathrm{km\,s^{-1}}$.

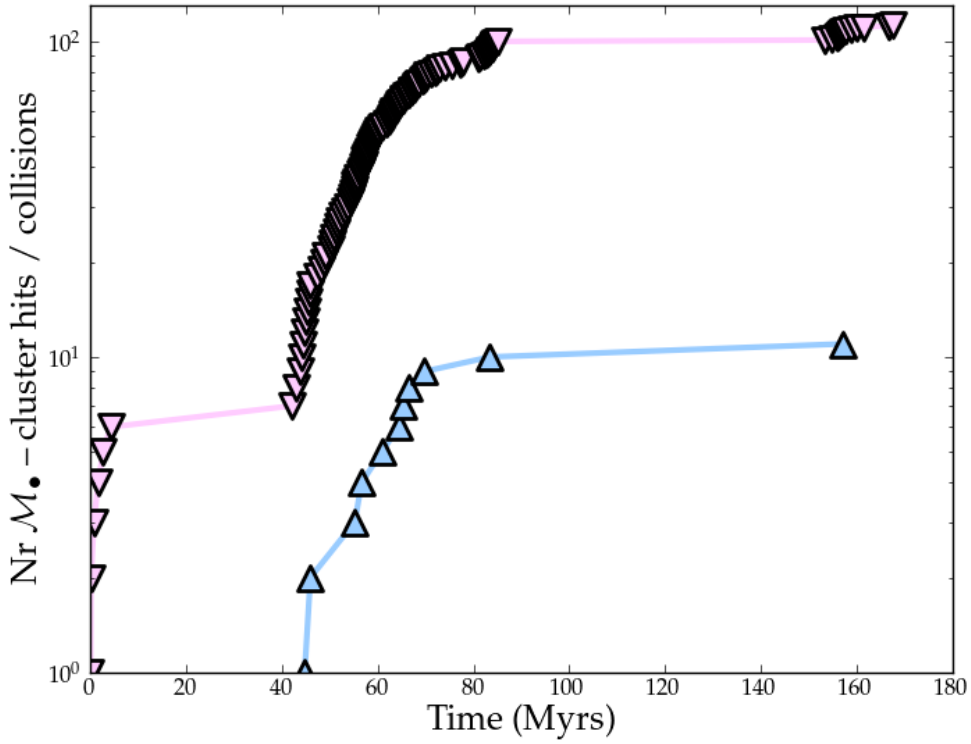

Figure 51: Cumulative number of IMBH and cluster hits for the simulation G3 (inverted, light magenta triangles) and of stellar collisions leading to a disruption (blue triangles) as a function of time.

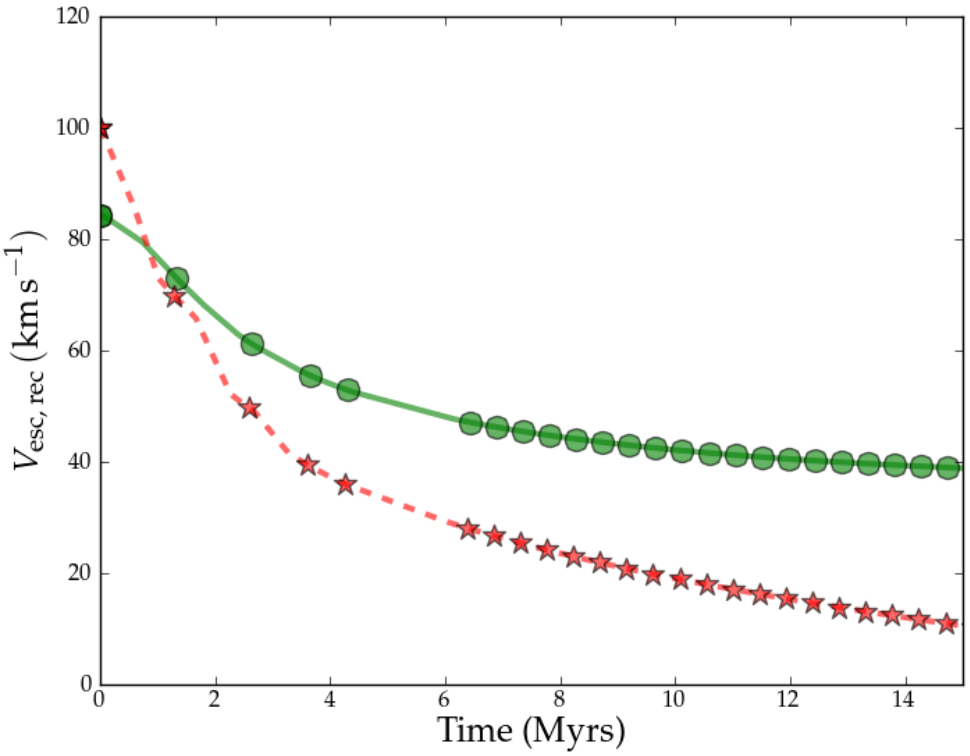

Figure 52: IMBH speed (dashed, red line with stars) and instantaneous escape velocity (solid, green curve with spheres) for the IMBH as a function of time in simulation G3. Even though initially the IMBH recoiling speed is higher than the required threshold to escape the CC, soon after ~ 0.80 Myrs the interactions with individual clusters lower its kinetic energy and it is trapped in the CC, in the meaning that the speed drops below the threshold.

ID	Coll	T[Myr]	R_{capt}[pc]	$\mathcal{M}_{cl}[M_\odot]$	$\mathcal{M}_{UCD}[M_\odot]$	T_{DF}[Myr]	T_{FH}[Myr]	T_{FC}[Myr]
E1	1	14	9.6	1.9×10^6	1.9×10^6	142	0.197	12.57
E2	0	38.2	10.3	1.2×10^6	1.2×10^6	129	0.09	33.59
F1	4	9.7	42	5×10^3	6.5×10^5	2400	0.047	2.14
F2	9	28.2	18.4	7.3×10^5	7.3×10^5	240	0.067	0.54
F3	6	118	15.4	2.9×10^6	2.9×10^6	367	0.1	0.28
G1	3	10.14	45.6	2.5×10^3	1.1×10^6	4300	0.011	0.35
G2	3	13.1	23.8	1.5×10^4	6.6×10^5	762	0.009	0.009
G3	11	167.4	92.7	2.5×10^3	4×10^6	7900	0.1	44.8
H1	4	11.7	15.5	5.6×10^5	1.3×10^6	26	0.012	3.65
H2	9	20.1	17.8	1.8×10^6	1.8×10^6	360	0.15	5.32
H3	11	49.9	30.2	1.5×10^5	9.7×10^5	167	0.28	9.54

Table 8: Data for the simulations where the IMBH was captured by a cluster of the CC. The first column shows the ID of the simulation (see table 7). The second column shows the number of stellar collisions triggered by the IMBH. The third column displays the time of capture of the IMBH by a single cluster. The fourth shows the distance from the centre of the CC, where the IMBH was captured. The next column gives us the mass of that cluster and the mass of the heaviest cluster in the CC by that time; i.e. the mass of the forming UCD. The sixth column corresponds to an estimate for the IMBH to reach the centre of the CC by dynamical friction (see text). The last two columns show the time the IMBH hits a cluster for the first time and the time of the first stellar collision in the CC. In the particular case of simulation F1 there was a tidal disruption of a star by the IMBH.

13.4 INTERACTIONS BETWEEN MULTIPLE RECOILING IMBHS AND CLUSTERS IN A CC

In this section we investigate a scenario in which $f_\bullet > 1$. We use the initial configuration of F3 as described in table 7 as our fiducial CC system and study the evolution of systems of five and ten IMBHs at large. For this, we set them initially close to the centre and allow them to be kicked off the host cluster at the same time, $T = 0$, as a simplifying assumption. In real systems there will be a time lag:

$$\tau_{\rm bin} = \tau_{\rm run}\, \tau_{\rm IMBH}\, \tau_{\rm merg}. \tag{144}$$

where $\tau_{\rm run}$ is the timescale for a cluster to evolve to the runaway phase, $\tau_{\rm IMBH}$ is the timescale for the VMS to become unstable and form an IMBH and $\tau_{\rm merg}$ is the timescale for the cluster to merge with another cluster. The phenomena involved are various and the assumptions inherent to $\tau_{\rm run}$ and $\tau_{\rm IMBH}$ prevent realistic estimates, as we explained in the introduction. On the other hand, Amaro-Seoane & Freitag (2006) estimate that $\tau_{\rm merg} \sim 7$ Myr, which compared to the timescale for the CC to reach the seed UCD phase, of the order of ~ 100 Myr, is a rather short interval of time and can be regarded as instantaneous. In view of these arguments, we assume that the IMBHs are expelled instantaneously from their host clusters at different places of the CC at $T = 0$.

In table 9 we show the results for the first simulation, in which we place five IMBHs around the centre, as indicated in column number three. IMBHs #2 – 5 have been distributed over the surface of a sphere of radius 17.32 pc and only one, #1, is very close to the centre, to avoid the artificial formation of various binaries of IMBHs when we start the simulation. We assign the holes initial recoil speeds between $50 - 100\,{\rm km\,s^{-1}}$ and different directions and then let the system evolve. We find that after some ~ 34 Myr all IMBHs have been either captured by an individual cluster which is sinking the the centre due to DF, or formed a satellite with a cluster. In figure 53 we show the CC at $T = 62.37$ Myr. We stop the simulation at that time because the satellites are consuming all of the computational power. In the process and up to that time, there are 7 stars that have been disrupted in the CC, as we can see in the table.

In table 10 we repeat the same exercise but for a system with 10 IMBHs. The initial setup is identical to the previous one. We find that in this case three holes leave the system due to an increase in their kinetic energy. The rest of them have formed a hard binary with a cluster and will eventually be captured.

13.5 LOWER KINETIC ENERGY LOSS

In the simulations of the previous sections we assumed a loss of relative kinetic energy of $\sim 20\%$ for the hits that led to a fly-through, although it could be much larger than that, as we saw in figure 47. While this is true for a bit less than 50% of all systems, the rest of them had a peak in the distribution around $\sim 5\%$. We have addressed the

IMBH ID	Outcome	R_{init} (pc)	V_{init}/V_{esc}	T (Myr)	R_{fin}^{UCD} (pc)	$M_{cl}(M_\odot)$	# Stellar disr
1	capture	0.0024	0.89	14.24	51.2	2.5×10^3	1
2	capture	17.32	0.70	12.41	103	7.85×10^5	2
3	satellite	17.32	0.71	34	0	9.6×10^5	2
4	satellite	17.32	0.94	9.45	9.5	5.44×10^5	1
5	capture	17.32	0.76	2.35	118.2	5×10^5	1

Table 9: Data for the simulation with five IMBHs in a CC. The first column shows the ID of the IMBH, the second column the outcome of the BH after 35 Myr, which can be either a capture, a satellite (the IMBH is orbiting a cluster and will eventually merge with it) or an escape (the IMBH escapes the whole CC). The third column displays the initial distance of the IMBH from the center of the CC. The fourth corresponds to the initial velocity of the normalised to the local escape velocity from the cluster. The fifth gives the time at which the outcome was measured. The sixth shows the final distance of the capturing cluster from the most massive cluster of the system, the seed UCD. In this case, IMBH #3 is captured by the seed, and thus this distance is zero. The seventh is the mass of the capturing cluster at the time of capture. Finally, the last column shows the number of stellar collisions in clusters that have been triggered by the IMBH.

IMBH ID	Outcome	R_{init} (pc)	V_{init}/V_{esc}	T (Myr)	R_{fin}^{UCD} (pc)	$M_{cl}(M_\odot)$	# Stellar disr
1	satellite	0.0018	0.56	1.9	130.7	7.5×10^5	2
2	satellite	17.33	0.97	23.8	130.7	1.6×10^6	2
3	satellite	17.33	0.99	8.9	112.2	1.44×10^6	3
4	satellite	17.33	0.89	9.1	163.5	2.2×10^6	1
5	escaper	17.33	0.56	-	-	-	5
6	escaper	17.33	0.59	-	-	-	0
7	escaper	17.33	0.88	-	-	-	7
8	satellite	17.33	0.90	10.2	8.7	2.7×10^6	1
9	satellite	17.33	0.56	5.7	140.5	7.75×10^6	0
10	satellite	25.99	0.72	4.4	140.5	1.47×10^6	1

Table 10: Same as in table 9 but for ten holes. In this case three IMBHs leave the CC. We find 22 stellar disruptions during the simulation.

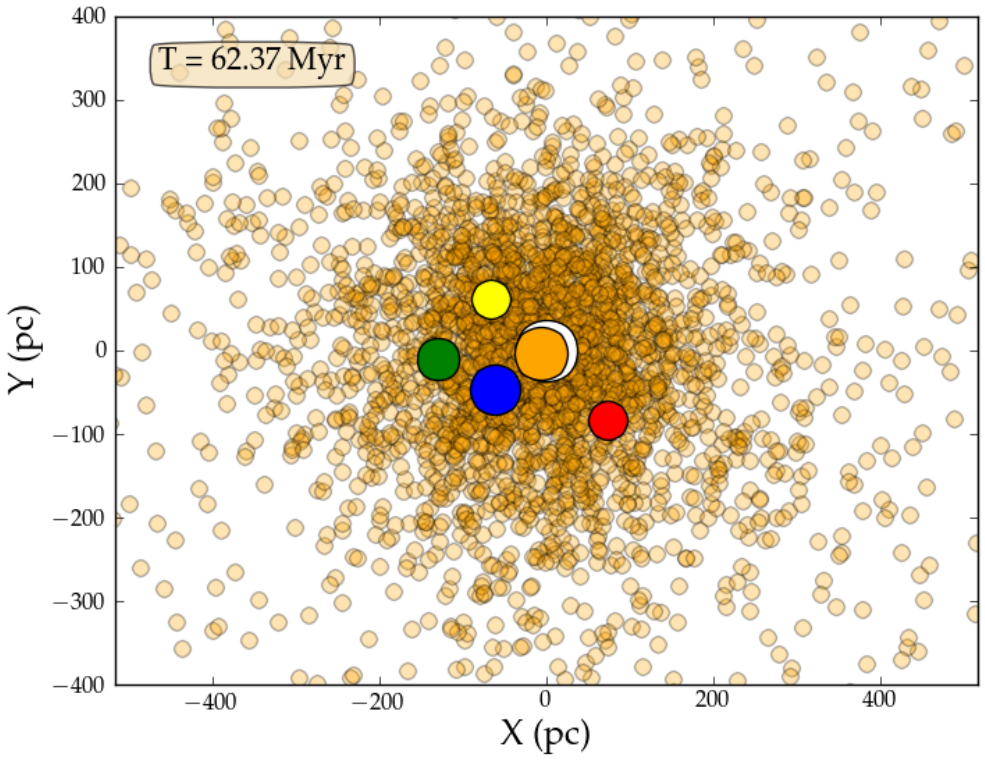

Figure 53: Projection in X–Y of all clusters for the simulation in which we have initially 5 IMBHs. We show in white, orange, blue, green, yellow, and red the clusters that captured the holes (or will capture, if in satellite, see text). For clarity we depict all other clusters with the same radius and colour (light orange). The green cluster harbours two IMBHs and the blue cluster too. The later one merged with an IMBH and after that with another one which contained another IMBH.

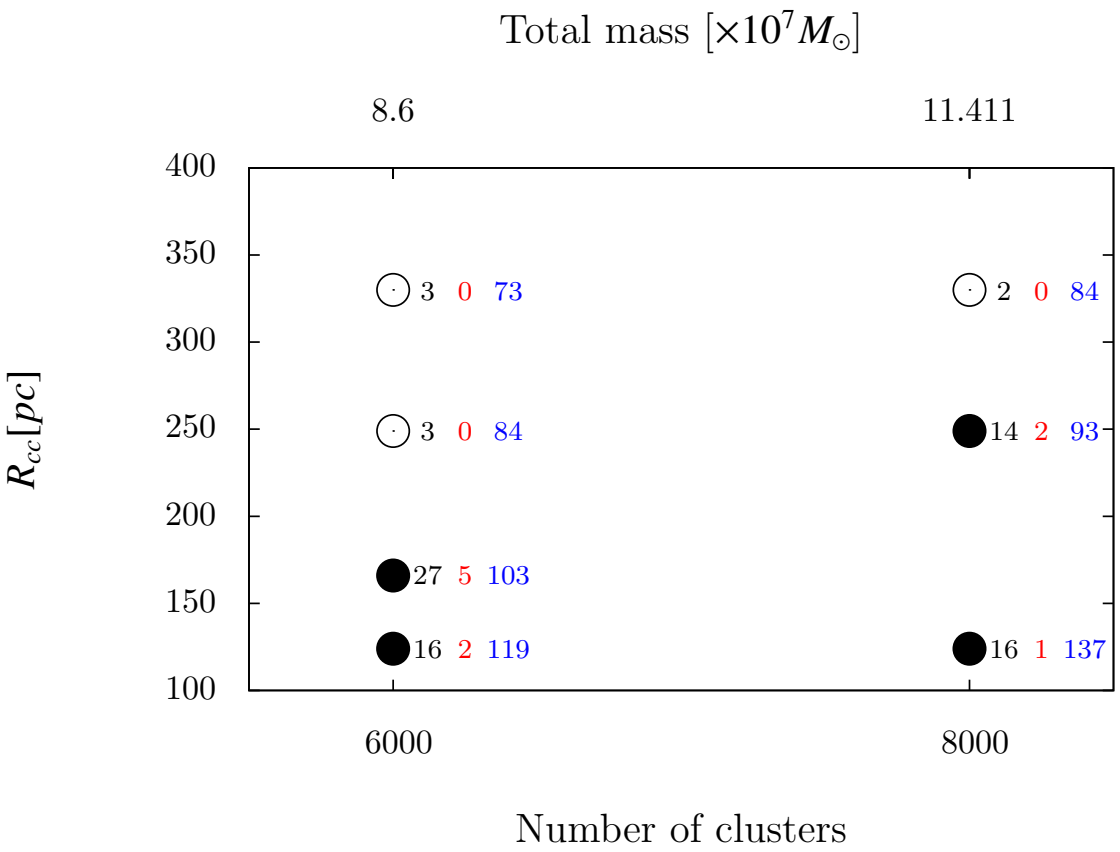

Figure 54: Same as figure (50) but assuming a fixed loss of kinetic energy of 5% after every hit for the fly-throughs.

situation of a larger loss first, because it leads to more interesting effects from a pure dynamical standpoint.

However, we deem it necessary to we repeat some experiments in the evolution of the CC to understand the other regime. Therefore, we repeat experiments G1, G2, G3, G4, H1, H3, H4 of table 7 but this time we assume a loss of 5% after every hit for the fly-throughs. In figure (54) we can see the results. We have reduced the exploration to the range of radii and total mass that could be more interesting for our analysis. We can see that although the total number of stellar disruptions is signficantly reduced, it is not zero. Also, in four configurations the IMBH at large is captured eventually by the forming CC.

13.6 SUMMARY AND CONCLUSIONS

In this work we have presented results that address the formation of UCD from young clusters, and the role of recoiling IMBHs in a CC. The formation of the IMBH in clusters is used as a working hypothesis, and hence also the possibility that these

interact with the young clusters. For that, we first ran a set of $\sim$ 200 direct-summation $N-$body simulations that covers the parameter space for individual IMBH–cluster encounters. We methodically varied the mass ratio between the IMBH and the cluster, the relative velocity, and the impact parameter. This allowed us to build a grid with the expected outcome of the interaction and the modification of the kinetic energy of the IMBH. Later we ran additional direct-summation $N-$body simulations for a scenario in which one IMBH is at large in a CC. The IMBH is assumed to be the result of the coalescence of two holes, which led to the expulsion of the hole from the initial host cluster. We studied the dynamical evolution of this single IMBH in an evolving CC. Parallel to the individual interactions between the IMBH and clusters in the CC, which are corrected using the above-mentioned table, clusters are colliding and merging with each other, which results in the formation of a run-away individual cluster, which typically after $\sim$ 100 Myrs contains almost all of the mass of the CC. This is what we designate "the seed of an ultra-compact dwarf galaxy", since this very massive cluster is the result of the successive amalgamation of smaller clusters in the initial distribution of the CC.

We find that for realistic CCs (i.e. those which resemble observations, such as the knots of the Antennæ), the IMBH is either eventually captured by the seed UCD (in those simulations less dense initially) or by a smaller cluster (in the simulations with the largest concentrations of clusters at the centre) which, however, is close to the centre of the CC, so that it will in the course of time sink down to the very centre, where the seed UCD is settled. The typical timescale for this trapping is of about $\sim$ 200 Myr.

We can see this by estimating the dynamical friction time $T_{\rm DF}$. This is the timescale for the IMBH captured in a cluster to reach the centre. For an object with mass m moving in a system of total mass M it is given by (see e.g. Binney & Tremaine 2008)

$$T_{\rm DF} = \frac{1.17}{\ln\Lambda}\frac{\rm M}{\rm m}\frac{\rm r}{\rm V_h}, \tag{145}$$

where r is the distance from the centre of the system, V_h is the root mean square (RMS) velocity dispersion of the system and $\ln\Lambda$ the Coulomb logarithm, which is of the order of unity. From table 8 we can see that in almost half of the cases in which the IMBH was retained in the CC, it is captured by the most massive cluster of the system, the seed UCD. $T_{\rm DF}$ is in all cases a few tens or hundreds of Myrs. On the other hand, when the IMBH gets captured by a smaller cluster (6 out of the 11 simulations), $T_{\rm DF}$ is of the order of $\sim$ 1 Gyr, still well below a Hubble time. We note also that this analytical calculation is an overestimate, because the CC evolves dynamically with time and there is a huge accumulation of mass in the innermost region which will significantly reduce the timescale for the IMBH to reach the seed UCD.

When the IMBH remains bound to the CC, the average time for it to hit a cluster is $0.16 - 0.43$Myr. On the other hand, the mean time taken by the IMBH to fly through a star cluster is of the order of 0.1Myr. Hence, after recoiling and before getting captured,

the IMBH spends 1/3 of its time interacting with clusters, so that the possibility to find an IMBH in a cluster of a newly formed (less than 100Myr old) CC is about $\sim 30\%$

We repeated the exercise with a CC harbouring initially 5 and 10 IMBHs which were distributed with different velocities. We find that after some $\lesssim 30$ Myr most of the holes are either captured by a single cluster or have formed a hard binary with one in regions relatively close to the runaway cluster, the seed of a UCD which is forming in the CC. We cannot follow the further evolution of the system due to the limitations inherent to our approach. We also note that gas is very likely to play an important role in the whole process. In particular, in some CCs the oldest cluster is located at the centre of the gas cloud (Whitmore et al. 2010). In our simulations we have neglected this, since we are limited by our codes, which rely on pure particle dynamics. Still, even if we could actually have implemented a (rough) approach for the gas with an external force, the complexity of the problem justifies our first approach. We have decided to postpone the role of the gas for upcoming work. The same applies to mass loss because of stellar evolution, although statistically, since the IMBH interacts with clusters of different masses, the global dynamical evolution is well represented by our models, within our limitations.

Also, reducing the relative kinetic energy loss for fly-throughs leads to a reduced number of tidal disruption events, but we still find some systems for which the implications are similar to the analysis that used a larger loss.

While the number fraction of IMBH in the mass-range of $10^{2-4}\,M_{\odot}$ in CCs is an unknown, they sink to the centre in a time which is much shorter than the Hubble time. The scenario that we have described here leads to the formation of a very massive black hole at the centre of the UCD, with a mass that depends on unknowns, such as the formation rate of IMBHs in the CC. The internal velocities of the systems we study are not as extreme as those explored by Merritt et al. (2009) in the context of hypercompact stellar systems, because the seed UCD inherits the central velocity from the resulting mergers between individual clusters. When the UCD is formed, the velocity will roughly be what one can expect from a dense stellar system in dynamical equilibrium. A very interesting feature of the process of sowing an UCD with an IMBH is that independently of whether the IMBH stays in the CC or escapes, it triggers star-star collisional disruptions in the clusters it hits. This could be envisaged as an electromagnetic signature of the scenario.

BIBLIOGRAPHY

Aarseth, S. J. 1999, The Publications of the Astronomical Society of the Pacific, 111

——. 2003, Gravitational N-Body Simulations (ISBN 0521432723. Cambridge, UK: Cambridge University Press, November 2003.)

Amaro-Seoane, P. 2006, in American Institute of Physics Conference Series, Vol. 873, Laser Interferometer Space Antenna: 6th International LISA Symposium, ed. S. M. Merkovitz & J. C. Livas, 250–256, arXiv:astro-ph/0610479

Amaro-Seoane, P., Eichhorn, C., Porter, E. K., & Spurzem, R. 2010, MNRAS, 401, 2268

Amaro-Seoane, P., & Freitag, M. 2006, ApJ, 653

Amaro-Seoane, P., Miller, M. C., & Freitag, M. 2009, ApJ Lett., 692, L50

Amaro-Seoane, P., & Santamaría, L. 2010, ApJ, 722, 1197

Baker, J. G., Boggs, W. D., Centrella, J., Kelly, B. J., McWilliams, S. T., Miller, M. C., & van Meter, J. R. 2008, ApJ Lett., 682, L29

Bastian, N., Emsellem, E., Kissler-Patig, M., & Maraston, C. 2006, Astronomy & Astrophysics, 445

Belkus, H., Van Bever, J., & Vanbeveren, D. 2007, ApJ, 659, 1576

Binney, J., & Tremaine, S. 2008, Galactic Dynamics: Second Edition, ed. J. Binney & S. Tremaine (Princeton University Press)

Boyle, L., & Kesden, M. 2008, Phys. Rev. D, 78, 024017

Bruens, R. C., Kroupa, P., Fellhauer, M., Metz, M., & Assmann, P. 2011, Astronomy & Astrophysics, accepted

Campanelli, M., Lousto, C., Zlochower, Y., & David, M. 2007a, Phys.Rev.Lett., 98

Campanelli, M., Lousto, C. O., Zlochower, Y., & David, M. 2007b, Astrophys.J., 659

de Grijs, R., Anders, P., Bastian, N., Lynds, R., Lamers, H. J. G. L. M., & O'Neil, E. J. 2003, MNRAS, 343, 1285

Fellhauer, M., & Kroupa, P. 2005, MNRAS, 359

Fregeau, J. M., Larson, S. L., Miller, M. C., O'Shaughnessy, R., & Rasio, F. A. 2006, ApJ Lett., 646, L135

Freitag, M., Gürkan, M. A., & Rasio, F. A. 2006a, MNRAS, 368, 141

Freitag, M., Rasio, F. A., & Baumgardt, H. 2006b, MNRAS, 368, 121

Gürkan, M. A., Freitag, M., & Rasio, F. A. 2004, ApJ, 604

Gallagher, S. C., Charlton, J. C., Hunsberger, S. D., Zaritsky, D., & Whitmore, B. C. 2001, The Astronomical Journal, 122

Gonzalez, J. A., Hannam, M., Sperhake, U., Brügmann, B., & Husa, S. 2007, Physical Review Letters, 98

Healy, J., Herrmann, F., Hinder, I., Shoemaker, D. M., Laguna, P., & Matzner, R. A. 2009, Physical Review Letters, 102, 041101

Herrmann, F., Hinder, I., Shoemaker, D., & Laguna, P. 2007a, Classical and Quantum Gravity, 24, 33

Herrmann, F., Hinder, I., Shoemaker, D., Laguna, P., & Matzner, R. A. 2007b, ApJ, 661, 430

Homeier, N., Gallagher, J. S. I., & Pasquali, A. 2002, Astronomy & Astrophysics, 391

King, I. R. 1966, AJ, 71

Kokubo, E., Yoshinaga, K., & Makino, J. 1998, MNRAS, 297

Konstantinidis, S., & Kokkotas, K. D. 2010, Astronomy & Astrophysics, 522

Konstantopoulos, I. S., Bastian, N., Smith, L. J., Westmoquette, M. S., Trancho, G., & Gallagher, J. S. 2009, The Astrophysical Journal, 701

Kroupa, P. 1998, MNRAS, 300

Kustaanheimo, P. E., & Stiefel, E. L. 1965, J. Reine Angew. Math.

Lousto, C., & Zlochower, Y. 2008, Phys.Rev., D79

Lousto, C. O., Campanelli, M., Zlochower, Y., & Nakano, H. 2010, Classical and Quantum Gravity, 27, 114006

Lousto, C. O., Nakano, H., Zlochower, Y., & Campanelli, M. 2010, Phys. Rev. Letters D, 81

Lousto, C. O., & Zlochower, Y. 2011a, ArXiv e-prints

——. 2011b, Phys. Rev. D, 83, 024003

Makino, J., & Aarseth, S. J. 1992, PASJ, 44

Makino, J., Fukushige, T., Koga, M., & Namura, K. 2003, PASJ, 55

Merritt, D., Schnittman, J. D., & Komossa, S. 2009, ApJ, 699, 1690

Pellerin, A., Meurer, G. R., Bekki, K., Elmegreen, D. M., Wong, O. I., & Knezek, P. M. 2010, The Astronomical Journal, 139

Peterson, C. J., & King, I. R. 1975, AJ, 80

Plummer, H. C. 1911, MNRAS, 71

Portegies Zwart, S. F., Baumgardt, H., Hut, P., Makino, J., & McMillan, S. L. W. 2004, Nat, 428, 724

Portegies Zwart, S. F., & McMillan, S. L. W. 2000, ApJ Lett., 528, L17

Pretorius, F. 2005, Physical Review Letters, 95

Sopuerta, C. F., Yunes, N., & Laguna, P. 2006, Physical Review D, 74

Suzuki, T. K., Nakasato, N., Baumgardt, H., Ibukiyama, A., Makino, J., & Ebisuzaki, T. 2007, ApJ, 668, 435

Toomre, A. 1977, In *The Evolution of Galaxies and Stellar Populations*, Yale

van Meter, J. R., Miller, M. C., Baker, J. G., Boggs, W. D., & Kelly, B. J. 2010, ApJ, 719, 1427

Whitmore, B. 2006, "Massive Stars: From Pop III and GRBs to the Milky Way", Cambridge University Press, astro-ph/0612695

Whitmore, B. et al. 2010, The Astronomical Journal, 140

Whitmore, B., Zhang, Q., Leitherer, C., & Fall, M. 1999, The Astronomical Journal, 118

Whitmore, B. C. et al. 2010, AJ, 140, 75

Zhang, Q., & Fall, S. M. 1999, The Astronomical Journal, 527

Zlochower, Y., Campanelli, M., & Lousto, C. O. 2010

Part III

DISCUSSION

DISCUSSION

13.7 FOREWORD

This dissertation reflects an important part of one of my main research topics during the last years. I studied theoretical physics in Spain, and I specialized in particle and mathematical physics. In Heidelberg, where I did both my *Diplomarbeit* and PhD, I studied stellar and gas dynamics in dense stellar systems, such as galactic nuclei and globular clusters. Later I moved to the Max-Planck Institute for Gravitational Physics (Albert Einstein Institute), where my main concern moved towards the connection between GR and theoretical astrophysics.

The connection between these two domains is the creation of gravitational wave (GW) sources, detectable with a space-borne GW observatory, such as eLISA, and also, at least to some extent, the tidal disruption of extended stars, such as our sun. Many disruption candidates may have already been detected with ROSAT, Chandra and Swift [2], and the number will surge with upcoming transient surveys like the Zwicky Transient Facility (ZTF), the Large Synoptic Survey Telescope (LSST), SRG/eROSITA, as well as the ESA L2 mission Athena+.

These two problems share one important characteristic: One has to understand how a star, a compact object or a stellar-mass black hole can reach the supermassive black hole, assumed to be the massive dark object lurking at the very centre of the host dense stellar system, which in the work presented here can be either a galaxy, or a globular cluster.

In the case of an extended star, a single close passage around the supermassive black hole is enough, since we do not address the problem of tidal heating in this dissertation. The star is torn apart and energy is released. This burst of electromagnetic radiation is very interesting and can provide us with information about the local environment where the disruption took place. However, in the case of a compact object, such as a white dwarf[3], a neutron star or a stellar black hole, one –or for all matters a few– pericentre passage is not enough, since we are interested in the accumulation of hundreds to thousands of coherent bursts of gravitational radiation[4]. This is the price that one has to pay. The reward is the first test ever of GR in the strong regime, to be able to confirm the existence of black holes, and to measure the characteristic parameters *with errors that have no precendent in the whole history of astronomy*. In particular, we will be able to:

2 See `http://astrocrash.net/resources/tde-catalogue`

3 Note that a white dwarf can be tidally disrupted by an intermediate-mass black hole.

4 Such *bursting sources* provide us with some information about the binary, but because of their very low signal-to-noise ratio, they are very difficult to detect, and the parameter extraction becomes extremely challenging.

- Establish the existence of black holes for the first time
- Measure the red-shifted mass $M_{\bullet,z}$ with an error of between 1-0.1%
- Directly measure the spin of the MBH with an error of 0.1 -0.01%

Although it might seem a too strong statement, I deem it fair to say that in astronomy there has not been any other mission conceived, planned or even thought of ever that can do the science that we can do with EMRIs.

13.8 DISCUSSION OF THE RESULTS IN THE BROADER CONTEXT OF THE HABILITATION

For this dissertation I have gathered nine articles that investigate the questions presented previously. I have decided to start from results that are directly related with what we know, with (of course) electromagnetic observations of the GC. The GC is an ideal laboratory for dense stellar systems and, hence, for stellar dynamics and also gas dynamics, since the current observations can be related to the past of the MW, when it contained more gas than now. Apart from understanding better these electromagnetic observations, by studying this problem we address also fundamental questions linked to sources of gravitational radiation.

> Indeed, in this context **[Frag1]**[5] provides us with a simple answer to the problem of missing bright RGs at the GC. In these 15 years, many different scenarios have been proposed, but none of them is efficient enough. In my work, and assuming a single episode of disc formation at the GC, I can explain the absence of these RGs. While one episode suffices, in my paper I note that the more likely situation is that many have occurred. I.e. even in the lower-limit assumption, my results can explain the observations from first-principle calculations. HB stars have an envelope 100 times denser in surface density, so that they require 100 more impacts. This leads to a partial depletion – Only a percentage of them (with low inclnations) will have received envelope damage. For EMRIs this is of particular relevance, because I predict that the removal of the envelope means that the released RGs' cores populate the GC. Galaxies with an SMBH that previously had a gaseous disc extending towards deep radii will have a larger population of EMRI candidates than we had expected so far. These cores are very difficult to detect in infra-red. The core will typically exhaust the H envelope in a few Myrs, so that the radiation will be very faint. Moreover, while it is consuming the remaining H, it will slowly shift in their peak emission to shorter wavelengths, making them invisible in infra-red filters.

Fragmenting discs are also important to investigate to understand how often do SMBHs coalesce in galactic nuclei. We expect that prior to the merger, the two SMBHs

5 For the full titles of the papers, acronyms, as well as an explanation of my contribution and journal references, please see table the table of papers

will be surrounded by a so-called circumbinary accretion disc. How efficiently the torques of the gaseous disc act on to the binary of SMBHs to make it shrink and approach the GW-dominated regime is a question deeply entwined with another one: How effective does gas turn into stars. Apart from the impact on the binary shrinkage, star formation in an accretion disc has a twofold interest: (i) Being so deep in the potential well of the SMBHs, many of these stars will approach one of them and hence are potential sources of TDEs and (ii) those that remain bound but are not tidally disrupted can in principle become a compact object and produce a prominent source of GWs if trapped by one of the SMBHs.

> In this context, **[Frag2]** explores a fragmenting disc, but in this case, and contrary to **[Frag1]**, which was a purely analytical paper, the analysis is based on heavy numerical simulations and the disc surrounds not just one MBH, but a binary of them. The motivation was to study the influence of a fragmenting, star-forming disc on to the evolution of the binary. For this, we adapted an SPH code, GADGET2, to account for star formation via an ad-hoc cooling function that turns overdensity regions into "stars". We run different coolings and explore different prescriptions for the growth of protostars and wait until the system has run out of gas (i.e. until the gas density is negligible), to then use the last snapshot of the simulations to feed pure dynamical integrations with NB6 running on GPUs. We find that the rate of decay in our NB6 simulations is slower than in similar pure SPH simulations in the related literature, which employ a rather rudimentary leap-frog integrator. One particular case that drew my attention had a full stellar cluster promptly falling on to the binary. To investigate it more closely, we run a dedicated NB6 simulation in which we modified the integrator to take into account the presence of the potential well of the gas. We observe for this case a particularly large one but in general an enhanced rate of TDEs, between one and two orders of magnitude than current (although uncertain) estimates for the TDE rate in standard galaxies (i.e. with a single MBH).

The depletion of gas and star-formation can lead to structures such as the one observed in our MW. The presence of the so-called S-stars at the GC is an enigma due to their age, and their dynamical properties –in particular their distribution of eccentricities, have remained a conundrum. Together with my postdoc, I have addressed this second point in an article which I deem to be one of the crucial results of my research, and which has been envisaged by colleagues pivotal towards understanding not only this kinematical characteristic of the S-stars, but the general properties of the innermost stellar dynamics of the GC.

> In the following paper, **[RER]** which can be regarded as the analytical continuation of **[Frag1]**, we study the impact of the stellar disc that results from the depletion of gas around our SMBH on to the stellar properties

of the GC. Making just one single assumption, namely that the currently observed stellar disc was in the past of gaseous nature and reached closer radii to the SMBH, we can naturally explain the observed super-thermal distribution of the S-stars and the absence of more massive stars, and show that both are naturally linked. Up to now these two observational facts had been thought to be unrelated. We predict the existence in the GC of a region of phase-space in which any dynamical object evolves on timescales much shorter than the common ones, which is why we call it the "rapid evolving region" (RER), and define its boundaries. We can explain current observations about the nonexistence of an old segregated cusp in the GC contrary to other works, which crucially rely on the cusp to thermalize the S-stars. Moreover, our theoretical work does not rely on where and how the S-stars were formed, while other models rely heavily on when S-stars were brought to the GC. Besides the obvious consequences for TDEs, the existence of the RER must be analyzed more closely to understand the implications for EMRIs.

These S-stars cannot have been born in-situ at the GC because it is a too violent environment that prevents star formation. If they are born farther away, they must be transported by a mechanism acting on timescales shorter than the ages associated with these very young stars. A possibility explored in detail has been the tidal separation of a binary by the gravitational forces of an SMBH.

[Sep] addresses this problem. With an analytical treatment which relies on a sample of numerical experiments, my colleagues and I proof that the bound star that remains close to the hole is eventually tidally disrupted from a moderate eccentricity orbit, the decay of the bolometric luminosity is slower than the standard case in which the star was initially on a nearly parabolic orbit relative to the black hole. In principle, sampling of the light curves of these electromagnetic flares could reveal the nature of the process. This has also implications for GW sources, since depending on how tidal energy is deposited, is it possible that there will be a gravitational wave signature that attends the electromagnetic signature of the TDE (personal communication by E. S. Phinney).

To obtain an answer to the question of how many EMRI events can we expect for a space-borne observatory, the very first question we need to look into is how stars distribute around an SMBH. This happens to be one of the oldest questions in the context of stellar dynamics and SMBHs, which goes back to the earlies 70's. Whilst we have a very good understanding in the approximation in which all stars in the galactic nucleus have only one kind of mass, the problem happens to be a much harder one when we consider the next logical step: To consider to well-separated mass groups.

[MS] looks into this problem and finds that the commonly-assumed answer based on calculations from the 70's, while mathematically correct, are

> not physically relevant. In this respect, I have found the correct solution to how stars segregate in galactic nuclei, and the solution is more efficient than what we had thought since the 70's. The implications for event rates of EMRIs are important, since our more rigurous mass segregation model predicts a boost factor in the rates that, for a MW-like galaxy can be of up to one order of magnitude more than we believed until now.

Our knowledge of how stars distribute around SMBHs in a cuspy way, following a power-law distribution, breaks when we are too close to the SMBH. Although it does not seem too likely that two stars are relatively close to each other at the scale of milliparsec, there is no guarantee that this is not the case. Motivated by papers that analyse migration and resonances in planetary systems, I investigated the possibility that an EMRI had a close-by perturbing star, and expected to see a Kozai-Lidov-like resonance affecting the evolution of the eccentricity. Per se this would already be fatal because for detection we would have to develop many more waveforms, but what I found was more dramatic: The absence of determinism in the evolution of the dynamical parameters of the system.

> In my **[BF]** paper I look into this problem with a set of numerical direct-summation simulations that take into account periapsis shift and energy loss in the form of GWs. I find that a deviation in the inclination of a perturbing star as small as 10^{-13} degrees as compared to a reference set-up drastically changes the evolution of the eccentricity of the EMRI. This means that the perturbing star destroys determinism in the system. If stars that close to EMRIs are frequent, the detection will be challenging. Moreover, the lack of determinism can also be wrongly interpreted as GR being a wrong theory. It is likely that the fault is to be attributed to a perturbing star than a failure of GR. This possibility is a risk that deserves a closer examination.

For many decades, the EMRI event rate has led us to examine the microphysics around MBHs in dense stellar systems. An EMRI has always been envisaged as a "fragile system", meaning that the captured CO can easily be scattered off from its inspiraling orbit by the successive gravitational tugs from other stars at apocentre[6] . This is so because whilst at pericentre the MBH and the CO are very likely to be alone (but see **[BF]**), the stellar density increases more and more the closer the CO is from apocentre, where the bulk of the stellar system is. A small deflection at apocentre can result into a large deviation at pericentre, so that COs venturing into "too large" apocentres are doomed to be deviated from the orbit, by either being reabsorbed by the surrounding stellar system in larger semi-major axes, or by plunging through the event horizon of the MBH after a few bursts of gravitational radiation, and is called a "plunge". The latter is the end result of the orbit becoming more and more eccentric,

6 One can estimate the radius from the MBH within which EMRIs "are safe", as discussed in my paper, which is of about 0.01 pc

to the point in which it is almost radial, so that it "hits" the MBH. There will be gravitational waves emitted in the process, but so few that the source is basically unobservable because of the low SNR. Moreover, even if it were observable, with a few bursts we cannot do the science that we can do with EMRIs, that comprehend hundreds to thousands of bursts from a coherent source.

> Nature's MBH are very likely spinning, i.e. Kerr black holes and not Schwarzschild. In **[Spin]** I prove that for a spinning MBH it is almost impossible for a CO to become a plunge. This has drastic consequences and implications, because EMRIs originating from the "safe" region have a very low event rate due to the simple reason that we do not have many stars in those radii ($\leq$ 0.01 pc). I show with an analytical relativistic calculation that EMRIs can originate at much larger radii, and that they have a much larger eccentricity. I estimate that the event rate, which depends on the spin and inclination, can be boosted up to two orders of magnitude. Again, this is because they originate where the bulk of the stellar density is. Moreover, since they are so eccentric, they are very loud, and the horizon distance should be located much farther, enhancing the observational volume of a space-borne mission. Also, in view of recent results by Alexander, Merritt, Mikkola and Will, as discussed in the paper, that predict that EMRIs born in the "safe region" are blocked due to a combination of secular effects and relativistic precession, leading to much lower event rates than expected, the EMRIs that I discuss do not suffer of this problem, because they are the end result of a chaotic process, which knows nothing about secularity.

LISA was originally an ESA-NASA concept, which later developed to what we call now eLISA, a 100% ESA L2 approved mission. We had to descope the concept, and this led to the sweet spot of the observatory shifting towards lower masses for the MBH, of about a few $10^5\,M_\odot$. Therefore, when looking for EMRIs, we are actually talking about IMRIs, i.e. mass ratios of about 10^{4-5}. This has important implications, since we must now investigate lower-mass MBH, and IMBHs. This objects are found in dwarf galaxies, ultra-compact dwarf galaxies, and globular clusters. The dynamics around these holes in these loci is quite different from what we have around SMBHs and MBHs in galactic nuclei. Interestingly, it is these kind of mass ratios that we can properly integrate with direct-summation $N-$body integrators. Larger mass ratios typically introduce numerical errors in the integration (although there are some work arounds), because these integrators were developed originally to deal with dense stellar systems without massive objects, in which the largest mass ratios between stars do not exceed more than two orders of magnitude.

> In my work **[IMRI]** I present the first and (to my knowledge and on this date) only existing numerical integrations of a globular cluster harbouring an IMBH with a relativistic capture of a stellar-mass black hole. The merger

leads to the ejection of the IMBH after coalescence. After that, the GC slowly starts to contract as a result of the absence of the heating source at the center. This might lead to another core collapse of the GC, something we do not observe in the simulation in the first 10 Myr after the ejection if the IMBH. I show that the IMRI enters the bandwidth of the detectors with a very high eccentricity, of $e = 0.9987$. One year before the final coalescence, the system still retains a residual eccentricity of $e \approx 0.12$, and ten minutes before merger of $e \approx 10^{-3}$, which is detectable by data-analysis techniques. The detections of this eccentricity, along with the information about masses, could be used as a probe to indentify the host system, where the IMRI formed.

Clusters like the one addressed in **[IMRI]** are very common in interacting galaxies, such as the Antennæ galaxies. There we observe the so-called "cluster complexes", which are relatively small regions (compared with the size of the galaxies) harbouring hundreds or thousands of young clusters. Observational work has proven that a number of them are gravitationally bound, so that the two clusters will merge into one in a relatively short time, as I have shown in another article which I have not added to this habilitation, because of space limit. If a fraction of these clusters in the complexes harboured an IMBH, it is likely that the IMBH will be ejected out of the host cluster because of a relativistic merger with a CO or with another IMBH. We have hence a free-floating IMBH in an environment in which we have a very high density of dense clusters, so that a collision among the two of them is not excluded. Besides from the obvious prominent source of GWs, short after it, the ejection process can also lead to a TDE. Having a coincident –or closely coincident– EM flare is a very attractive possibility, because it would provide us with the associated redshift of the source.

In **[UCDs]** I address this scenario with a combination of two numerical schemes to cover most of the parameter space. On the one hand, I had to explore the different possibilities of how an IMBH collides with a cluster, with a set of about 200 direct-summation $N-$body simulations, and on the other, I had to take into account the fact that the cluster complex evolves with time, it is not static. This leads to cluster-cluster interactions, and a segregation of the more massive clusters to the centre of the complex, which leads to the formation of a very massive cluster, the seed of an ultra-compact dwarf galaxy. For complexes which resemble observations the IMBH is either eventually captured by the seed UCD (in those simulations less dense initially) or by a smaller cluster (in the simulations with the largest concentrations of clusters at the centre) which, however, is close to the centre of the CC, so that it will in the course of time sink down to the very centre, where the seed UCD is settled. The escaping IMBH leads to TDEs and star-star collisions, and both emit an EM flare that might be linked to the previous source of GW as a red-shift indicator.

Part IV

ACKNOWLEDGEMENTS

ACKNOWLEDGEMENTS

I am indebted with Marc Freitag, Tal Alexander, Massimo Dotti, Steve Drasco, Cole Miller, Rainer Spurzem, Rainer Schödel, Simos Konstantinidis, Miguel Preto and Bernard Schutz, both for discussions and their friendship. Philipp Richter has been an excellent mentor in all the time that this work has required, and has shown guidance and patience.

Matrī meæ nīmīrum (id est, nōn mīrum est) vitam meam debeō, aliquid quod verbīs scrībitur exprīmiturque nōn potest. Ea deinde culpābilis est huius horrendæ atrōcem carnificinæ, quam hīc vōbis ostendeō.

Si a alguien le debo haber podido llevar a cabo no sólo la habilitación académica, la de la vida, al hacerme poder recuperar el aliento y energía vital, es a Sonia. Sólo me cabe expresar probremente lo que quiero decir con aquellas palabras de siempre, combinadas con un poco de verso de L. Trinidad: "Rohayhu, roheka, rohechárõ ikatu che ñe'ã opytu'u."